Paul J.A. Zsombor-Murray

ON THE MECHANISMS INVOLVED IN SUPERCALENDERING

Department of Mechanical Engineering

Doctor of Philosophy

ABSTRACT

The operating problems of supercalenders and previous studies of supercalendering mechanisms are reviewed. In spite of observations which suggest random variations in heat source strength a one-dimensional periodic heat source model which describes the heating-up of a supercalender filled roll is found to approximate radial temperature distributions, measured at a number of combinations of speed and load, within filled rolls. Subsurface deformations in a transaxial plane of a filled roll and the rolling friction of supercalender nips have been measured over a range of speed and load. Friction torque varies as $\sqrt{P^3}$ where P is the nip load per unit axial length of roll contact. No correlation between friction and speed or roll temperature was revealed. These measurements, as well as those of filled roll surface topography and hardness, indicate that friction and roll heating are surface phenomena dependent on random deformations of the filled roll.

ON THE MECHANISMS INVOLVED IN SUPERCALENDERING

ON THE MECHANISMS INVOLVED IN SUPERCALENDERING

by

Paul J.A. Zsombor-Murray
B.Eng.(Mech.), M.Eng.(Mech.) (McGill)

A Thesis submitted to the Faculty of Graduate
Studies and Research in partial fulfillment of
the requirements for the degree of
Doctor of Philosophy

Department of Mechanical Engineering
McGill University
Montreal

June 1971

FOREWORD

Supercalenders have existed for about 100 years; about the same length of time as has the Fourdrinier papermachine. Significant design improvements, brought about through increased understanding of how a paper web is formed and dried, have resulted in almost a tenfold increase in speed of the papermachine and product quality and process reliability have been improved, notwithstanding. Although a supercalender is no more than a number of hard and soft roll pairs which rotate and are pressed together while a paper web passes between them so as to be smoothed and polished no corresponding insight or improvement has marked its history. Bigger and faster supercalenders, made to serve bigger and faster papermachines, incur high cost whenever, through faulty operation, they require unscheduled maintenance or produce inferior paper finish. Thus supercalendering has become an expensive way of introducing a relatively small, sometimes negligible or even negative, contribution to the paper manufacturing process. On this account, abandoning the supercalender altogether has been seriously considered.

Because supercalendering is a minor step in the manufacture of paper and because most grades of paper are not finished in this manner it has, in spite of disproportionate cost incurred through the attempt to keep pace with production, received the attention of no more than 200 published articles of all types and no more than perhaps two dozen research projects. These have inevitably been limited and somewhat superficial. The most exorbitant claim which can be made for this work is that, having survived some seven years of evaluation and re-evaluation, it tends to be less limited and less superficial. No design improvements spring forth; at any rate none which the author can visualize. It is felt, however, that a little light has been shed on the fundamental mechanisms which govern the operation and malfunction of supercalenders. The heating-up and subsurface deformation of filled rolls and the rolling friction of a supercalender nip have been measured. These measurements as well as those of filled roll surface topography and hardness support the conclusion that roll heating is predominantly a surface phenomenon brought about through random deformation of the fill material of the soft rolls.

One is sorely tempted to say that now, at last, a few additional experiments will provide answers upon which a better supercalender can be built. But that has already been said; once at the outset of this project and from time to time during its course.

ABSTRACT

The operating problems of supercalenders are reviewed along with previous studies of the basic supercalendering mechanisms. A one-dimensional periodic heat source model is developed to simulate the heating-up of a supercalender filled roll. This model is compared with experimental data obtained at a number of combinations of speed and load and is found to approximate the radial temperature distribution within a filled roll reasonably well in spite of temperature measurements which suggest random variations in heat source strength. The subsurface deformations in a transaxial plane of a filled roll and the rolling friction of a supercalender nip have been measured over a wide range of speed and load. The friction torque is seen to vary as $\sqrt{P^3}$ where P is the nip load in force per unit length of roll face. There appears to be no relationship between rolling friction and speed or filled roll temperature. These measurements as well as those of filled roll surface topography and hardness support the conclusion that roll heating is predominantly a surface phenomenon caused by random deformation of the filled roll.

ACKNOWLEDGEMENTS

I wish to thank:

Dr. D. Atack for his guidance and encouragement throughout the project;

Mr. L.J. Vroomen for designing instrumentation, running apparatus and reducing test data;

Professors W. Bruce and B.G. Newman for making available services and facilities;

Professor S.S. Hyder and Mr. W.D. May for their suggestions and proofreading;

Mrs. V.R. Read for typing drafts and the final thesis.

This work has been financially supported by:

McGill University Department of Mechanical Engineering;

The Pulp and Paper Research Institute of Canada;

The Beloit Corporation;

The National Research Council of Canada.

TABLE OF CONTENTS

	page
GENERAL INTRODUCTION	1
Patents and Prior Investigations	8
Development of an Experimental Program:	
Part-I (Heat Generation)	18
Development of an Experimental Program:	
Part-II (Deformation and Friction)	20
Experimental Apparatus and Instrumentation	25
Laboratory Supercalender Apparatus	25
Nip Loading and Speed Control	30
X-ray Instrumentation	36
Data Logging and Signal Conditioning Instrumentation	39
PART I: THE DEVELOPMENT OF TEMPERATURE IN A SUPERCALENDER	
FILLED ROLL	42
Synopsis	42
Symbols	43
Theoretical	45
Formulation and Analysis of the Model	49
Experimental	58
Instrumentation	58
Results and Discussion	67
Nonuniformity and Instability	72
Application of the Theoretical Model to Experimental Data	89
Approximation of Temperatures Measured in Roll A	96
Application of the Model to the Prediction of Roll Burning	105

TABLE OF CONTENTS (Cont'd)

page

Friction Coefficients Predicted from Heat Source Strength....... 110

Resumé of Results.. 117

PART II: THE MEASUREMENT OF ROLLING FRICTION OF A SUPERCALENDER

NIP AND THE DEFORMATION WITHIN A FILLED ROLL.................... 119

Synopsis... 119

Symbols.. 121

Filled Roll Structure.. 123

Inhomogeneity Due to Air Entrapped in the Fill................. 125

Experimental... 130

Rolling Friction... 130

Filled Roll Surface Hardness................................... 132

Surface Table Measurement of Filled Roll Surface Topography..... 135

X-ray Tracer Instrumentation................................... 135

Results and Discussion... 140

Rolling Friction: High Speed................................... 140

Rolling Friction: Low Speed.................................... 147

Filled Roll Surface Hardness................................... 164

Filled Roll Surface Profile Measurement........................ 175

X-ray Measurement of Fill Deformation.......................... 182

Conclusions.. 200

Direct Conclusions... 200

Suggested Hypothetical Mechanisms of Energy Dissipation......... 202

Claims of Original Contribution................................ 206

Topics for Further Study....................................... 207

TABLE OF CONTENTS (Cont'd)

page

Bibliography.. 209

APPENDIX I

Data Logging and Signal Conditioning Instrumentation.

APPENDIX II

Numerical Computations to Simulate Filled Roll Heating.

APPENDIX III

An Unsuccessful Attempt to Develop a Friction Model Based on Thermodynamically Irreversible Compression of Air Entrapped in the Fill Material.

APPENDIX IV

On the Determination of Friction in Rolling Element Bearings.

APPENDIX V

Description of Equipment, Test Apparatus and Instruments.

APPENDIX VI

X-ray Deformation Data Reduction Programs

ADDENDUM TO APPENDIX V

Mechanical Drawings (folder)

LIST OF FIGURES

FIGURE		page
1	196in. wide industrial supercalender....................	2
2	Supercalender stack schematic...........................	4
3	Tangential extension of material by contact stress......	15
4	No lateral extension caused by contact stress...........	16
5	Tractive strain...	17
6	Supercalender test apparatus............................	26
7	Gear reducer drive with standard configuration..........	28
8	Bearing friction torque calibration apparatus...........	29
9	Pressure control apparatus..............................	31
10	Schematic of nip load controls.........................	32
11	Tachometric pulse generator............................	33
12	Torque calibration.....................................	35
13	X-ray unit...	37
14	X-ray film holder......................................	38
15	Film cutter..	40
16	Convective heat loss from roll surface.................	46
17	Qualitative analogy of heat build-up in supercalender filled rolls..	47
18	One-dimensional heat flow..............................	50
19	Characteristics of subsequent times [Eqn.(16)].........	55
20	Characteristics of subsequent times [Eqn.(17)].........	56
21	The effect of successive heat sources..................	57
22	Instrumented filled roll...............................	60
23	Thermocouple location..................................	61

LIST OF FIGURES (Cont'd)

FIGURE		page
24	Mounting of thermocouples	63
25	Routing of leads	65
26	Temperatures within roll A operating at 470 pli. and 650 fpm	68
27	Temperatures within roll A operating at 940 pli. and 650 fpm	69
28	Temperatures within roll A operating at 1400 pli. and 1700 fpm	70
29	Temperatures within roll B operating at 1400 pli. ~~and 1050 fpm~~	71
30	Irregular rise of temperature within roll A	74
31	Temperature recorded at 3/32in. below the surface at 4 transaxial planes	76
32	Variations in filled roll surface profile roll A	77
33	A typical surface hardness profile of roll A after about 50 hours of running	78
34	Typical fluctuation of gross torque over successive single revolutions of roll A	79
35	Irreproducibility of temperature distribution at constant load	82
36	Oscillograms of temperature fluctuation in roll A at disc 6	85
37	Oscillograms of temperature fluctuation in roll A at disc 4	86
38	Oscillograms of temperature fluctuation in roll A at disc 8	87
39	Thermocouple output resulting from a blow upon the surface of roll A at disc 8 with a plastic hammer	90
40	Free convection about a pair of counter-rotating rolls	93

LIST OF FIGURES (Cont'd)

FIGURE		page
41	Fit of one-dimensional periodic heat source model to experimental data (470 pli. and 1050 fpm.)	98
42	Fit of one-dimensional periodic heat source model to experimental data (940 pli. and 650 fpm.)	99
43	Fit of one-dimensional periodic heat source model to experimental data (1400 pli. and 1700 fpm.)	100
44	Fit of one-dimensional periodic heat source model with heat loss to experimental data (1400 pli. and 1700 fpm.)	101
45	The effect of varying the depth of heat source and the surface heat loss parameter	107
46	A charred section of supercalender roll fill material	109
47	Filled roll manufacture	124
48	Filled roll surface skin	126
49	Simple chains of viscous and elastic elements	128
50	Experimental filled rolls	131
51	Distribution of Rho hardness measurements on filled roll surface	132
52	Rho-meter schematic and application	134
53	Measurement of filled roll surface profile	136
54	Disposition of X-ray tracer elements in a transaxial plane of roll E	138
55	Schematic of set-up used to measure filled roll deformation	139
56	Net friction torque at 4 loads plotted against speed	141
57	Net friction torque at 9 combinations of load and speed plotted against roll surface temperature	143
58	Average net friction torque for two filled rolls plotted against nip load	144

LIST OF FIGURES (Cont'd)

FIGURE		page
59	Average net friction coefficient for two filled rolls plotted against load and speed..................	148
60	Typical fluctuation of gross torque over successive single revolutions of roll D..........................	150
61	Average rolling friction coefficient characteristics of roll A on a speed vs. load plane....................	152
62	Average rolling friction coefficient characteristics of roll B on a speed vs. load plane....................	153
63	Average rolling friction coefficient characteristics of roll C on a speed vs. load plane....................	154
64	Average rolling friction coefficient characteristics of roll D on a speed vs. load plane....................	155
65	Average rolling friction coefficient characteristics of roll E on a speed vs. load plane....................	156
66	Rolling friction coefficient fluctuation characteristics of roll A on a speed vs. load plane.............	157
67	Rolling friction coefficient fluctuation characteristics of roll B on a speed vs. load plane.............	158
68	Rolling friction coefficient fluctuation characteristics of roll C on a speed vs. load plane.............	159
69	Rolling friction coefficient fluctuation characteristics of roll D on a speed vs. load plane.............	160
70	Rolling friction coefficient fluctuation characteristics of roll E on a speed vs. load plane.............	161
71	Average low speed rolling friction coefficients for 5 rolls plotted against load and speed.................	163
72	Typical surface hardness profile of roll A.............	166
73	Typical surface hardness profile of roll D.............	167
74	Typical surface hardness profile of roll E.............	168
75	Hardness contours of rolls E and D....................	169

LIST OF FIGURES (Cont'd)

FIGURE		page
76	Hardness contours of rolls A and C......................	170
77	Hardness contours of roll B............................	171
78	Average friction coefficient vs. average hardness for five filled rolls.................................	174
79	Surface profile roll A.................................	176
80	Surface profile roll B.................................	177
81	Surface profile roll C.................................	178
82	Surface profile roll D.................................	179
83	Surface profile roll E.................................	180
84	Average friction coefficient vs. maximum difference in radius for five filled rolls........................	181
85	Roll E in stack with attached X-ray film cassette.......	183
86	Contact prints of a transaxial view of a loaded supercalender nip......................................	184
87	Tracer image parallax and its correction................	187
88	Tracer displacements in sparse array...................	190
89	Tracer displacements in dense array....................	191
90	Relative position of four adjacent tracers..............	192
91	Direct circumferential and radial displacement differences in roll E while stationary..................	195
92	Changes in direct circumferential and radial displacement difference during a chronological sequence of static loading of roll E....................	196
93	An elementary mechanism of torsional strain energy dissipation....................................	203
94	Data logging and signal conditioning instrumentation....	I-3
95	A cycle composed of reversible gas processes which combine to produce energy dissipation..................	III-1

LIST OF FIGURES (Cont'd)

FIGURE		page
96	The expansion process	III-4
97	Work done during expansion process	III-5
98	Compression processes	III-6
99	Decrease in circumferential porosity through fill compression	III-11
100	Axial compression of randomly oriented fill fibres in transaxial planes	III-11
101	Fibre compression results in the formation of axial, tubular fascia	III-12
102	Possible structure of hypothetical tubes	III-12
103	Deformation of hypothetical tubes under simple radial compression	III-13
104	Isobars in simple radial compression	III-14
105	Possible air pumping through a supercalender nip	III-15
106	Estimated volume of air expelled	III-16
107	Overlap between intruding cylinder and a typical isobar	III-17
108	Dimensions of overlap	III-18
109	Geometry of overlap	III-18
110	Air mass flow carried by rotating fill	III-21
111	Schematic drawing of bearing dynamometer	IV-2
112	Bearing dynamometer installed in stack	IV-3
113	Bearing dynamometer assembly	IV-4
114	Bearing dynamometer components	IV-5
115	Friction characteristics: high speed	IV-6
116	Friction characteristics: low speed	IV-7

LIST OF FIGURES (Cont'd)

FIGURE		page
117	Total drive torque as a function of time.............	IV-10
118	Multigrade oil lubrication as compared with conventional grease packed bearings.....................	IV-11
119	Nip load cell circuit...............................	V-15
120	X-ray firing circuit................................	V-26

MECHANICAL DRAWINGS: EXPERIMENTAL LABORATORY SUPERCALENDER

SC-C-0001	Main frame
SC-C-0003 SC-C-001 SA	Roll blocks and ram
SC-B-0001	Steel roll
SC-C-0002	Bearing block assembly
SC-C-002 SA**	Drive, roll, bearing and frame
SC-B-003 SA	Dynamometer subassembly
SC-A-0004*,-1,-2	Coupling bell housing
SC-A-0005*	Roll end coupling adaptor

GENERAL INTRODUCTION

An important finishing operation in the manufacture of certain high-quality grades of paper involves passage of the paper web between alternate rigid and deformable cylinders in series. This operation, which imparts smoothness and gloss to the paper, is known as supercalendering and it is performed on a machine known as a supercalender.

Fig. 1 is a photograph of a typical industrial supercalender or "stack". It consists of a number of contacting rolls pressed together with their axes in a vertical plane. Only one roll, generally near the bottom of the stack, is externally driven and all other rolls turn as a result of surface traction. In papermaking, supercalendering is employed as a final operation to introduce two desirable properties to the paper surface:-

1) To impart high surface smoothness necessary for good printing. Intricate print detail is more clearly defined on smoother sheets. Supercalendering reduces the thickness of the sheet and hence its opacity. However, the showthrough of inked portions of a sheet printed on both sides is not significantly altered by supercalendering since less ink is required for satisfactory coverage of the smoother surface.

2) To impart gloss. For psychological reasons a glossy sheet is often considered more pleasing to the eye. Some papers are heavily coated and then supercalendered so that colour illustrations will appear like glossy photographs. Such papers are used in advertising copy, magazine covers or book dust-jackets.

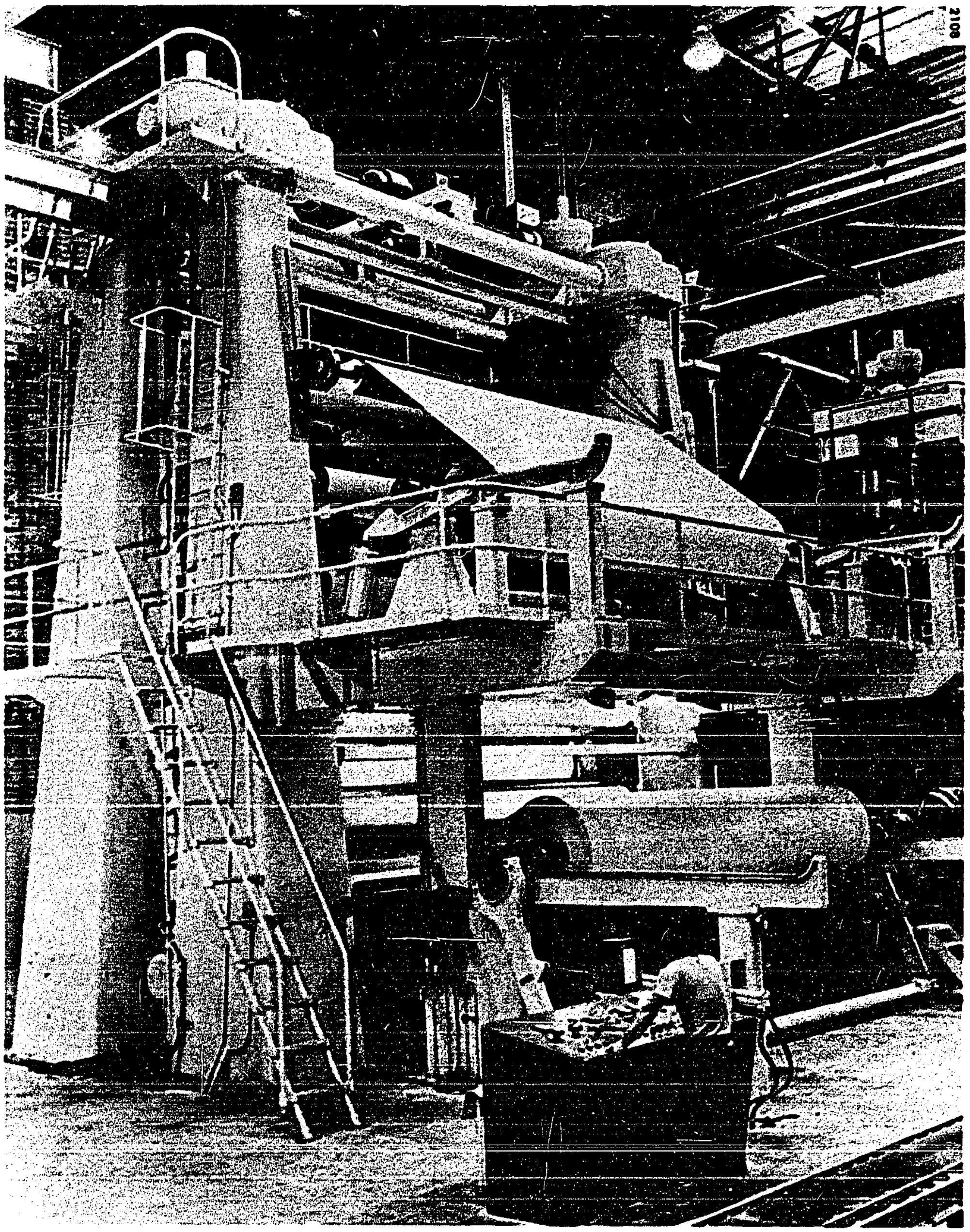

FIG. 1.

196in. Wide Industrial Supercalender

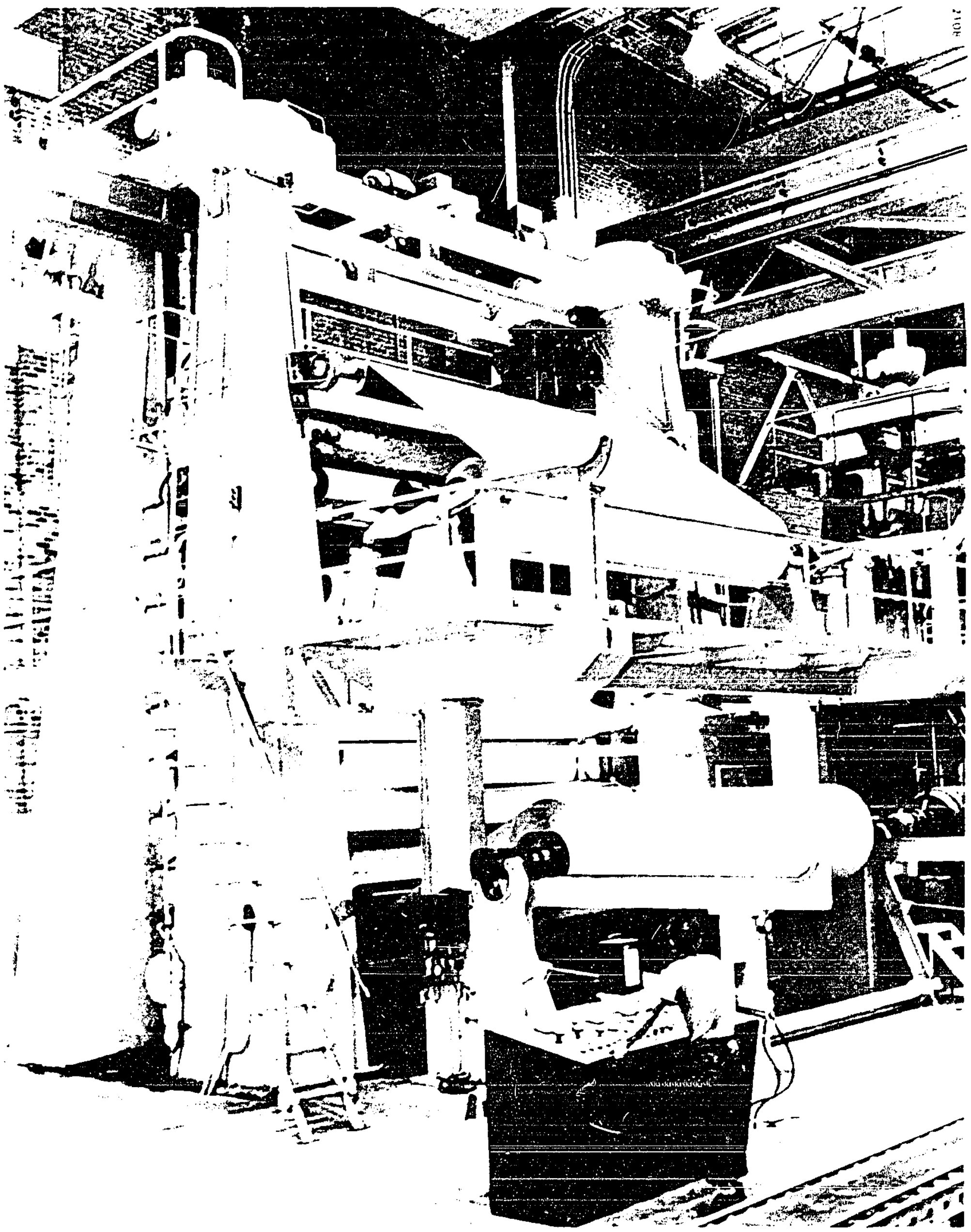

A schematic of a typical supercalender configuration (1) is shown in Fig. 2. It consists of alternate hard, polished steel or chilled iron rolls, and soft rolls. The soft rolls have a thick annular covering or "fill" of axially compressed, transaxially oriented textile fibre. A roll of paper, U, to be supercalendered is hoisted on an unwind stand and threaded into the nips between the hard, I, and soft, F, rolls. In the threading operation the paper web first passes over a pretensioning roll, T, prior to the first hard roll. Between successive nips the web is carried around flyrolls, FL, to remove wrinkles and corrugations. This is accomplished by helical grooves of either hand which are cut into the flyroll surface and proceed towards either end from the centre face of the roll. One or more laterally spring loaded spreader rolls, SP, are used after the first few nips to take up the slack which might develop in the web.

The surface temperature of the rolls is allowed to reach a value of about 150°F through frictional heating since paper and coating binder materials flow more readily at this high temperature. If frictional heating is insufficient to maintain the desired temperature, heat is supplied to the metal rolls which in this case are bored to permit the circulation of a hot fluid such as water, oil, steam or gaseous products of combustion. Sometimes heat is supplied by electrical inductive heating of the roll surface or by resistive heaters embedded in the steel rolls. If the frictional heating is excessive, the steel rolls are cooled either externally by compressed air jets or internally by cool fluid.

In addition to a somewhat elevated temperature, effective super-

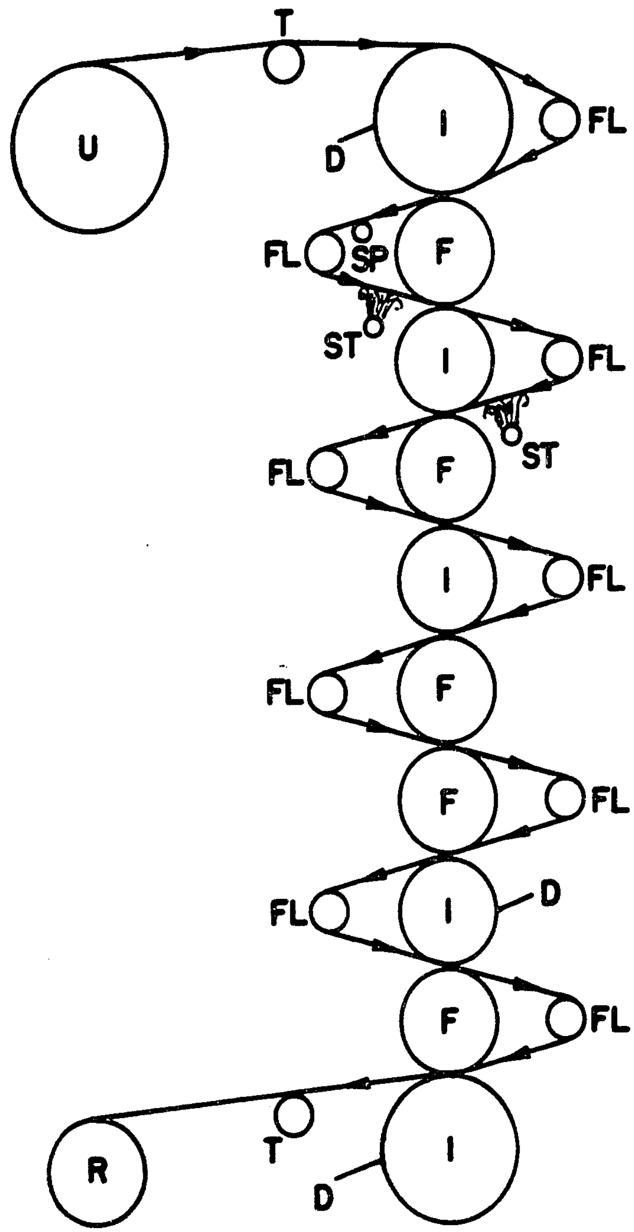

FIG. 2.

Supercalender Stack Schematic

U-Roll of paper on unwind stand, T-Web tensioning roll, I-Steel or chilled iron roll, FL-Flyroll, F-Filled or soft roll, SP-Spreader roll, D-Doctor blade, ST-Steam shower, R-Rewind stand; takeup of paper, ——►—— -Paper sheet; direction of motion.

calendering requires that the paper have a uniform prerequisite moisture content. Moisture and temperature of both sides of the web can be adjusted somewhat by steam showers, ST. Debris are cleared from the steel roll surfaces by doctor blades, D. These are adjustable knife edges which are parallel to the roll axes and just touch the roll surfaces. The doctor blades are oscillated in a direction parallel to the roll axes to help shed debris and control local wear on blades and roll surfaces. Paper emerging from the last nip is held taut by a second tensioning roll, T. To ensure smooth wind-up a Mount Hope roll, not shown, precedes the rewinder, R. This is a rubber covered roll whose axis can be bowed or deflected laterally.

It is generally acknowledged (1) that most of the finishing action occurs in the first two or three nips and that the finishing effect is virtually the same whether the sheet surface passes against a steel or a filled roll. Nevertheless, most supercalenders are usually run with 9 or 10 nips and have, at about mid-stack, an opposing pair of filled rolls so as to reverse the contacting sides of the paper sheet from a steel to a filled surface and vice-versa. At any appropriate operating temperature changes in roll speed appear to have little effect on the degree of paper finish (1, 2).

Operating variables over which there is immediate control are speed and the gross force with which the rolls are pressed together. The density and composition of the material with which the rolls are filled and the axial compressive force to which the fill is subjected during manufacture can, to a certain extent, be specified.

Supercalenders are operated off line with the paper machine owing to the difficulties involved in their operation. In spite of savings in material handling and storage implied by an on-line installation, virtually no one is willing to risk production loss due to faulty or inefficient supercalendering. To reduce the possibility of web breaks, supercalenders are generally operated as slowly as can be economically tolerated. Higher nip loading would permit equivalent finish with fewer nips but only at the expense of shorter filled roll life.

Design specifications of supercalenders and filled rolls are based on pragmatic experience.

Problems and Difficulties

Supercalenders are susceptible to operating problems. Difficulties arise when the paper is too moist or too dry, is too irregular in thickness or moisture content or is improperly coated. The supercalendering operation may suddenly fail to produce the desired finishing effects when any of these objectionable paper properties are encountered. To permit their safe passage through the nips, splices in the paper web, which are the result of breaks which occurred on the paper machine must be indicated by paper tabs or "flags" inserted between successive wraps in the roll so that the supercalender may be slowed and unloaded. Even so, a fold, crease or weak or coarse splice may, as it passes a nip, cause a break in the web or damage to a filled roll. Possible damage to filled roll surfaces caused by sheet defects and foreign material passing through the nips, can be controlled only through careful operating procedures.

Excessive heat, which accompanies high nip loading and high speed, produces soft irregularities or "hot-spots" in the fill. The resulting lack of uniform pressure and temperature along the nip, especially along the first two or three, will cause an uneven paper finish and result in large differences in cross-sheet thickness. Eventually, if such conditions are not corrected, the fill material will burn and spall. A burned filled roll inevitably requires costly repair.

Currently there are a number of popular hypotheses which have been developed to explain certain aspects of supercalender nip finishing action. Most investigators agree that the moist paper surface is subjected to combined compressive and shear stresses at elevated temperature. Under these conditions the surface becomes plastic and flows, acquiring smoothness and gloss. This superficially clear statement of supercalendering mechanism is not reflected in supercalender design or by operating procedures. There is little agreement regarding the stack configuration and operating conditions which would best finish a specific grade of paper. This is probably because no two stacks are alike and because operators must finish all paper grades manufactured by their mill on the few, possibly only one, supercalender at their disposal. In order to save time, an operator will attempt to adapt his machine to a change in paper grade with a minimum change in operating conditions. He will operate at the lightest nip loading, lowest speed and fewest nips compatible with acceptable product quality. To rectify supercalendering faults as they arise, the operator will first make adjustments to nip load, to sheet temperature and moisture with steam showers or to overheated areas of the rolls with compressed air jets. A change in the number of active nips or the replacement of one or more filled rolls is only contemplated as a last resort.

An apparent understanding of supercalender finishing mechanism can be reconciled with somewhat arbitrary design and operating procedures if it is noted that there is no clear indication of how heat and shear stress are produced in a supercalender nip. The hypotheses, like the procedures, remain neither justified nor refuted by conclusive evidence. It is therefore felt that no significant improvement in finishing performance or filled roll life will take place until there is a better understanding of how heating and shear occur in a supercalender nip.

Patents and Prior Investigations

The patent literature on supercalenders is quite extensive. It deals in the main with novel types of filled roll materials, control of roll temperature, control of the magnitude of the pressure and the uniformity of the pressure distribution along the nip, the design of novel roll supporting mechanisms and other ancillary features. Inevitably, patents provide little insight into the basic mechanics involved in the rolling contact between a rigid and a deformable roll which may in turn lead to a better understanding of the paper finishing process.

Some technical literature on supercalendering deals with practical aspects of operating industrial supercalenders (1 - 9). It includes a considerable amount of information regarding changes in the properties of a paper web as it passes through successive nips. Individual studies in this category generally deal with one or two specific grades of paper processed on a specific installation. Such studies do not contribute much to a better understanding of the fundamental mechanisms involved in the process.

In a small number of papers direct attempts have been made to obtain an understanding of supercalender nip mechanics and to develop instrumentation relevant to such studies. Before reviewing this literature, it should be noted that the study of the paper finishing process is confused not only by analytical and experimental difficulties but also by the fact that supercalender design has proceeded through various stages of technological evolution. Schoonkind (10) mentions three historical paper finishing methods which represent stages of development between 1000 and 1800 AD:-

~~1) Hand burnishing of paper sheets~~, placed on a wooden plank, with a smooth piece of stone or glass.

2) The impact of a polished power driven hammer on the sheet placed on a smooth metal anvil.

3) The passage of sheet paper between loaded copper or steel rolls. Sometimes a number of sheets were sandwiched between polished zinc plates as they passed between the rolls.

The means by which paper was finished involved successively less slip between the paper and the polishing members. As higher calendering speeds were sought, the primitive supercalender, in which a finite difference in roll peripheral velocity was introduced through braking the driven roll, gave way to a machine in which roll braking was eliminated and in which roll bearing friction was reduced. Not surprisingly, some of the first experimental investigations into supercalendering dealt with slip between roll surfaces and paper. It was found, as reported by Schacht and Kirchner (11), that paper could be effectively glazed in the absence of intentional slip by applying higher nip loads. By measuring speed at which paper entered and left a nip these authors reported that the roll to roll slip was in the range 0.27% - 0.42%. Mackin, Keller and Baird (12) measured the peripheral speed of the top and bottom rolls in a machine calender stack consisting of hard metal rolls only. Operating at a high nip load of 2040 pli. they reported a speed increase through a stack of 6 nips, of slightly less than 0.25% per nip. They concluded that this speed increase was mainly due to stretching or extrusion of the paper.

Van den Akker (13), by combining the results reported in the two preceding sources, concluded that roll to roll slip is trivial or even nonexistent. He suggested that the combined action of hydrostatic and shear stress was responsible for the finishing action of the supercalender and he referred to Bridgeman's experiment (14) wherein torsional shear was applied to various materials while they were subjected to hydrostatic pressures of up to 710,000 psi. Organic materials appeared to undergo severe structural modification which Bridgeman attributed to atomic or molecular rearrangement. When paper was subjected to the highest hydrostatic stress in the absence of torsion no material transformation was observed. This experimental evidence is claimed by Van den Akker as support for his pressure-shear hypothesis although he admits that pressure in supercalender nips is no more than 10% of that used in Bridgeman's experiments.

Schoonkind (10), however, insisted in including roll to roll slip as a supercalender glazing mechanism. It was claimed that the nip provided three important conditions:-

1) Normal stress for pressing the paper.

2) Tangential stress for plastic deformation.

3) Differences in velocity which produce gloss by polishing the web.

It was also claimed that there were two distinct regions which give rise to a difference in peripheral velocity:-

1) A region of apparent slip due to radial and tangential deformation of the contacting surfaces. In this zone there is no velocity difference between contacting points.

2) A zone of actual velocity difference in the nip caused by slip between contacting points.

Schoonkind felt that an increase in bearing friction accounted for an extended region of actual slip and that if bearing friction were eliminated the glazing effectiveness of the supercalender would be impaired.

A definite peripheral velocity difference between contacting hard and deformable cylinders is supported by reliable experimental data only in cases where the soft material is clearly isotropic, homogeneous and relatively incompressible. Parish (15) shows why a rubber covered roll has the lower peripheral velocity, whether driving or driven by a rigid cylinder. Through a high Poisson's ratio, which is peculiar to rubber, the indentation produces a tangential stretching. This condition would persist so long as nip loading produced a finite radial indentation of the rubber surface and even if the traction between the cylinders approached zero. An explanation, involving tangential shear strain produced by traction, was presented in order to account for a smaller peripheral velocity ratio which was measured when the rubber covered roll drove the rigid cylinder.

Malmstrom and Nash (16) calculated the friction losses incurred in rolling contact between a pair of supercalender rolls. Their calculations were based on the following assumptions:-

1) That only the soft roll is deformed.
2) That the soft roll may be regarded as an isotropic elastic body whose deformation is governed by continuum mechanics theory.
3) That hysteresis losses occur in the soft roll; the extent of these losses is determined by its material properties and the total elastic strain energy incurred in deformation.

An expression for the friction loss, or more specifically the energy loss per second per unit length of the roll face, was developed in terms of the elastic constants of the soft roll, a dimensionless numeric factor describing the hysteresis loss, the normal load, or force, per unit length of roll face, the peripheral speed and the roll diameters. This expression was used to calculate the power required to drive actual commercial supercalender stacks. Fairly good agreement with the measured values was obtained. The treatment was extended to calculate the radial temperature distribution in a typical filled roll under operating conditions and it was predicted that a maximum temperature would travel inward from the surface and reach an equilibrium position at a depth of about 0.6in. It was suggested that this maximum temperature was responsible for the onset of subsurface charring which leads to burn-out, a fairly common failure of overheated supercalender filled rolls. No attempt was made to measure actual temperature distribution within a filled roll nor was the finishing mechanism investigated. No recommendations were made for the improvement of filled roll performance.

Larsson and Gregersen (17) have measured a radial temperature distribution with a maximum some 0.10 to 0.15in. below the surface of a filled roll. They claimed that these measurements supported Malmstrom and Nash's model which was based on a constant roll surface temperature provided by the cooling effect of a paper web. Larsson and Gregersen, however, conducted their experiment without paper.

Mack and Schlegel (18) attempted to apply elasticity theory to supercalender nip mechanics. They formulated a model which described tangential extension of the filled roll surface in the nip due to indentation and traction. The Young's moduli of four filled rolls were measured. These were found to increase continually as the applied load was increased, but at a diminishing rate. Considerable differences in the four moduli versus load characteristics were noted although measurements were made on four supposedly identical filled rolls. Peripheral velocity differences were measured between a pair of adjacent filled rolls, between a pair of adjacent steel rolls and between the paper entering and leaving the stack. The first measurement indicated that the driven roll ran 0.64 to 0.71% slower than the driver, the second failed to produce meaningful results while the third indicated that, on the average, there was a peripheral speed reduction of from 0.075 to 0.46% per nip. The model predicted velocity differences 5 to 10 times larger than any which were measured.

Leporte (19) attempted a viscoelastic extension to the work of Mack and Schlegel and presented evidence of stretching of the filled roll surface in the nip. Peel and Hudson's tachometric measurements (20) of roll to roll angular velocity differences seem to be in agreement with the general consensus that peripheral velocity decreases through a supercalender stack at an average rate of less than 0.5% per nip.

On the other hand Pfeiffer (21) shows, through a series of very convincing photomicrographs, that light scratch patterns cut into the steel roll surface replicate quite perfectly on a sheet passing through the nip. Peel (22) has suggested, however, that the scratches intentionally introduced by Pfeiffer could easily have increased the local tractive effectiveness in the nip, thereby eliminating the local slip or creep which would have otherwise occurred.

Three fundamental mechanisms comprise the essential features of previous work on supercalender nip mechanics. These mechanisms, which might account for observed differences in peripheral or angular velocity between contracting rolls, are:-

1) Tangential stretching of the contacting surface by a normal force or compression.
2) Decrease in distance between the contacting surface and the centre of rotation.
3) Tangential stretching of the contacting surface by a shear force or traction.

The first mechanism can be most clearly illustrated by a material of Poisson's ratio 0.5 in plane strain. Such a material extends in a direction normal to that of an applied compressive stress so that its cross-sectional area remains constant. Referring to Fig. 3, even if no traction is transmitted by the contacting surface, the compressed material, which is in tangential extension under the rigid roll, must proceed from left to right at a greater speed than the tangentially unextended material outside the nip. In this case the deformable cylinder turns more slowly than the indenting rigid cylinder of identical diameter. It might be considered, as a useful concept,

FIG. 3. Tangential extension of material by contact stress

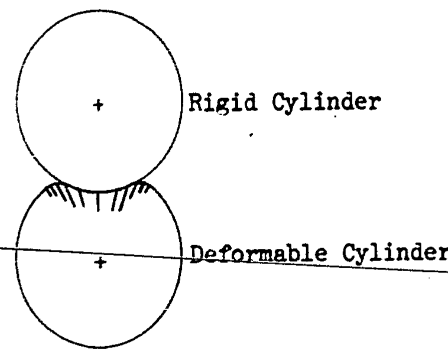

that the deformed cylinder undergoes an increase in effective radius. Slipping need occur in the zone of contact only to the extent necessary to accommodate the progressive stretching, then relaxation, of the deformed material.

The second mechanism, shown in Fig. 4, can best be understood by considering a deformable cylinder made of a material with a Poisson's ratio approaching zero or of an anisotropic material whose radial Young's modulus is much less than the tangential modulus. In plane strain the cross-sectional area of such materials, when deformed by compression, is reduced in proportion to the normal strain. When such a cylinder rotates against an indenting rigid cylinder, the deformed cylinder will tend to turn faster as the indentation is increased. This effect is opposite to that produced by the previous mechanism. The deformed cylinder actually sustains a reduction in radius on its contacting surface. This mechanism implies that, except at points of maximum normal stress, there is slip throughout the entire zone of contact.

FIG. 4. No lateral extension caused by contact stress

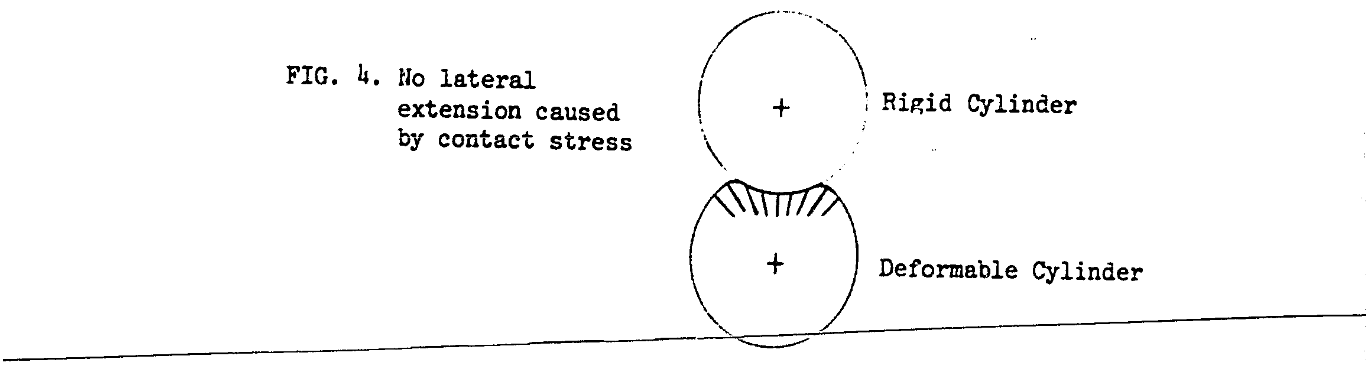

A direct tangential extension or contraction of a deformable surface can be produced by traction. This mechanism can be most clearly visualized if it is assumed to take place between surfaces with a high coefficient of friction so as to transmit traction with negligible compressive strain. Fig. 5a shows a region of the deformable surface in extension as the rigid cylinder is driven. Fig. 5b shows a corresponding region of the deformable surface in compression as the rigid cylinder drives. This effect will produce a difference in angular velocity between a contacting pair of rigid and deformable cylinders of identical diameter only if the deformable material is not perfectly elastic. A perfectly elastic cylinder in single nip contact will incur a skew-symmetric tractive strain distribution as shown in Fig. 5c. In order to produce a velocity difference the deformable material must transmit tractive force to successive nips, must be plastic or viscoelastic or must have a strain propagation rate which is finite in magnitude.

Greenwood, Minshall and Tabor (46) describe how mechanical hysteresis can account for friction when a material such as rubber is deformed in rolling contact: "For example, when a hard sphere rolls over a plane rubber surface the rubber in the front portion of the circle of contact is compressed so that elastic work is done on it; the rubber in the rear portion of the circle of contact recovers elastically and urges the ball forward. If the rubber were ideally elastic the energy restored as the rubber recovered would be exactly equal to the energy stored in the front portion of the contact region and no net force would be required, on this account, to roll the ball over the rubber. In practice, however, all rubbers lose energy when they are deformed, by internal friction or hysteresis, and it is this loss which is reflected in the work required to roll the ball along." Furthermore these authors show, by invoking purely elastic contact deformation, that the energy stored in the forward half of a rolling nip between a rigid cylinder and a rubber plane is

$$\phi_1 = \frac{W^{3/2}}{R^{1/2}} \left(\frac{16}{9\pi^3} \left(\frac{1 - \nu^2}{E} \right) \right)^{\frac{1}{2}}$$

where W is the load per unit length of axial contact, R is the cylinder radius, ν is the Poisson's Ratio and E is the Young's Modulus of the rubber. Thus it is argued that if only a constant fraction of ϕ_1 is recovered in the trailing half of the nip then the torque necessary to overcome rolling resistance is proportional to the 3/2 power of the specific nip load, W. This velocity difference is produced by asymmetric tractive strain distribution as shown in Figs. 5d and 5e. Barring tractive effort large enough to initiate skidding, this mechanism is similar to the first. Slip in the zone of contact is limited to that which is made necessary by a stretch gradient, i.e. if the tangential extension of the deformable surface changes in the contact zone, the deformable surface must move with respect to the rigid surface.

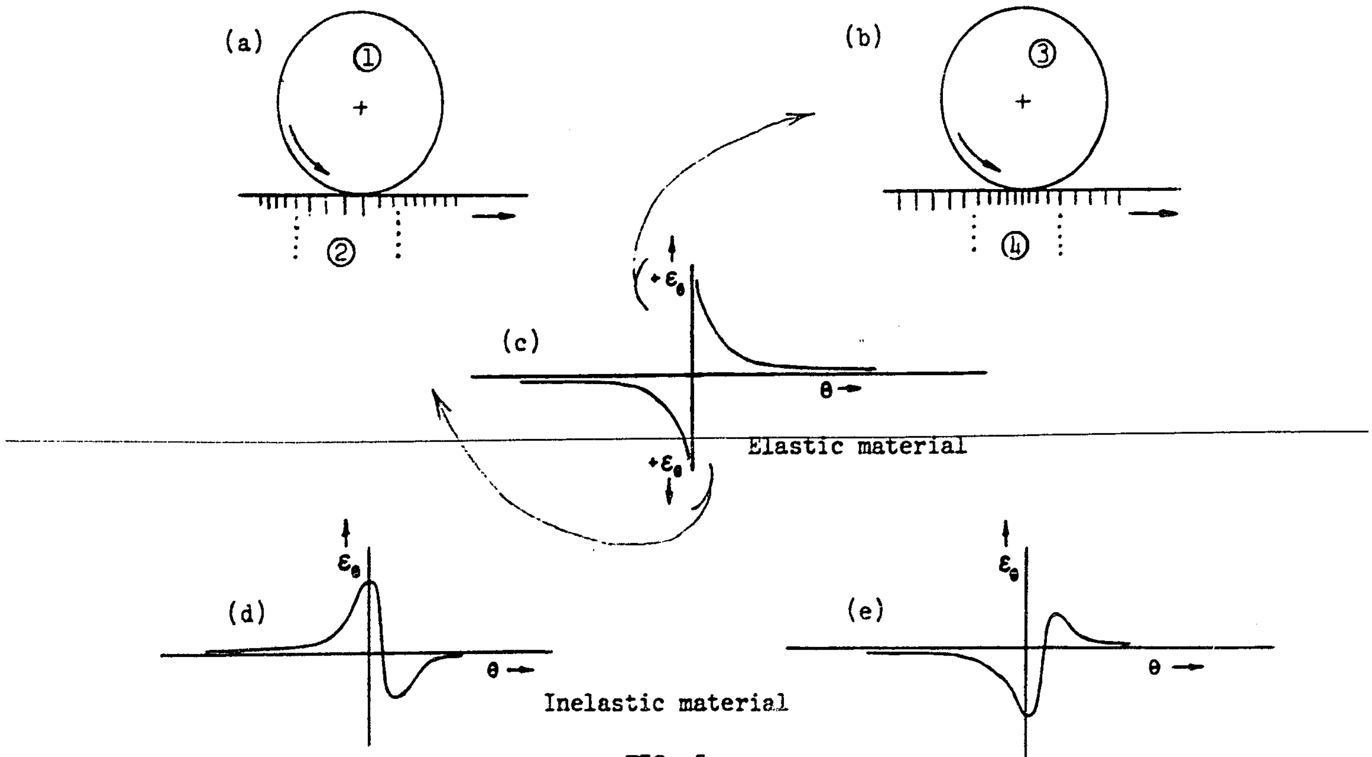

FIG. 5.

① - Rigid cylinder driving, ② - Upstream extension transmits traction,
③ - Rigid cylinder driven, ④ - Upstream contraction transmits traction,
ε_θ - Tangential strain induced by traction,
θ - Angle of rotation from nip centre.

Aside from mechanical hysteresis of the deformable material, the only fundamental concept which is embodied in the preceding descriptions is that the rolling kinematics of contacting cylinders is altered by deformative changes in radius and circumference localized in the region of contact. Nevertheless, it is indicated that such changes can be brought about by three possible mechanisms. One which tends to decrease the speed of a filled roll with increasing nip load, another which tends to increase it. If the filled roll is driving a steel roll the third mechanism will tend to decrease the speed of the latter with an increase in tractive force. This relationship between speed and traction remains if the driving order is reversed.

Desirable finishing effects, as well as undesirable effects which burn or otherwise damage filled rolls, appear to depend solely upon the way in which filled rolls are deformed and upon the extent to which this deformation involves energy loss. Prior experimental investigations on the heat build-up in filled rolls and the rolling friction which causes it have not been satisfactory and no one has measured the internal deformations sustained by a filled roll operating in a supercalender. It was the purpose of this work to pursue these important experimental aspects of supercalender nip mechanics which have been neglected thus far.

Development of an Experimental Program: Part-I (Heat Generation)

The entire published work on heat build-up in supercalender filled rolls consists of the analysis of Malmstrom and Nash (16) and the presentation, by Larsson and Gregersen (17), of a single plot of temperature versus depth beneath the fill surface of a supercalender roll which was run for 15 minutes at a specific load and speed. Considering that damage to filled rolls through burning remains an unresolved problem it was felt that further analysis and more exhaustive measurement of temperature in operating filled rolls would lead, if not directly to a satisfactory solution, to a better understanding of a phenomenon which, in view of its importance, has received woefully little attention.

Malmstrom and Nash's analysis of heat generation and conduction in a filled roll was based on the following assumptions:-

1) The roll surface is maintained at some arbitrary constant temperature because of the cooling effect of the paper web.
2) The heat source and temperature distributions are axi-symmetric about the axis of the filled roll.

The first assumption is unrealistic because in a supercalender the web does not wrap the filled roll but passes through the nip more or less tangentially as illustrated in Fig. 2. The surface of the roll cannot be considered isothermal. A convective boundary condition, wherein the negative temperature gradient is proportional to the instantaneous temperature, is more appropriate. Furthermore, a paper web at some constant ambient temperature will acquire heat from a hot surface, if equilibrium is attained, in direct proportion to the temperature of that surface; even the nip region is convective rather than isothermal. The second assumption may be attacked on the grounds that if heat is continually generated in the fill near the nip, the heat source is moving with respect to the material of the filled roll. With respect to a point in the fill material the source is thus periodic but not axisymmetric.

It was therefore decided to undertake the development of a thermal model of a supercalender filled roll based on a convective boundary condition and a periodic heat source. In order to test this model, measurements of filled roll temperature were made. Three rolls of different material composition were instrumented with miniature thermocouples at 8 radial positions in each of a number of cross-sectional planes. These rolls were run in turn, in conjunction with a steel roll but without paper, over a wide range of speed and nip load. Fill surface temperature at the centre of the roll was measured with a total radiation pyrometer while the thermocouples measured temperatures at various depths between 3/32 and 2 in. Tests were started at ambient temperature and run at constant speed and load while all temperatures were recorded versus time.

Temperature at a given depth versus time as predicted by the thermal model was compared with experimental data. It was shown that the heating up of a filled roll was adequately simulated. Rolls were found to behave as if heated by an axial line source on the surface and that in the presence of surface cooling, a temperature maximum exists beneath the surface for more than half of each revolution. The depth of the maximum at any angle downstream of the nip varies directly as the rate of surface heat loss.

Development of an Experimental Program: Part-II (Deformation and Friction)

The deformations and stresses within elastic bodies in static contact were investigated by Hertz (23, 24). Conditions of contact involving traction between bodies of identical elastic properties were studied by Carter (25) and later by Poritsky (26). Morland (27, 28) extended the work on the rolling contact of cylinders to include the effect of visco-elastic material behaviour. Bentall and Johnson (45) have developed a numerical solution to the problem of contact between rolling cylinders of different elastic modulus. As Schoonkind (10) realized, losses due to supercalender roll bearing friction, however small, cannot be ignored because the rolling resistance of the nips themselves is small and a stack contains 2(N + 1) bearings, where N is the number of nips. Friction loss in ball and roller bearings was treated by Harris (29) and empirically by Palmgren (30) who represented rolling resistance as a function of bearing load, speed, size, type and lubricant viscosity. Attempts (16, 18, 19) to apply existing theory on rolling contact phenomena to supercalender nips have, in the absence of thorough experimental investigation, been unsuccessful in producing improvement of supercalender performance.

Apart from Pfeiffer (20) who carried out an individualistic photomicrographic study of supercalendered paper, investigators have tried to define mainly the stress, strain and slip distribution in a supercalender nip through measurements of:-

1) angular speed of rolls and peripheral speed of roll and paper surfaces,
2) applied nip load,
3) the static Young's modulus of roll fill material in compression and the reduction under load of axial centre-to-centre distance of a pair of rolls in a supercalender stack,
4) rolling friction in a stack from the electrical power consumption of the drive,

and by applying the theories of classical elasticity and continuum mechanics to their own concepts of how a supercalender filled roll is deformed by a rigid cylinder, so as to establish agreement with values of those variables which were amenable to measurement.

Prior to our investigation on a stack consisting of an 8in. diameter steel roll driving a similar roll through an intermediate 12in. diameter filled roll, measurements of the angular velocity of the two steel rolls were made over a speed range of 50 to 500 rpm. and at nip loads from 250 to 2000 pli. These measurements were accurate to one part in 600 at the highest speed and proportionally less at lower speeds. At no time was there recorded a difference in angular velocity between the two steel rolls. Measurements made over the same ranges of load and speed on a 12in. diameter steel and filled roll pair also failed to detect an angular speed difference between the rotating elements although 5 filled rolls of different material composition and fill pressure were tested. The digital counting method used to measure speed could easily have been adapted to yield any desired degree of resolution. It was felt, however, that experimental techniques more powerful than speed measurement could be devised to aid in the study of filled roll deformation and supercalender nip mechanics.

It was not intended to embark upon yet another analysis of a hypothetical supercalender nip. It was felt that measurements of the distribution of subsurface deformation in the filled roll and the rolling friction coefficient of a single nip stack would yield critical information or insight necessary to develop a good mechanical model of a supercalender nip. These two measurements were deemed fundamental to our study because:-

1) The deformed surface of a body is defined by the distortion of material beneath the surface.

2) Mechanical hysteresis of a single nip system is, in the absence of other losses, defined by the torque necessary to overcome resistance to rolling.

Previous investigators have not measured subsurface deformation, and have only expressed rolling friction as the total power supplied to a multinip stack, paying attention neither to the transmitted traction necessary to drive successive nips nor to the obvious losses in the drive system, the bearings and the ancillary equipment.

In order to reduce the number of experimental variables we chose to make our measurements on a stack of the simplest possible configuration; a single nip, without paper, between a 12in. diameter steel roll and driven filled rolls with a face length of 12in. and similar diameter. The deformation of a typical cross-section of fill in a supercalender nip was studied by obtaining X-radiograms of patterns, in polar array, of 1/32in. diameter platinum-20% iridium spheres. These were mounted on a stiff annular cardboard disc which was included between the fill material when the roll was manufactured. Friction loss or the resistance to rolling associated with a single supercalender nip was measured with a strain gauge torque cell. This instrument was mounted so that the only source of friction which was measured, other than the contacting roll faces, was that of the 4 bearings supporting the supercalender rolls. It was found necessary to measure the bearing resistance separately and to subtract this from the total driving torque.

Friction torque measurements were found to be unreproducible. At slow speeds, as the rolls turned through a fraction of a revolution, the measured resistance to rolling was seen to change drastically; sometimes to double the long term mean value and on occasion to become negative for an instant. The deformation measurements revealed large, and apparently random displacements of the fill. The unexpected behaviour of rolling resistance and deformation led us to make profile and hardness measurements over the surfaces of all available filled rolls. These rolls had been finished to within 0.001in. of a perfect cylindrical surface. However, measurements revealed that radial differences of as much as 0.015in. had developed. Surface hardness variations were found to be as much as 30% of the mean value while surface hardness distribution was completely altered during the period over which a filled roll was in operation.

There appeared to be no relationship between the data and the speed at which a particular test was conducted, however, the crude approximation that resistance to rolling varies as $\sqrt{P^3}$, where P is the nip load, appears to be valid. Although a supercalender filled roll can, with some reservation, be regarded as a homogeneous continuum for purposes of heat conduction, no such assumption can be made in connection with its deformative behaviour and rolling friction.

EXPERIMENTAL APPARATUS AND INSTRUMENTATION

Laboratory Supercalender Apparatus*

The supercalendering test apparatus used in this experimental program is shown, along with the panels containing controls and instrumentation, in Fig. 6. Previous experience obtained on a small conventional single nip vertical stack clearly showed the need for equipment adaptable to instrumentation. For this reason and because, a number of times in the course of the experiments, several filled rolls had to be installed in and removed from the stack, an open horizontal stack rather than the usual vertical configuration was adopted.

The frame was made entirely of structural steel plate and rolled sections. The "ways" or parallel tracks, upon which the stack roll bearing blocks rest, were formed by machining a length of the centre portion of the upper flanges of the two channel sections. Other structural steel components were used to ensure the rigidity of the frame, to support the motor and to provide for stack loading and support. A 6in. diameter bore by 4in. long stroke pneumatic cylinder was mounted at the end of each way channel. These cylinders could be operated at pressures up to 750 psi. and apply a loading force on the stack of up to 12 tons. The force is transmitted to the roll bearing blocks from the cylinder piston rods through spacer blocks which rest on the ways. All rolls have a standard shaft end. The roll bearings and bearing blocks are also identical and interchangeable. Each shaft has a 3in. diameter bore all the way through to accommodate either a drive shaft or instrument

---

* See APPENDIX V for a more detailed description and drawings.

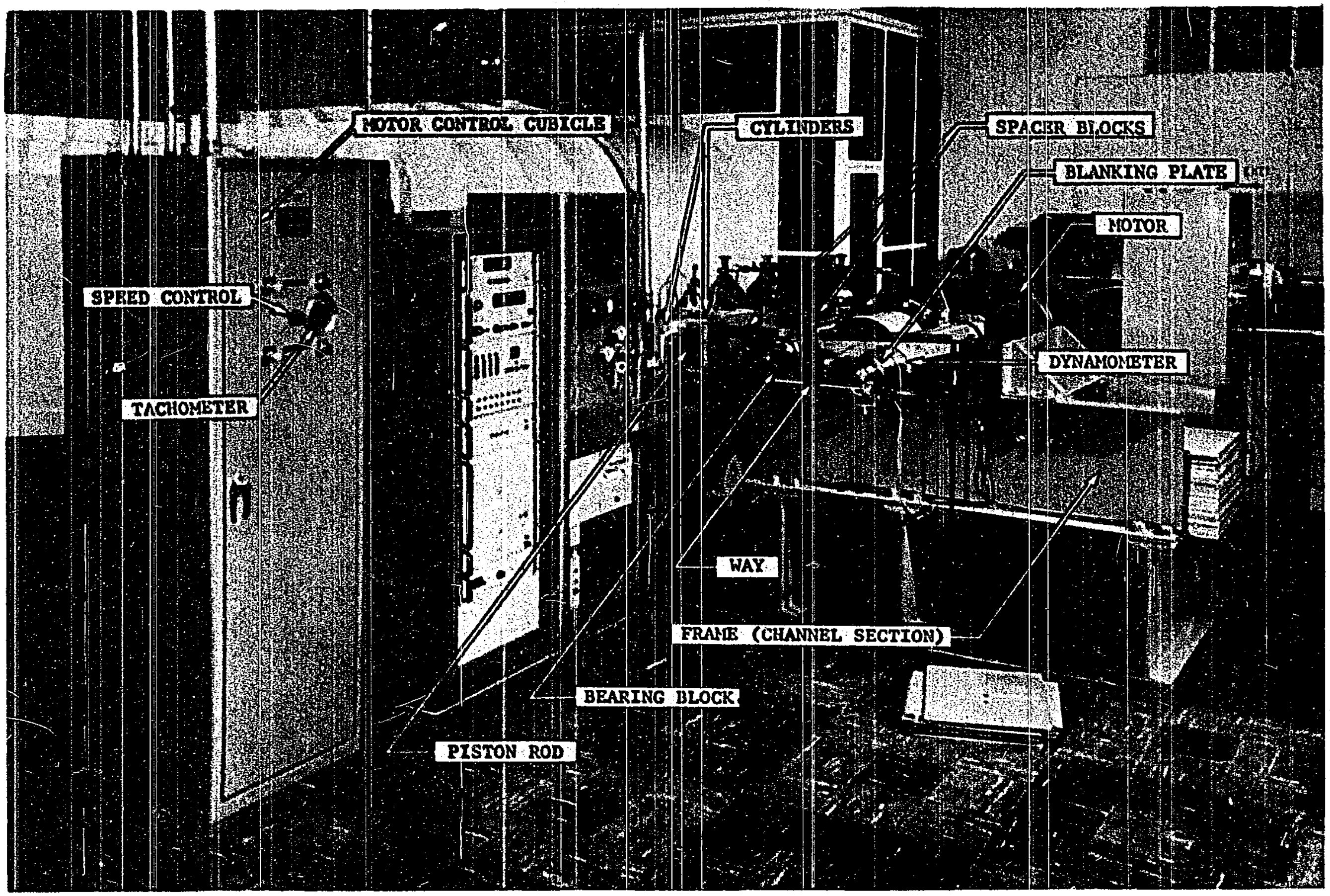

FIG. 6.

Supercalender Test Apparatus

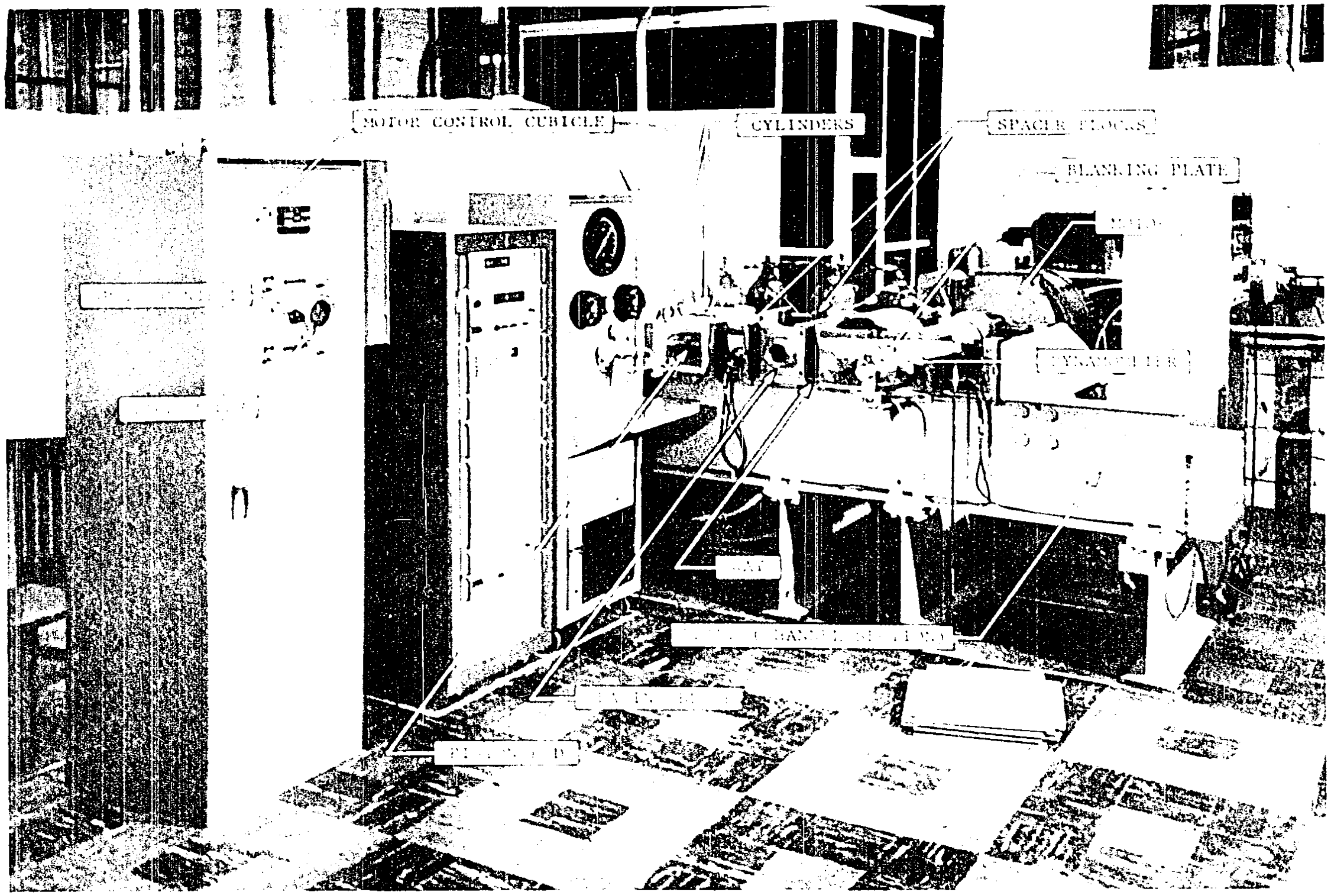

FIG. [illegible]

[illegible] Test Apparatus

signal leads.

The stack is driven by a separately excited shunt-stabilized 30 hp. direct-current motor whose speed is infinitely variable down to 1/40 of full speed. The motor can operate over two speed ranges to a maximum of 1150 rpm. or 2600 rpm. Power is supplied by a motor-generator set and speed control is provided by a modified Ward-Leonard system. The drive transmission was designed so that any roll in the stack could be driven through a torsion dynamometer or torque meter simply by moving the motor to the appropriate position on its mounting. An automotive universal coupling connects the motor to a 32in. long shot-peened steel quill shaft which passes through the roll bore and connects to a second universal coupling. The dynamometer is contained in an extension sleeve bolted coaxially to the end of a roll. A second universal coupling is attached to the inside of a blanking plate on the sleeve. This drive is self-aligning and whenever it is disassembled and reinstalled or whenever the motor is moved no subsequent adjustments are necessary. A 25:1 double helical gear reduction unit can be installed, as shown in Fig. 7, between the motor shaft and the first universal coupling to permit operation of the stack at very low rolling speeds and to permit the measurement of rolling friction on impending motion or breakaway.

Friction torque of the stack bearings can be conveniently measured on this apparatus by mounting the bearings, four at a time in their bearing blocks, as shown in Fig. 8. Further details of these measurements, along with other work on the losses in rolling element bearings, is given in APPENDIX IV.

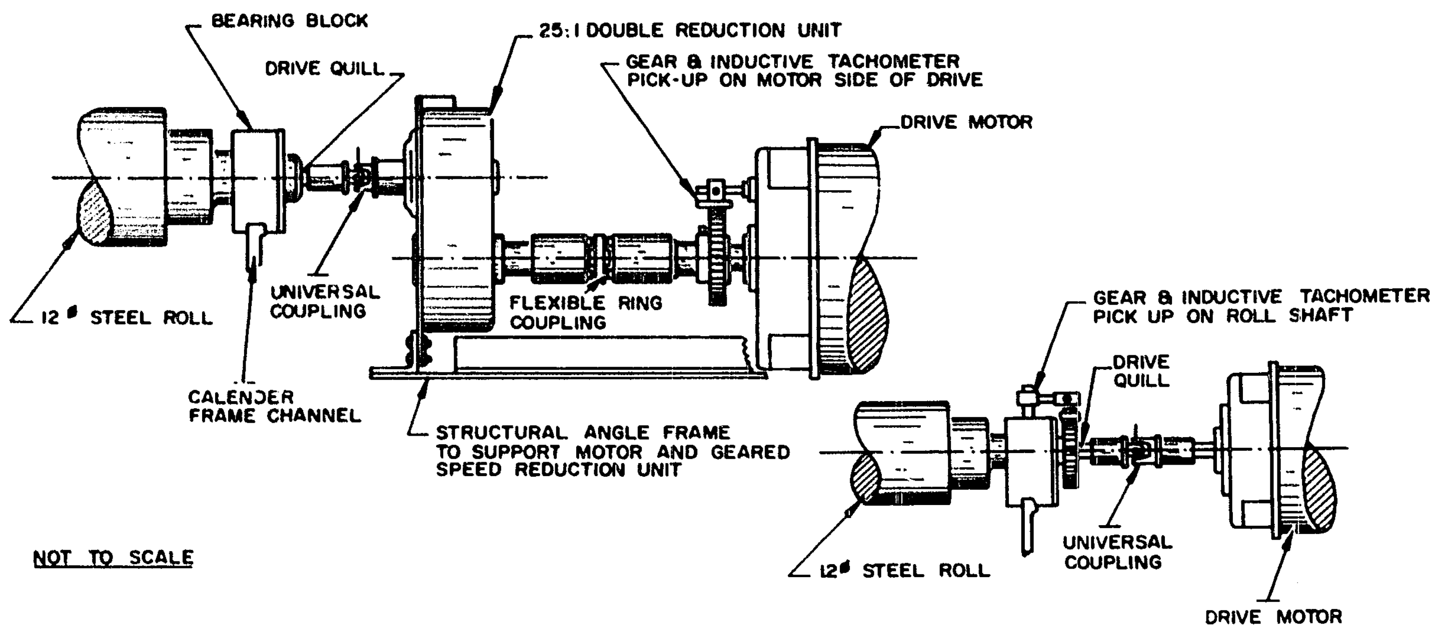

NOT TO SCALE

FIG. 7.

Gear Reducer Drive with Standard Configuration (inset) for Comparison

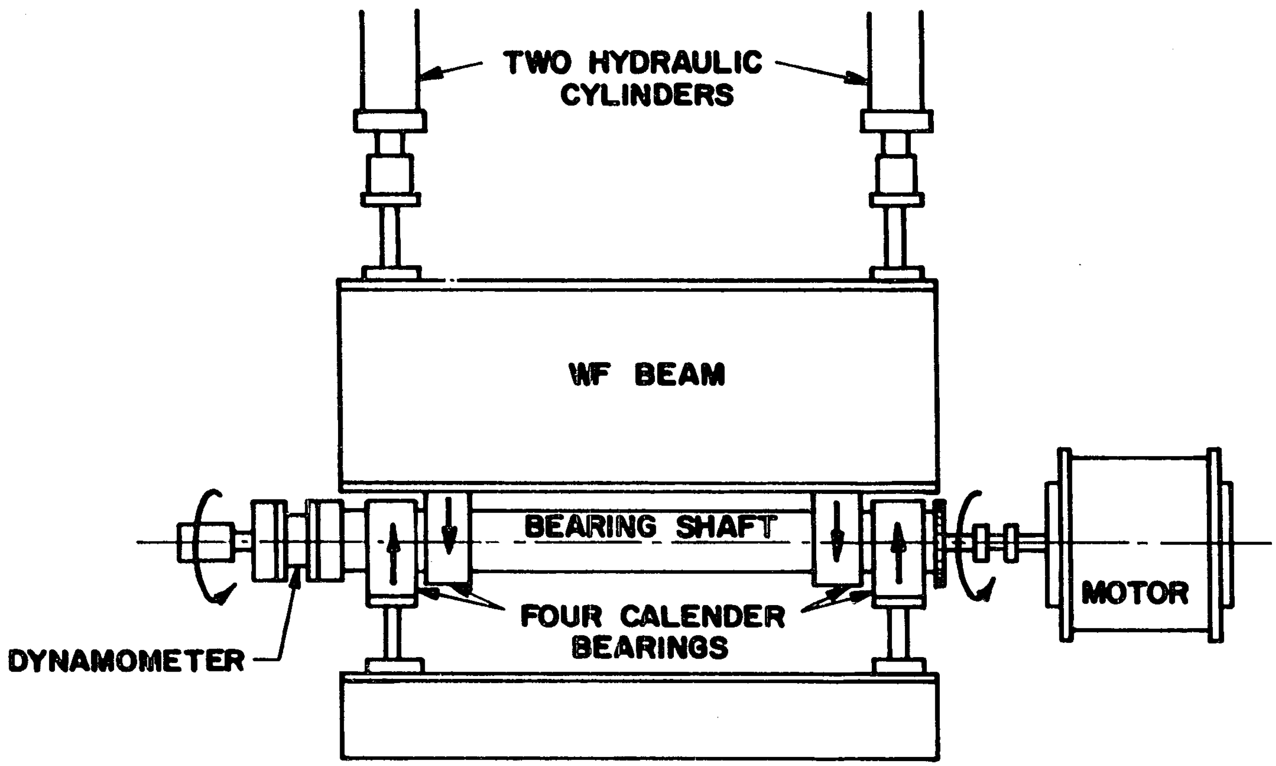

FIG. 8.

Bearing Friction Torque Calibration Apparatus

Nip Loading and Speed Control

The stack is loaded by supplying compressed gas to the rear ports of the two pneumatic cylinders. The pressure control apparatus, the cylinders and the five high pressure gas reservoirs are shown in Fig. 9. Pressure can be applied independently to either cylinder. Utility compressed air supply can be used to provide nip loads up to 500 pli. on a 12in. long roll face. Nitrogen, from the reservoirs, is used to apply higher loads. Total load applied to the nip was measured as

$$F = A(p_1 + p_2)$$

p_1 and p_2 are the pressures applied to the first and second pneumatic cylinders respectively and A is the cross-sectional area each cylinder bore. Fig. 10 is a labelled schematic of the nip load controls.

The motor control cubicle is shown in Fig. 6. Speed control is effected by a 10-turn potentiometer or variable resistor with micrometer adjustment. A tachometer is located immediately to the right of the speed control. This instrument monitors the speed of the motor shaft. Each roll in the stack is equipped with a tachometric pulse generator as seen in Fig. 11. The angular velocity of each roll in the stack can thus be measured independently. Each pulse generator consists of a 72 tooth, 6in. diameter steel gear mounted on the end of a roll shaft and a telephone receiver cartridge located, with its diaphragm removed and the pole pieces of its permanent U-magnet at a minimum clearance from the gear teeth, on an adjustable support attached to a bearing block. This arrangement can be seen in Fig. 11. The

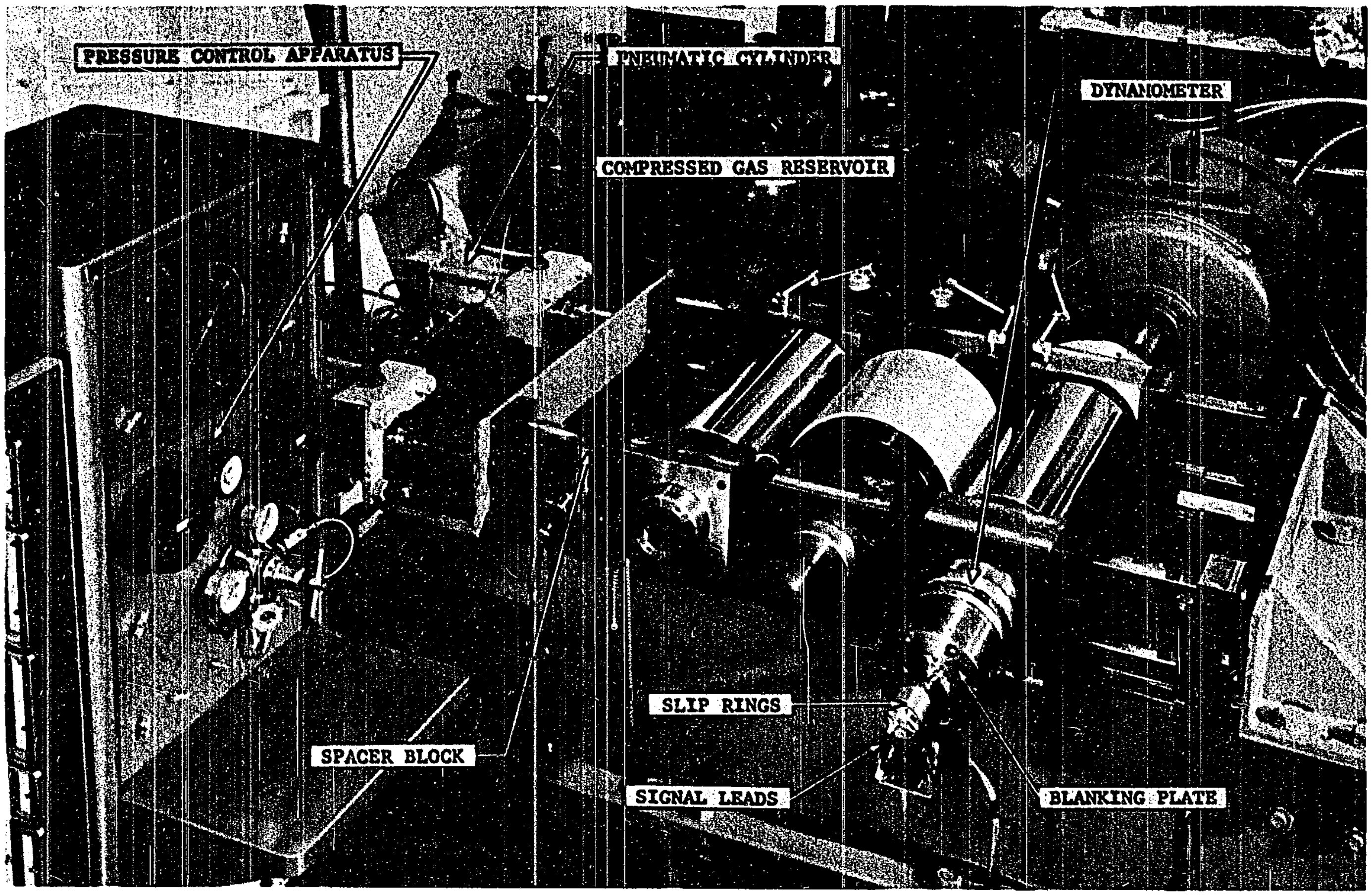

FIG. 9.

Pressure Control Apparatus

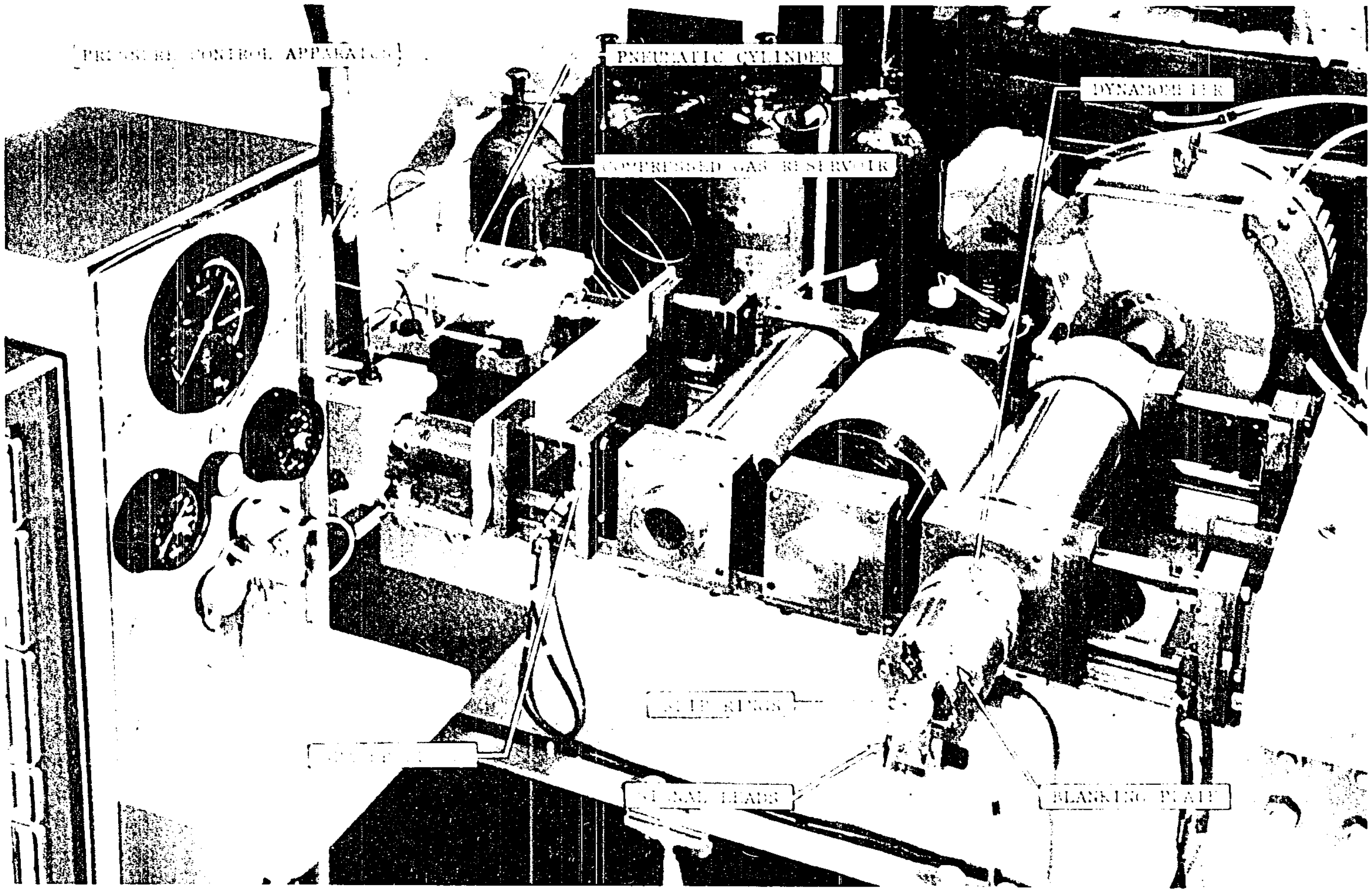
PRESSURE CONTROL APPARATUS
PNEUMATIC CYLINDER
COMPRESSED GAS RESERVOIR
DYNAMOMETER
SLIP RINGS
SIGNAL LEADS
BLANKING PLATE

[illegible]

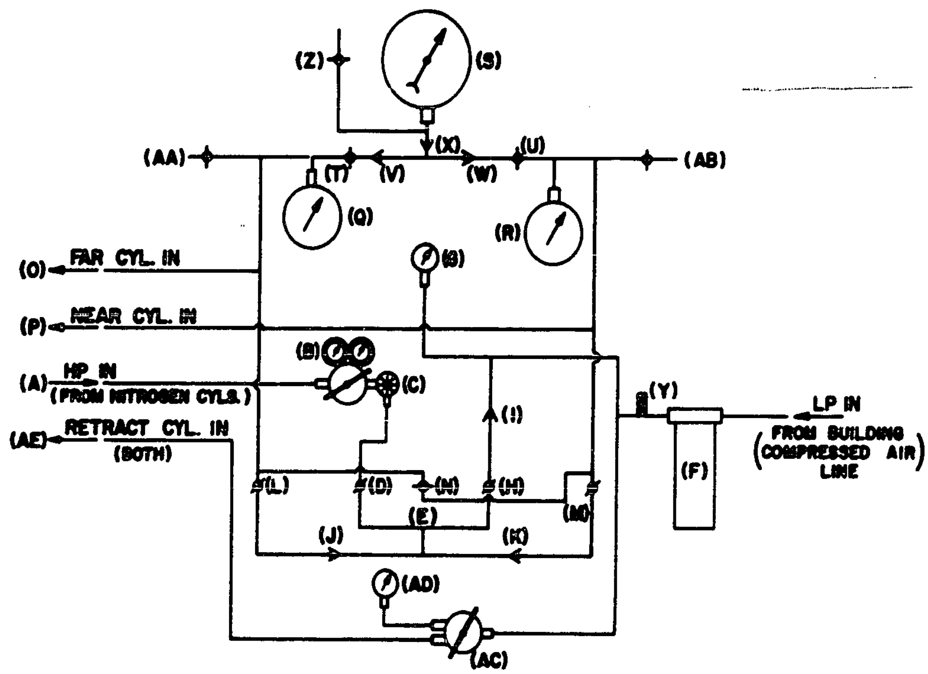

FIG. 10

Schematic of Nip Load Controls

A-Nitrogen reservoirs, B-Pressure reducing and relief valve, C-Rate control needle valve, D-Shut-off cock, E-Distribution branch to either cylinder, F-Air filter, G-Compressed air supply gauge, H-Compressed air supply shut-off cock, I-High pressure check valve, J&K-Separate cylinder check valves, L&M-Separate cylinder shut-off cocks, N-Equalizing cock, O&P-Separate cylinder supply lines, Q&R-Separate cylinder monitoring gauges, S-Precision gauge, T&U-Separate cylinder connections to precision gauge, V,W&X-Cylinder isolation check valves, Y-Safety valve, Z,AA&AB-Vent cocks for each gauge, AC-Cylinder retraction pressure reducing valve, AD-Cylinder retraction pressure gauge, AE-Common cylinder retraction pressure supply line.

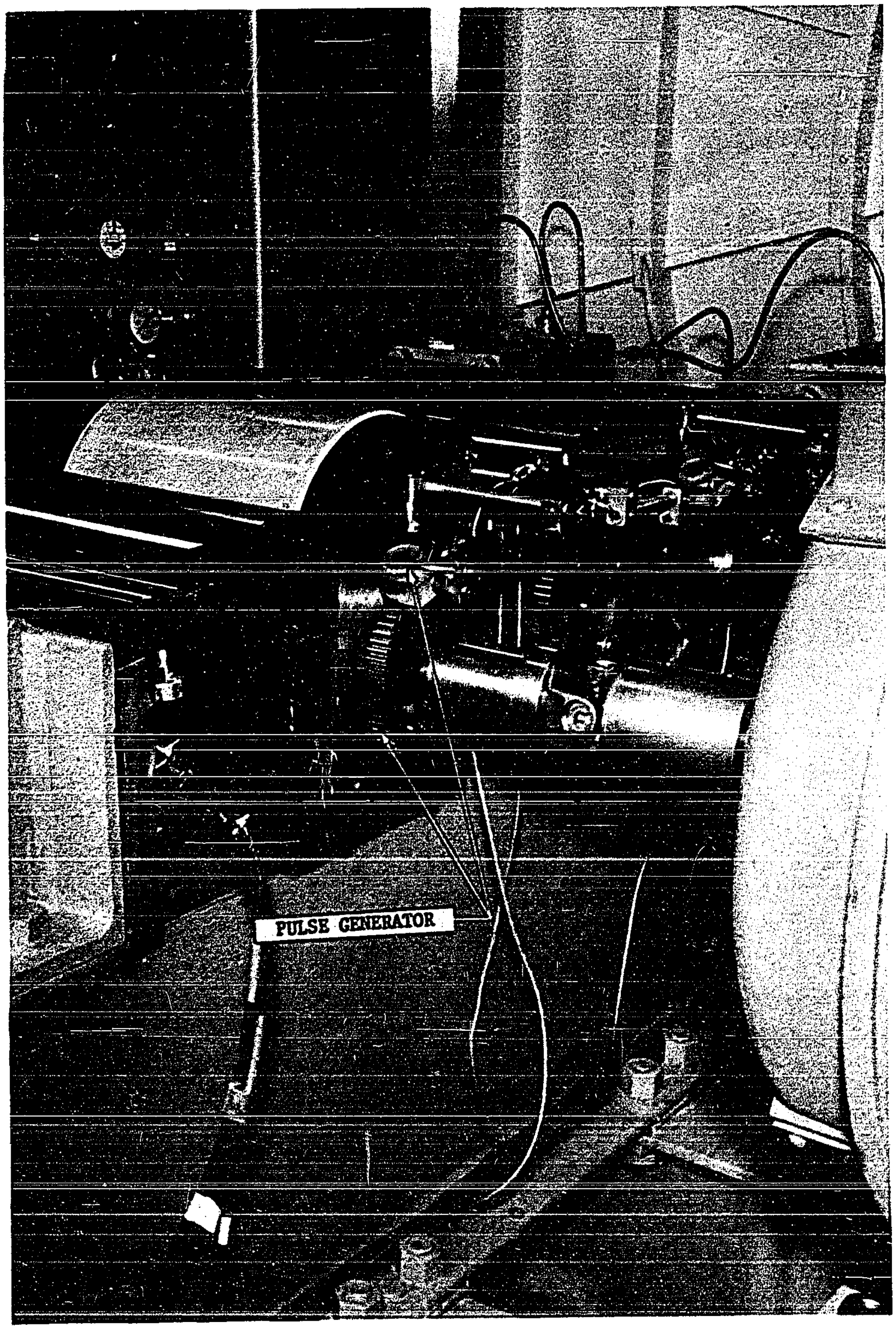

FIG. 11.

Tachometric Pulse Generator

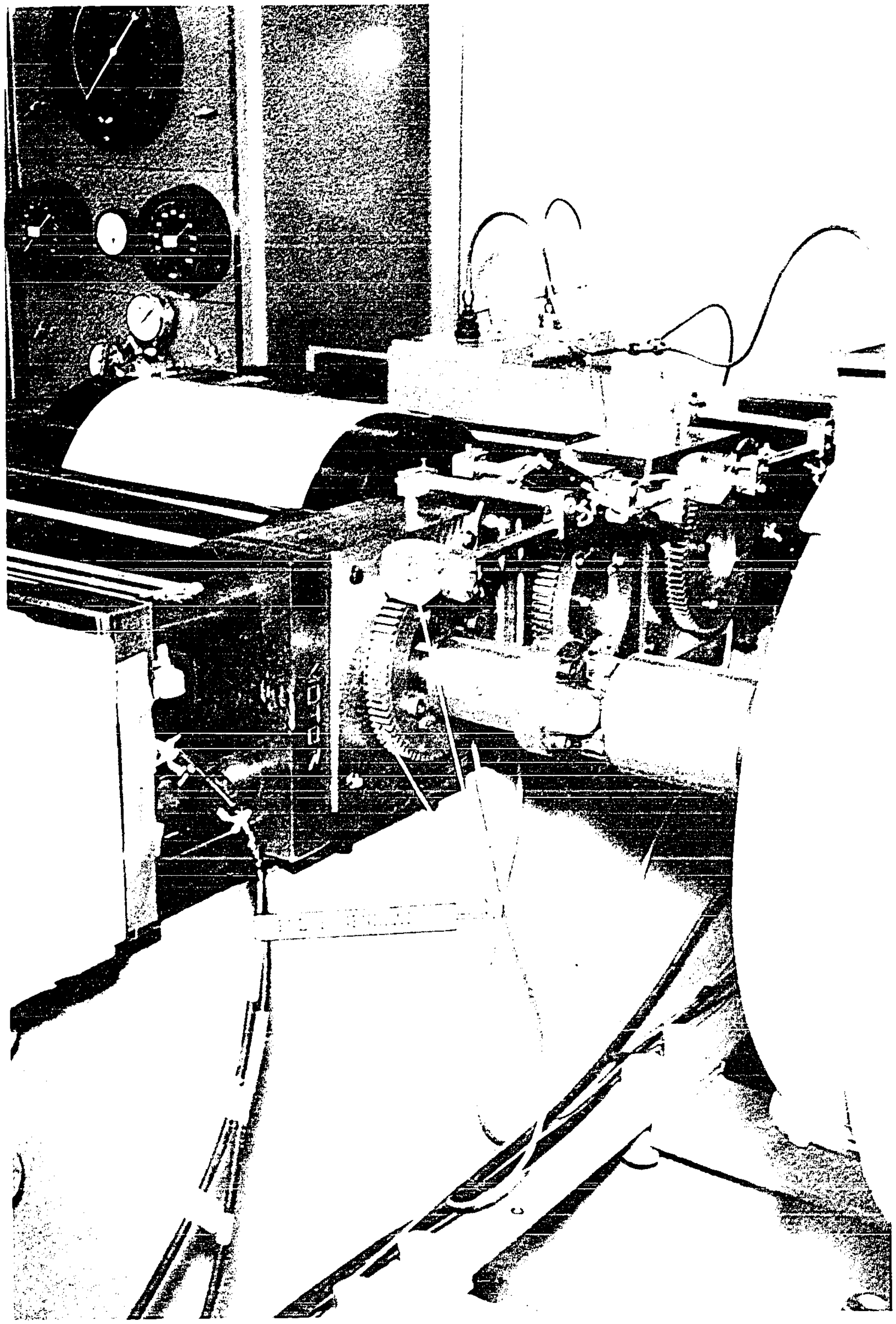

frequency of the alternating voltage produced by the rotation of the gear is induced in the coil of the receiver and is proportional to the speed of the roll on which the gear is mounted. This frequency is measured, without amplification, by a digital counter. The pulse generator produces 72 cycles per revolution and is accurate to ±1 Hz. over the entire speed range down to 20 Hz. Accuracy can be maintained at very low speeds, while using the gear reducer, by using a single pulse tachometer on the motor shaft. In this way, 1860 cycles per revolution of the roll are produced.

Drive torque was measured by a reaction type, bonded strain gauge torque cell shown in Fig. 9. This dynamometer rotates with the roll and the signal leads are attached to instrument slip rings. Torque calibration was carried out as illustrated in Fig. 12 by applying weights, up to 1000 lb., in 25 lb. increments, to a calibrating yoke.

Specifications of the torque cell and the instrument slip rings are as follows:-

1) Lebow Associates, Inc. Reaction Torque Cell #2406-101

   Output: linear to 40 mv. at 10,000 lb. in. torque

   Input: 20 v. D.C.

   Capacity: 10,000 lb. in. maximum with 50% overload

   Type: temperature compensated single full bridge bonded wire strain gauge.

2) Northern Precision Laboratories Instrument Slip Rings #800050-1

   Number of conductors: 6; 4 used

   Speed range: 0 to 3000 rpm.

   Ring material: coin silver

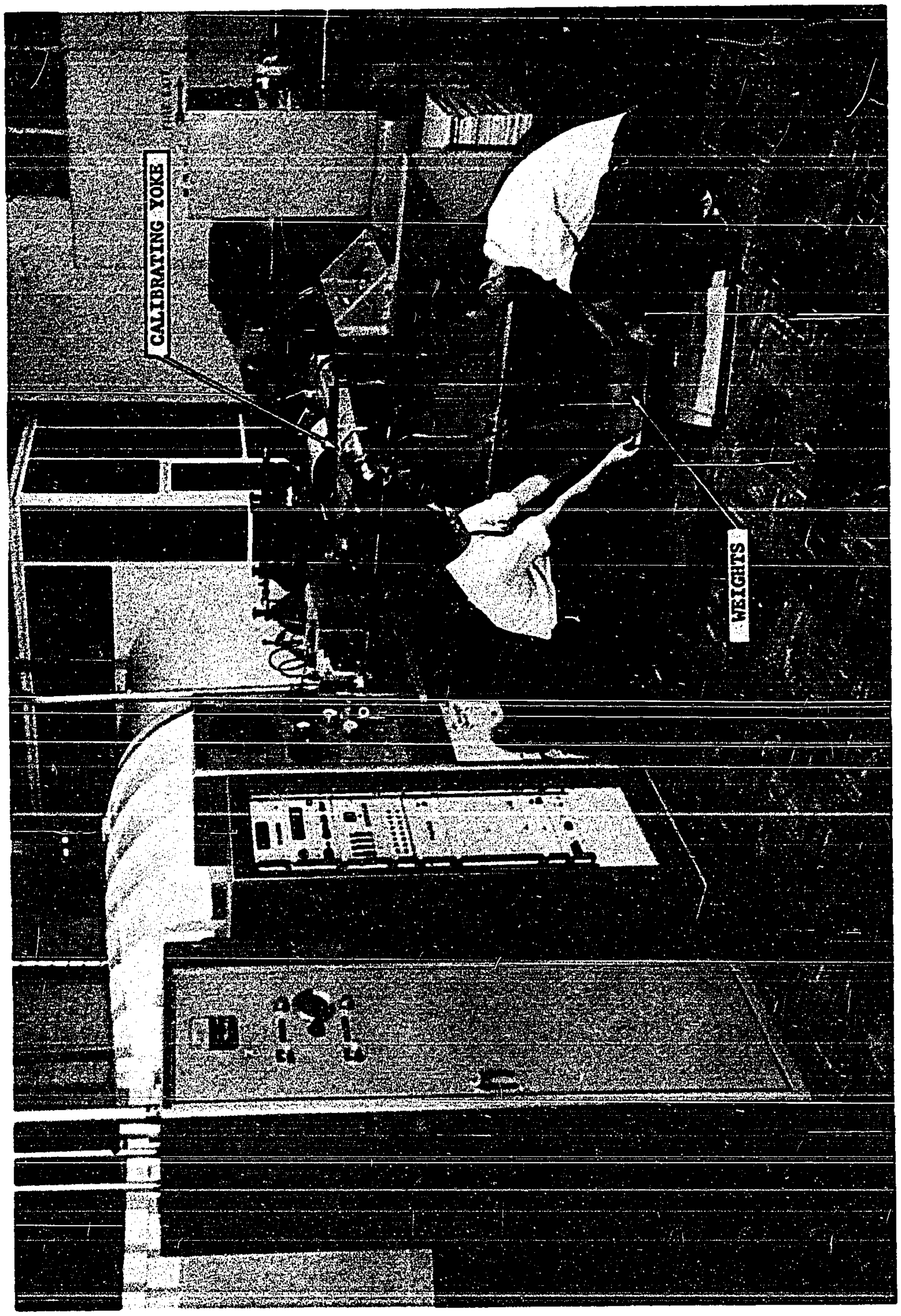

FIG. 12.
Torque Calibration

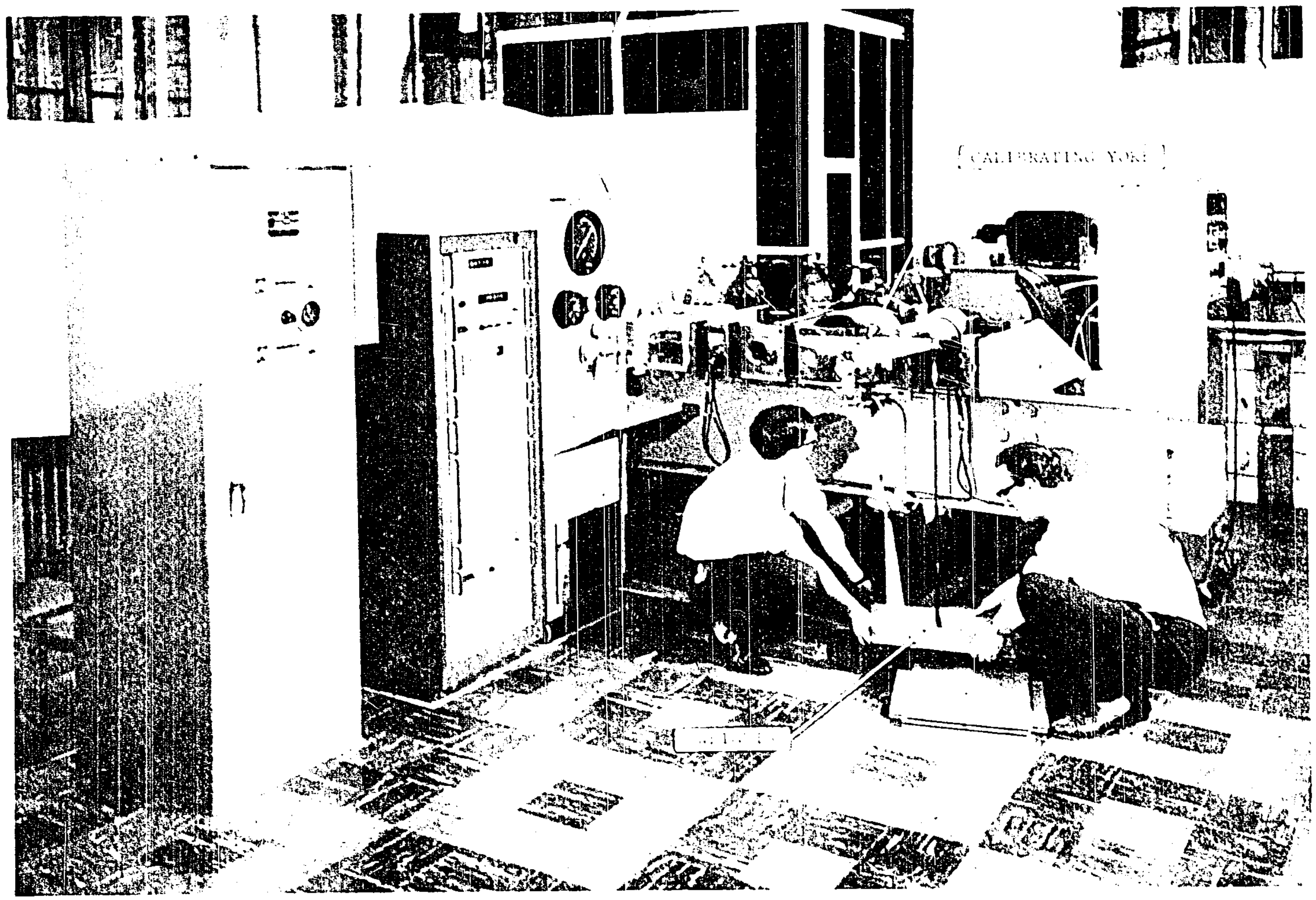

FIG. [illegible]

[illegible] Calibration

Brush material: silver/graphite

Maximum noise: ≤ 0.5 µv.

X-ray Instrumentation

The subsurface deformation of a supercalender filled roll was measured in the nip region in a specific transaxial plane using a high speed X-ray apparatus. Radiograms, taken while the supercalender was operating, were used to map the disposition of an array of small dense metal spheres embedded within the fill material.

The X-ray unit, shown in Fig. 13, consists of a 30 kv. power supply, a parallel/series capacitor bank or pulser, the delayed trigger amplifier for accurate adjustment and synchronization of the occurrence of the X-ray "flash", the X-ray tube and its holder and a distribution system for dry nitrogen and "Freon-12" high voltage insulation gases.

A special X-ray film holder or cassette, shown in Fig. 14, was constructed. It has the shape of an annular disc and is attached to the nut of a filled roll, concentric with, and perpendicular to, the roll axis so as to rotate with the roll. Two pieces of arc shaped film are inserted under light-tight plastic covers and are sandwiched between "Radelin-TI2" intensifying screens. For this application a high speed X-ray film, such as "Kodak Royal Blue Medical" or "Dupont Cronex-II Metallurgical" is required.

Since the array of spheres is in a transaxial plane 4in. from the film and the distance from the X-ray source to the film plane is 25in., the images of the spheres are spread or fanned out about the

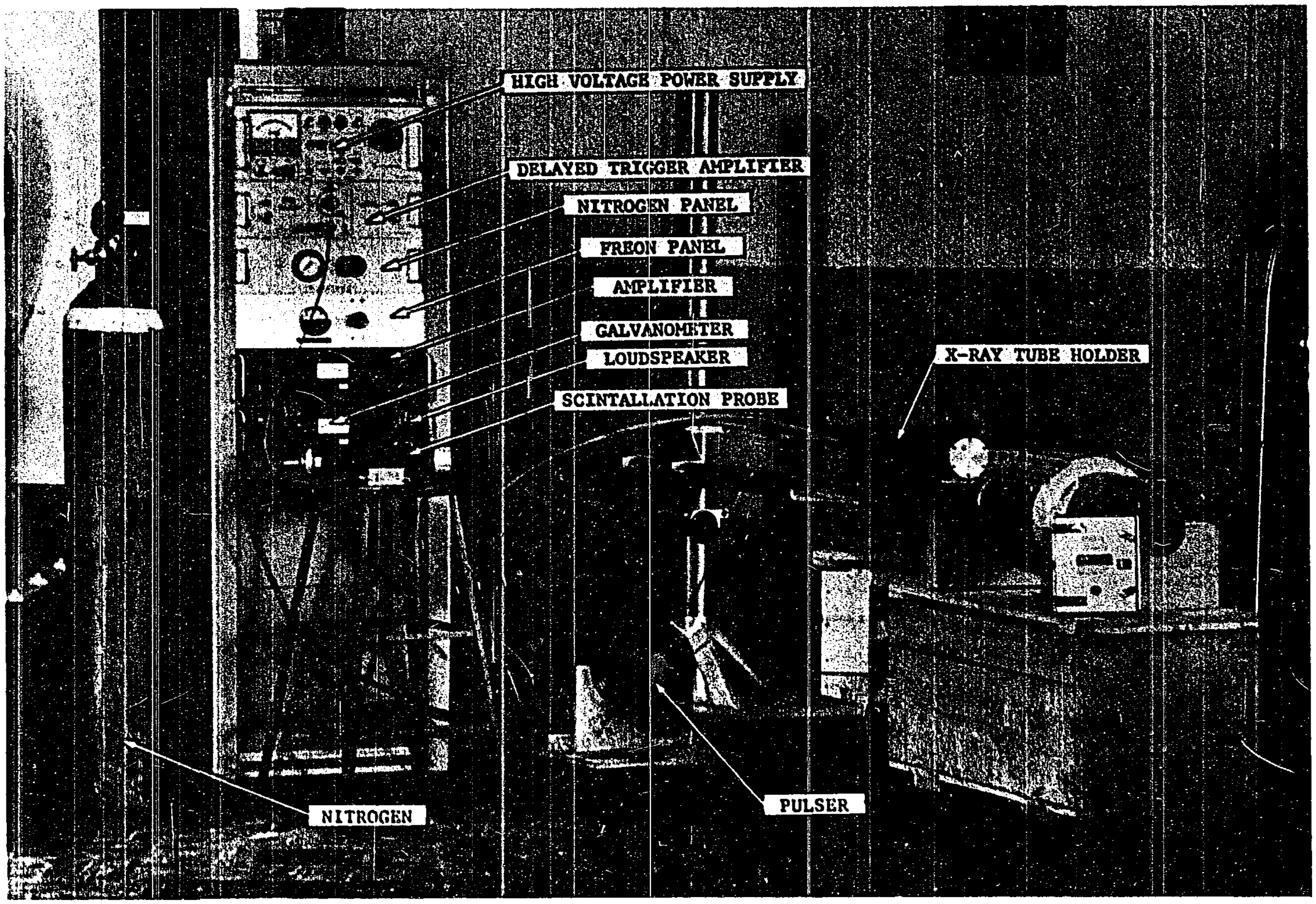

FIG. 13.

X-ray Unit

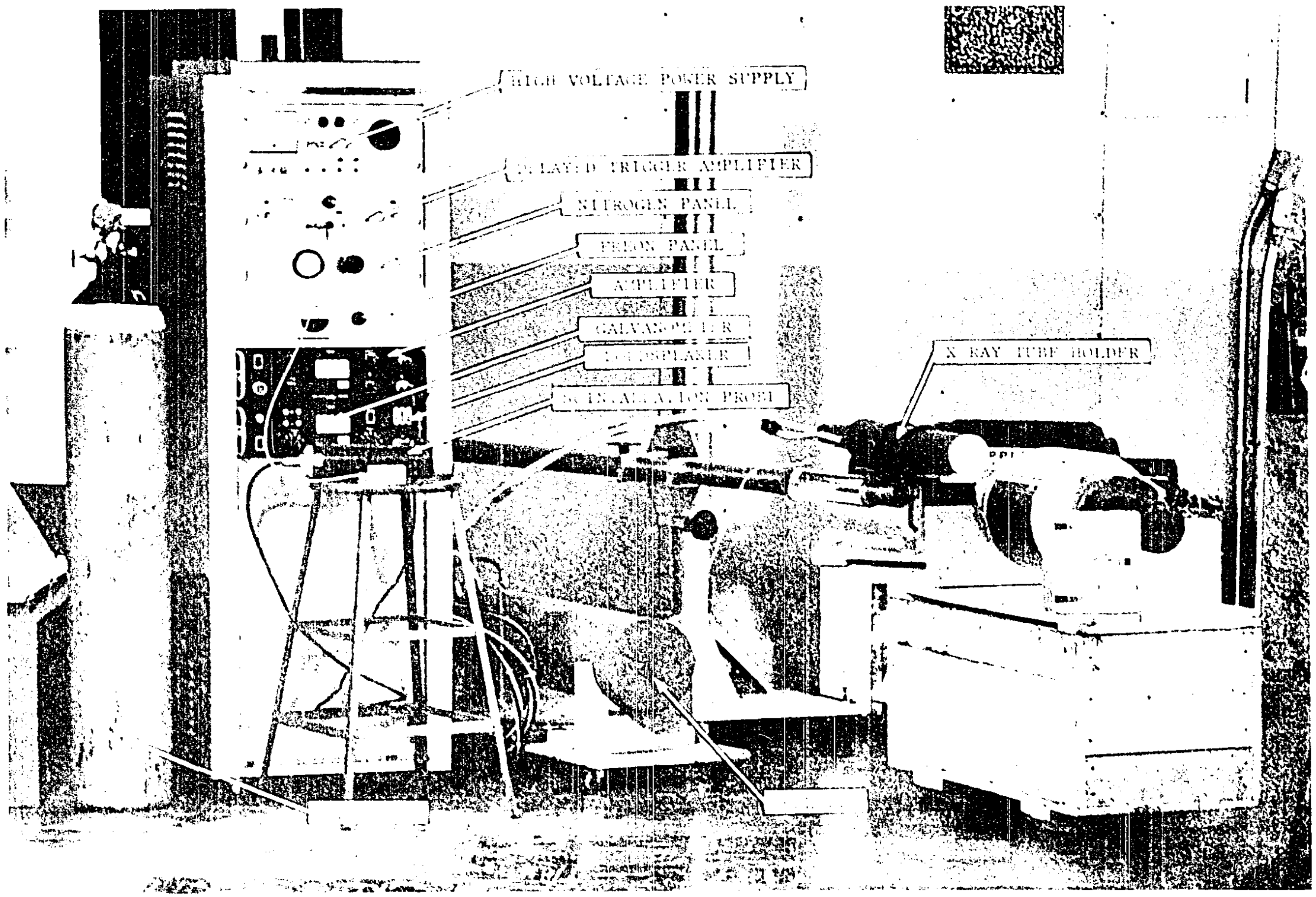

FIG. [illegible]

X-ray Unit

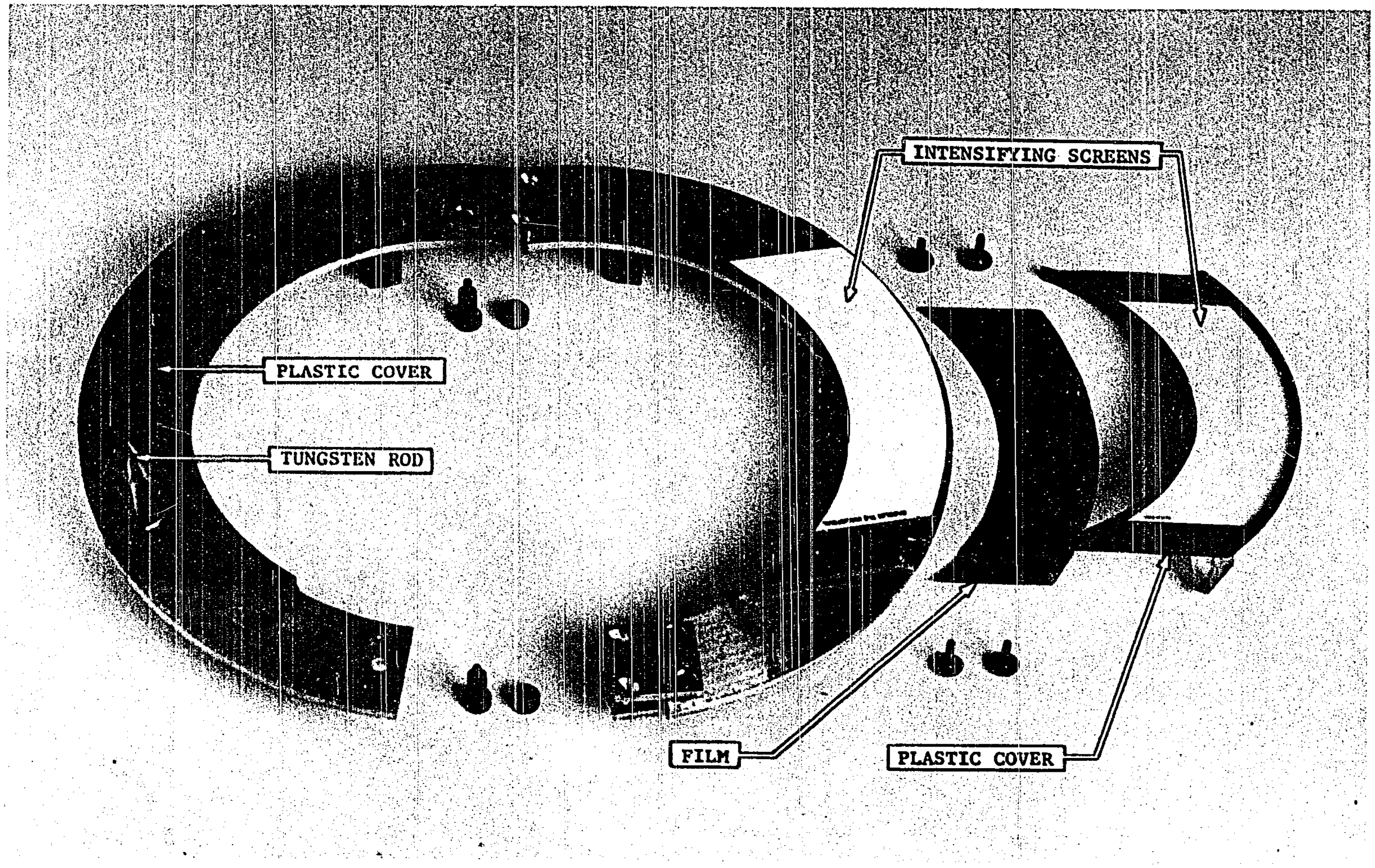

FIG. 14.
X-ray Film Holder

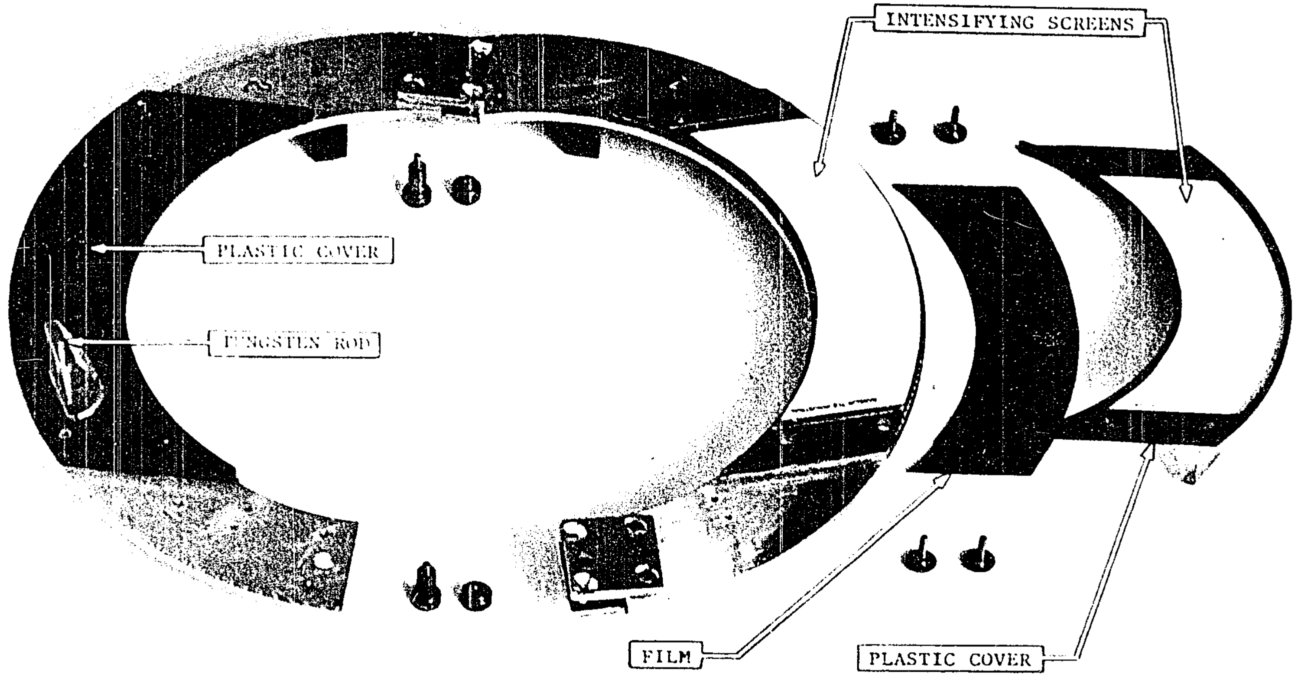

FIG. 14.
X-ray Film Holder

point which describes the line, from the radiation source, perpendicular to the film plane. It is thus necessary to apply a coordinate correction to each of the images to obtain a parallax free pattern. For this purpose a 1/16in. diameter, 1½in. long tungsten rod was attached to each film cover. The direction and length of the image cast by these rods were used to locate the centre point of the X-ray beam on each radiogram.

A film cutter, shown in Fig. 15, which consists of two rowel-blades equidistantly constrained on a radius arm to run in grooves of parallel circular arc trajectories, was devised. It cuts the required arc shaped film from standard 6½in. wide sheet.

In order to obtain an X-ray picture of the deformation field within the filled roll the X-ray unit must be flashed by a firing interlock, as described in APPENDIX V, when a pattern of spheres is in position beneath the nip.

A scintillation probe, shown in Fig. 13, connected to an amplifier with an audio output or loudspeaker and a visual output or galvanometer needle gives a quantitative indication of the momentary rise in background radiation when the X-ray apparatus is fired. Abnormal functioning of the equipment or a faulty tube can thus be detected without wasting time and film. Electroscopic pocket dosimeters were used by the experimenters to monitor radiation dosage absorbed during the test program.

Data Logging and Signal Conditioning Instrumentation

Readings from as many as 50 separate instrument transducers were recorded for periods up to 6 hours during certain tests in the program. On occasion readings had to be made at a rate of 5 per second. Transducer

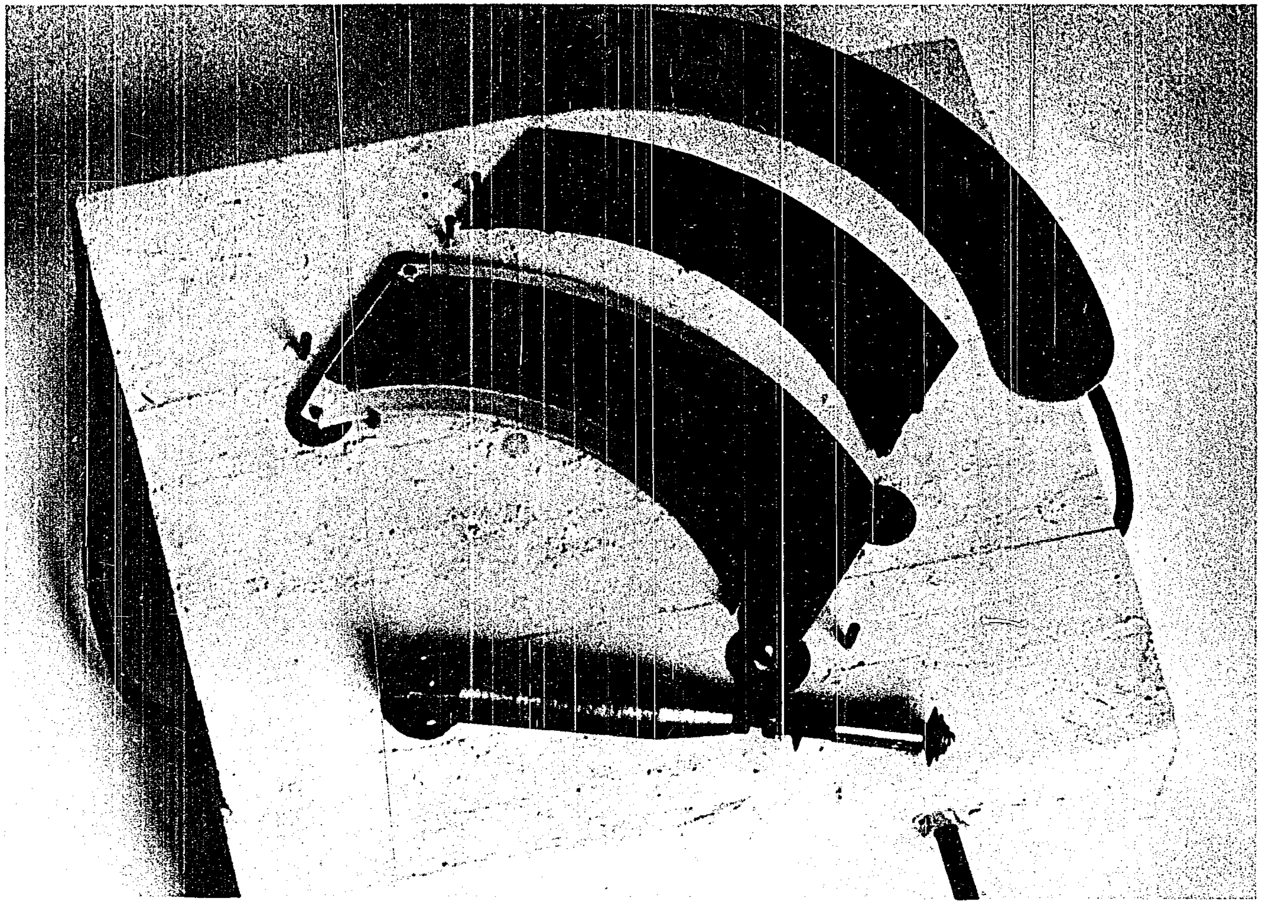

FIG. 15.
Film Cutter

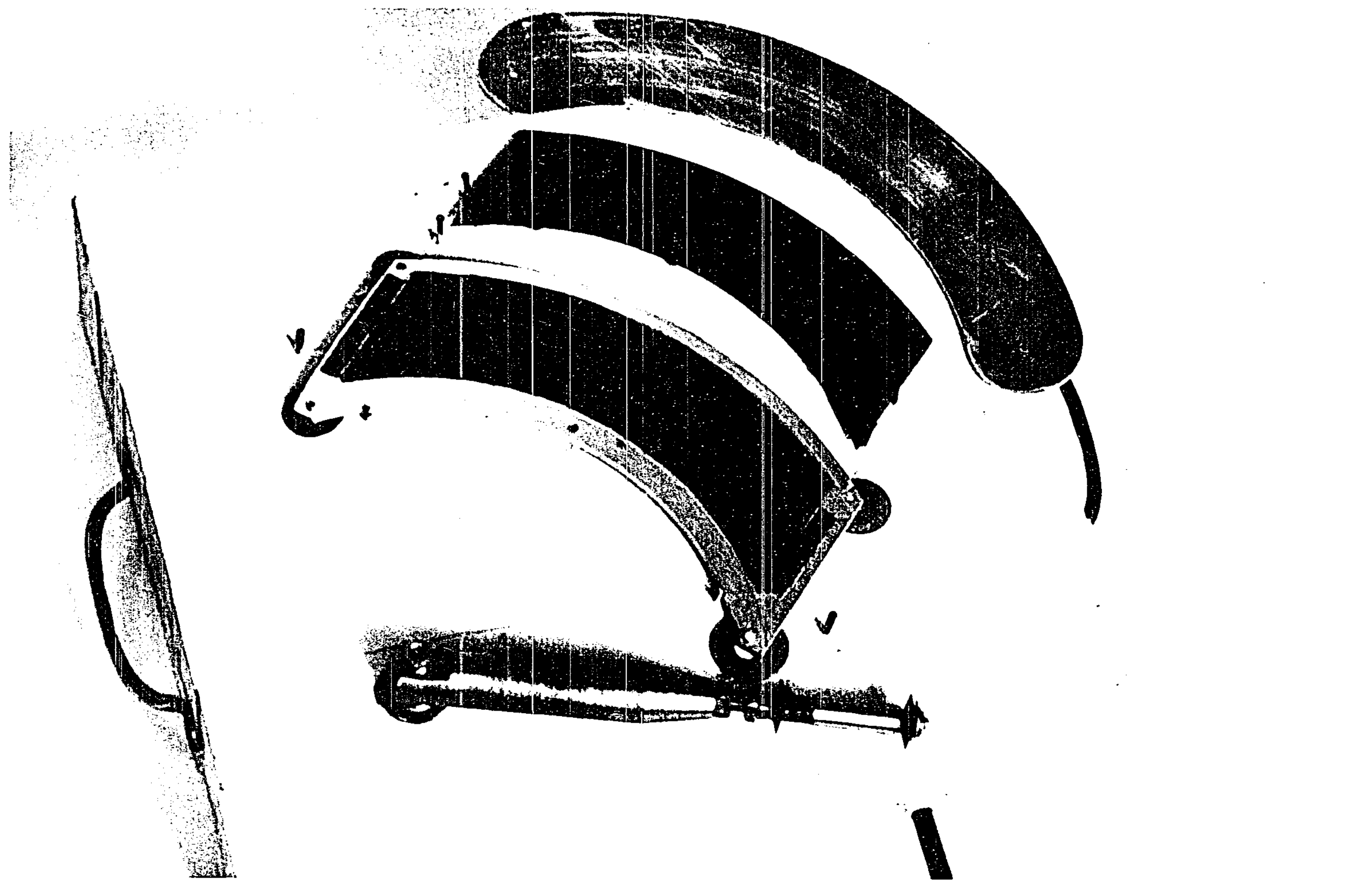

FIG. 15.

Film Cutter

outputs of frequency, from 50 to 2000 Hz., and D.C. voltage, from 10 mv. to 20 v., had to be accommodated. Voltage resolution of 0.5 µv. was required. These measurements were made by a digital data acquisition system which was capable of keeping a real time record of all these readings. This system consisted of the following intercommunicating modular units:-

1) Digital Clock
2) Integrating Digital Voltmeter
3) Analogue Input Scanner
4) Data Entry Keyboard
5) Perforated Paper Tape Punch
6) Guarded Data Amplifier
7) Digital Printer
8) Digital to Analogue Convertor

A 24 channel thermoelectrically cooled, thermostatically controlled thermocouple reference system was provided for filled roll thermocouple compensation. When more than 24 temperature points were logged this was supplemented with a conventional Dewar flask ice bath.

The data logging and signal conditioning instrumentation is described in detail in APPENDIX I.

PART I: THE DEVELOPMENT OF TEMPERATURE IN A SUPERCALENDER FILLED ROLL

Synopsis

A one-dimensional theoretical model of the development of the radial temperature distribution within a supercalender filled roll is formulated. The model has a simple closed form solution which can be used to compute the temperature distribution as a function of time.

The technique used for the instrumentation of supercalender filled rolls with miniature thermocouples is described. Two instrumented filled rolls were run in turn in single nip configuration against a steel roll without a paper web. Runs were made at various speeds up to 1700 fpm. (580 rpm) and at loads up to 1400 pli. Temperatures were measured at 20-40 preselected locations within the fill as a function of time. It was discovered that compressed fill material is inhomogeneous and that the distribution of inhomogeneity alters as the roll operates. However, measured values of the temperature profiles agree with those predicted by the model. It has been demonstrated that the predominant fraction of heat due to rolling friction in supercalender nips is generated in a surface layer no deeper than 0.01in.

Symbols

		Units
$\dot{Q}$	Strength of a line heat source (continuous)	$(^{\circ}F\ in^3)/in.min.$
ω	Angular speed of filled roll	$min.^{-1}$
r	Radial coordinate	in.
θ	Angular coordinate	-
H	Film coefficient of heat transfer	$Btu./^{\circ}F\ min.in^2$
k	Thermal conductivity of fill material	$Btu./^{\circ}F$ min.in.
v	Temperature	$^{\circ}F$
t	Time	min.
x, y, z	Cartesian coordinates	in.
x'	Depth of source below surface	in.
n	An integer implying a revolution of the filled roll	-
T	Period of revolution of the filled roll	min.
N	Number of complete revolutions executed by the filled roll	-
u	Temperature function due to a plane source	$^{\circ}F$
w	Temperature function due to a mirror image of u and convection at the plane of symmetry	$^{\circ}F$
K	Thermal diffusivity of fill material	$in^2/min.$
h	Surface film coefficient/thermal conductivity of fill	$in.^{-1}$
L	Laplace transformation operator	-
$\bar{u}$	The Laplace transform of u	-
q	A function of p and K	-

		Units
p	The transform of the variable t	-
A	Coefficient required to satisfy negative exponential root of transformed differential equation	-
B	Coefficient required to satisfy positive exponential root of transformed differential equation	-
$\bar{w}$	The Laplace transform of w	-
$\bar{v}$	The Laplace transform of v	-
erfc	Complement of the error function, erf (i.e. $\mathrm{erfc}(x) = 1 - \mathrm{erf}(x)$ $= 1 - \frac{2}{\sqrt{\pi}} \int_0^x e^{-\xi^2} d\xi = \frac{2}{\sqrt{\pi}} \int_x^\infty e^{-\xi^2} d\xi$)	-
S	Strength of an instantaneous plane source per unit area	$^\circ F\ in^3/in^2$
ε	A vanishingly small time increment	min.
ψ	An arbitrary, constant angle of rotation of the filled roll which signifies the time at which a temperature measurement is made	-
ρ	Density of fill material	$lb./ft^3$
c	Specific heat of fill material	Btu./lb. $^\circ$F
μ	Coefficient of rolling friction	-
E	Energy dissipated per unit length of nip	lb.in./in.min.
E'	Energy generated per unit area of source	lb.in./in^2 min.
s	Source area per unit length	in^2/in.
V	Peripheral velocity of roll	in./min.
N	Roll speed	$min.^{-1}$ (rpm.)
F	Time scaling factor	-

THEORETICAL

When a steel roll is run in loaded rolling contact with a filled roll heat is generated within the fill in the nip region. Under all conditions of loading the arc subtended by the nip is small compared to the circumference of either roll.

This heat is conducted to the surface of the filled roll, to the steel shaft which forms the core of the roll and to the steel nuts or end plates which confine the fill. Heat is also lost by convection from the filled roll surface to the surrounding air and, by conduction through the nip, to the contacting steel roll. Heat will be generated at some point along any radius of the filled roll at a recurring period $2\pi/\omega$, where ω is the angular speed of the roll. Based on these general observations the following assumptions can be made:-

1) Heat is generated by a line source parallel to the axis of and within the filled roll.
2) The source moves within the fill in a circular path concentric with the roll axis and at an angular speed ω.
3) Heat is lost from the whole surface of the filled roll at a uniform rate proportional to the surface temperature.
4) The effect of heat conduction to the steel core may be ignored since maximum temperatures and temperature gradients are known to occur within 1in. of the fill surface.
5) The effect of heat flow to the end plates and hence the axial temperature gradient is ignored because the length of the filled rolls is large compared to the radial depth of fill

and because bearing friction heats the roll shafts and nuts tending to limit axial heat flow.

Based on these assumptions the important heat source and sink in a typical transaxial plane of the filled roll are shown in Fig.16.

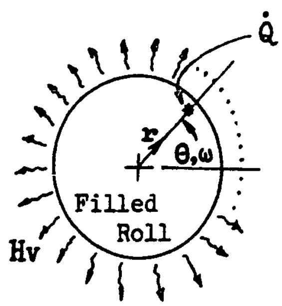

FIG. 16.

Convective Heat Loss from Roll Surface Hv(0,θ,t)
Heat Source $\dot{Q}(r,\omega,t)$.

This model can be simplified to a one-dimensional representation; a half-space with surface heat loss and a periodically recurring infinite plane heat source parallel to the surface. By employing the qualitative analogy illustrated in Fig. 17, a suggested temperature distribution within a typical filled roll cross-section consistent with the features shown in Fig. 16 can be obtained. Consider the heat source to be replaced by a thin stream of viscous liquid flowing axially and striking near the edge of the rotating disc which represents the filled roll cross-section. The strength of the heat source is represented by the rate of fluid flow. As heat-fluid strikes the disc it builds up to some depth or temperature. As flow proceeds, part of the liquid falls off the edge

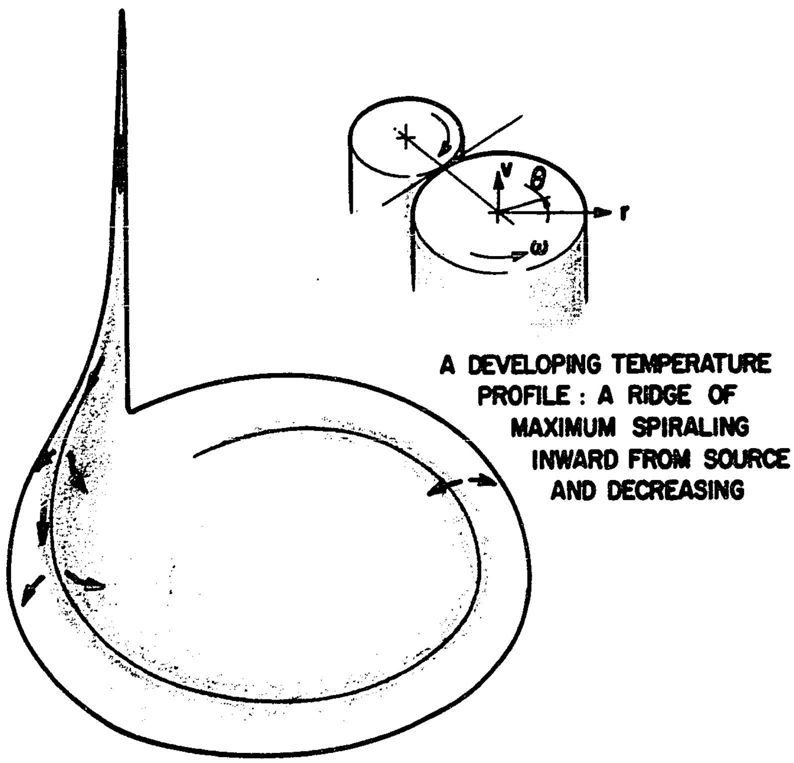

FIG. 17.

Qualitative analogy of heat build-up in supercalender filled rolls.

of the disc analogous to the convective heat loss from the surface and the remainder flows toward the centre analogous to heat conduction in the fill. At any section, cut by radial plane perpendicular to the disc but not containing the source, there is a ridge of maximum temperature. This maximum spirals at decreasing radius in the direction of rotation of the filled roll or in a direction opposite to the motion of the source. This flow is maintained by a spiral "tail" of heat supplied from the source. Thus the following propositions may be put forward:-

1) A surface source can produce a temperature distribution with maxima below the surface.

2) Although a roll might eventually achieve a temperature distribution resembling the second or developed profile, intuitively the first or developing profile appears to be the more valid approximation of a typical fill temperature distribution. In this regard it will be noted that an industrial supercalender runs for about 20 minutes and is then shut down to remove the finished roll of paper and install the next. It will be shown that in tests run in this program filled rolls did not reach equilibrium temperature in one or even two hours of continuous operation.

3) Tangential flow of heat, i.e. along the ridge, is secondary. Thermal gradients are predominantly radial.

Using the preceding arguments a one-dimensional model can be justified for the following reasons:-

1) The third proposition implies that significant temperature gradients occur only in the radial direction.
2) It was assumed that heat loss to the roll core could be ignored and that it was unnecessary to analyze thermal behaviour at depths over 1in. below the fill surface. Furthermore, the second proposition was formulated because of the fact that rolls burn where the highest effective temperatures occur; in regions of the fill near the surface.

A one-dimensional polar configuration can be approximated by a one-dimensional cartesian system if the space variable encompasses a relatively small radial distance. By implication the fill becomes a half-space or semi-infinite solid with uniform convective heat loss from its infinite plane surface. The point source, or end view of a line source as shown in Fig. 16, is replaced by an infinite uniform instantaneous plane source at some depth below and parallel to the surface.

Formulation and Analysis of the Model

The proposed model can be defined concisely as: The temperature distribution within a semi-infinite solid, initially at constant ambient temperature, v = o, with an instantaneous plane source located at a depth, x = x' parallel to and beneath the surface. The source recurs at equal period, T. Heat is lost from the body by uniform convection, at the surface, x = o, into a medium at constant ambient temperature, v = o.

There is uniformity in the direction y and z and the model is represented diagrammatically in Fig. 18.

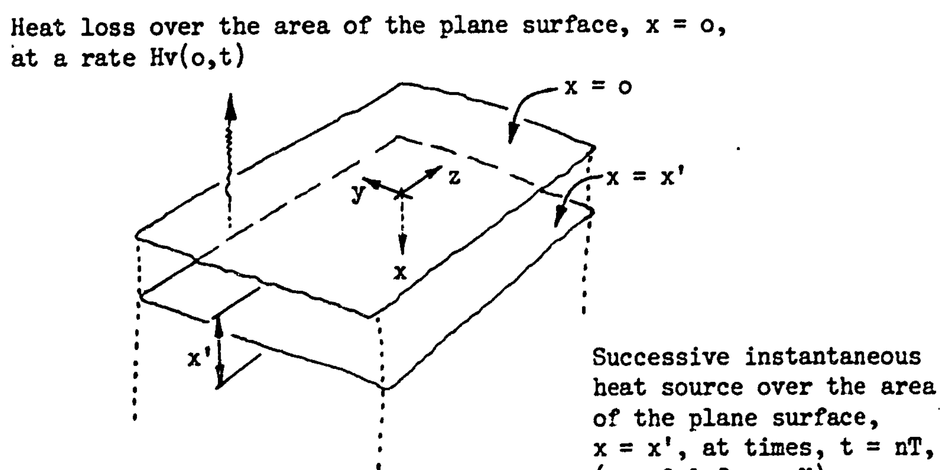

FIG. 18.

One-Dimensional Heat Flow.

The mathematical development of this model will proceed via the following steps.

1. The solution of a one dimensional temperature distribution in an infinite body due to an instantaneous plane source of unit strength* at x = x' and occurring

* A source of unit strength is defined as that which liberates a quantity of heat sufficient to raise the temperature of a unit volume of the body being heated by one degree.

at time $t = o$.

2. The addition of a linear term to this solution to account for the convective heat loss at the plane at $x = o$. This is a boundary condition of temperature gradient at the surface proportional to the surface temperature.

3. Investigation of a possible alternate solution generated by the analysis.

4. Formation of a solution consisting of a finite series of terms of 1 and 2. Each term has a time argument less, by the period T, than the time argument of the preceding term. In this way the thermal contribution of successive sources is accumulated. The number of terms is equal to the number of complete and partial revolutions which the filled roll has undergone.

Steps 1 and 2 are from (31)

1. The temperature at any depth, x', and any time, $t > o$, in an infinite solid in which a unit plane source occurred at $t = o$ is given as $u(x,t)$.

$$u = \frac{1}{2\sqrt{\pi K t}} e^{-(x-x')^2/4Kt} \qquad - (1)$$

2. The addition of a plane of symmetry at $x = o$ from which convective heat loss occurs will be accounted for by a term $w(x,t)$ which may be added to $u(x,t)$. The temperature distribution now becomes $v(x,t)$.

$$v = u + w \qquad - (2)$$

The function $w(x,t)$ must have the following properties

i) It must approach o as time approaches o; an initial condition $w \to o$ at $t = o$

ii) It must satisfy the conduction or diffusion equation

$$\frac{\delta w}{\delta t} = \frac{K\delta^2 w}{\delta x^2}$$

iii) It must cause the temperature function, v, to satisfy a boundary condition such that the surface temperature gradient be proportional to the surface temperature. The boundary condition of convective heat transfer from the surface is

$$\frac{\delta v}{\delta x} = hv \Big|_{x = o}$$

It is intended to obtain v via Laplace transformation, i.e.

$$L(w) + L(u) = L(v) \qquad - (3)$$

where L is the operation of transformation and L^{-1} is inverse transformation

$$\therefore \; v = L^{-1}[L(v)] \qquad - (4)$$

define $L(u) \equiv \bar{u}$ and $q \equiv \sqrt{p/K}$ where p is the variable in the transformed equation which has replaced time, t.

$$\therefore \; \bar{u} = \frac{1}{2Kq} e^{-q|x-x'|} \qquad - (5)$$

$$\text{and} \quad L\left(\frac{\delta w}{\delta t} = \frac{K\delta^2 w}{\delta x^2}\right) \quad \text{gives} \quad \frac{d^2\bar{w}}{dx^2} - q^2\bar{w} = o \qquad - (6)$$

The transformed equation is a total differential equation with the solution

$$\bar{w} = Be^{qx} + Ae^{-qx} \qquad - (7)$$

It is noted that as $e^{qx} \rightarrow \infty$ when $x \rightarrow \infty$ we must have $B = o$ for finite temperature to exist at very great depth beneath the surface. Therefore $\bar{w}$ is retained as

$$\bar{w} = Ae^{-qx} \qquad - (8)$$

and $$\bar{v} = \frac{1}{2Kq} e^{-q|x-x'|} + Ae^{-qx} \qquad - (9)$$

The parameter, A, is evaluated from the Laplace transformation of the equation which represents the surface condition, i.e.

$$L\left(\frac{\delta v}{\delta x} = hv\right)\Bigg|_{x=o} \quad \text{gives} \quad \frac{d\bar{v}}{dx} = h\bar{v}\Bigg|_{x=o}$$

From (9) $$h\,\bar{v}\,(o) = \frac{h}{2Kq}\,e^{-qx'} + Ah \qquad - (10)$$

and $$\frac{d\bar{v}}{dx} = \frac{-q}{2Kq}\,e^{-q|x-x'|}\,\frac{d|x-x'|}{dx} - Aqe^{-qx} \qquad - (11)$$

For (11) to remain finite for all x the exponent $-q|x-x'|$ must be non-positive. This is accomplished by selecting $q \equiv +\sqrt{p/K}$, the positive root only, and the modulus $|x-x'|$. However, $(x-x')$ can be negative. Thus it is evident that $\frac{d|x-x'|}{dx} \equiv \pm \frac{d}{dx}(x-x')$ where the appropriate sign is invoked to preserve non-negativity.

$$\therefore \quad \frac{d\bar{v}}{dx} = \frac{q}{2Kq} \quad e^{-q|x-x'|} - Aqe^{-qx}$$

$$\text{and} \quad \frac{d\bar{v}(o)}{dx} = \frac{q}{2Kq} \; e^{-qx'} - Aq \qquad - (12)$$

$$\text{to satisfy} \quad \frac{d\bar{v}}{dx} = h\bar{v}$$

$$A = \frac{q-h}{q+h} \; \frac{e^{-qx'}}{2Kq} \qquad - (13)$$

When A is substituted into (9),

$$\bar{v} = \frac{1}{2Kq} e^{-q|x-x'|} + \frac{(q-h)}{(q+h)} \frac{e}{2Kq}^{-q|x+x'|} \qquad - (14)$$

Equation (14) can be simplified to a sum of individual terms contained in a table of Laplace transforms

$$\bar{v} = \frac{1}{2Kq} e^{-q|x-x'|} + \frac{1}{2Kq} e^{-q(x+x')} - \left(\frac{h}{q+h}\right) \frac{e}{Kq}^{-q(x+x')} \qquad - (15)$$

which has an inverse transform

$$v = \frac{1}{2\sqrt{\pi Kt}} \left[e^{-(x-x')^2/4Kt} + e^{-(x+x')^2/4Kt} \right]$$

$$- he^{Kth^2+h(x+x')} \; \text{erfc} \left[\frac{x+x'}{2\sqrt{Kt}} + h\sqrt{Kt} \right] \qquad - (16)$$

The diagram, Fig. 19, illustrates the physical significance of the term $\frac{1}{2\sqrt{\pi Kt}} \left[e^{-(x-x')^2/4Kt} + e^{-(x+x')^2/4Kt} \right]$ in equation (16).

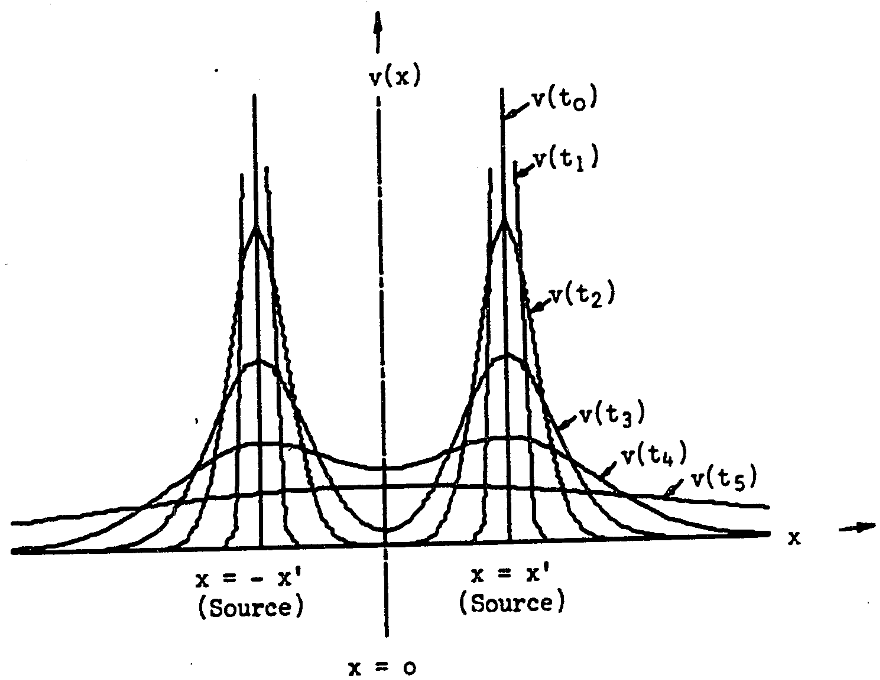

FIG. 19.

Characteristics of Zero and Subsequent Times, t_1, t_2,...
[Eqn.(16)]

Notice that $\delta v/\delta x = o \Big|_{x=o}$ and there is symmetry about the surface plane, x = o. This configuration precludes heat transfer across the boundary by placing companion sources at x = ± x'. Such a temperature distribution would be expected if h = o, which is equivalent to dropping the term, $he^{Kth^2+h(x+x')}\text{erfc}\left[\frac{x+x'}{2\sqrt{Kt}} + h\sqrt{Kt}\right]$, in equation (16).

Note that, as well as making $\delta v/\delta x > o \Big|_{x=o}$, this term decreases v at positive values of x. Such temperature depression is expected to accompany surface heat loss.

3. On the other hand, if $h \to \infty$, the convective boundary condition reduces to an isothermal boundary condition, $v\big|_{x=o}=o$, then equation (16) yields the following expression for v

$$v = \frac{1}{2\sqrt{\pi Kt}} \left[e^{-(x-x')^2/4Kt} - e^{-(x+x')^2/4Kt} \right] \qquad - (17)$$

The diagram Fig. 20, illustrates the physical significance of this solution.

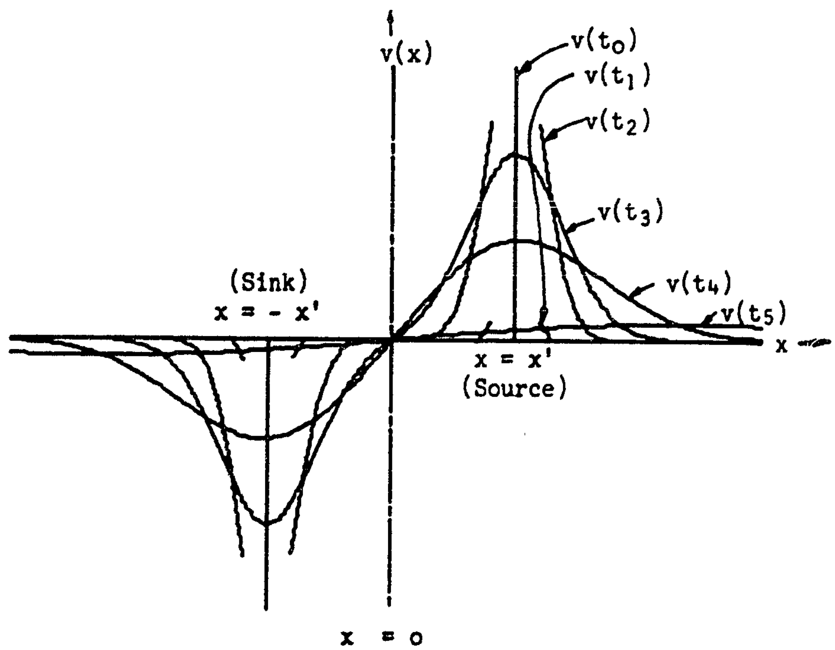

FIG. 20.

Characteristics of Zero and Subsequent Times, t_1, t_2,... [Eqn.(17)]

This is a mirrored source-sink configuration with an inflection at the origin as well as the temperature v = o by skew-symmetry.

4. By linear superposition the temperatures resulting from the effect two sources may be added at all times after the occurrence of the second source. For example, consider the decay of temperature at or very near the plane x', first with a source occurring at t = o, then with a source occurring at t = T and finally the combined effect. This superposition is shown in Fig. 21.

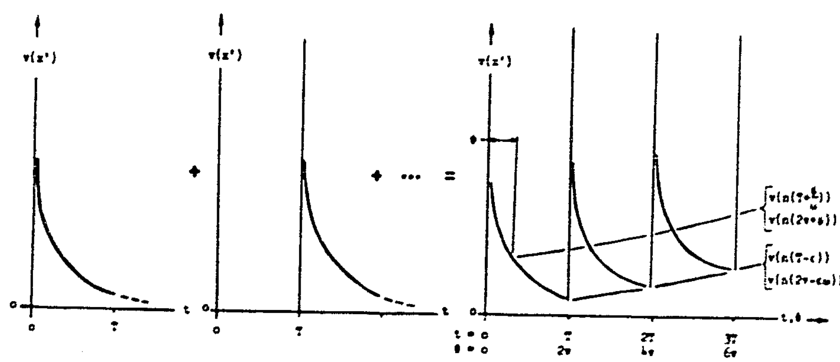

FIG. 21.

The Effect of Successive Heat Sources.

If sources continue to occur at integer intervals nT, the minima, or any other arbitrary points at intervals of T, in the train of decaying temperature spikes describe an ascending temperature envelope corresponding to the general heating-up of the filled roll. This heating along with the combined effect of successive sources is shown in Fig. 21 and is represented mathematically by equation (18). Temperatures for any number of sources are described for all depths, x, below the surface and all times, $t \neq nT$, $n = o,1,2,\ldots,N$, by the finite series

$$v = S\sum_{n=o}^{N} \frac{1}{2\sqrt{\pi K(t-nT)}} \left\{ e^{-(x-x')^2/4K(t-nT)} + e^{-(x+x')^2/4K(t-nT)} \right\}$$

$$- he^{K(t-nT)h^2+h(x+x')} \operatorname{erfc}\left\{ \frac{x-x'}{2\sqrt{K(t-nT)}} + h\sqrt{K(t-nT)} \right\} \qquad - (18)$$

where a scale factor, the source strength, S, has been included for the sake of generality.

EXPERIMENTAL

Instrumentation

Temperature measuring instrumentation was included in two filled rolls described and illustrated in Fig. 22. The rolls were filled with "Filmat-2" which was mounted on a 6in. diameter steel shaft or core and finished to 12in. outer diameter. Filmat is the trade name of a cotton fill material available in sheet form in various grades which cover a range of fibre length and precompaction. For example, Filmat-2 has longer fibre and is softer than Filmat-3. Roll B was "locked-up" under a mean axial compression of 10,000 psi. and contained a 25% proportion by weight of glass fibre mixed with the Filmat. Roll A was pressed at 8000 psi. In both rolls the axial length of fill between the retaining nuts was about 12in. after pressing.

The test rolls contained miniature iron-constantan thermocouples. Fill temperatures, at the various transaxial planes depicted in Fig. 22, were measured while the supercalender was operating. The instrumentation was similar in both rolls. Roll B contained 6 planes of 8 thermocouples and roll A had only 4 planes of couples. Note the differences in axial spacing of the instrument planes or discs and that the four discs in roll A have serial numbers 8, 7, 4 and 6. These discs will be subsequently identified by these numbers. Eight thermocouples were placed at equal angular spacing on 0.020in. thick annular paper cards. Fig. 23 shows the location of couple junctions which were from 3/32in. to 2in. beneath the finished surface of the filled rolls. All thermocouples were commercially fabricated from either 0.002in. diameter wire with 0.005in. diameter spherical junction beads or from 0.005in. diameter wire. It was thought that the larger wire may withstand the pressing phase of the roll manufacturing process better than the finer wire. However, probably due to its greater flexibility, the 0.002in. diameter wire proved to have a better record of survival.

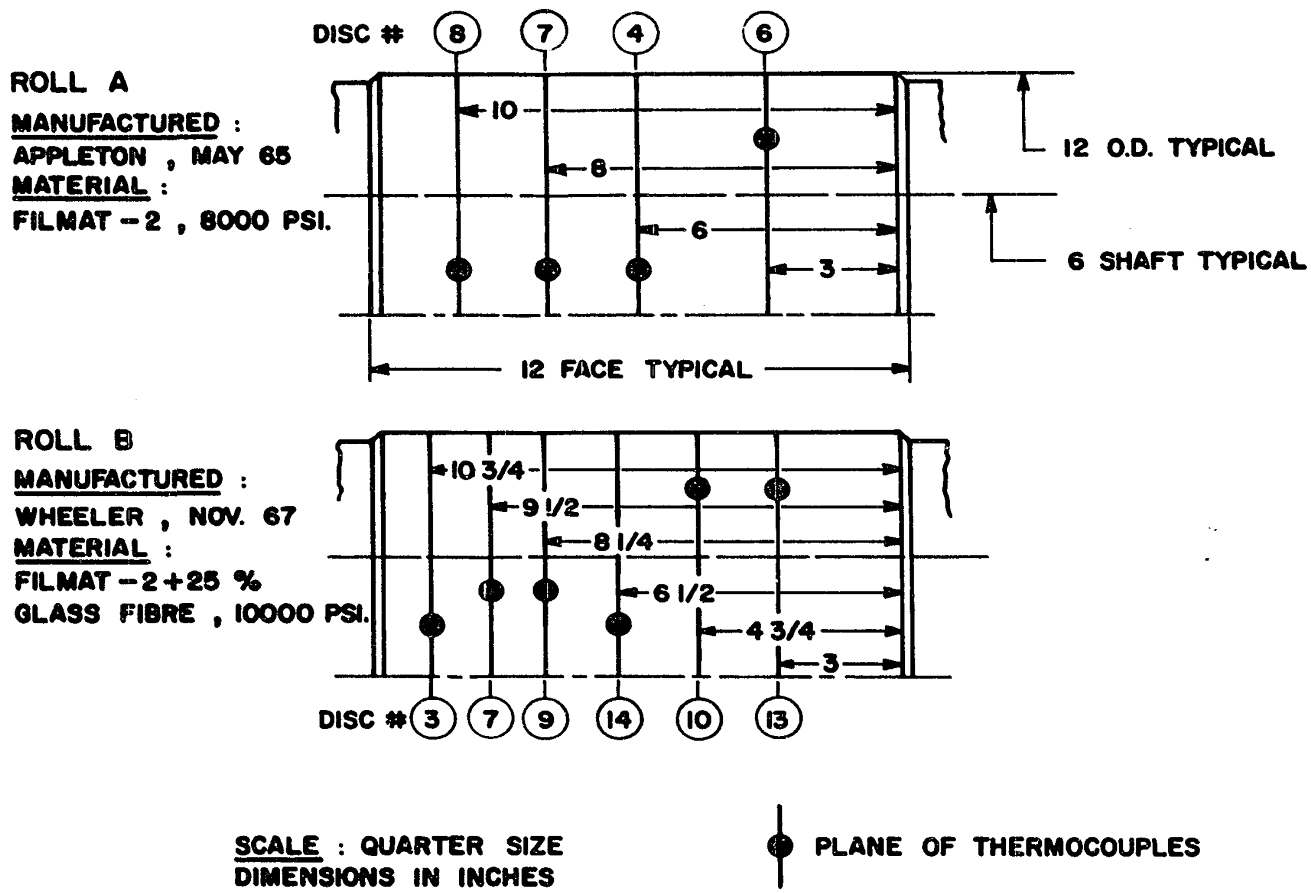

FIG. 22.

Instrumented Filled Roll.

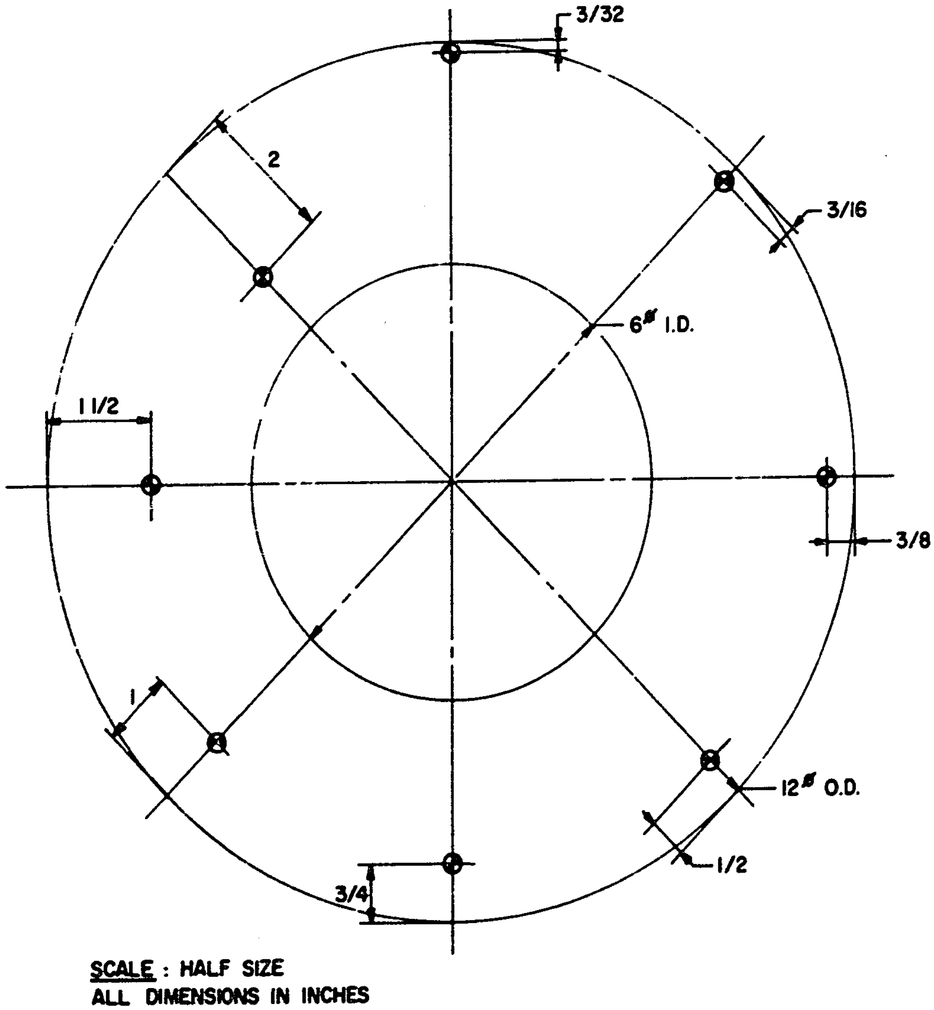

FIG. 23.

Thermocouple Location

Thermocouple junctions were located accurately on their mounting cards by threading one lead of each couple through pinholes and drawing the beads into these locating holes. The bare wire leads were passed, on either side of the cards, towards the centre of the roll annulus. The leads were fixed to the card by lacing them through pinholes near the inner circumference as shown in Fig.24. Thirty-gauge iron-constantan extension leads, individually insulated with "Teflon" covering, were connected to the couple leads near where they were laced to the card. Connections were made by striking a 10v. A.C. arc between two hand held miniature electrodes of either soft pencil or brush graphite. Oxidation of the welds was prevented by flushing the region of the arc with helium or argon.

The thermocouple mounting cards and the elements of Filmat from which the rolls were built have three equidistant cutouts on their inner circumference. There are three corresponding axial grooves in the outer surface of the roll shafts over which the cards and fill material were assembled. In one of these channels was placed a steel key to prevent rotation of fill relative to the shaft. The other two channels provide paths for the thermocouple extension leads which run from the welds, circumferentially along the inner edge of the cards and converge at the cutouts in groups of four pairs of leads per card. In the two rolls which contain six cards, each groove carries three lead bundles, in either direction, through the roll nut and via radial holes in the shaft, to the roll bore.

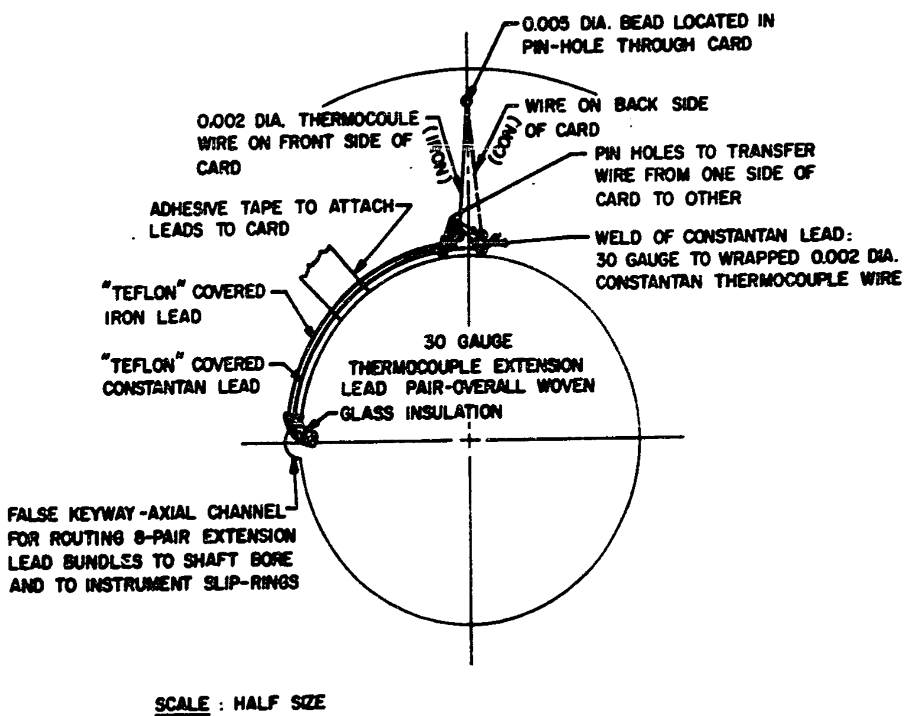

FIG. 24.

Mounting of Thermocouples.

Extension leads emerge from either end of the roll. These leads terminate in a perforated circular plastic plate shown in Fig. 25. The terminations are collet couplings individually press fitted into the plate. Plug-in connection of the leads was thus made to the rotating side of a Northern Precision Laboratories fifty channel instrument slipring driven by the roll through a miniature universal coupling. A slipring terminal assembly was provided at either end of the roll. The signals from the thermocouples were transmitted via further extension leads through ice bath reference junctions to the scanner and integrating digital voltmeter which recorded all temperature measurements.

Filled roll surface temperature was measured by an "Ardonox" (33) total radiation pyrometer in which incident radiation emitted from a three inch wide circumferential strip at centre face is focused by a parabolic mirror onto a thermopile. Correction for roll emissivity was made by making two static temperature measurements on the roll surface under the pyrometer with a hand held indicating thermocouple surface pyrometer. The first calibration measurement was made at room temperature before a test was run. The second was made immediately after the test run and the rate of surface temperature change due to cooling was small enough so as to yield a constant measurement. These two measurements, typically at 70°F and some other temperature above 120°F respectively, were used in conjunction with a calibration curve supplied by the instrument manufacturer. This curve represented the instrument output as

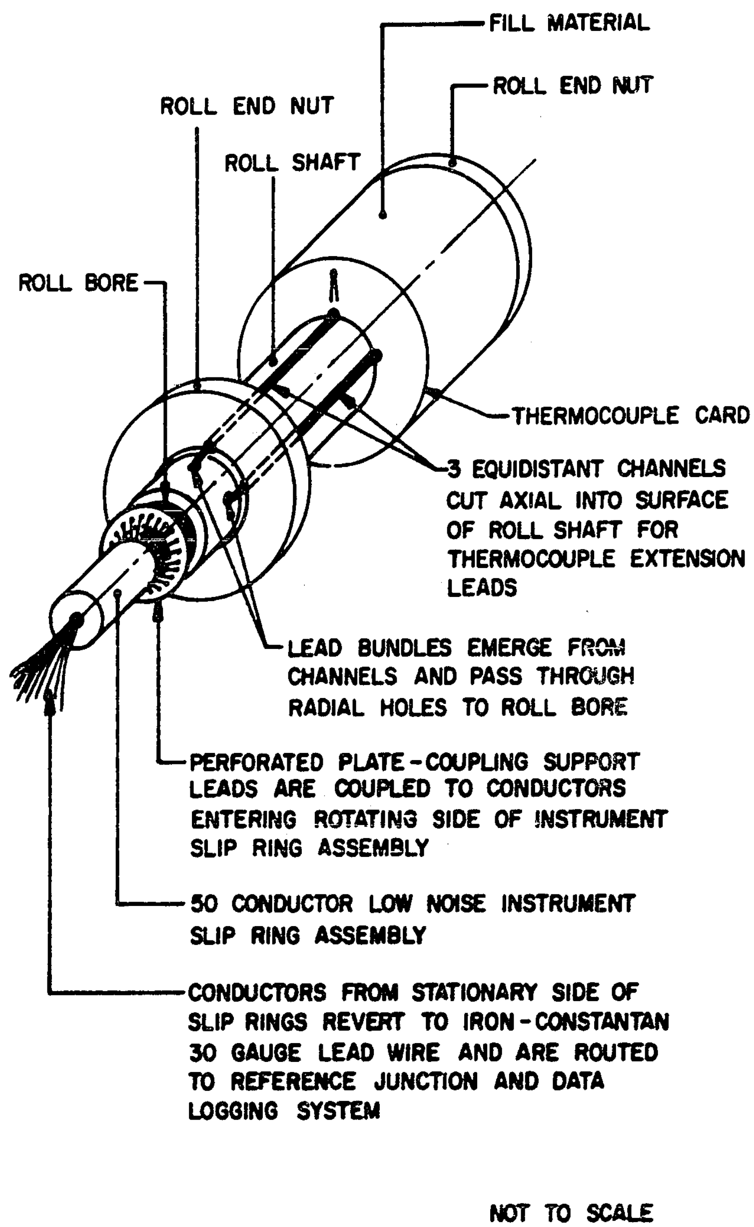

FIG. 25.

Routing of Leads.

a function of "black-body" temperature.

Temperature measurements made with thermocouples in the fill and with the radiation pyrometer were averaged over intervals of one second. This technique of signal integration yields accurate measurement of the mean temperature in the interval during which the signal is monitored. The model represented by equation (18) implies that temperatures at the plane of the source are infinite when a source occurs and decay, due to diffusion and surface loss, to a minimum just before the occurrence of the subsequent source. At all but the lowest speed of operation, a number of roll revolutions take place during one second, therefore a number of oscillograms of thermocouple output voltage were taken in order to investigate temperature fluctuations which occur as the roll rotates and the fill surrounding a given thermocouple passes under the nip. The surface pyrometer neither rotates nor passes through the nip. It stands 90° downstream of the nip and averages the temperature of points on the surface all of which passed the nip 1/4 revolution previously.

RESULTS AND DISCUSSION

Temperatures were measured on rolls A and B as a function of time at all combinations of four loads, 240, 470, 940 and 1400 pli., and three speeds, 650, 1050 and 1700 fpm. respectively, in a sequence of tests in which load was progressively increased. Although a statistically designed experiment, in which loads and speeds are chosen in a random sequence, would have been preferable the approach of progressive load increase was adopted in order to maintain the integrity of the thermocouples and hence obtain a maximum amount of data. It was not known how well the couples would withstand high loads or at what temperature the filled roll might sustain surface damage or be burned. An additional series of 15 tests was made to establish the reproducibility of the measurements.

Most of the operative thermocouples were monitored in each test. About 20% of the couples were broken during the roll manufacturing process before the test program was begun, and most of the couples at 3/32in. depth were broken during the test program. Despite these breakages sufficient data were obtained to give a reasonably comprehensive picture of the thermal behaviour of both rolls.

Typical temperature versus time data are shown in Figs. 26-29 from which it may be seen that both rolls exhibit similar general trends. Under all conditions of operation there is an initial steep increase of temperature which subsequently tends to flatten out. Surface temperatures, which were measured only over the central transaxial plane, are shown in Figs. 26 and 28. They are seen to be higher at all times than temperatures within the roll in this plane.

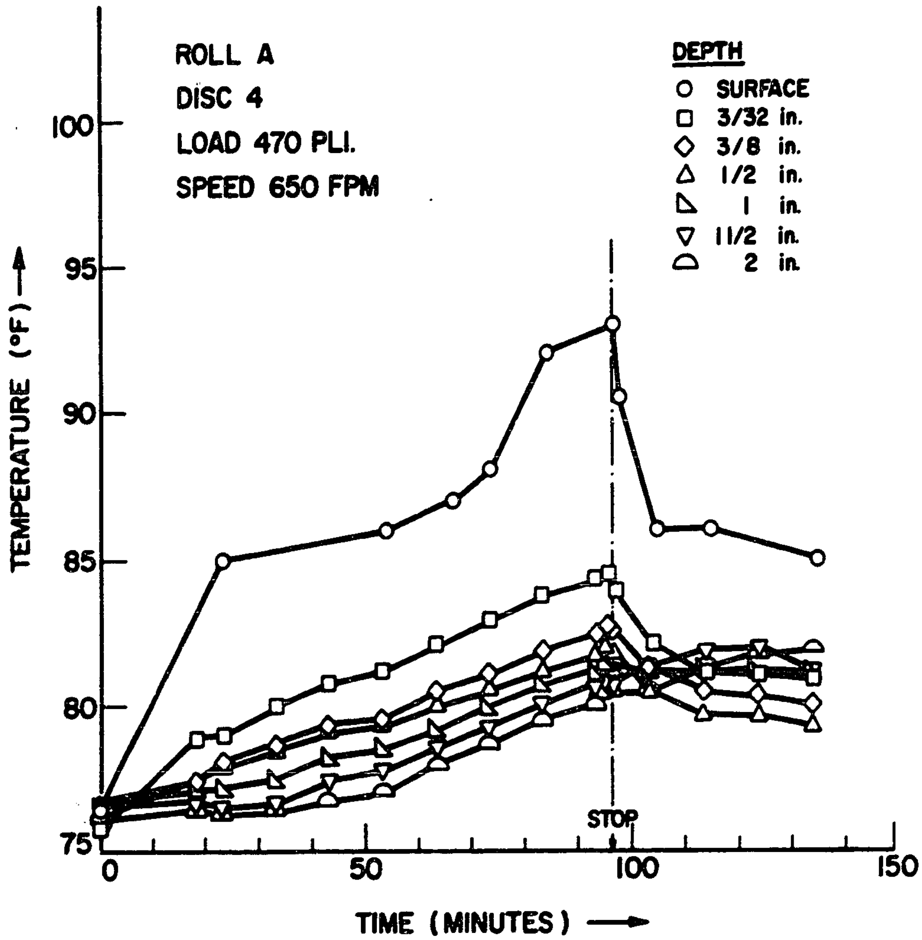

FIG. 26.

Temperatures within Roll A operating at 470 pli. and 650 fpm.

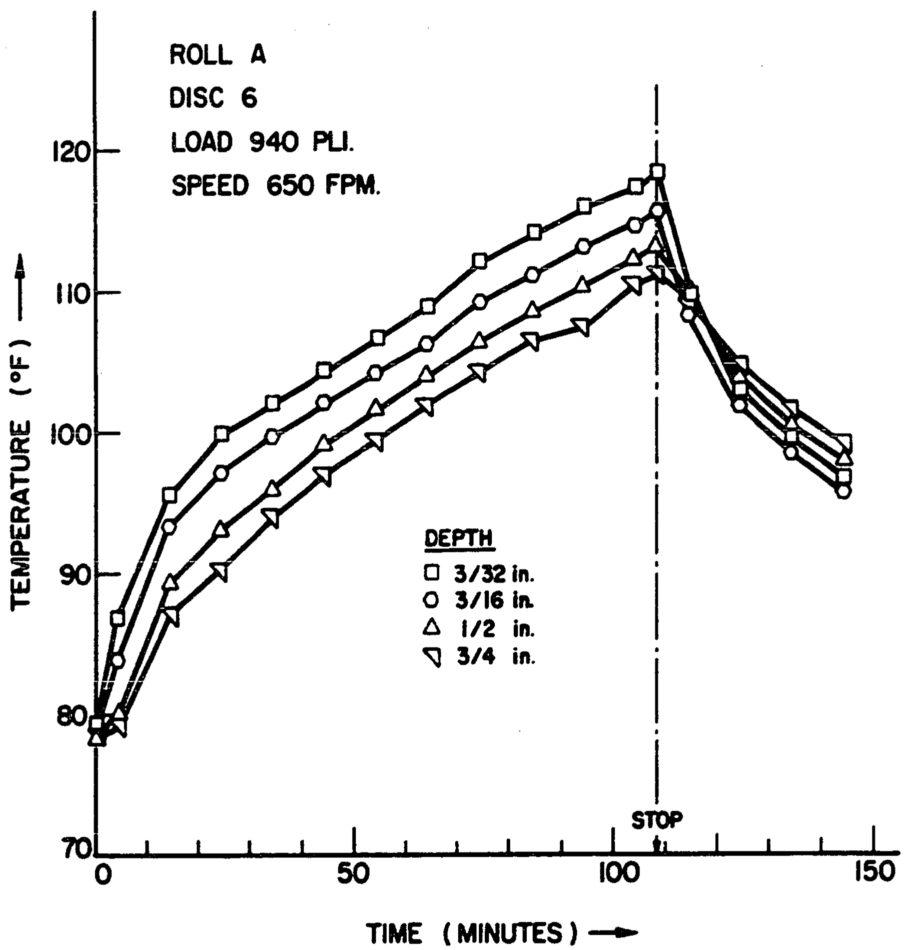

FIG. 27.

Temperatures within Roll A operating at 940 pli. and 650 fpm.

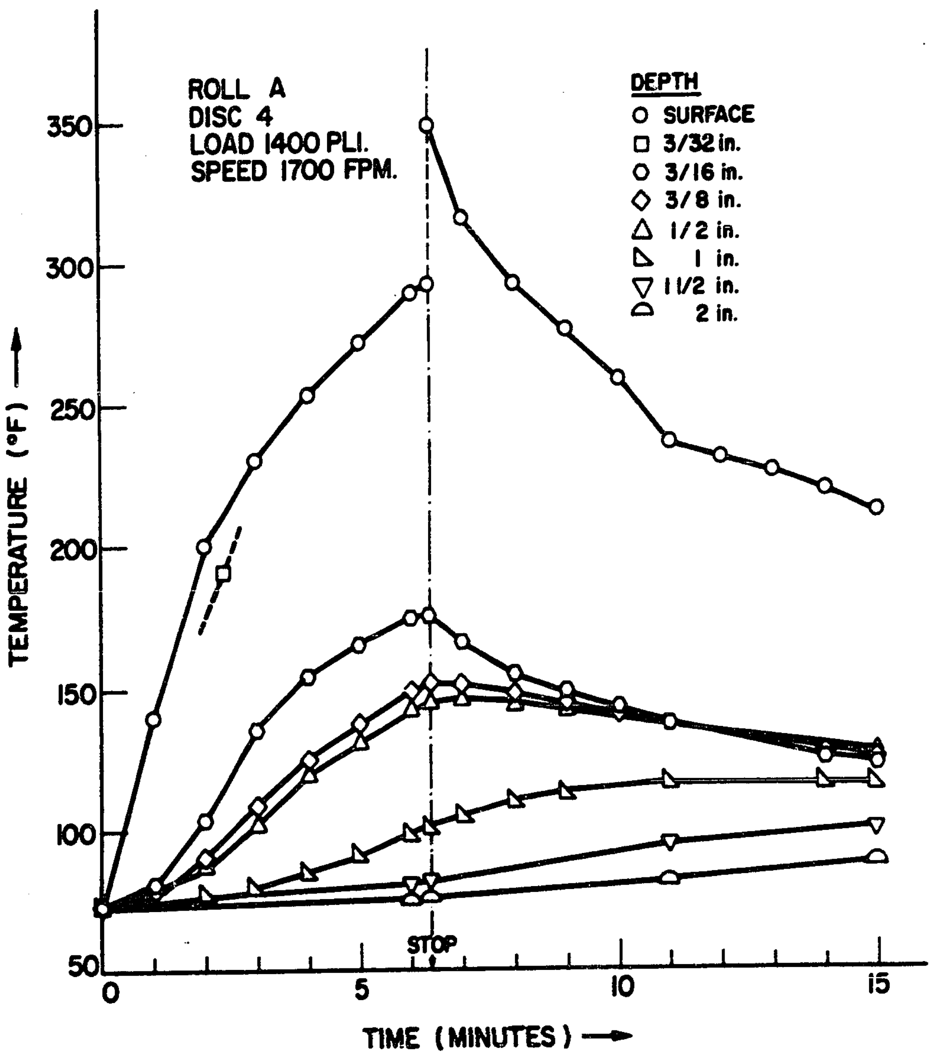

FIG. 28.

Temperatures within Roll A operating at 1400 pli. and 1700 fpm.

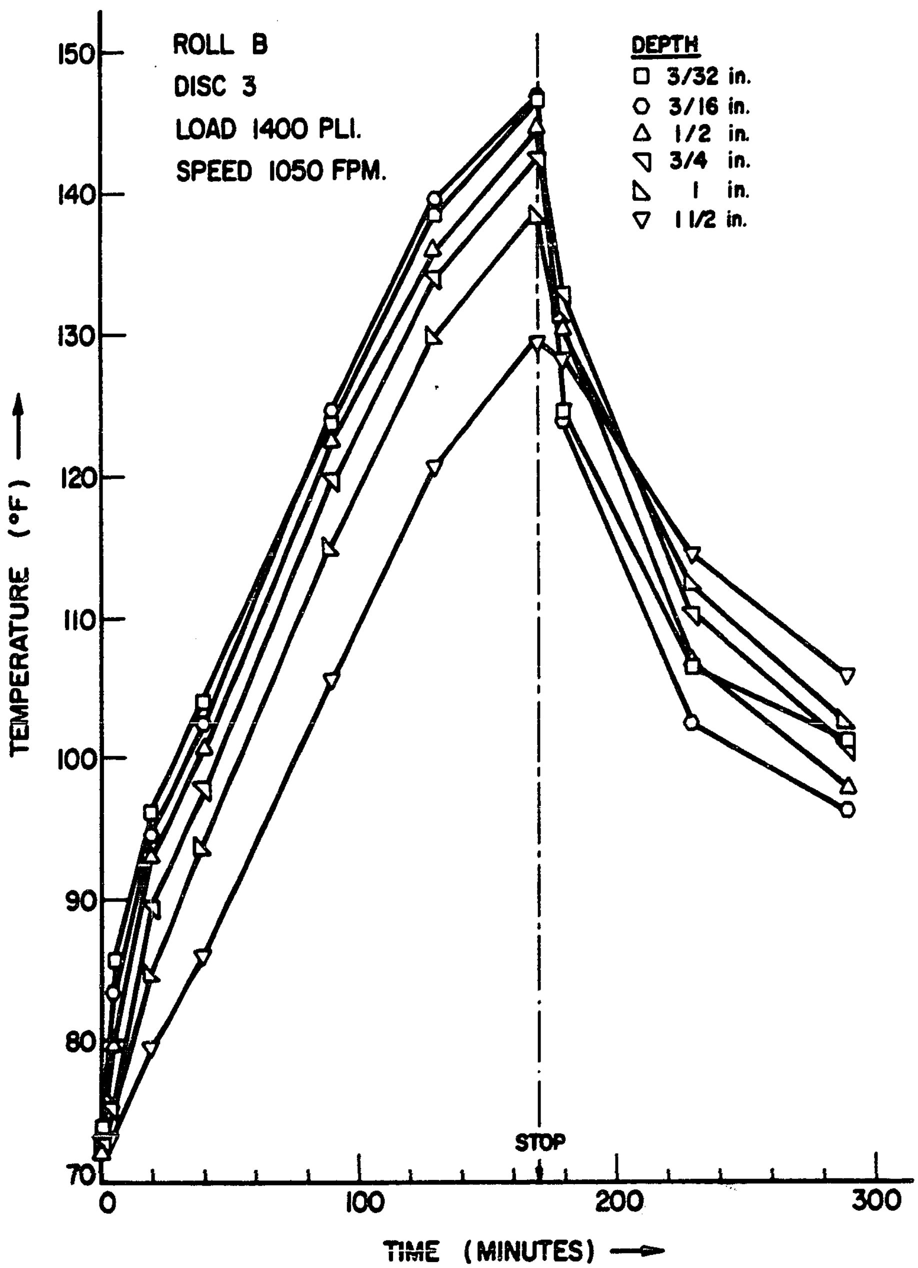

FIG. 29.

Temperatures within Roll B operating at 1400 pli. and 1050 fpm.

The manner in which the temperature decreases below the surface would, at first sight, appear to be consistent with the assumption, made in the theoretical treatment, that a supercalender filled roll behaves like a homogeneous continuum. However, inspection of the temperature measurements provides evidence to show that the thermal properties of the filled roll cannot be fully explained without reference to its heterogeneous nature and its thermomechanical instability. Indeed, possibly the most important conclusion to emerge from this study is that random property variations, which have not previously been considered in this context, play an important part in filled roll behaviour. This evidence will be presented before proceeding to determine how well the temperature measurements fit the theoretical predictions of equation (18).

<u>Nonuniformity and Instability</u>

Certain features of the data shown in Figs. 26-29 are not consistent with the behaviour of a homogeneous continuum.

1) In Fig. 26 it may be seen that temperatures, especially those on or near the roll surface, do not increase smoothly with time. There are a number of abrupt changes in slope of the curves.

2) In Fig. 28 it is seen that a very rapid temperature rise of 70°F occurred at the surface of the roll when the stack was stopped. This phenomenon was observed in several other, though not all, test runs, the sudden temperature rise being usually only a few degrees. Sudden temperature drops may also have occurred but these would go unnoticed as the surface

temperature, which is invariably the greatest, decays rapidly when the stack is stopped.

3) While temperatures were rising during operation, the temperature at a given distance beneath the roll surface was on occasion exceeded by that at a greater depth. Such an inversion appears in Fig. 29 where the temperature at 3/16in., for a time, exceeds that at 3/32in.

In order to account for these phenomena it should be recalled that thermocouples at adjacent depths in the same transaxial plane are separated by 45° or 1/8th of the roll circumference while the surface temperature of the filled roll was always measured at a position 90° downstream of the nip. The behaviour described in items 2) and 3) above is most probably caused by circumferential variations in either the heat source strength or the thermal diffusivity of the fill material. Variations in values of thermal diffusivity for most organic solids such as cotton over a wide range of density are very small and it is unlikely that changes in this property would account for the observed effects.

The phenomenon described in item 1) suggests that the heat source strength distribution changes as the fill material undergoes compaction or dispersion during the course of operation of the filled roll.

In Fig. 30, which shows temperature versus time characteristics obtained at 1-minute intervals, short term temperature fluctuations are noticeable at all depths. Temperature inversions also occurred in this test as the couples at 3/4in. and 1/2in. below the roll surface showed a higher temperature than that recorded at 3/8in.

In addition to circumferential variations there are also varia-

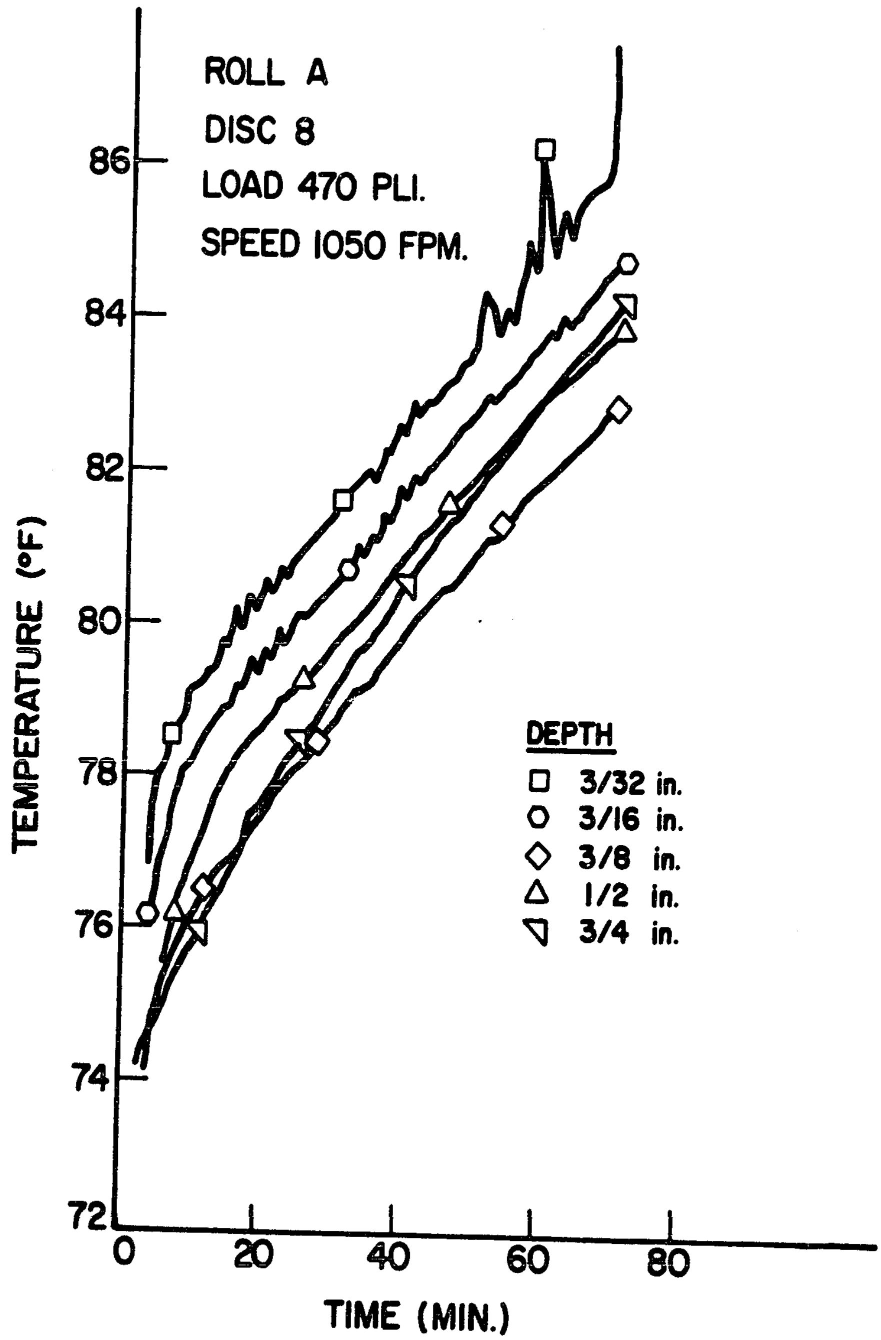

FIG. 30.

Irregular Rise of Temperature within Roll A.

tions in heat source strength along the nip in the axial direction as may be seen from Fig. 31 in which temperature-time curves are plotted for all four thermocouples located at a depth of 3/32in. in roll A. This behaviour, in which temperatures are higher at one end of the filled roll and decrease towards the other end, was common to both roll A and B in all tests. The effect was more pronounced when the stack was lightly loaded. Axial temperature gradients may arise in part from topographical variations in the surface of the filled roll. A contour mapping of the topography of roll A, shown in Fig. 32, is displayed as a geometrical development, or unwrapping, of the roll surface in which the vertical profiles indicate the clearances at intervals of 45° between the filled roll surface and a rigid flat plane. It can be seen that the surface profile variations are predominantly axial.

Variations in hardness over the roll surface may also contribute to the variations in heat source strength. In Fig. 33 a hardness parameter, ρ, is plotted on a development of the roll surface for roll A. There are large variations in roll hardness in both axial and circumferential directions.

Another measure of the local property variations is provided by variations in the rolling friction during successive single revolutions. Friction torque measurements for the steel roll against roll A at speeds sufficiently low to resolve fluctuations are shown in Fig. 34. These torque curves include bearing friction, which was at all times about 25% of the gross torque, however, fluctuations in bearing friction are negligible compared with those visible in Fig. 34. These fluctua-

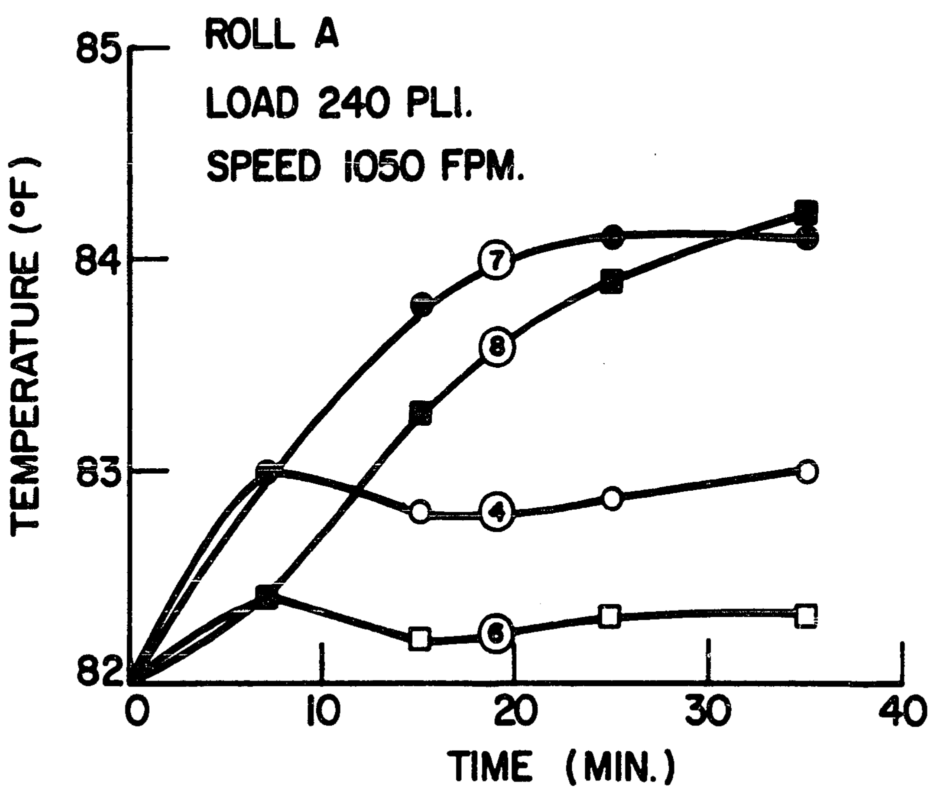

FIG. 31.

Temperature recorded by thermocouples at 3/32in. below the surface at 4 transaxial plane.

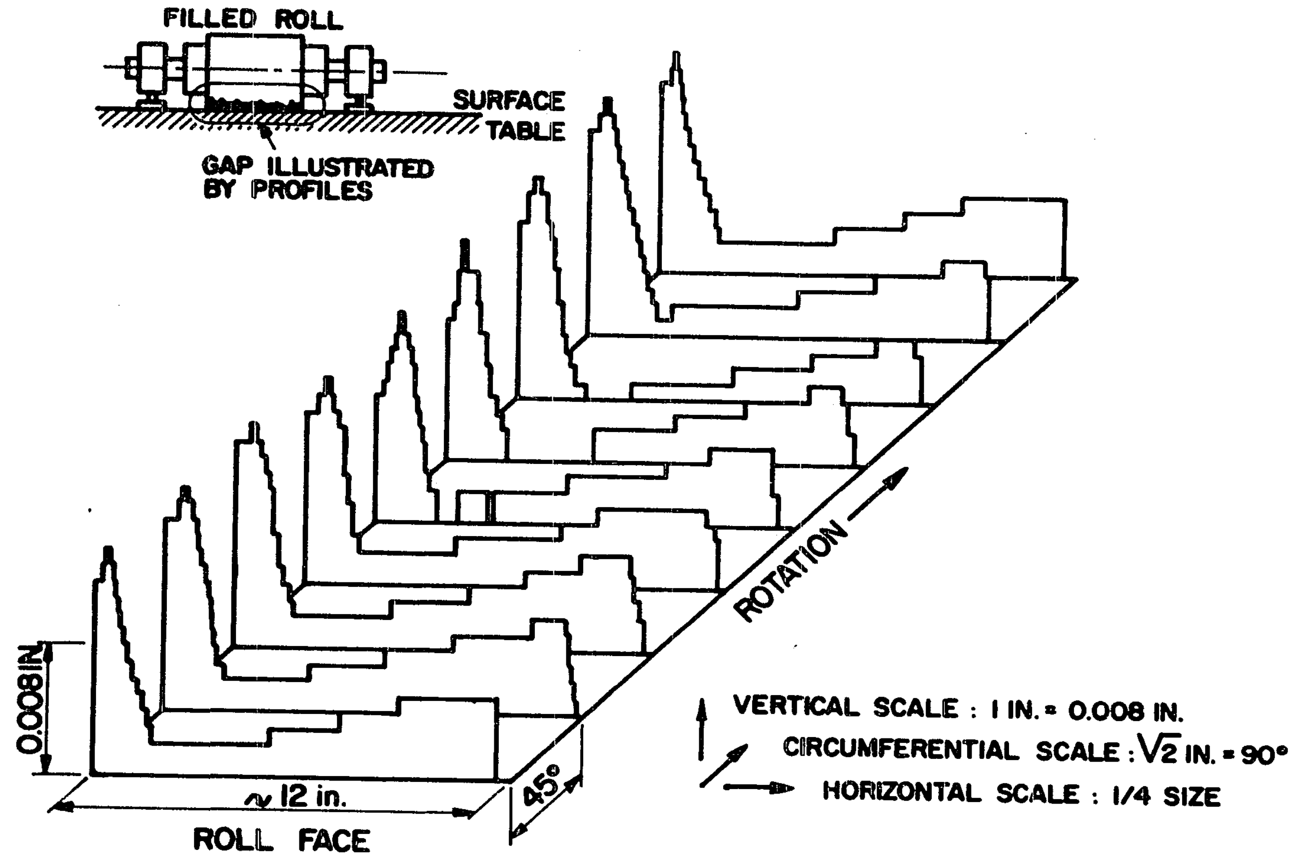

FIG. 32.

Variations in filled roll surface profile
Roll A.

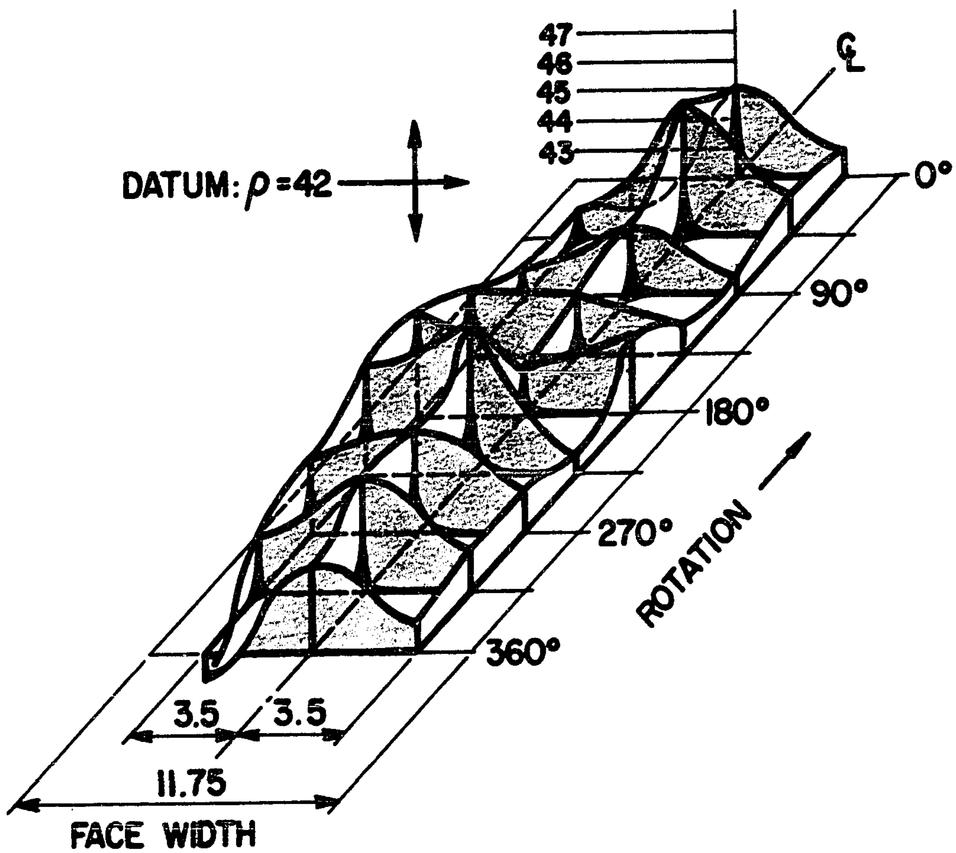

FIG. 33.

A typical surface hardness profile of roll A after about 50 hours of running.

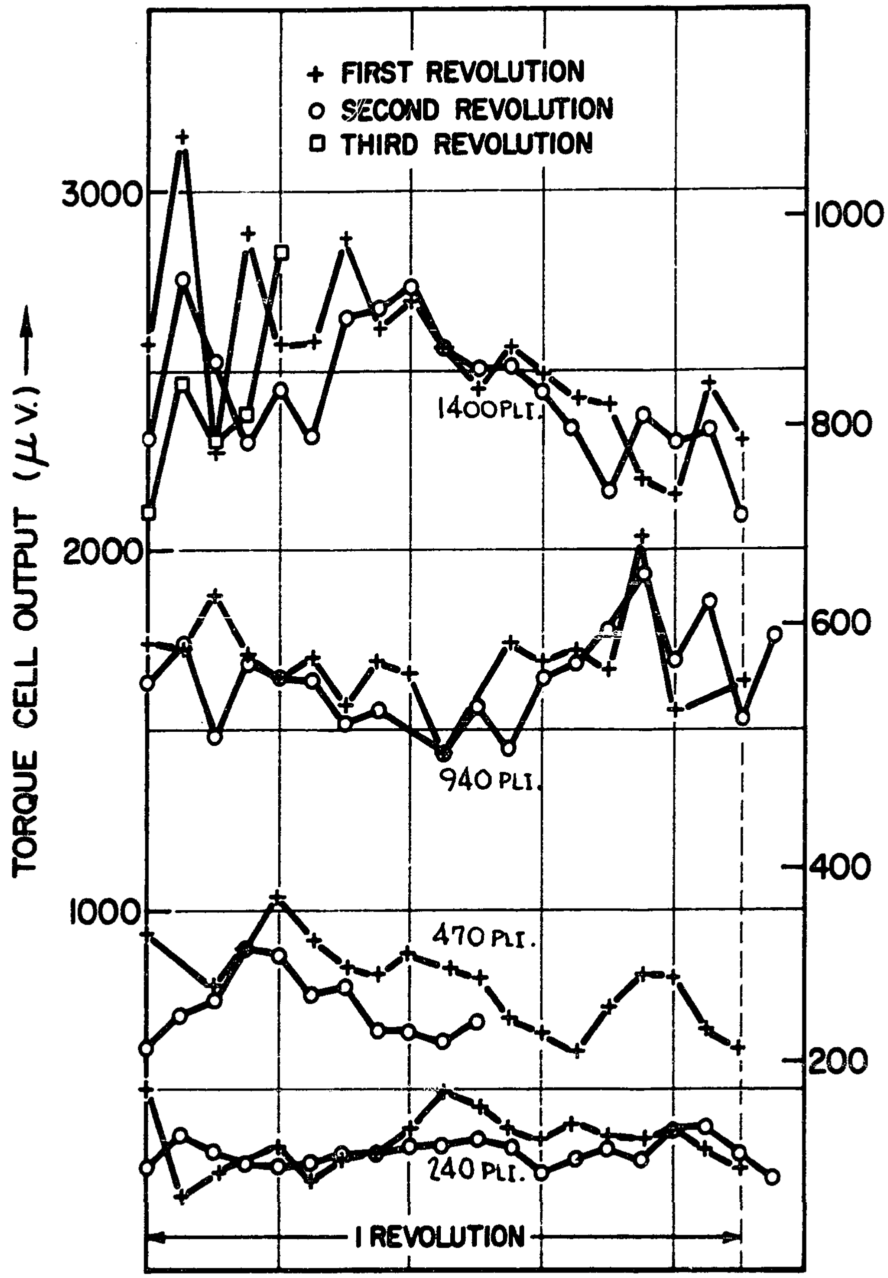

FIG. 34.

Typical fluctuations of gross torque over successive single revolutions of roll A.

tions in friction are consistent with circumferential differences in heat source strength.

Roll B, which was filled with a 25% by weight mixture of glass fibre with Filmat-2, was used in this test program because it was thought by the manufacturer that the inclusion of glass fibre in a filled roll would promote rapid thermal diffusion and thus arrest overheating and hence charring of the fill. If this mixture proved successful it would reduce the risk of roll damage and filled roll life would be prolonged. Potentially, an increased resistance to overheating would permit the application of higher load and speed with corresponding reduction in number of nips and increase in production. Since glass has a thermal diffusivity which is not remotely different from that of cotton and other organic materials it is not surprising that the thermal behaviour of roll B was quite similar to that of roll A which was filled with unblended Filmat-2, a pure cotton fibre. This similarity can be seen by comparing Figs. 26-28 with Fig.29. Roll B, however, sustained generally lower rates of temperature increase than did roll A operating at the same load and speed. By measuring the respective rolling friction while operating with either roll and by observing temperature rise within both rolls, while stationary, as they were heated by an electrical resistance heater wrapped around their surfaces, it was established that the lower rate of temperature increase in roll B sustained during operation was due to a lower coefficient of rolling friction rather than a higher thermal diffusivity. It was thus demonstrated that the addition of glass fibre to Filmat in this proportion does not, through superior diffusive properties, provide an attractive alternative to pure cotton fibre. Roll C, to be described in Part-II, was manufactured at the same time and under the same conditions as roll B but contained no glass fibre. In a control experiment, roll C exhibited an average rolling friction coefficient only slightly higher than did roll B. It would appear that glass fibre does not significantly reduce the rolling losses of fill material.

Data such as presented in Figs. 32-34 will be described in more detail in Part-II. They are mentioned above, however, because they provide further evidence for a heat source distribution which is variable with time over the roll surface.

A measure of the irreproducibility of temperatures within roll A is shown in Fig. 35. This is a resumé of the results of three successive tests run at 950 pli. Typical temperature versus time curves obtained at the roll surface and by thermocouples in the plane of disc 4 at depths of 3/32in. and 1/2in. during the first test which was run at 1050 fpm. are shown. Temperatures, measured at the two intermediate depths and not shown, were at all times between the two shown. The surface temperature is marked 4 surface as it may be recalled that this was measured at the location of disc 4, the centre of the roll face. Curve segments for temperatures at 3/32in. and 1/2in. depth in the plane of discs 6 and 8 are also shown and a typical axial temperature gradient can be seen as the 3/32 - 1/2in. temperature band at disc 6 is higher than at disc 4 which in turn is above that at disc 8. Curve segments for surface and 3/32 - 1/2in. depth temperatures are shown for the second test, marked 4**, which was run at 1700 fpm. Discs 6 and 8 are not shown in the second test as the temperature curves recorded at these two locations were essentially

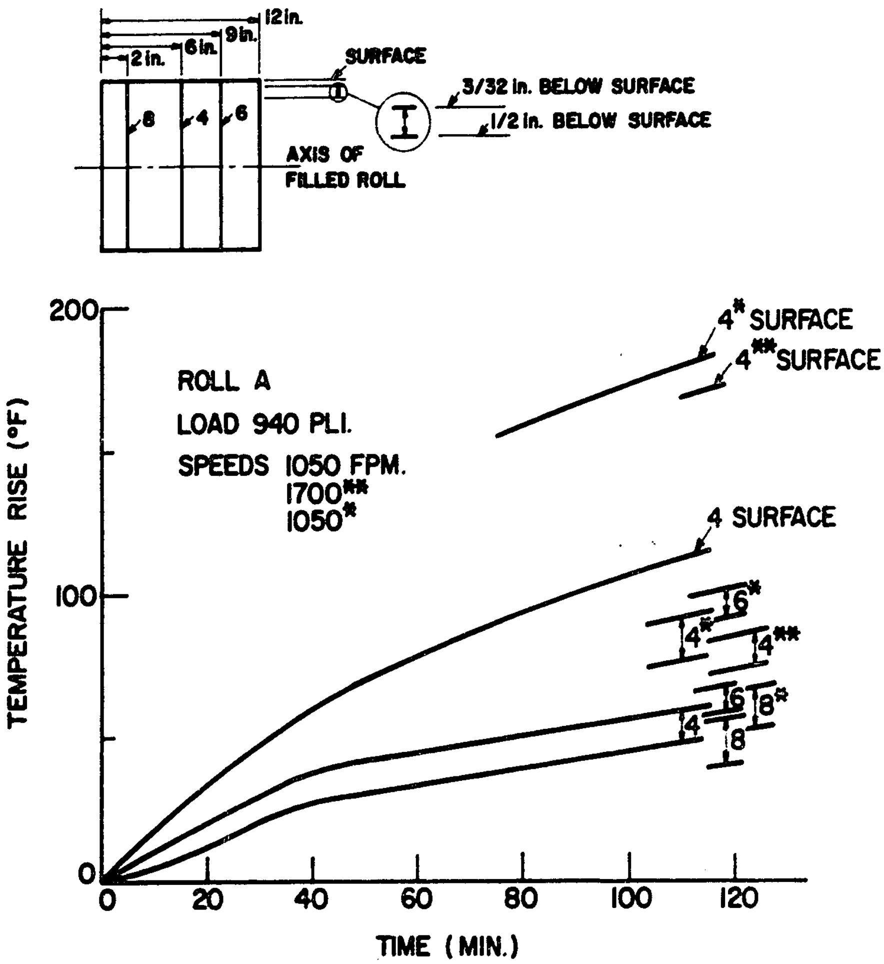

FIG. 35.

Irreproducibility of Temperature Distribution at Constant Load.

the same as those for disc 4. This test was atypical in that there was no appreciable axial temperature gradient. It may be noted that temperatures attained in the second test were at all times some 70% higher than those in the first. This increase in energy dissipation, which is proportional to the increase in speed, was to be expected. Before running the third test, which was a repeat of the first, roll A was operated for the first time at 1400 pli. in a test run at 650 fpm. The curve segments representing temperature at discs 4, 6 and 8 and on the surface are shown as 4*, 6*, 8* and 4s* respectively. It can be seen that temperatures during the third test rose somewhat more rapidly even than during the second test at the same load but 70% higher speed and that the usual axial temperature gradient was re-established. This sort of irreproducibility seems to occur when a test at a given load is repeated after an intervening test at higher load. It is possible that the increased heating, hence rolling friction, evident in the repeated test is a consequence of filled roll surface conditioning sustained at the highest load at which the roll had been previously run. It is not clear, however, why the running-in process should incur an increase in overall net friction, especially since running-in is synonomous with the development of a smooth glossy surface on the filled roll and an apparent compaction of the surface. Intuitively, one would expect a decrease in overall rolling friction under these conditions. The same cautious policy of conducting tests in stages of successively increasing load was adopted with both rolls and testing was stopped after the failure of thermocouples at 3/32in. depth on the assumption that the rolls had in fact sustained minor but significant subsurface damage and that temperature data which did not include measurements at the depth of 3/32in. had greatly reduced value. It was thus not possible to determine whether, after a filled roll has been conditioned at a given high load, its temperature behaviour becomes reproducible at loads less than the maximum load to which the roll has been previously subjected. It is thus strongly suspected that the irreproducibility shown in Fig.35 is a running-in or surface conditioning phenomenon and suggests or at least does not preclude the possibility of subsequent reproducible behaviour. However, Fig. 34 shows that, certainly, on a short-term basis and at low speeds large torque fluctuations, subtending no more than 20° of the filled roll circumference, persist thereby suggesting that the so-called conditioning process continues; possibly on a smaller scale, but indefinitely.

Measurements of the short-term periodic temperature fluctuations for a few revolutions of roll A are shown in oscillograms in Figs. 36-38. These were all obtained at a nip load of 470 pli. and a speed of 315 fpm., the highest load-speed combination which gave a temperature signal with an acceptable signal/noise ratio. Figs. 36a and 36b show the temperature variations measured by thermocouples at depths of 3/32in. and 3/16in. respectively in the plane of disc 6. Figs. 37a and 37b and Figs. 38a and 38b show similar data obtained in the planes of discs 4 and 8 respectively. Although these temperature fluctuations are not of the form predicted by equation (18) they show evidence of axial and circumferential variations in heat source strength. The amplitude of the temperature fluctuation is a measure of heat source strength and it can be seen in Figs. 36-38 that these amplitudes decrease in the same sequence as do the axial temperature gradients described in Figs. 31 and 35. If the heat

(a)

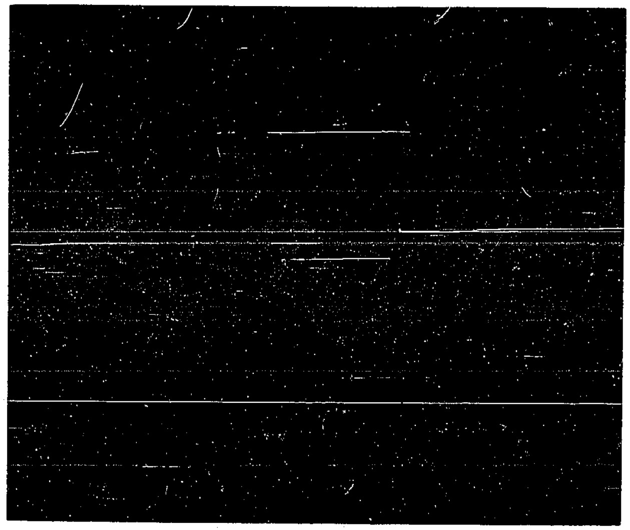

(b)

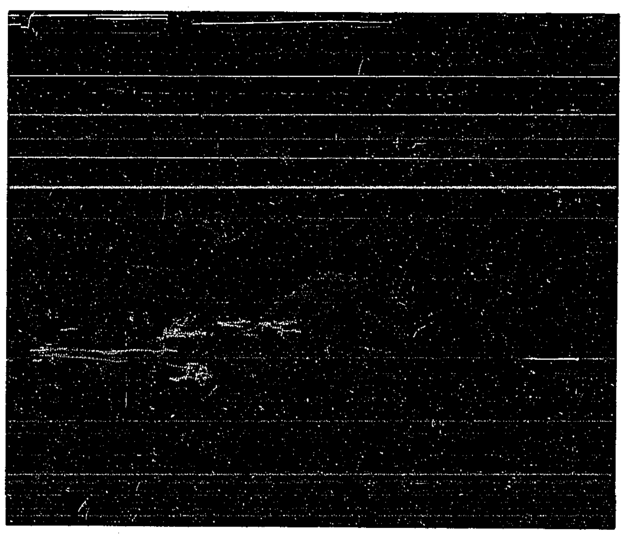

FIG. 36.

Oscillograms of Temperature Fluctuation in Roll A at Disc 6. Horizontal scale = 0.2 sec./division, Vertical scale = 0.7°F/division, Load = 470 pli., Speed = 315 fpm.

(a)

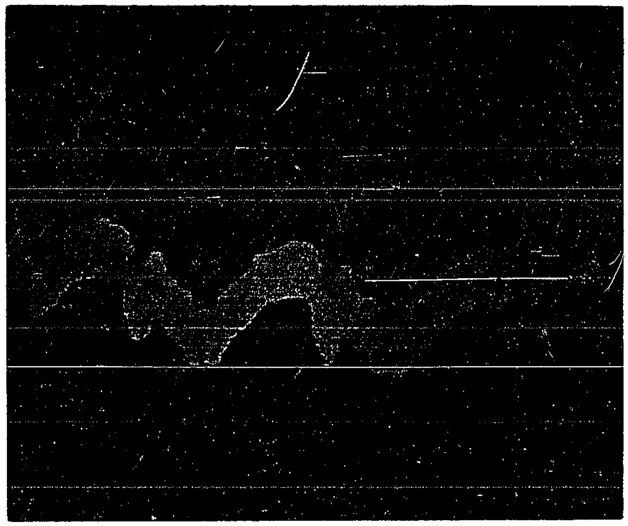

(b)

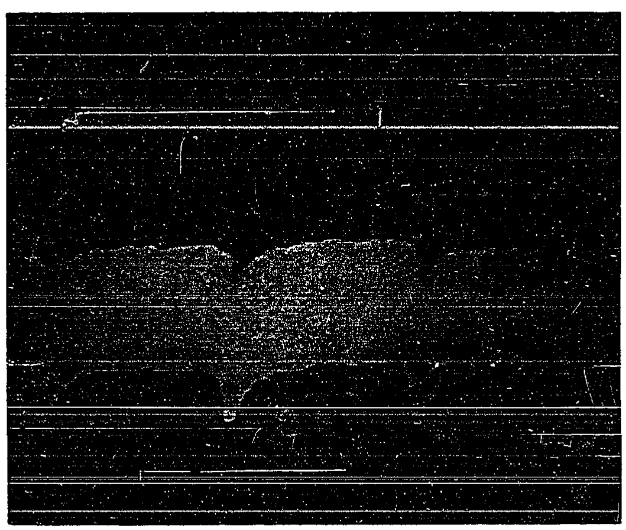

FIG. 37.

Oscillograms of Temperature Fluctuations in Roll A at Disc 4. Horizontal scale = 0.2 sec./division, Vertical scale = 0.7°F/division, Load = 470 pli., Speed = 315 fpm.

(a)

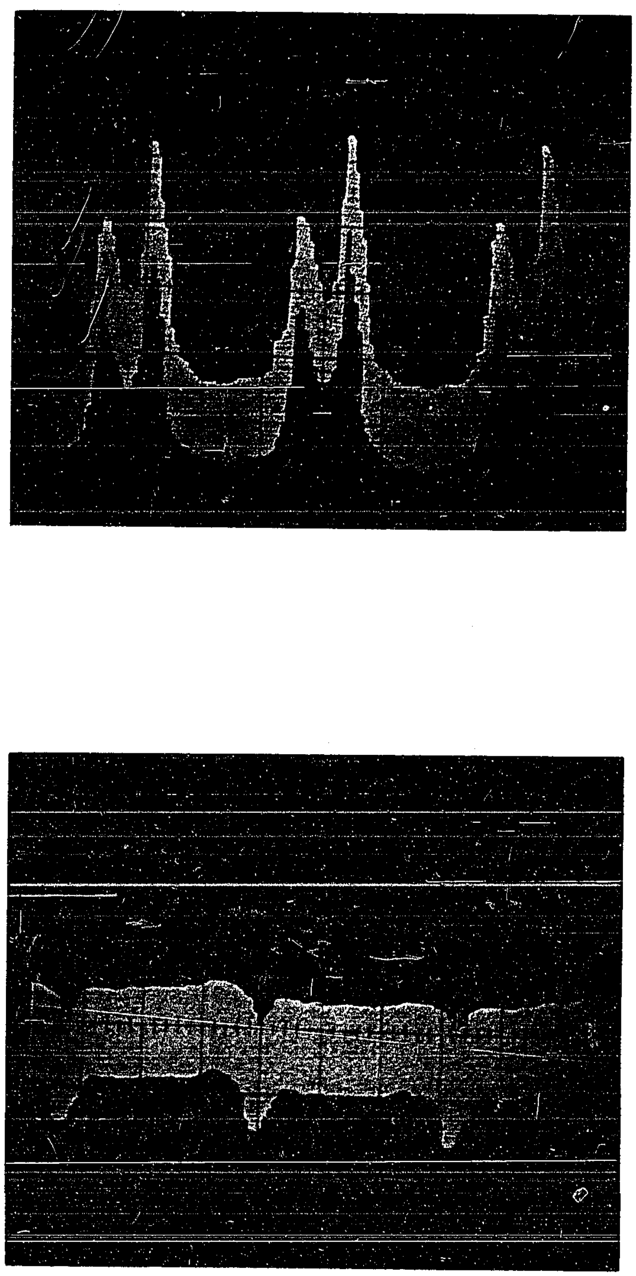

(b)

FIG. 38.

Oscillograms of Temperature Fluctuations in Roll A at Disc 8. Horizontal scale = 0.2 sec./division, Vertical scale = 0.7°F/ division, Load = 470 pli., Speed = 315 fpm.

source was uniform in the circumferential direction the temperature traces obtained from thermocouples at successive depths in the same transaxial plane, but separated by an angular interval of 45° as shown in Fig. 23, would be similar. In fact, they are not and there is greater similarity between the axially separated pairs, Figs. 37a and 36b and Figs. 37b and 38b, than between the circumferentially adjacent pairs, Figs. 36a-b, 37a-b and 38a-b. It is therefore concluded that circumferential variations in heat source exist. This conclusion is supported by sudden jumps in temperature, such as the one described in Fig. 28, which indicate a difference between the circumferential average and the temperature at a specific region on the roll surface which happened to stop under the radiation pyrometer. More convincing evidence might have been obtained if attempts to monitor the surface temperature with an oscilloscope had succeeded. Although the time response of the radiation pyrometer is adequate for this purpose, its output signal is only 10-20% of that generated by the iron-constantan thermocouples. Excessive noise, greater even than that evident in Figs. 36-38, rendered any transient temperature measurement made with the pyrometer useless. Important features of Figs. 36-38 may be summed up as follows:-

1) At any point, temperature fluctuations are reproducible over successive revolutions.

2) Although periodic, none of these exhibit the instantaneous temperature rise and subsequent exponential decay predicted by equation (18). Fig. 38a might conceivably approximate the predicted behaviour if it were not for the double peak

which can be seen to subtend about 90° of rotation of the roll.

3) All other traces show negative peaks or negative peaks combined with sinusoidal fluctuation.

Although sinusoidal fluctuations are not readily explained, negative and positive voltage peaks might be produced by transient stresses on a thermocouple junction. Fig. 39 shows the effect of a sharp blow with a plastic hammer upon the surface of roll A just above the couple at 3/32in. depth in the plane of disc 8. This oscillogram shows a negative voltage spike of 160μv. followed by a positive spike of half this amplitude. These features are superimposed on a background noise of 60 Hz.

Application of the Theoretical Model to Experimental Data

In the preceding discussion it was pointed out that there are considerable variations in heat source strength over the surface of a filled roll and that this source distribution changes during operation. It is felt, however, that the theoretical model represented by equation (18) serves a useful purpose in describing the development of a radial temperature profile within filled rolls. This model also helps one to understand how a filled roll may become overheated and thus burned beneath its surface. Calculated curves of temperature, at various depths beneath the roll surface, as a function of time will be fitted to experimental data obtained with roll A. Radial temperature profiles will be calculated and compared qualitatively to the radial distribution of discoloration sustained by an industrial supercalender roll cross-section which has been burned

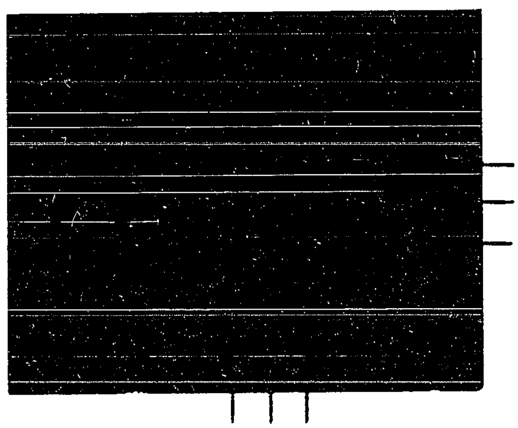

FIG. 39.

Thermocouple output resulting from a blow upon the surface of roll A at disc 8 with a plastic hammer. Horizontal scale = 0.05 sec./division, Vertical scale = 70 μv/division, 1°F = 30 μv (as shown in Figs. 36-38).

during operation. The method of calculation and the physical implications of the model will be discussed before presenting experimental temperature data comparisons or evidence of filled roll burning. This discussion is undertaken to show how equation (18) is fitted and scaled to approximate temperature data and to relate rolling friction coefficient to heat source strength as well as to predict conditions under which burning takes place. The program used to perform temperature calculations and the numerical approximations used therein are given in APPENDIX II.

In the following paragraphs the physical relationship between equation (18) and an operating supercalender filled roll will be dealt with in regard to the following points:-

1) Values of fill material thermal properties and the parameters which define heat loss from the roll surface.
2) Other physical parameters contained in equation (18); source strength in a half-space related to source strength in a filled roll; a velocity independent relationship between source strength and the coefficient of rolling friction.
3) Reduction of computation time through scaling of source strength and thermal diffusivity.

The fill material properties which are relevant to heat transfer are density, ρ, thermal conductivity, k, and specific heat, c. In addition an appropriate value of surface film heat transfer coefficient, H, must be estimated. These four parameters appear implicitly in equation (18) as the thermal diffusivity, K, and the surface heat loss parameter, h, which are defined as

$$K = k/\rho c \quad \text{and}$$

$$h = H/k,$$

respectively. The density of fill material in roll A, estimated from roll dimensions and the mass of fill used, is 90lb/ft.^{3} and this is within 5% of the density of any commercial roll. In a passive calorimetric experiment which produced values repeatable to within 5% specific heat of compressed fill samples was measured as 0.22 Btu./lb.°F and compares favourably with values quoted for cotton (31). Because the thermal diffusivities of many diverse organic solids, including cotton, which have densities in the range 5-100 lb/ft.^{3} are quoted (31,32) as about 0.025in.^{2}/min. it can be seen that the thermal conductivity of filled rolls is about 0.006 Btu.in./min.°F in.^{2}. Therefore at a typical low value of free convective heat transfer coefficient, H = 1 Btu./hr.°F ft.^{2}, the parameter h is about 2×10^{-2}in.$^{-1}$. It has been determined that at roll surface temperatures up to 100°F above ambient the parameter h can be ignored thereby simplifying temperature calculations. Such low values of film coefficient/thermal conductivity are reasonable in the case of experiments wherein there is no cooling of filled roll surface by a paper web or compressed air jets. Even though tests were run in which the rolls had, on occasion, a fairly high surface speed the heat loss due to convection is thought to have been small because counter-rotation as shown in Fig.40 tends to inhibit the build up of air circulation.

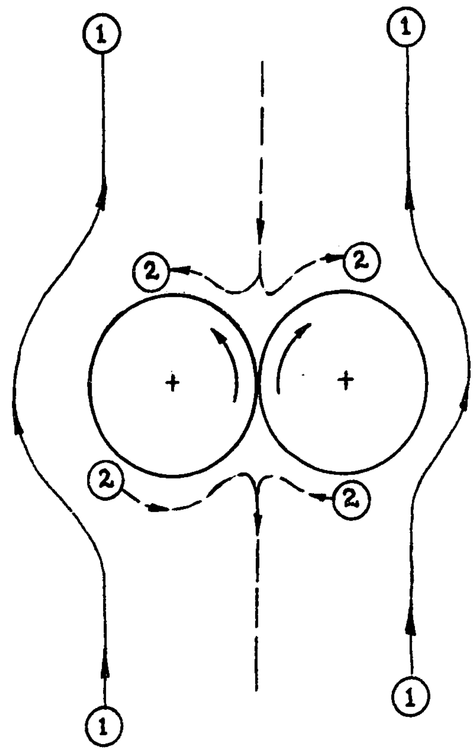

FIG. 40

Free Convection about a pair of Counter-rotating Rolls
1 - Flow induced by free convection
2 - Flow induced by counter-rotation

It should be recalled that the temperature v at any depth x due to a heat source located at x' in a material of thermal diffusivity K with a heat loss from its surface characterized by the ratio of surface film heat transfer coefficient to material thermal conductivity $h = H/k$ is given at any time t after the occurrence of the first source, by equation (18) as:

$$v = S \sum_{n=o}^{N} \frac{1}{2\sqrt{\pi K(t-nT)}} \left\{ e^{-(x-x')^2/4K(t-nT)} + e^{-(x+x')^2/4K(t-nT)} \right.$$

$$\left. - he^{K(t-nT)h^2+h(x+x')} \operatorname{erfc}\left\{ \frac{x-x'}{2\sqrt{K(t-nT)}} + h\sqrt{K(t-nT)} \right\} \right\}$$

where N is the number of sources, hence completed revolutions of the filled roll, which have occurred since time t = o with a period T. Note that in the above equation the source strength S is given in units of $^{o}F.in.^{3}/in.^{2}$ where the area, $in.^{2}$, refers to a unit area of the instantaneous uniform plane source parallel to the surface of the half-space of the one-dimensional model. When referred to a supercalender nip, wherein heat is continuously generated and not liberated in discrete gross quanta with period T, the source strength S reflects a rate of heat generation per unit area, at the depth of the assumed source, which has passed under the nip in one revolution and has produced the quantity of heat liberated by a single source. S represents a temperature rise sustained by a unit volume of material when a quantity of heat $S\rho c$ $Btu./in.^{2}$ is liberated in a material of density ρ and specific heat c. Thus S must not be confused with either the rate of uniform heat production which can be assigned to an inch of nip length or with the actual rate of heat production divided by the filled roll surface area. Both of these are speed dependent. The area rate of heat generated associated with the heat source strength S corresponds to a single source occurrence, hence to a single revolution. It is therefore independent of the operating speed or rate of source occurrence. Thus the heat source strength S can easily be related to a mechanical loss factor, say the coefficient of rolling friction μ, without recourse to any specific value of operating speed of the filled roll.

$$\mu = 9336\frac{\rho c S}{P} = 108\frac{S}{P} \qquad - (19)$$

for previously mentioned values of ρ and c. μ is the friction coefficient which will produce, through surface traction under a nip load of P pli., the torque necessary to drive a single nip. ρ and c are fill density and specific heat which change the units of S from °F. in.^{3} to Btu. 9336 is the mechanical equivalent of heat in lb.in./Btu. The above relationship (19) can be shown by considering the rate, E, of energy dissipated in an inch length of nip per minute as:-

$$\frac{E(\text{lb.in.})}{(\text{in.min.})} = \mu P \frac{(\text{lb.})}{(\text{in.})} V \frac{(\text{in.})}{(\text{min.})}$$

and the rate, E', of heat generated per square inch of source parallel to or concentric with the roll surface per minute due to N revolutions as:-

$$\frac{E'(\text{lb.in.})}{(\text{in.}^2\ \text{min.})} = 788 \times 12 \frac{(\text{lb.in.})}{(\text{Btu.})} \rho \frac{(\text{lb.})}{(\text{in.}^3)} c\frac{(\text{Btu.})}{(\text{lb.°F.})}$$

$$\frac{S(\text{°F.in.}^3)N(\text{min.}^{-1})}{(\text{in.}^2)}$$

where it can be seen that:-

$$E = E's$$

and the velocity, V, of the roll surface or source surface is:-

$$V = Ns$$

where s is the area per inch of nip length of a circumferential strip at the depth of the source, the dimensions of all quantities are shown thus ( ) enclosed.

There are only two time dependent parameters in equation (18); the thermal diffusivity K and the period of source recurrence or of roll revolution T. Because the temperature v at any time t is the summation of the discrete contributions of individual heat sources which have occurred (t-NT), (t-(N-1)T), (t-(N-2)T),...., (t-2T) ago, the temperature after 10 minutes, for example, is identical to the temperature after only 1 minute in a material with a 10 times greater value of thermal diffusivity K in which an identical amount of heat has been liberated by N/10 sources. This property permits the representation of a given roll model by a version of equation (18) in which the number of terms have been reduced by any given factor F of which the actual number of roll revolutions to be simulated is an integer multiple. Therefore N need not be the actual number of revolutions of the filled roll in a simulated test which has run for some time tF, but merely a fraction 1/F thereof, if the thermal diffusivity K has been increased by the same factor F. Because the heat liberated in the interval t must be identical to that actually liberated in the real-time interval tF in order that the F-accelerated model version predict temperatures the same as real-time temperatures, the source strength used in the accelerated model must be SF where S is the actual strength per square inch of source-surface in every interval T.

Approximation of Temperature Measured in Roll A

The one-dimensional thermal model was used to approximate experimental data of temperature plotted against time at various radial distances within roll A operating at three typical but widely different conditions of load and speed, i.e. 470 pli. and 1050 fpm., 940 pli. and 650 fpm. and 1400 pli. and 1700 fpm. These approximations are the solid curves shown in

Figs. 41-44. It was found that all three sets of data were best described by a surface source and, except for the last set by negligible heat loss from the roll surface. Calculations made with a heat source located some finite distance beneath the roll surface invariably failed to predict sufficiently high surface temperature or sufficient difference in temperature between radially adjacent couples straddling an assumed subsurface source location.

The solid curves in Fig. 41, which were calculated using equation (18), agree reasonably well with experimental data obtained in two separate tests, both run at 470 pli. and 1050 fpm. These calculations were made with a source strength, $S = 1.09 \times 10^{-3}$ °F in^3/in^2, arbitrarily chosen so that the characteristic which represents the temperature at 3/16in. below the filled roll surface falls on one of the data points, as shown, recorded at 3/32in. after 80 minutes of operation. Actually, the temperature calculations for the theoretical curves shown in Figs. 41-44 were performed with SF = 1 but then the temperatures thus obtained were, in each case, multiplied by an arbitrary fraction to obtain an ordinate value, at some time t, as required, i.e. indicated on Figs. 41-42 as "point of fit". The data indicate that greater temperature differences exist between the four couple locations than those which are predicted by the model. On closer examination, however, it can be seen that the model fits, in some regions, either one set of data or the other. Failing this, the data from either test straddle the predicted curves. In all cases, save a single datum point, the ambient temperature spread at the beginning of the tests, as shown in the inset, is greater than the

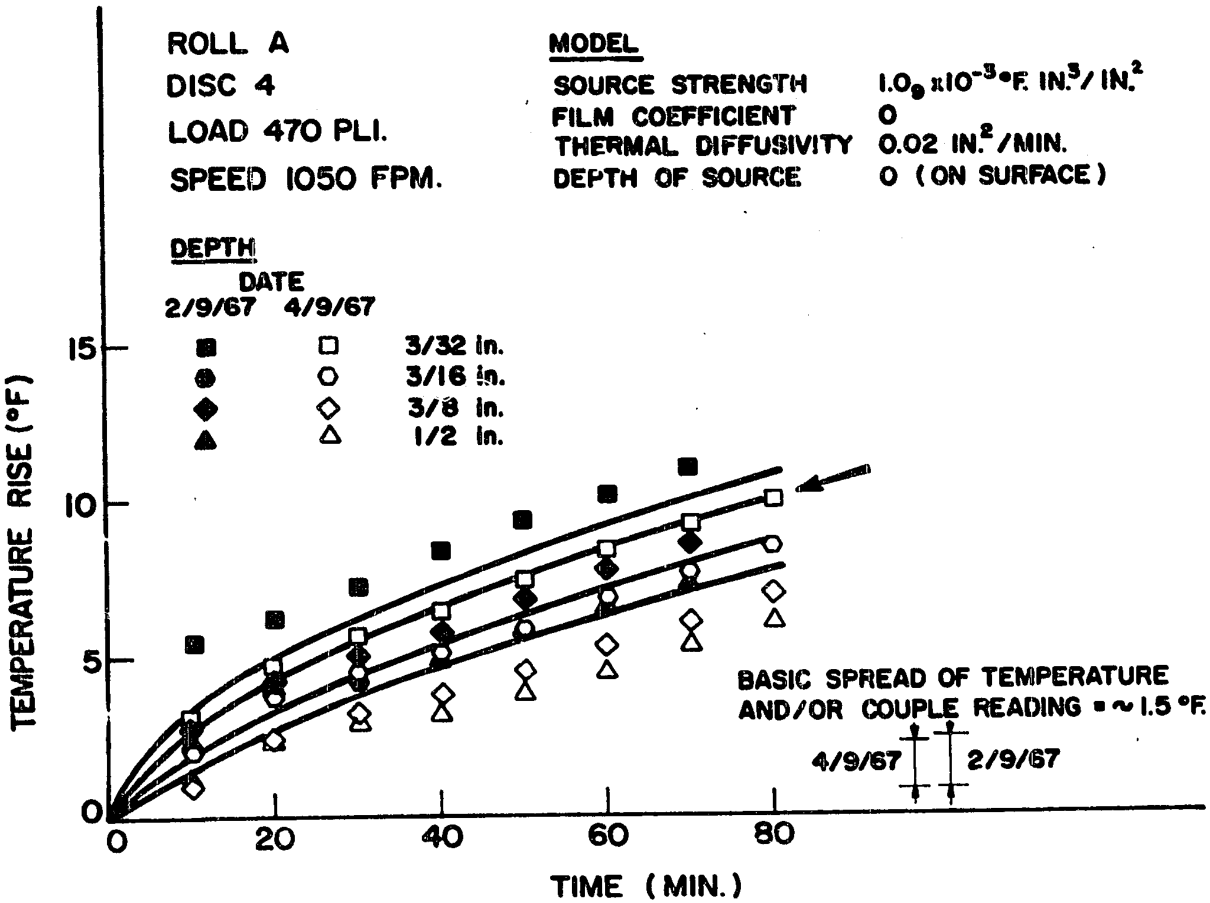

FIG. 41.

Fit of One-Dimensional Periodic Heat Source Model to Experimental Data

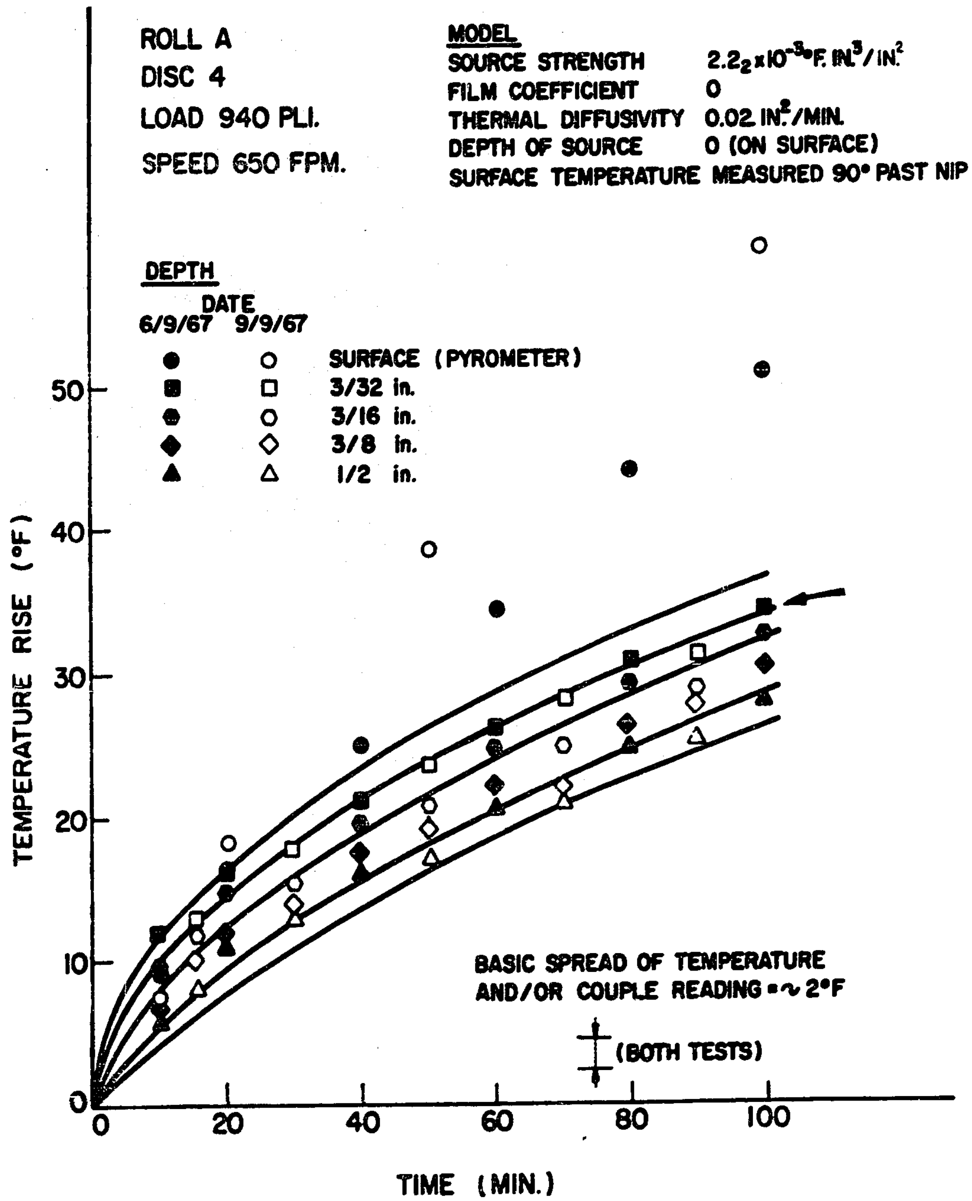

FIG. 42.

Fit of One-Dimensional Periodic Heat Source Model to Experimental Data.

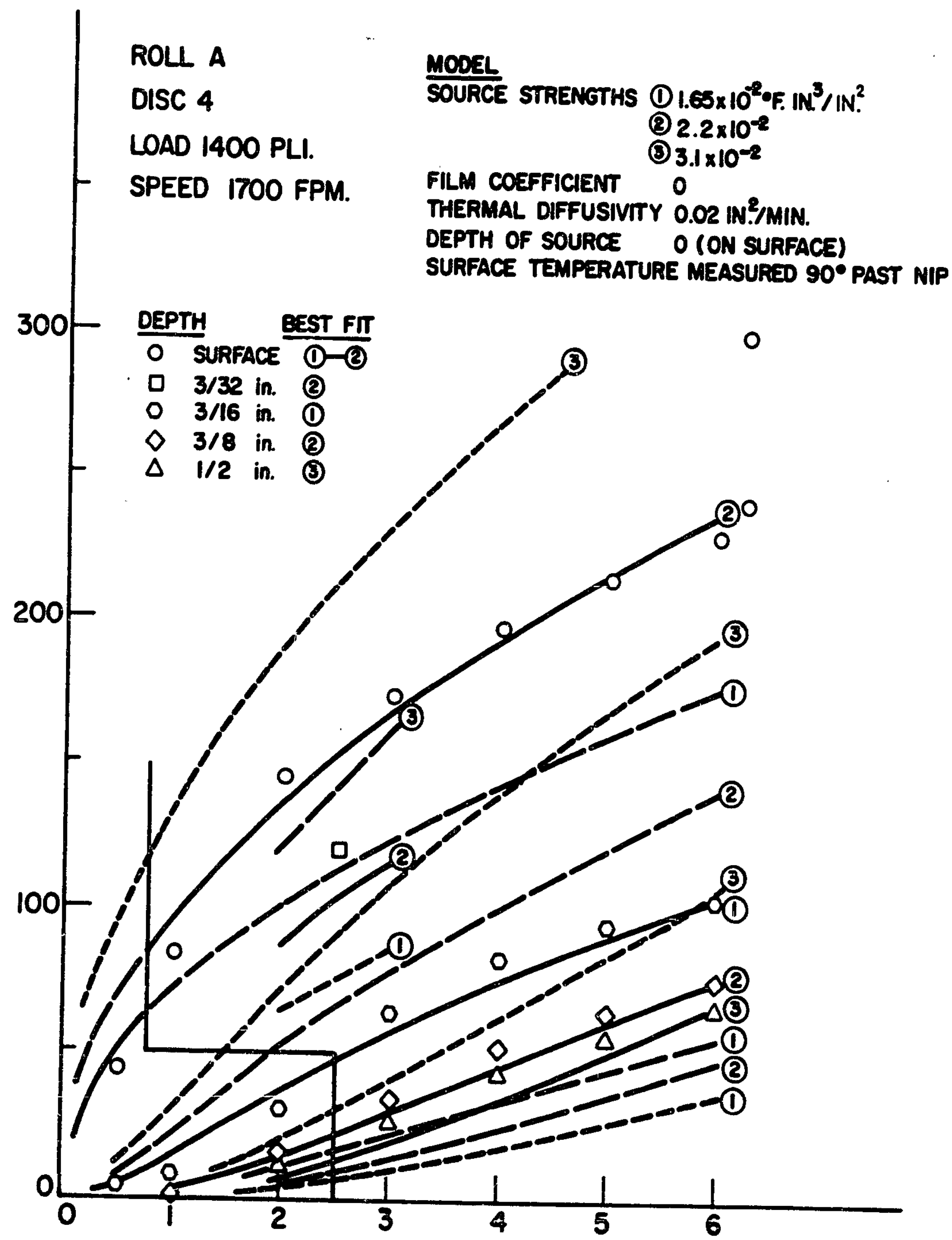

FIG. 43.

Fit of One-Dimensional Periodic Heat Source Model to Experimental Data.

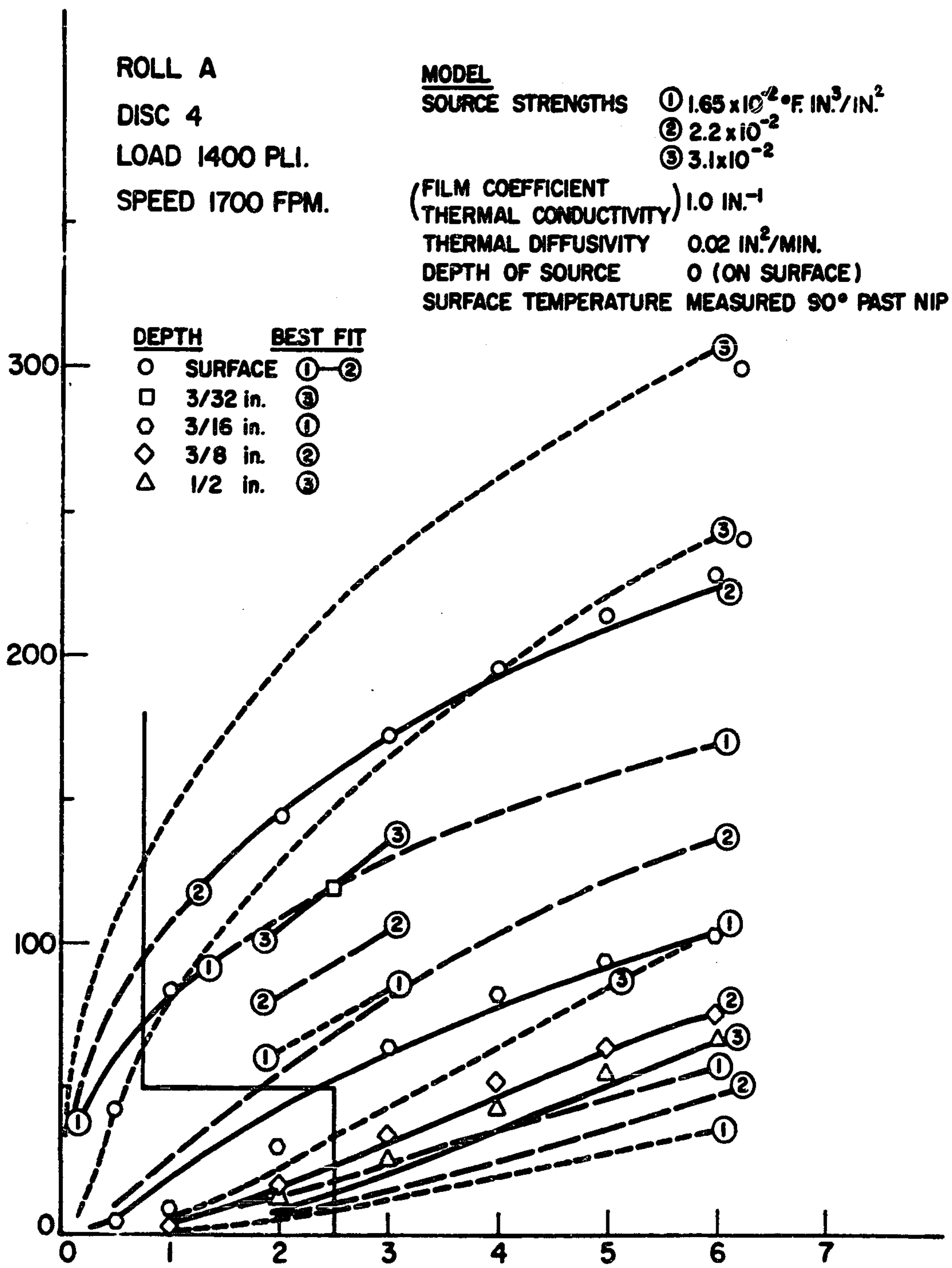

FIG. 44.

Fit of One-Dimensional Periodic Heat
Source Model to Experimental Data.

displacement of data points from the curves. No surface temperature measurements are included in Fig. 41 because the radiation pyrometer is accurate to about ± 5°F. and readings of surface temperature rise in the range 10-15°F. would be unreliable.

In the second example, shown in Fig. 42, the theoretical model was fitted to temperature data obtained in two separate tests run at 940 pli. and 650 fpm. The model parameters which produced the best fit were similar to those chosen for the previous example except that a source strength of 2.22×10^{-3} °F.in.^{3}/in.^{2} was chosen in order to have the curve representing the temperature at 3/32in. depth fall on a data point recorded at this depth after 100 minutes of operation. This example shows better agreement between predicted and measured values of temperatures beneath the filled roll surface than did the example presented in Fig. 41 wherein predicted radial temperature differences appeared to be too small. The discrepancies between data and theory in Fig. 42 are just the opposite and again the vast majority of temperature readings on the curves to within the latitude of the initial temperature spread in the roll. There is fair agreement between the curve of surface temperature and the experimental data up to about 40 minutes of operation. The divergence between prediction and measurements of surface temperature after this time were probably due to circumferential variation in heat source strength. This will be dealt with in the next example illustrated in Figs. 43-44.

Figs. 43-44 show data obtained during a very short test, run at 1400 pli. and 1700 fpm., in which temperatures rose rapidly throughout the roll and there was no time for thermal relaxation between the points of large circumferential separation at which the thermocouples were located. A model with unique value of source and surface loss condition does not adequately represent the experimental data. Therefore an attempt was made to acknowledge:-

1) The increase in heat loss from the surface, represented by a finite value of film heat transfer coefficient, due to a large difference between the roll surface and the ambient temperatures.

2) Large circumferential differences in heat source strength which probably occur over angular intervals no larger than the 45° circumferential spacing of adjacent thermocouples.

Temperature data, shown in Fig. 43, up to a surface temperature about 100°F. above ambient, were represented, as in Figs. 41-42, by a surface heat loss parameter $H/k = h = o$. Above this value of surface temperature a better approximation of data was obtained with $h = 1.0 \text{in.}^{-1}$ as shown in Fig. 44. To show the effect of possible large circumferential differences in heat source strength, temperature data obtained at 3/16in., 3/8in. and 1/2in. below the roll surface were individually fitted using three appropriate values, 1.65×10^{-2}, 2.2×10^{-2} and 3.1×10^{-2} °F. in.^{3}/in.^{2} of source strength. The characteristics for temperature at the surface and at the four depths of 3/32in., 3/16in., 3/8in. and 1/2in. were calculated for all three values of source strength. The comparison of all these curves with the relevant data produces a number of important observations.

1) The curves, 1, produced by a source strength of 1.65×10^{-2} °F. in.^{3}/in.^{2}, chosen to produce a fit to data at 3/16in. depth,

resulted in predicted values of surface temperature which, compared to the measured data, were generally too low except for the initial period of operation up to 1-2 min. This fit also produced unacceptably low temperature predictions for the depths of 3/8in. and 1/2in.

2) The curves, 2, produced by a source strength of 2.2×10^{-2} °F. in.^{3}/in.^{2} chosen to fit data at 3/8in. below the roll surface, describe the surface temperatures very well while predicting excessively high temperatures at 3/16in. and excessively low temperatures at 1/2in. depth. Because the surface temperature measurement is a circumferential average and not, like those measured by thermocouples, an average at a specific point within the roll it is not surprising that it is best approximated by the second source strength whose value is between the largest and smallest.

3) The curves, 3, produced by a source strength of 3.1×10^{-2} °F. in.^{3}/in.^{2}, which were scaled to fit the temperature data measured at a depth of 1/2in. predicted excessively high temperatures at the surface as well as for the depths of 3/16in. and 3/8in. The sudden rise in surface temperature, represented by a single high temperature data point, recorded just as the roll was stopped was assumed to be caused by a region of high surface temperature coming to rest in the field of view of the radiation pyrometer. This assumption is supported by the fact that this single data point falls quite

near the characteristic produced by the highest of the three values of source strength.

4) High loading severed the connection to the 3/32in. depth couple. As a result, only one reading was obtained from this sensor as a connection was briefly re-established by chance contact between the broken wires. Note that the single data point measured with the damaged couple at 3/32in. in depth lies between the curves predicted by the 3.1×10^{-2} and 2.2×10^{-2} °F. in.^{3}/in.^{2} sources.

5) The differences in temperature distribution produced by the three source strengths, none of which are by themselves an entirely satisfactory description of the heating behaviour represented by the data in Figs. 43-44, are of the same order of magnitude as the differences between temperature distribution measured in two separate tests run at 950 pli. and 1050 fpm. shown in Fig. 35.

Application of the Model to the Prediction of Roll Burning

The preceding examples of filled roll heating were best approximated by a surface source and in spite of variations in source strength, the heating behaviour was reasonably well described by the model represented by equation (18). The predominant fraction of the heat generated was most certainly concentrated in an extremely thin surface layer, a layer much less than 3/32in. thick. Although only results obtained with roll A have been presented, similar results were obtained with roll B. There is no reason to believe that filled rolls in a large industrial supercalender stack behave differently except, of course, for the strong surface cooling effect of compressed air jets, a moist paper web and evaporation of condensate from the steam showers. An attempt is made in Fig. 45 to describe radial temperature distributions within filled rolls operating under industrial conditions. This shows radial temperature distributions, calculated with equation (18) using unit heat sources located at various depths, x', Fig. 45a shows the distribution after 70 minutes operation at 100 rpm. with moderate cooling where $H/k = 3\text{in.}^{-1}$ and Fig. 45b the distribution with very severe surface cooling where $H/k = 1000\text{in.}^{-1}$. Under the assumed condition of severe surface cooling shown in Fig. 45b an evaporative film coefficient as high as 1500 Btu./hr. °F.ft.^{2}, which could conceivably occur in the presence of condensed moisture, will account for only a fraction of the assumed value of $h = 1000\text{in.}^{-1}$. It is also necessary to assume a decrease in material thermal conductivity from 0.006 to 0.0002 Btu.in./min. °F.in.^{2}. This is possible only through a small local separation of the fill surface from the substrate. Such separation would account for reported (35) measurements of abnormally low local surface hardness in overheated regions of a filled roll. In all cases temperatures were calculated at 180° or opposite to the nip, and representing half the period of recurrence of the heat source was chosen to approximate a mean effective temperature distribution. For the first half of a revolution the resulting radial temperature distribution would be skewed with a maximum nearer to the surface than that shown at 180°. In the second half of any revolution the maximum temperature would be at a depth greater than that shown. In the case of moderate surface cooling

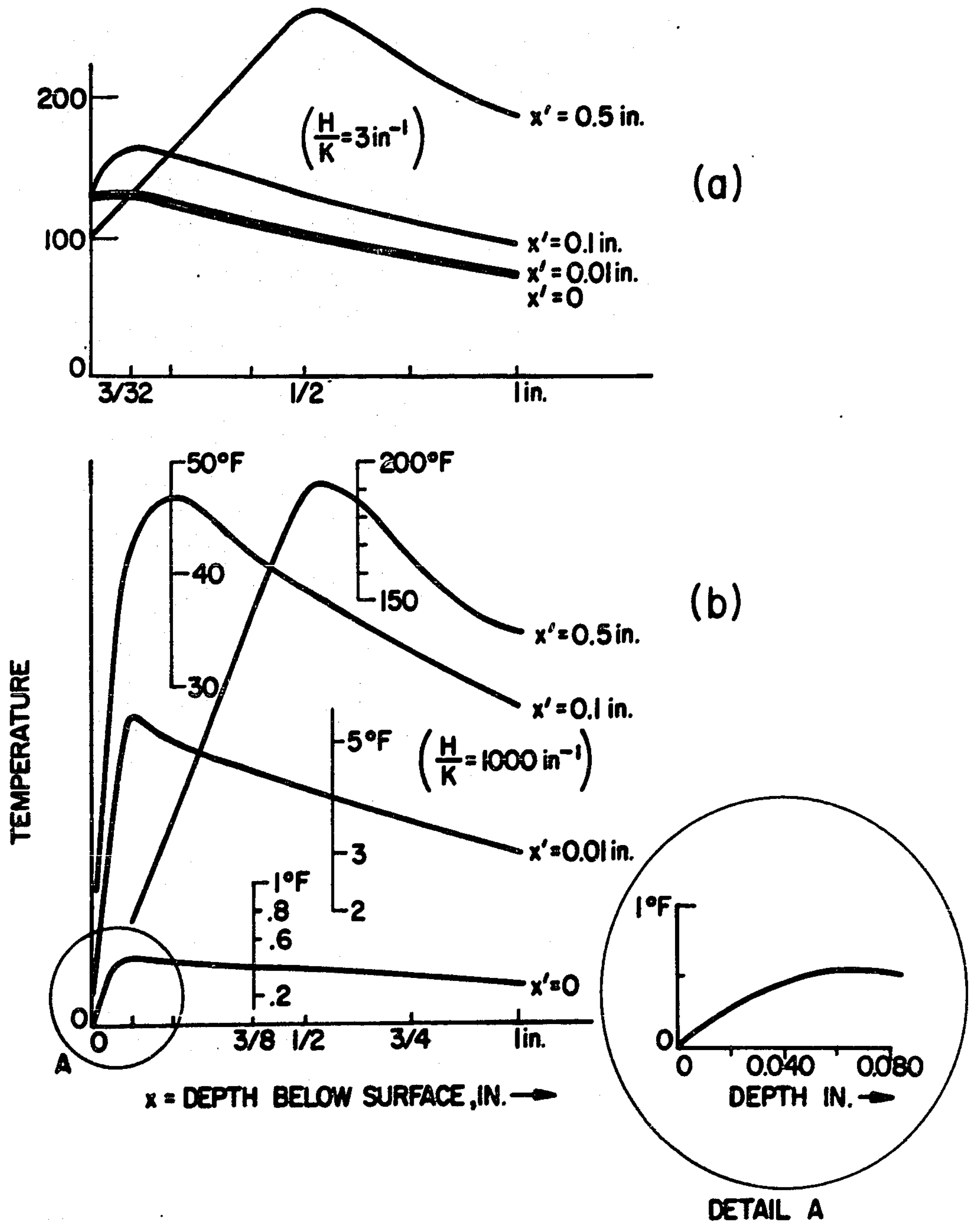

FIG. 45.

The effect of varying the depth, x', of heat source and the surface parameter, h, as predicted by one-dimensional thermal periodic model. All temperatures calculated as occurring 180° downstream of nip.

there is little difference between the radial temperature distributions produced by a source at 0.01in. depth and one on the surface, i.e. at $x' = o$. Note that none of these distributions shown in Fig. 45a correspond to the discolouration which occurred in a typical burned fill section shown in Fig. 46. The discolouration extends from about 1/32in. below the surface, with a maximum darkening at about 1/16-3/32in., to a depth of 1 in. This lack of correspondence can be easily shown by constructing vertical lines at these three depths on Fig. 45a so as to intersect all the temperature curves. It can be seen that such constructions would not produce similar temperatures at depths of 1/32in. and 1 in. Assuming that similar temperatures would have to have been produced at the radial limits of discolouration shown in Fig. 46, none of the curves in Fig. 45a describe the condition at which burning occurred. In Fig. 45b, however, a similar construction would produce temperatures, at 1/32in. and 1 in., in both the $x' = o$ and the $x' = 0.01$in. characteristics, which are more nearly equal than any pair of other intersections with the six other curves in Figs. 45a and 45b. In both the $x' = o$ and the $x' = 0.01$in. curves in Fig. 45b the maximum temperature agrees with the location of the area of darkest fill in Fig. 46, i.e. at a depth between 1/16in. and 3/32in. Note that it is the shape of these temperature distributions which is important, not the magnitude of temperature which occurs at any radial displacement. The heat source strength, which for convenience was unity for all calculations plotted in Fig.45, can be adjusted to any appropriate value as in the case of the curve fitting process used in Figs. 41-44.

It would seem that the example of roll burning which was presented

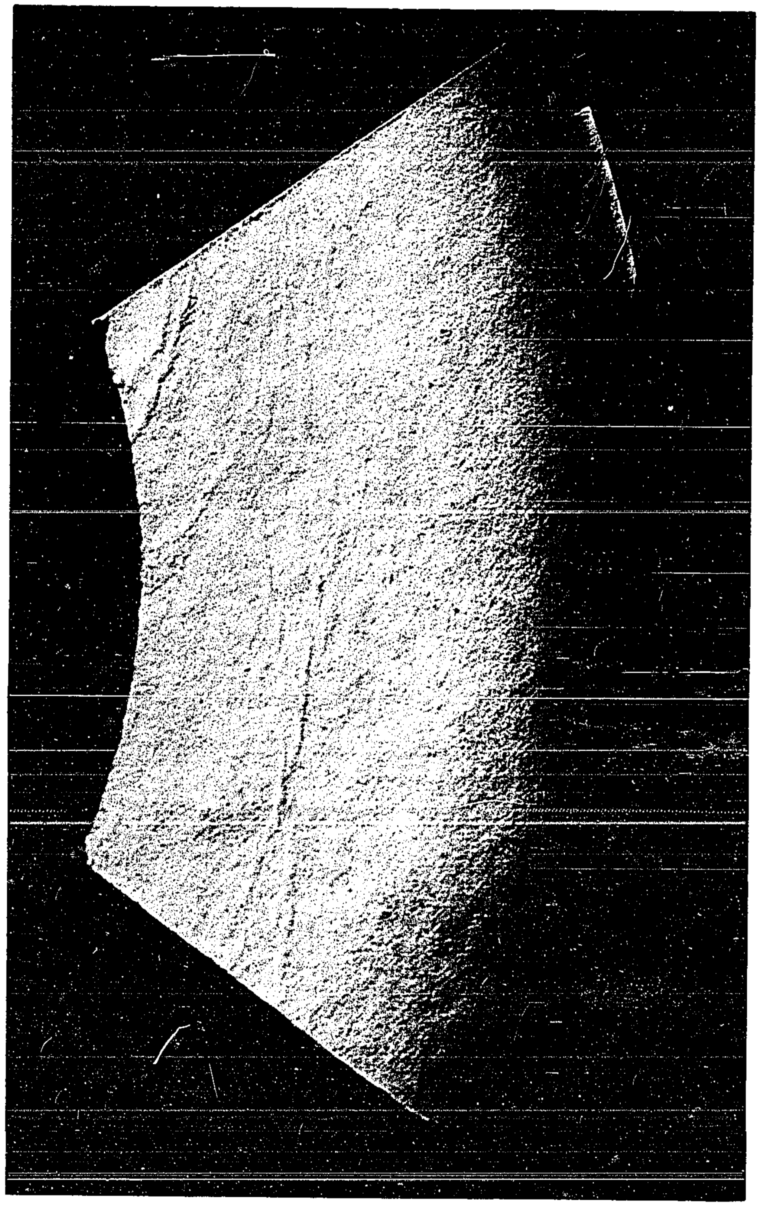

FIG. 46.

A charred section of supercalender roll fill material.
Annular thickness of disc section is about 3-1/2 inches.

is best described by a heat source on the surface and very severe surface cooling. It is known that overheated filled rolls are subjected to strong surface cooling and that a filled roll often burns after it has become wet, a condition which promotes rapid surface cooling through evaporation and which could conceivably bring about surface delamination. Through measurements of temperature within filled rolls operating in an experimental stack and through examination of burned cross-sections of industrial filled rolls, the application of the thermal model represented by equation (18) has proved that heat generated in a supercalender nip is, for all intents and purposes, produced on the surface of the filled roll, notwithstanding the distribution of heat source and its instability.

Friction Coefficients Predicted from Heat Source Strength

Although a rational approach to the comparison of filled roll heating with rolling friction in a supercalender nip would have been to translate the measured values of rolling friction coefficient into equivalent values of heat source strength and to use these to calculate temperatures vs. time curves to fit temperature data as shown in Figs. 41-44, this procedure was not followed. Recall that the thermal model used to fit experimental data accounts only for heat loss from the exposed surface of the filled roll and that in cases where surface temperatures did not exceed 100°F. above ambient this loss could be ignored. This does not imply that no heat is lost from the filled roll; on the contrary, the steel roll has a much higher thermal diffusivity than the filled roll with which it is in contact. Since it was assumed that heat is generated in the nip region and it has been shown that this generation occurs at or very near the fill surface it is reasonable to expect that a large fraction of the heat is conducted to the steel roll. However, this has been ignored in the formulation of the model for the following reasons:-

1) The model was developed to describe heating which occurs within the filled roll because it, not the steel roll, is damaged through overheating. Therefore the heat generation reflected by the heat source strength S represents that fraction of the heat which remains in an element of the filled roll which has passed under the nip.
2) The area of nip contact was not measured or calculated.
3) If heat loss over a small fraction of fill surface were included, the model would no longer be a case of one-dimensional transient heat conduction; a most simple and convenient representation.
4) At high load and speed it might be expected that conduction to the steel roll is diminished by:-
    i) the heat source occurring at some small distance beneath the filled roll surface at increased load so as to provide insulation during nip contact,
    ii) the reduced time available for heat transfer from a surface element in nip contact at higher speed.

It was, therefore, decided to calculate apparent rolling friction coefficients based on those arbitrarily chosen values of source strength which produced the best approximations to temperature data. The values of source strength, S, used to produce the curves shown in Figs. 41-44 andthe previously derived equation (19).

$$\mu = 9336\frac{\rho c S}{P} = 108\frac{S}{P}$$

and values of μ measured with roll A as reported in Part II, Fig.59 produced the following table of comparison:-

Fig.	P (pli.)	S ($^\circ$F.in^3/in^2)	μx10^3 calc.	μx10^3 meas.	$\frac{\mu \text{ meas.}}{\mu \text{ calc.}}$ (%)
40	470	1.09×10^{-3}	0.23	2.0	8.3
41	950	2.2×10^{-3}	0.25	2.9	11.1
43-44	1400	1.65×10^{-3}	1.3	3.3	2.6
43-44	1400	2.2×10^{-3}	1.7	3.3	1.9
43-44	1400	3.1×10^{-3}	2.4	3.3	1.4

It can be seen that the values of friction coefficient calculated on the basis of heat source strength are low; about 10-70% of the measured values. It would appear that under the operating conditions during which the temperature measurements were made, a large fraction of the heat generated is conducted to the steel roll. Refer to Fig.45b, however, and consider the magnitude of source strength necessary to bring about charring. Recall that the unity source strength, used to predict the shape of the radial temperature distribution at conditions which led to charring of a section of fill shown in Fig. 46, is time scaled for a 70 minute run in 7 minutes and is, therefore, a real-time source strength of 0.1 $^{\circ}F.in.^3/in.^2$. Assume that operating conditions which lead to charring can be approximated by a load of 2000 pli. or greater, a speed of 500 rpm or higher* and a two-nip configuration*. Assume further that these conditions result in a temperature maximum of 400°F. above ambient caused by a source located 0.01in. beneath the surface; a temperature maximum shown to be only 5.5° in Fig. 45b. It can thus be seen that where the F factor is $(\frac{100}{500} \times 0.1)$ the actual source strength is of the order:-

$$\frac{400^{\circ}F.}{5.5} \times \frac{100}{500}\ \text{rpm.} \times 0.1^{\circ}F.in.^3/in.^2 = 0.72_5\ ^{\circ}F.in.^3/in.^2$$

with a predicted value of:-

$$\mu = 108\frac{S}{P} = 108 \times 0.72_5 = 3.9 \times 10^{-2}$$

a value some 10 times as high as any measured. Similarly, if the source was assumed to be located on the roll surface, i.e. $x' = o$, as shown in Fig. 45b to produce a temperature maximum of 0.6°F., a value of μ approximately 100 times greater than any measured should have occurred. It is therefore reasonable to conclude that filled rolls which char, begin to burn locally where the value of heat source strength, which has been shown to vary both axially and circumferentially with respect to the filled roll, is some 10 times as high as the average. Furthermore it appears that the maximum rate of heat generation is at a depth of about 0.010in. and although severe evaporative surface cooling may be provided heat loss in the nip is negligible.

---

*Not 100 rpm. in a single nip configuration as implied by the hypothetical calculation represented in Fig. 45.

Differences in values of rolling friction coefficient, as measured and as calculated from heat source strength, can be explained by the following points:-

1) Low values of μ might be partially accounted for if in a specific transaxial plane of the filled roll where the temperature measurements were made heat were generated at a rate significantly less than the axial average rate.

2) The model does not account for heat, generated in the nip and on the filled roll surface, being carried away by the cool surface of the steel roll before the region, thermally excited in the nip, can escape contact with the steel surface. It may be recalled that the test described in Fig. 41 was run at low load, a probable condition of surface heat generation. The test described in Fig. 42, although run at higher load, was run at the lowest speed hence any region of surface would remain longest in nip contact. These two tests yielded the lowest values of friction coefficient based on heat source strength.

3) In the third test, described in Figs. 43-44, the three calculated values of μ are only 27-60% less than measured values. This test was run at the highest load and speed of 1400 pli. and 1700 fpm. respectively. The thermal model is not sensitive to a 0 - 0.01in. change in assumed source location nor does it take into account

heat transfer to the steel roll. Diffusion from a depth of a few thousandths of an inch can be assumed to be instantaneous compared to the period of revolution of the filled roll, but so can the period during which a point on the fill surface remains in nip contact. Although a model which ignores heat conduction in the nip predicts similar temperature distributions with either a surface heat source or one at 0.010in. depth, such a small distance can and probably does insulate a high temperature region beneath the surface from heat loss to the steel roll. Hence the higher proportion of heat, due to rolling friction, retained in the filled roll under conditions of high load.

4) Heat source strengths sufficient to initiate burning predict local values of μ some 10-100 times higher than any measured with roll A. Recall, however, that no tests were conducted at nip loads above 1400 pli. although it is assumed that burn-out conditions occur at loads in excess of 2000 pli. High source strength can be partially, though not entirely, explained by increase in friction coefficient with load. It is more likely that abnormally high rates of heat generation, compatible with burning, are local phenomena due to random variations in heat source strength. Such variations are implied by experimental evidence presented in Figs. 30-35. Although discoloura-tion of fill shown in Fig. 46 is typical in that some burned fill samples show more or less uniform circumferential

darkening; it has been reported (36) that others reveal local darkening where a relatively small region of fill surface has spalled off. It may thus be suspected that burning is in fact initiated at a point from which it spreads circumferentially and axially, As the length of a typical filled roll, unlike the short experimental rolls used in this program, is much greater than its circumference, burning, even if it proceeds at similar rates in circumferential and axial directions, will have propagated completely around the roll before it has affected the fill end to end. It may also be conjectured that burning, initiated by a random, high local value of μ, may then propagate by a self-sustaining exothermic reaction in which combustible volatiles are expelled from a burned region where the reaction then proceeds more slowly. Such a reaction is consistent with the observation that local spalling occurs with violent expulsion of fill material from the roll surface; hence the term "blow-out".

Resumé of Results

1) Analysis of supercalender filled roll heating by Malmstrom and Nash (16) has led to the implicit but erroneous conclusion that although strong surface heat sources exist it is the heating which occurs some distance below the surface which accounts for the development of high subsurface temperature.

2) Considering differences in roll size, fill pressure and composition the results presented herein agree favourably with the single curve of radial temperature distribution reported by Larsson and Gregersen (17) except that these authors reported a lower surface temperature than that which they measured at 0.1in. This could easily have come about if the surface temperature measuring thermocouple used in their experiment was located near the ingoing side of the nip or failed to reach equilibrium with the surface.

3) All experimental data, presented in the preceding pages, which included surface temperature measurements, inferred that the highest temperatures experienced by the roll fill were located at depths much less than 3/32in., possibly on the roll surface.

4) Data presented in Figs. 41-44 were best approximated by the model with a source depth x' = o, a surface source. Setting the location of the theoretical heat source, x', some small distance, say, 0.01in. below the surface results in negligible change in the shape of the radial temperature distribution. Increasing x' to the order of 3/32in. or greater yields temperature distributions which qualitatively describe neither the

experimental data presented herein nor the degree of discolouration sustained by a typical section of burned fill from an industrial supercalender filled roll.

5) It is felt that equation (18) described filled roll heating reasonably well. Considering the existence of unpredictable variations in heat source strength, it would appear that refinement of this model to account for the cylindrical geometry of the filled roll and to include a distributed rather than the assumed discrete heat source is unwarranted. Furthermore it has been shown why it is not necessary, especially at high rates of heat generation, to include the complication of heat loss in the nip.

PART II: THE MEASUREMENT OF ROLLING FRICTION OF A SUPERCALENDER NIP AND THE DEFORMATION WITHIN A FILLED ROLL

Synopsis

Certain aspects of filled roll manufacture are reviewed briefly. These reveal a fundamental inhomogeneity in fill structure; a large volumetric fraction of fill material is not solid but contains air. A simple mechanism, based on irreversible gas compression and described in APPENDIX III, can be put forth to account for losses due to the deformation through rolling with a rigid body of a material containing entrapped gas. Such a mechanism might explain losses in certain types of porous material and to a limited extent, gas compression must occur in filled rolls, but one cannot seriously entertain this to be a predominating effect nor can this explain irreproducible measurements of temperature and randomly varying friction or deformation. In this regard it is noted that previous investigations into supercalender finishing action and rolling friction phenomena make no reference to irreproducible measurements and a variable distribution of friction coefficient and heat source strength such as were introduced in Part I.

The experiments devised to measure rolling friction, surface hardness and profile and subsurface deformation are described. The results of these measurements are presented without prior theoretical analysis. The experiments in this program were designed in the belief that measurements would yield reproducible and continuous functional relationships of rolling friction and filled roll deformation versus operating speed and nip load. This assumption was proven to be false. Results of these experiments emphasize that rolling friction in a supercalender nip is like no other hitherto investigated and lead to the suggestion of two plausible rolling friction mechanisms. One is based on axial torsion in the fill the other on buckling or wrinkling of the compacted surface skin of the filled roll. Both involve high energy dissipation at the surface of the filled roll and are thus compatible with the thermal behaviour reported in Part I. However, the validity of these mechanisms cannot be established until the surface and subsurface microstructures of filled rolls are described and related to the random deformations which have been measured directly by X-radiography and have been observed indirectly as variations in supercalender rolling friction and filled roll surface hardness as well as in the development of irregularities in filled roll surface profile.

Symbols		Units
Γ	Torque necessary to overcome rolling resistance	lb.in.
P	Nip load per unit length of roll face (pli.)	lb./in.
μ	Coefficient of rolling friction	-
L	Length of roll face	in.
R	Roll radius	in.
high	Subscript indicating maximum value	-
low	Subscript indicating minimum value	-
Δ	Prefix indicating a finite difference or a range of values	-
-	Overbar indicating a mean value	-
ρ	Percentage of full-scale reading of Rho-meter	-
D_1	Distance between X-ray source and film plane	in.
D_2	Distance between plane of tracer arrays and film plane	in.
D_3	Height of reference object	in.
D_4	Length of shadow cast by reference object	in.
D_5	Distance from tip of shadow to foot of perpendicular from X-ray source to film plane	in.
D_6	Distance from foot of perpendicular to any tracer sphere image	in.
D_7	Parallax error of sphere image	in.
Δx	Circumferential component of displacement from datum of a tracer image	in.
Δy	Radial component of displacement from datum of a tracer sphere	in.
DXX	Circumferential difference in displacement from datum of two circumferentially adjacent spheres	in./in.

		Units
DXY	Circumferential difference in displacement from datum of two radially adjacent spheres	in./in.
DYX	Radial difference in displacement from datum of two circumferentially adjacent spheres	in./in.
DYY	Radial difference in displacement from datum of two radially adjacent spheres	in./in.
t	A subscript which indicates the difference between values of DXX and DYY in a load increasing and decreasing sequence	-
θ	Angle of rotation of concentric tractive component	-
ϕ	Angle of ration of eccentric tractive component	-
a	Eccentric displacement	in.

Filled Roll Structure

Supercalender filled rolls have a unique structure. They comprise of a high tensile steel shaft with an annular steel disc at either end. Typically these discs are about twice the diameter of the shaft and half as thick. The discs are supported by nuts attached to the shaft by a heavy screw thread. In this way the fill material mounted on the shaft between the discs is maintained under high compressive force by axial tension in the shaft. The average compressive stress applied to the fill material is 5000-20000 psi. The roll filling process is illustrated in Fig. 47. Fill material is commonly supplied as felt sheets about 1/4in. thick. From these are die-cut annular discs which have an internal diameter so as to fit snugly over the roll shaft. Precautions are taken in the manufacture of these felts to ensure that their fibres lie with completely random orientation in planes perpendicular to the roll axis. Fill fibres are mostly cotton although in Europe wool blends are favoured. Hard, highly compressed rolls are sometimes filled with denim paper sheets about 0.01in. thick. Felts used in hard rolls are more highly precompressed and contain shorter length fibres than felts used to form softer rolls. Rolls intended for high gloss calendering are sometimes filled with extra long fibre natural carded cotton. Prior to pressing this raw material is scarcely a felt but a die-cut wad about 1ft. thick which has the density and appearance of surgical or absorbant cotton. Inorganic fibres such as asbestos and glass are occasionally added to the fill in proportions up to 25% by weight. Such additives are alleged to promote rapid heat conduction

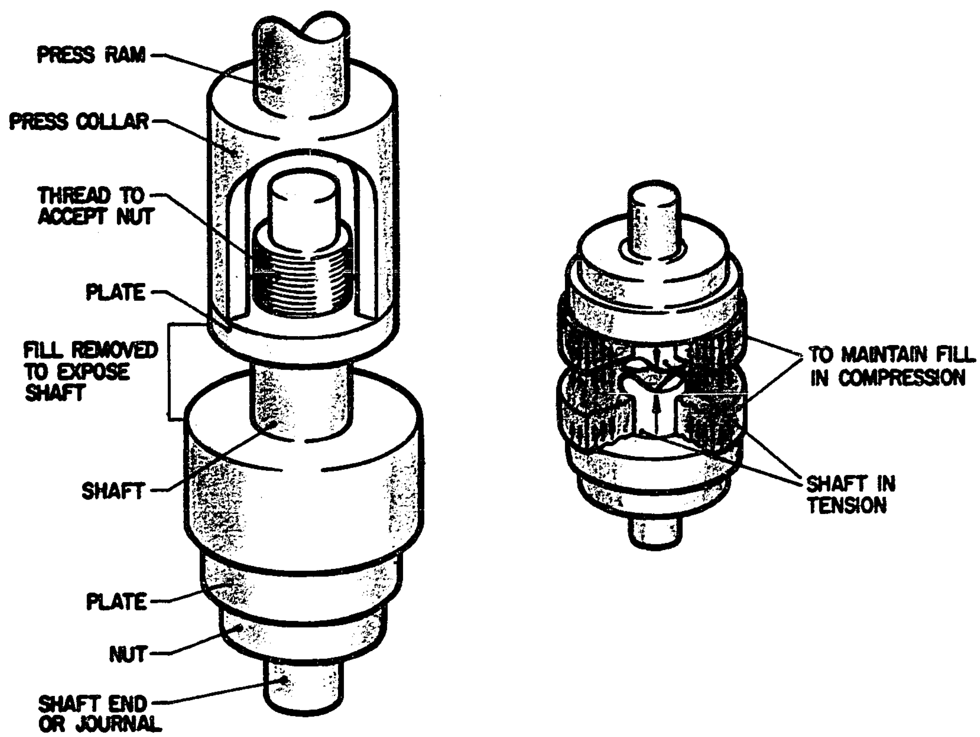

FIG. 47.

Filled Roll Manufacture

but their effectiveness is questionable and in the case of glass fibre it was shown in Part I that no advantage is to be gained.

The outer surface of a filled roll is machined to a satin smooth finish and to within a 0.001in. cylindrical tolerance. A new roll does not, however, finish paper effectively until it has undergone a period of operation and developed what appears to be a thin, dense outer skin with a glossy surface. An examination of such a surface under a low-power stereomicroscope reveals that surface fibres have been flattened and pressed into predominantly circumferential orientation as shown in Fig. 48. The erose regions shown in the enlarged inset come about naturally and appear to be caused by abrasion or breaking off of surface fibres. These can be produced also by teasing the glossy surface with a sharp, pointed instrument. This texture is the same as that of the surface of a newly machined or unrun roll. Rolls, A, B, and D, which had been operated for a sufficiently long period of time so as to develop gloss, all exhibited regions of surface erosion. These are evidence of a continuous process characterized by alternate sloughing and re-establishment of glazed surface fibres.

Inhomogeneity due to Air Entrapped in the Fill

Precompacted Filmat felts used in the manufacture of rolls undergo a 30-75% reduction in volume when pressed and carded cotton fill is compressed to less than 10% of its original volume. The softest, least dense fills undergo the largest volumetric change but at a given pressure fill density decreases with fibre length and increases with the degree of

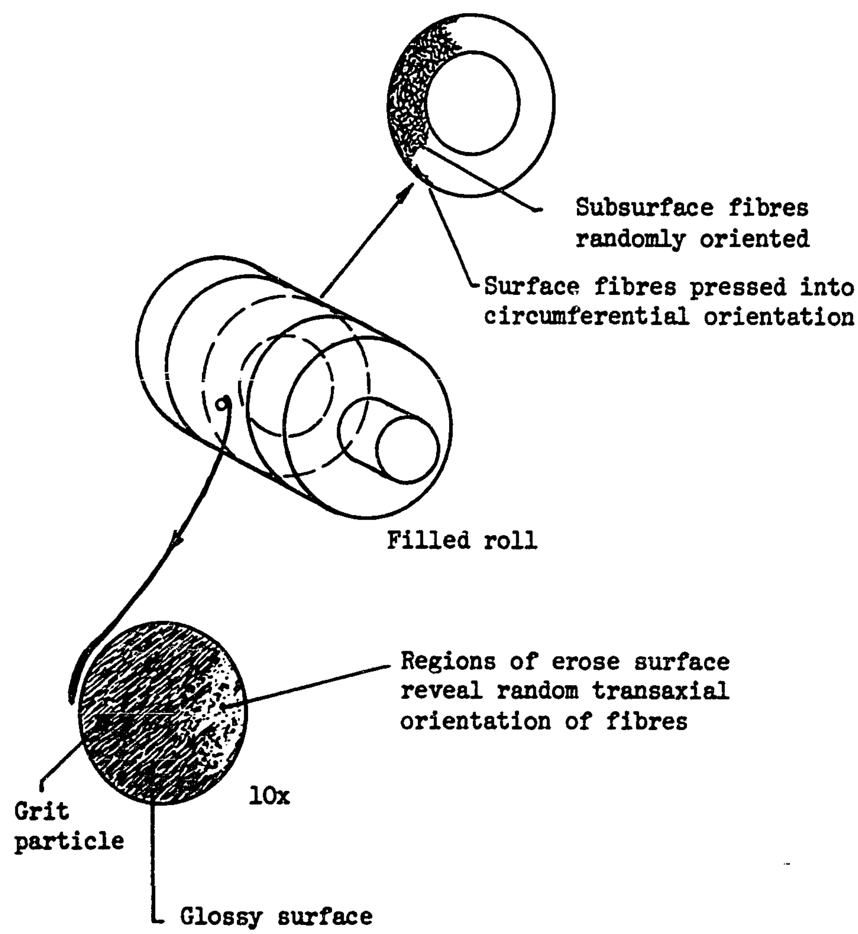

FIG. 48.

Filled Roll Surface Skin.

precompaction of the original felt sheet. Thus by using different grades of fill material considerable differences in fill density can be produced at a given pressure. These differences are due to air entrapped within the interfibral spaces. Measurements indicate that voids account for 10-35% of fill volume. It is well known that large rolls, with diameters and lengths of 12-30in. and 100-300in. respectively, creep for a number of days under the force of the filling press. A few hours of pressing was sufficient to fill the 12in. outside by 6in. inside diameter by 12in. long rolls used in this experimental program. Small test rolls, of 3in. outside diameter and various inside diameters and lengths from 1-2in. and 3-5in. respectively which were pressed at 5000-10000 psi., stopped creeping after a few minutes of applied load. This behaviour cannot be described as the simple viscoelastic creep of a solid because chain models of elastic and viscous elements, as shown in Fig. 49, will relax and creep, respectively, for times which are proportional to their length. The order of magnitude of the three pressing times mentioned above is more nearly proportional to fill volume than to roll length. The effusion of air compressed among the fill fibres might account for a creep phenomenon which varies as the volume of the material under compression. In assessing the rolling friction of a supercalender nip the effect of air compression within the fill cannot be discounted.

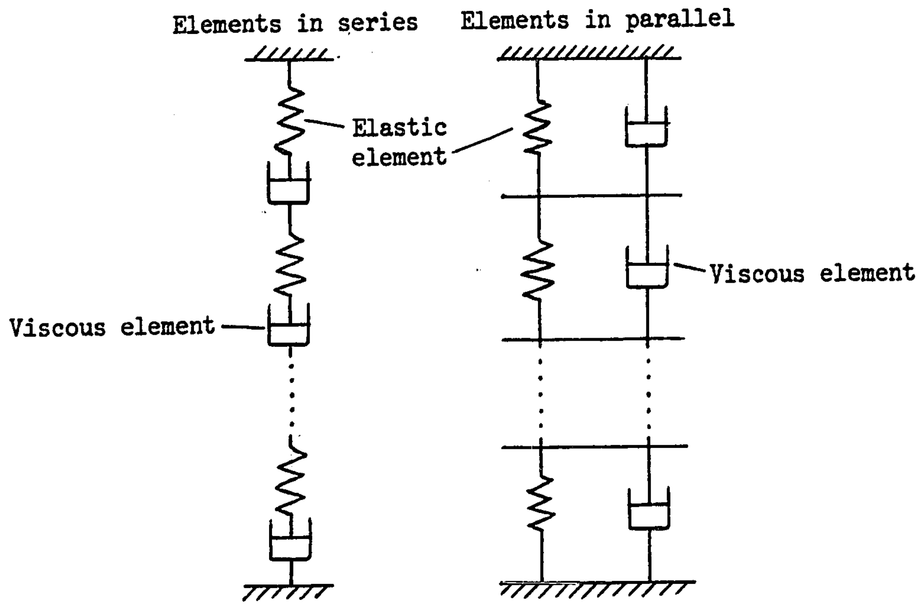

FIG. 49.

Simple Chains of Viscous and Elastic Elements.

APPENDIX III deals with a hypothetical rolling friction mechanism based on the thermodynamically irreversible compression of air within the fill material. Although such a mechanism might, with certain modification, explain satisfactorily the rolling behaviour highly deformable cellular materials such as soft rubber or plastic foams, it must be rejected as a predominant mechanism in supercalender rolling friction. For air to be effectively compressed, the containing walls must have at least one degree of freedom in which negligible resistance to compressive load is offered by the solid material, e.g. like a balloon, soap-bubble or even a piston in a cylinder. From mechanical experience with various ensembles of cellulose fibres such as wood and paper, both of which have much lower density than compressed fill, it is well known that such a material is capable of supporting compressive stress without the hydrostatic assistance of entrained fluid. Another possible effect connected with interfibral spaces in the fill is the pumping or squeezing of air by nip compression. This effect might be in part due to the movement of air already trapped in the voids. It is conceivable, however, that air, in the boundary layer of the counter-rotating steel and filled rolls, might be squeezed into the fill on the ingoing side of the nip, especially into the eroded regions which are probably more pervious than the glossy regions. This forced infusion of air would imply a similar expulsion on the outgoing side of the nip. An air pumping mechanism cannot be evaluated as no experiments on fill permeability have been performed, nor has air flow in the boundary layer of the nip been measured.

EXPERIMENTAL

Rolling Friction

Rolling friction was measured in a single supercalender nip operating without paper and consisting of a 12in. diameter filled roll of 12in. face length driven by a 12in. diameter steel roll. Two series of tests were run. One covered the speeds from 200-2000 fpm. in 5 approximately equal steps. This is the typical operating range of industrial supercalenders. The other test series was run at 8 steps of speed between 7.5 and 105 fpm. These low speed tests were run so as to provide data over a decade of speed regulation without incurring appreciable increase in fill temperature. Filled rolls A and D were tested at the higher speeds and all 5 rolls shown in Fig.50 were tested at the lower speeds. Tests were run at four nip loads, 240, 470, 940 and 1400 pli., starting at the smallest load and lowest speed. Before the next higher load was applied the speed was increased, then decreased, through the steps. All tests were repeated at least once at each load. The loads for these repeated tests were chosen in a random sequence. Torque required to drive this stack, including that at impending motion, required to overcome static friction, was measured by the dynamometer and recorded by the data acquisition system. At least 10 readings were taken at each load and at each speed as the latter was increased, then decreased. Torque was measured also during extended periods of operation at constant load and speed with roll A while the temperature data for Part I were obtained. Although roll D

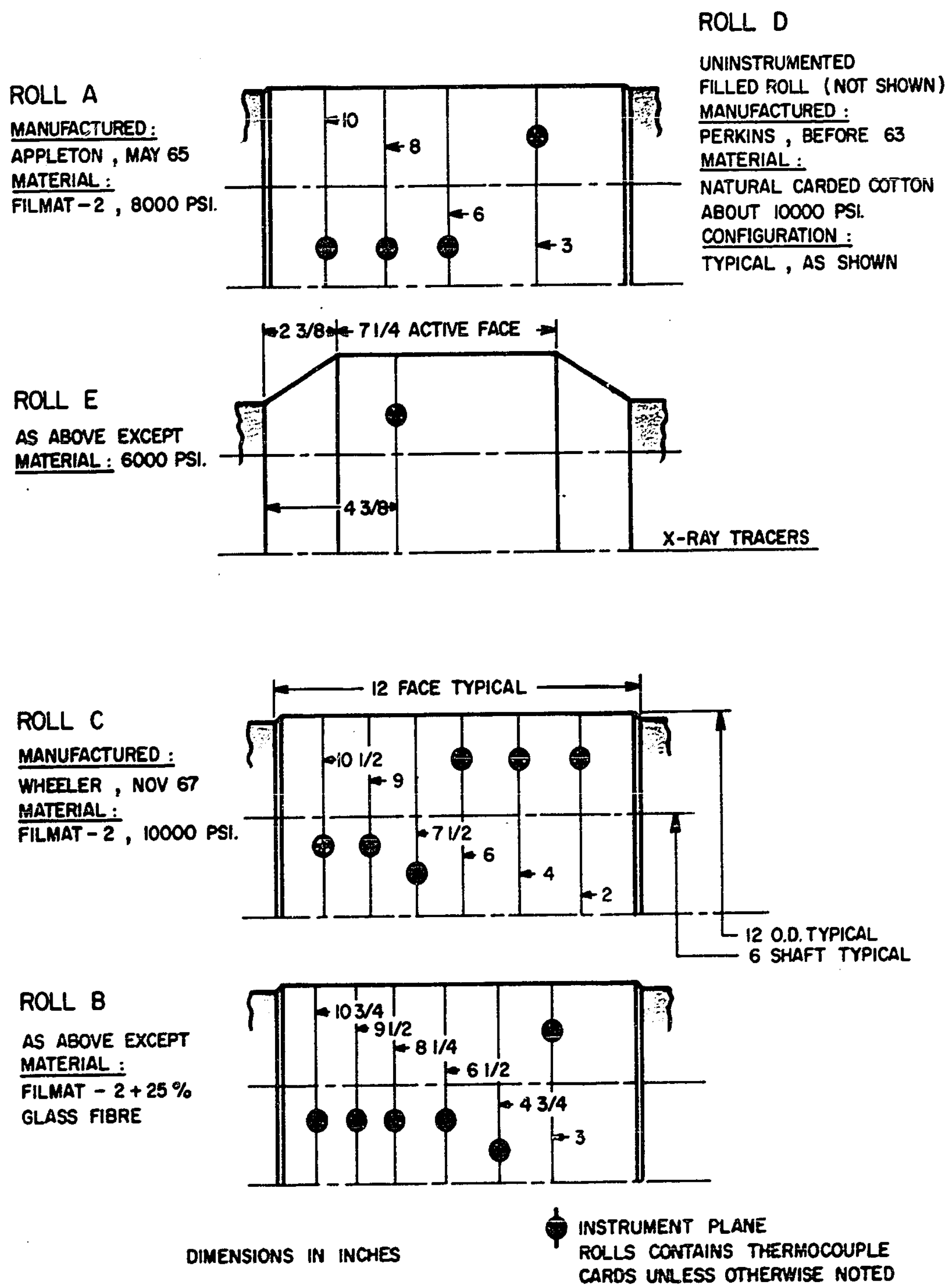

FIG. 50.

Experimental Filled Rolls.

was not instrumented, it too underwent exhaustive testing at the same 12 combinations of constant load and speed. Corresponding experiments, run over both high and low speed ranges, were conducted to measure the torque required to drive only the stack bearings. A schematic of the equipment used to perform the bearing calibrations was shown in Fig. 8. To obtain a measurement of rolling resistance in the nip, bearing torque was deducted from the gross torque.

Filled Roll Surface Hardness

The hardness of all five filled rolls was measured with a Beloit "Rho-meter". Readings were taken at 24 positions on each roll as shown in Fig. 51.

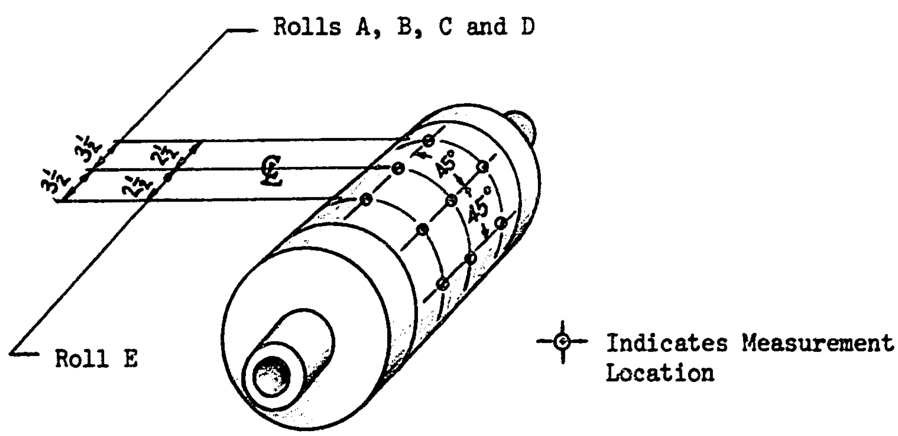

FIG. 51

Distribution of Rho Hardness Measurements on Filled Roll Surface.

When the Rho-meter was acquired roll B was the only new, unrun roll which was subsequently subjected to extensive testing. Although measurements were repeated on all rolls, the hardness distribution on roll B was measured when the roll was unrun, then after it had been operated for about 15 hours at moderate speeds and loading and finally after it had sustained a number of hours of operation at a load of 1400 pli. and speeds up to 2000 fpm.

The Rho-meter is a recent development (34) by J.D. Pfeiffer of The Beloit Corporation. This instrument was designed specifically for measuring hardness of filled rolls and wound rolls of paper. For the former application it is superior to the Shore "Durometer", a spring-loaded needle penetrometer commonly used to measure filled roll hardness. The Rho-meter is sensitive to smaller differences in hardness than is the Durometer and is not prone to gross error because of interlaminar insertion. The Rho-meter measures hardness by recording the maximum inertial deceleration force experienced by a strain gauge accelerometer attached to a spring-loaded hinged hammer. The smooth rounded head of this hammer strikes a surface at a specific velocity which is predetermined by the initial spring tension. A simplified mechanical schematic of the active elements of this instrument are shown in Fig. 52a. Fig. 52b shows the application and external appearance of this instrument. The hardness reading takes into account inertial, elastic and any dissipative or frictional components of retarding force experienced on impact with a surface. The relationship of these properties to the instrument reading is not defined. Spring tension and hammer mass cannot be conveniently altered. In spite of these short-

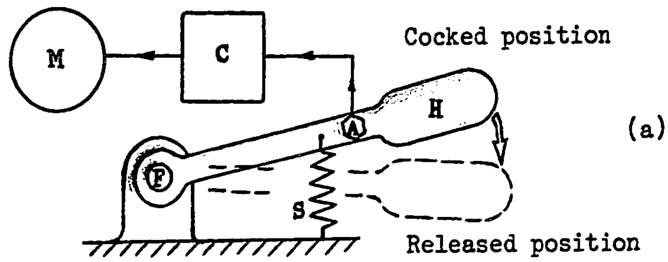

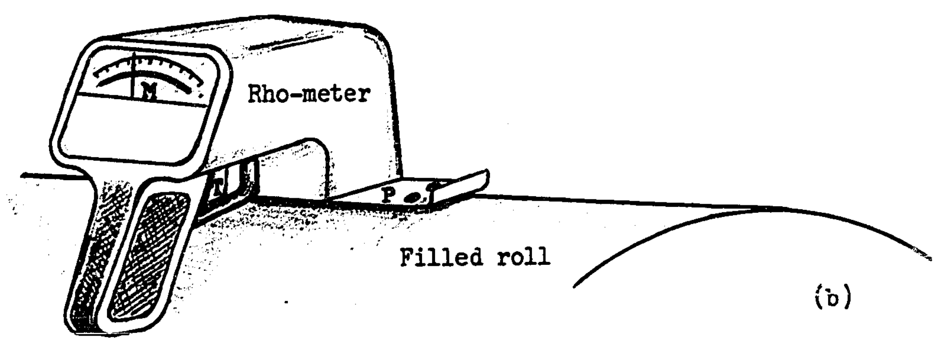

FIG. 52.

Rho-meter Schematic and Application.

Maximum deceleration signal from accelerometer, A, is sensed, amplified and stored by electronic circuit, C, and reading appears on meter scale, M. Depression of trigger, T, draws hammer, H, to cocked position against spring, S. Further trigger depression releases hammer which pivots about fulcrum, F, and strikes the filled roll surface against which the instrument foot-plate, P, is firmly pressed.

comings, measurements, whatever they may represent in terms of rheological fill properties, were always repeatable and accurate to within 2-3%.

Surface Table Measurement of Filled Roll Surface Topography

Each of the five filled rolls, together with its bearing blocks, was placed on a large granite surface table. This set up is shown in Fig. 53. Foot screws were adjusted so that the roll rotated freely, but had minimum clearance between points at maximum radius and the surface of the table. As the roll was rotated through eighths of a revolution, a profile of each gap between the roll and surface table was measured to within 0.001in. with a set of shim stock feeler gauges.

X-ray Tracer Instrumentation

Roll E, used for nip deformation studies, was pressed at the lowest fill pressure commonly applied in the manufacture of supercalender rolls of this type. The low pressure of 6000 psi., was chosen because it was assumed that a soft roll thus produced would sustain larger, more easily discernible deformations under load than a harder roll. To interpose a minimum mass of fill material that had to be penetrated by the X-ray beam and to eliminate metal, other than the tracers, from its path the diameters of the two fill retaining nuts were reduced from just under 12in., to 9in. and the fill was symmetrically bevelled to this reduced diameter, leaving a 7 1/4in. active cylindrical face length. In spite of this gradual conical buttress, which for reinforcement was partially filled with hard card instead of Filmat, the unsupported lateral surfaces of the bevelled roll filling might be squeezed out if such a roll were pressed harder, hence a second reason for employing a low fill pressure.

Two arrays of small metal spheres were placed in roll E at a

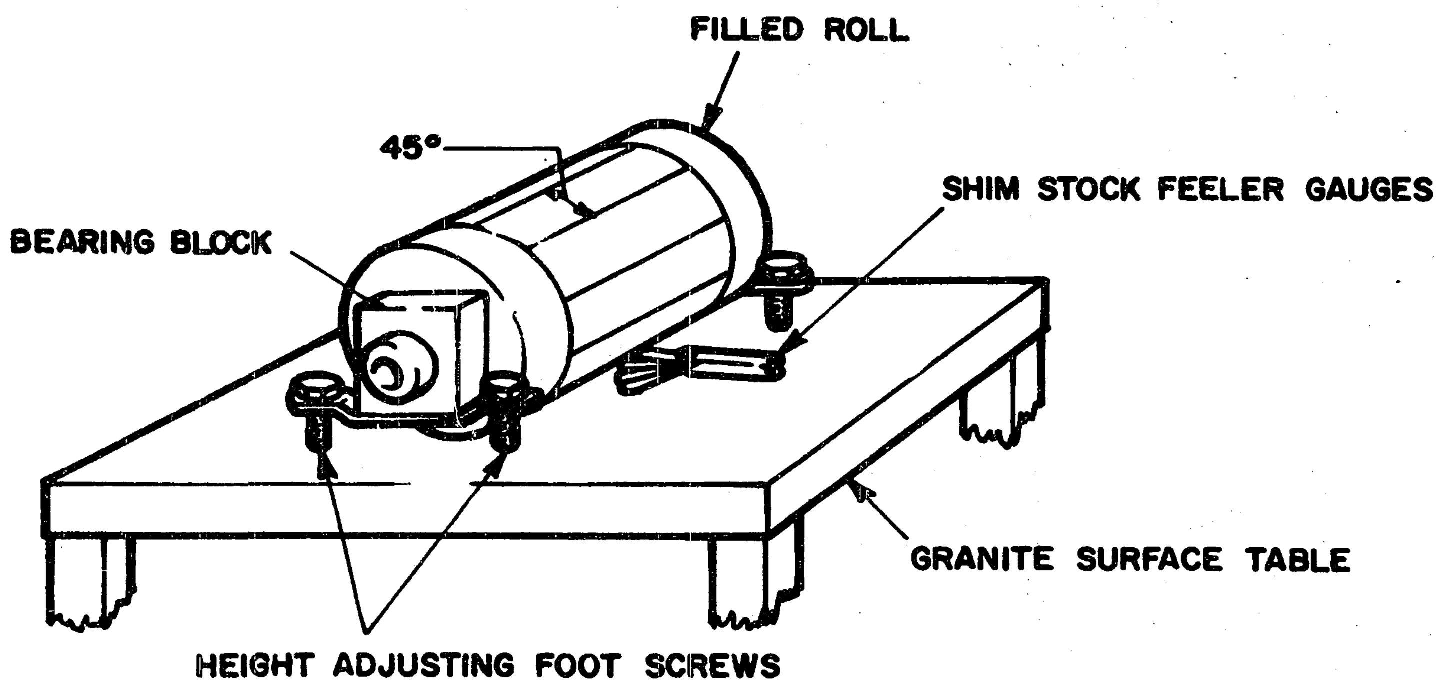

FIG. 53.
Measurement of Filled Roll Surface Profile.

transaxial plane 4 3/8in. from one end of the fill material as shown in Fig. 50. These arrays, laid out as shown in Fig. 54 were not located at the axial nip centre as this would incur a subject to film distance of over 6in. in a total distance from the X-ray source to the film, as shown in Fig. 55, of about 22in. In order to obtain the best definition and minimum distortion from the radiograms, the subject should be as close as possible to the film. Measured deformations should, to as great an extent as possible, be free of end effects. Therefore, the arrays should be placed at nip centre. Thus the actual location of the plane containing the tracer arrays was chosen as a compromise between practical requirements which to a certain extent are in conflict.

The elements of the tracer pattern are 1/32in. diameter platinum/20% iridium shot, ground to a spherical shell tolerance of 0.0005in. This material was chosen for its optimal combination of physical properties; density or X-ray opacity, corrosion resistance, high strength and machinability. The tracer spheres were mounted on a card in a manner similar to that used to mount thermocouples and described in Part I. The spheres were pressed firmly into pin holes laid out in the required patterns. A dense pattern of 155 spheres and a sparse pattern of 19 spheres were installed in the roll so that two regions of wide angular separation could be examined. The sparse pattern, with its fewer elements, served as a convenient data source to develop the numerical routines to process these X-ray test results.

A schematic diagram of equipment used to measure subsurface deform-

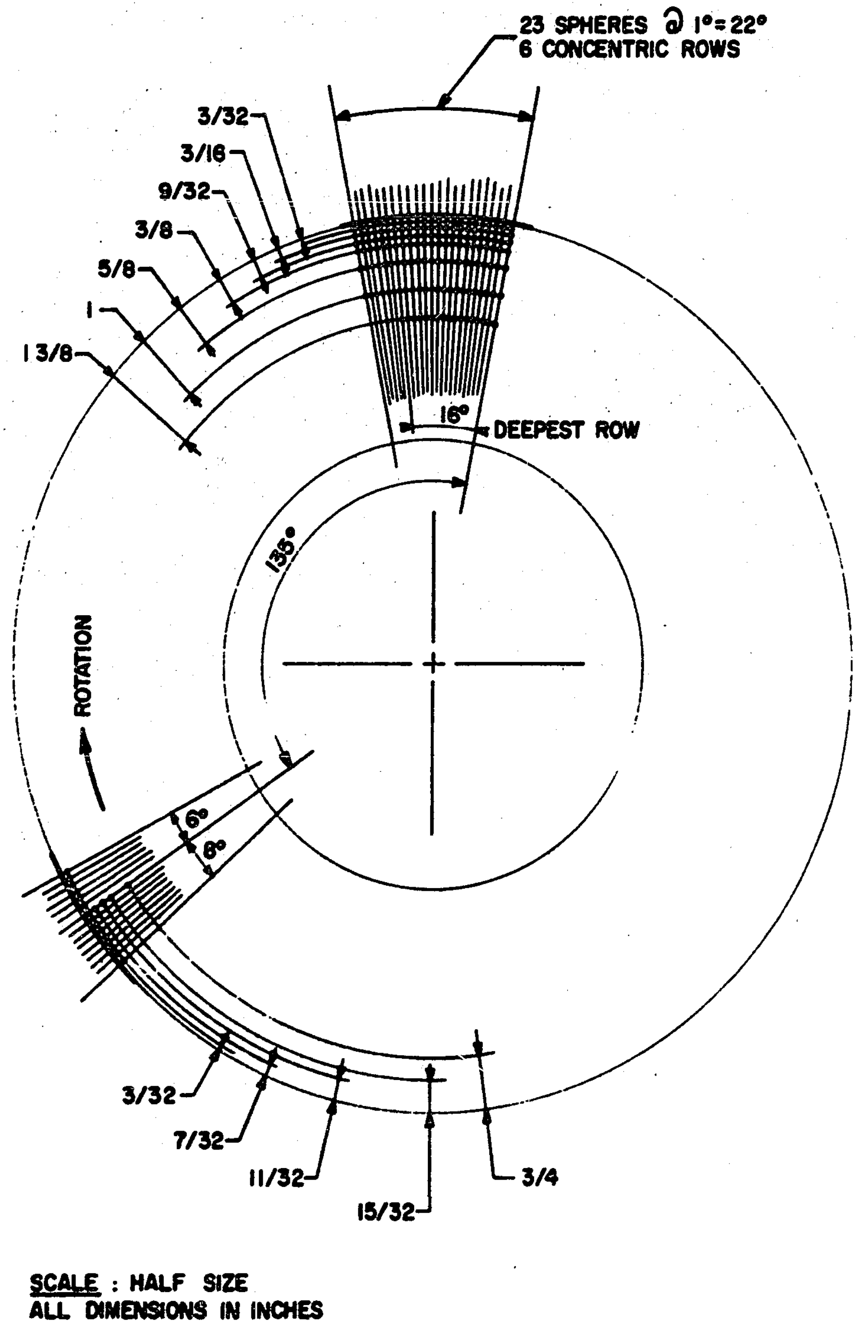

FIG. 54.

Disposition of X-Ray Tracer Elements
in a Transaxial Plane of Roll E.

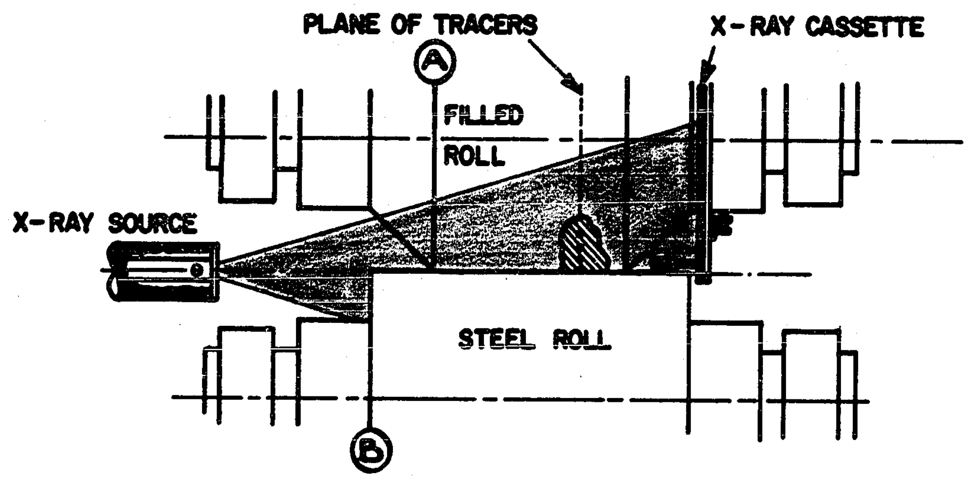

FIG. 55.

Schematic of set-up used to measure filled roll deformations

ation of the filled roll is shown in Fig. 55. The X-ray film cassette is shown, in edge view, mounted on a fill retaining nut and concentric with the roll axis. The X-ray source is aligned with the nip so as to cast an image of the tracers upon the film plane. Radiograms, which produced a transaxial image of the nip between 12in. diameter steel and filled rolls, were taken at nip loads of 240, 470, 940 and 1400 pli. while stationary and at speeds of 6.5 and 62 fpm.

RESULTS AND DISCUSSION

Rolling Friction: High Speed

Rolling friction of a single supercalender nip, run without paper, was measured in order to obtain relationships between friction torque and speed, filled roll surface temperature and nip load and establish the extent to which the friction torque is reproducible.

Effect of Speed:

Fig. 56 shows a typical set of net friction torque data obtained with roll D, plotted against speed. At each of four loads the speed was increased, then decreased through five steps. Each data point is the average of 10 or more measurements taken in quick succession. In order to incur a minimum temperature rise during these tests a given speed was maintained for no more than 2 minutes. Note that during steps of decreasing speed the friction torque is invariably less than when the speed is being increased. In successive tests at a given speed and load there are considerable differences in net friction torque. The irreproducibility is largest at the smallest load, i.e. 50% of the average net torque at 240 pli., and is least at the maximum load of 1400 pli., i.e. less than 20%. Except for slightly lower friction losses, results obtained with roll A are similar to those shown in Fig. 56 and obtained with roll D.

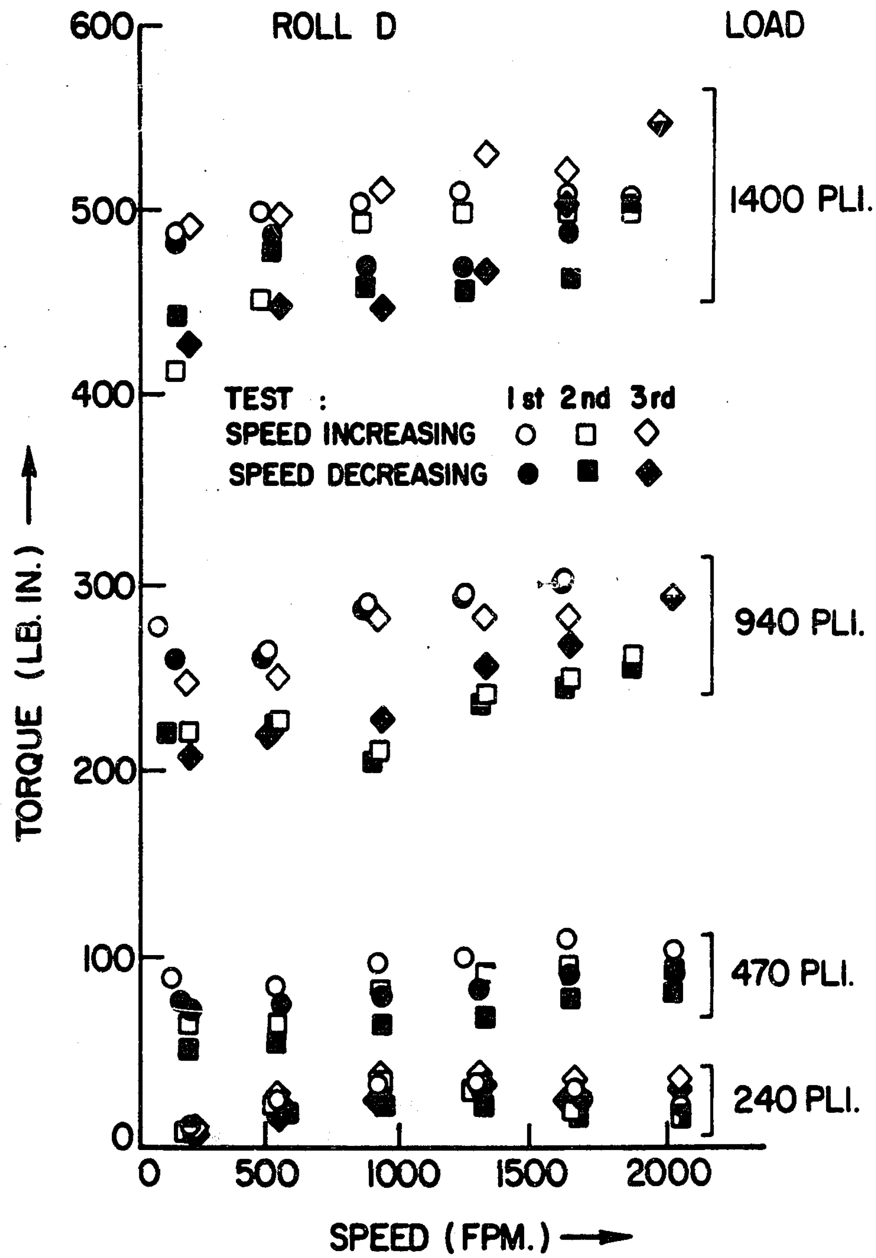

FIG. 56.

Net Friction Torque at 4 Loads
Plotted against Speed.

Effect of Temperature:

It was thought that the differences between friction torque measured at any given load and speed were related to the inevitable increase in temperature sustained by a filled roll as it heats up during operation. A plot of net friction torque against filled roll surface temperature for nine combinations of speed and load is shown in Fig. 57. The successive data points, obtained with roll A, were taken at 10-minute intervals and these data show that in fact there is proportionally less change in rolling friction torque at higher load and speed, i.e. at the conditions which incurred the greatest temperature increases, than at low speed and load, conditions which resulted in nearly isothermal operation. Data obtained with roll D were similar to those shown in Fig. 57 obtained with roll A.

Effect of Load:

As is evident from Figs. 56-57 there is, with both rolls A and D, an obvious trend of increasing friction torque with load, but there is apparently no discernible correlation of friction with either speed or temperature. Data presented in Fig. 58, which shows net friction torque, averaged over all speeds, plotted against nip load, supports the suggestion made by Malmstrom and Nash (16) that rolling friction losses in a supercalender nip are proportional to $\sqrt{P^3}$, where P is the nip load per unit length of roll face. Note that this supports the contention that rolling friction can be accounted for by hysteresis within the bulk of the filled roll as implied in the analysis of rolling friction of rubber given in (46). No quantitative explanation can be put forth, however, to account for the sizeable difference in rolling friction, as

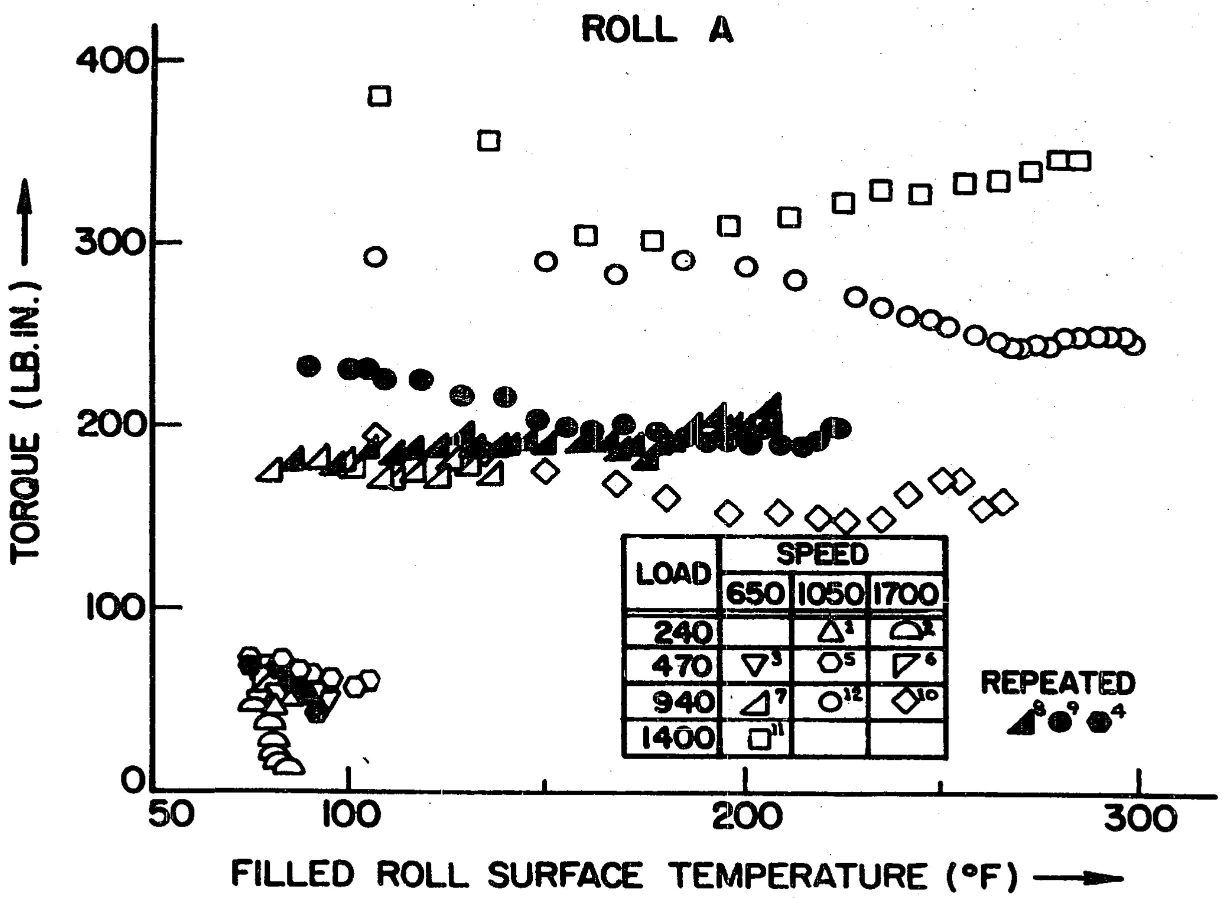

FIG. 57.

Net Friction Torque at 9 Combinations of Load and Speed
Plotted against Roll Surface Temperature.

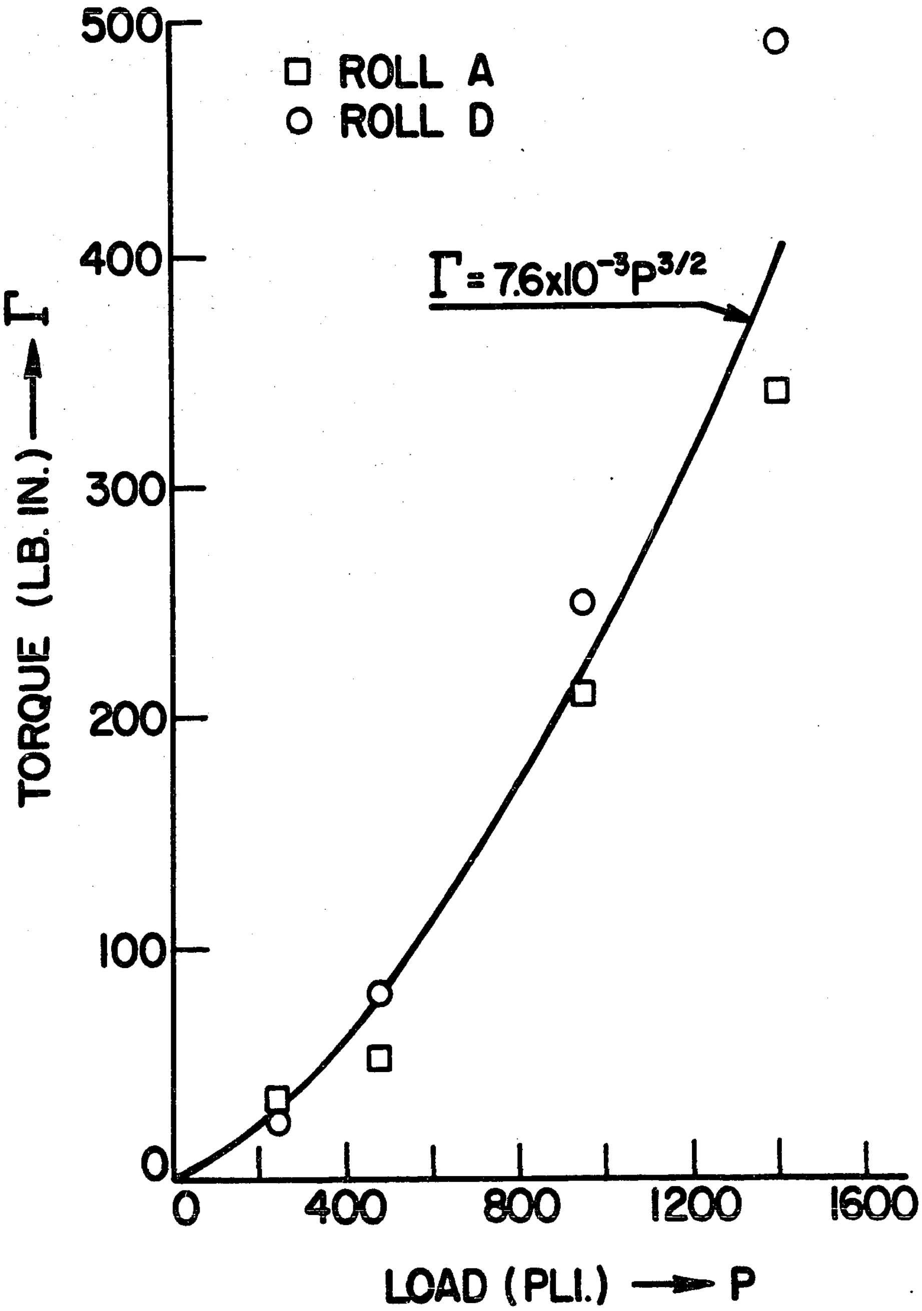

FIG. 58.

Average Net Friction Torque for Two Filled Rolls Plotted Against Nip Load.

shown in Fig. 58, obtained with rolls A and D at high load. In this regard it may be recalled that roll A was pressed at the higher pressure, but is made of natural carded cotton which is softer than Filmat-2, the filling used in roll A. The relationship which best describes the relationship between friction torque and load for both rolls is

$$\Gamma = 7.6 \times 10^{-3} \sqrt{P^3}$$

Irreproducibility:

In spite of the relationship between friction torque and nip load it was shown in Fig. 56 that measurements with roll D, as was also the case with roll A, were somewhat irreproducible. It has been established that this is not, to any appreciable extent, due to the irreproducibility of bearing friction. Similar irreproducibility was evident in the measurements of friction torque obtained with roll A shown in Fig. 57. The numbers which appear next to the data symbols in the data symbol table in Fig. 57 are in the same sequence as that in which various tests at a given load-speed combination were run.

On one occasion the friction torque measured at 940 pli., and 1050 fpm., as indicated by $\bigcirc^{12}$ in Fig. 57 was some 50% higher than that which was previously obtained at the same load and speed and indicated by $\bullet^{9}$. Note that the test $\bullet^{9}$ was immediately succeeded by a test at 940 pli., and 1700 fpm., $\diamond^{10}$, which resulted in somewhat lower friction torque and then by a test, $\square^{11}$, at 1400 pli., and 650 fpm., which resulted in the highest friction torque measured with roll A at high speed. This high degree of irreproducibility did not occur in other instances when tests at a given load and speed were repeated. Similar data were obtained during the successive pair of tests $\triangle^{7}$ and $\blacktriangle^{8}$ at 940 pli., and 650 fpm., and the successive pair at 470 pli., and 1050 fpm., $\bullet^{4}$ and $\circ^{5}$. One is, therefore, led to believe that the large difference in friction torque between tests $\bullet^{9}$ and $\circ^{12}$ was due to a running-in or compaction which the fill material experienced during the intervening test $\square^{11}$ at highest load. It is pointed out that this test sequence with roll A resulted in a similar degree of thermal irreproducibility which was described in Part I and shown in Fig. 35. No explanation can be offered, however, as to why a process of compaction should result in higher, not lower, value of friction torque.

Friction Coefficient:

Losses may be expressed as the coefficient of rolling friction, μ:-

$$\mu = \frac{\Gamma}{PLR}$$

where Γ(lb.in.) is the net torque and P(pli.), L(in.) and R(in.) are the nip load, length of the roll face and roll radius respectively. The torque vs. load relationship which was used to approximate the data shown in Fig. 58 can be rewritten as

$$\mu = 1.05_6 \times 10^{-4} \sqrt{P}$$

and this curve is shown in Fig. 59 for rolls A and D. These show μ plotted against P ($\downarrow\!\rightarrow$) and against speed ($\leftarrow\!\uparrow$). The broken curves represent data obtained at the beginning of each test and the solid curves represent data obtained at the end. It may be seen that friction is lower after the stack has been in operation for some time. The curves plotted against load represent values of μ averaged over all speeds and those plotted against speed are from values of μ averaged over all load. Because of the obvious variation of friction with load it might be considered that the procedure of plotting a load averaged friction coefficient against speed is unjustified. It will be shown in the forthcoming description of tests run at very low speeds that rolling friction data at individual values of speed had no apparent correlation with load, but that when these data were averaged over speed it became evident that, in tests involving all five rolls, the friction coefficient decreased, then increased with load. In the case of high speed rolling friction plotted against speed and shown in Fig. 59, it was hoped that a similar averaging procedure would reveal just such a slight but consistent trend which is not evident from discrete data.

Rolling Friction: Low Speed

Even though the previously presented rolling friction measurements yielded no significant correlation with either speed or temperature they clearly showed, through irreproducibility, that supercalender nip friction is not a simple, purely load dependent phenomenon. The random changes which apparently occur suggest inelastic, irreversible, random deformations within the filled roll. In order to discover whether there is, in fact, any discernible short-term reproducible variation of rolling friction with speed or during a single revolution of the filled roll the

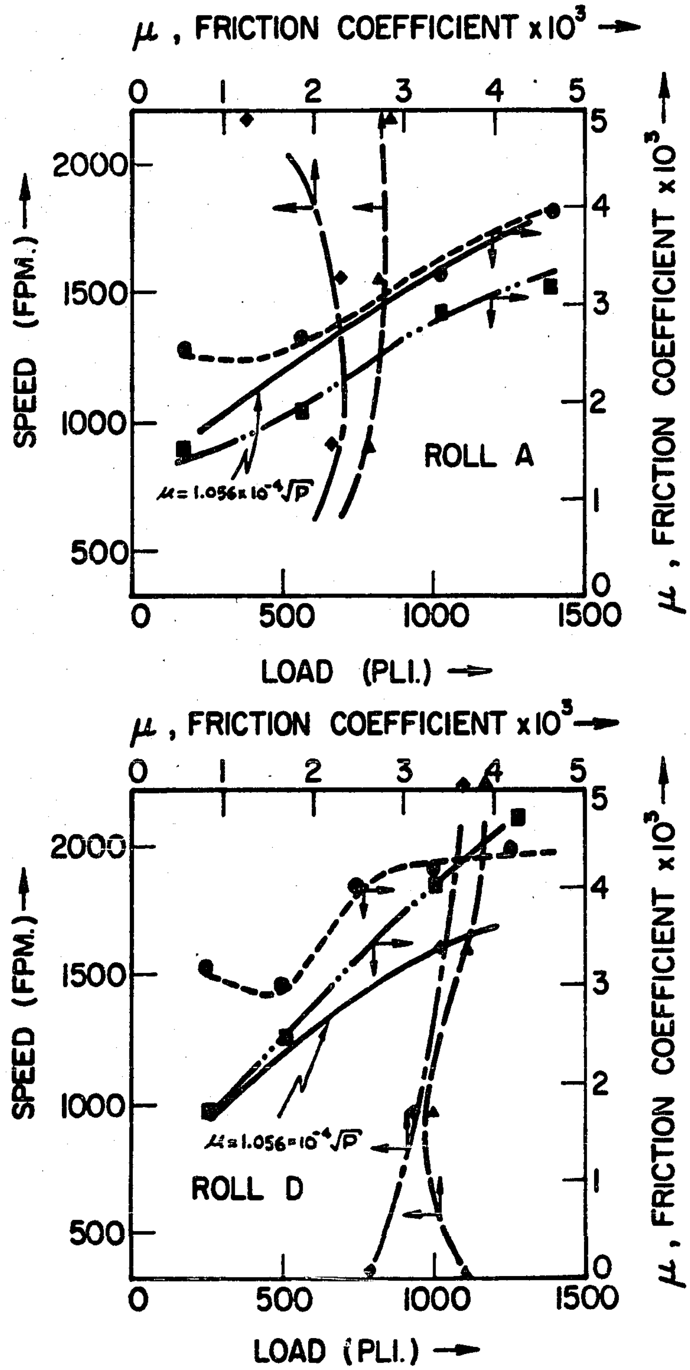

FIG. 59.

Average net friction coefficient for two filled rolls plotted against load and speed.

stack was run at 7.5 - 105 fpm., which is 1-10% of normal operating speed. In this regard it may be recalled that temperature fluctuations shown in Figs.36-38 were quite reproducible over successive revolutions. It was thought that compaction or other such variation in fill structure which apparently occurs over extensive periods of operation would be minimal over the relatively few successive revolutions of the filled roll which take place at such low speeds. Similarly, the heating effect would be minimized and although temperature did not appear to directly affect rolling friction, it was thought that heating and subsequent cooling might initiate changes in fill structure which show up as changes in rolling friction during subsequent tests.

Figure 60 shows the gross torque measurements obtained with roll D at the lowest speed of 7.5 fpm. and at nip loads of 240, 470, 940 and 1400 pli. Nineteen readings were taken at equal intervals over each revolution and in the curves for the three higher loads at least two complete, successive revolutions of the filled roll are represented. These curves show wide variations in friction torque during any given revolution and they show that the torques measured at a given angle in successive revolutions are not the same. Although about 25% of the gross torque is due to bearing friction, which also fluctuates at low speeds, this effect is sufficiently small so that the fluctuations in Fig. 60 may be assumed to be due to the nip alone. The torque curves for roll D are shown because two of the other four rolls tested exhibited greater fluctuations in friction torque than those shown in Fig. 60, two exhibited somewhat smaller fluctuations. All rolls yielded irreproducible

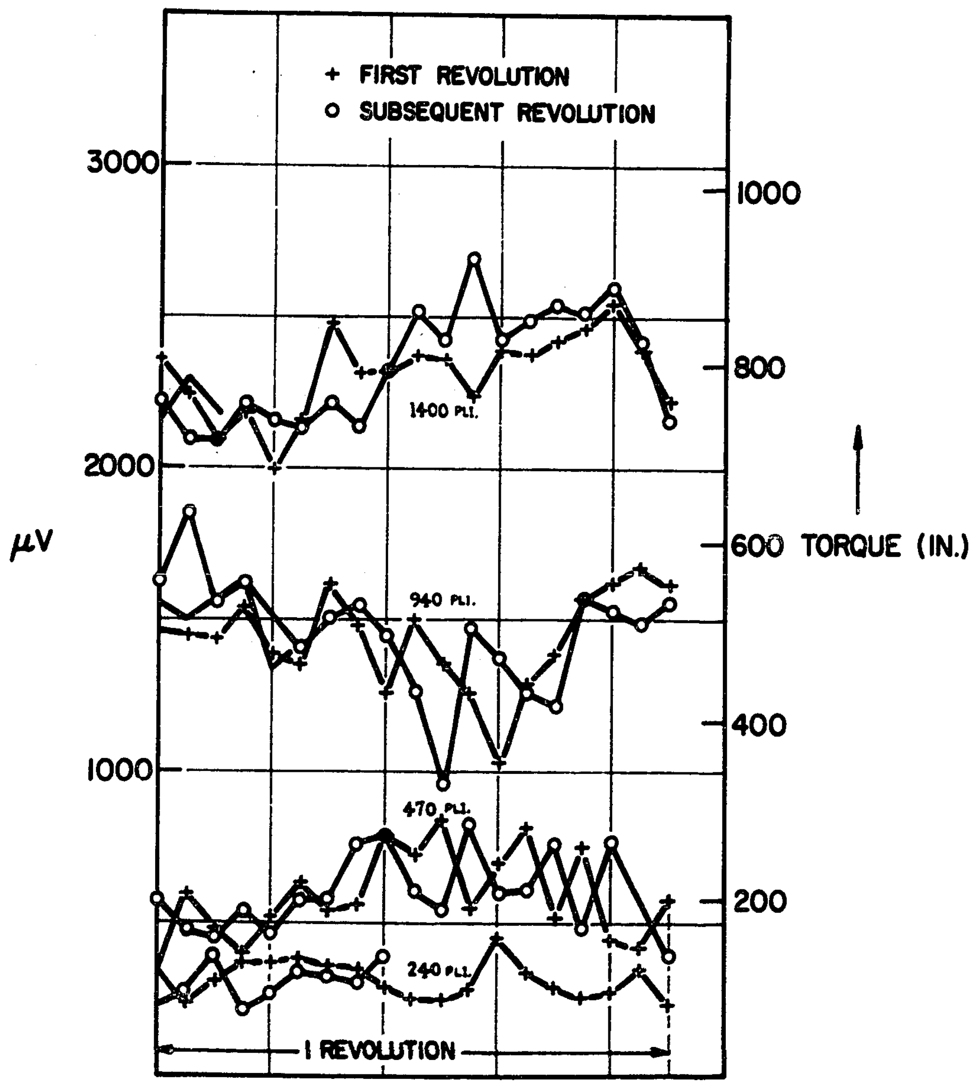

FIG. 60.

Typical fluctuation of gross torque over successive single revolutions of roll D.

friction torque measurements in successive revolutions. It should be noted, however, that the mean torque in each successive revolutions is approximately constant. At higher speed the torque fluctuations remained but measurements with highest angular resolution were those carried out at the lowest speed. These were the best approximation of a series of instantaneous readings which was obtained. The mean torque values were corrected for bearing friction and used to calculate the mean rolling friction coefficient, μ. Values of mean friction coefficient were plotted for all five rolls, in Figs. 61-65, on planes of speed against load, and these values were used to construct contours of constant friction coefficient. In four out of five plots these contours depict no particular dependence of rolling friction coefficient upon either load or speed although it may be recalled that high speed data presented previously displayed distinct increase of μ with load. Only roll E shows a consistent increase of friction coefficient with load. An attempt was then made to correlate the percentage component of fluctuation in friction coefficient with load and speed for each of the five rolls. Contours of percentage friction fluctuation are plotted in Figs. 66-70. These data, plotted in a manner similar to that used in Figs. 61-65 are the maximum range of friction coefficient fluctuation, $\left(\mu_{high}-\mu_{low}\right)$, expressed as a percentage of the mean coefficient at that condition of speed and load. None of these five diagrams reveal any particular relationship between friction fluctuation and load or speed. What is revealed, however, is that rolls B and C sustained a band width of net torque fluctuation which was so large as to produce instantaneous torques which were negative, torques which imparted instantaneous forward

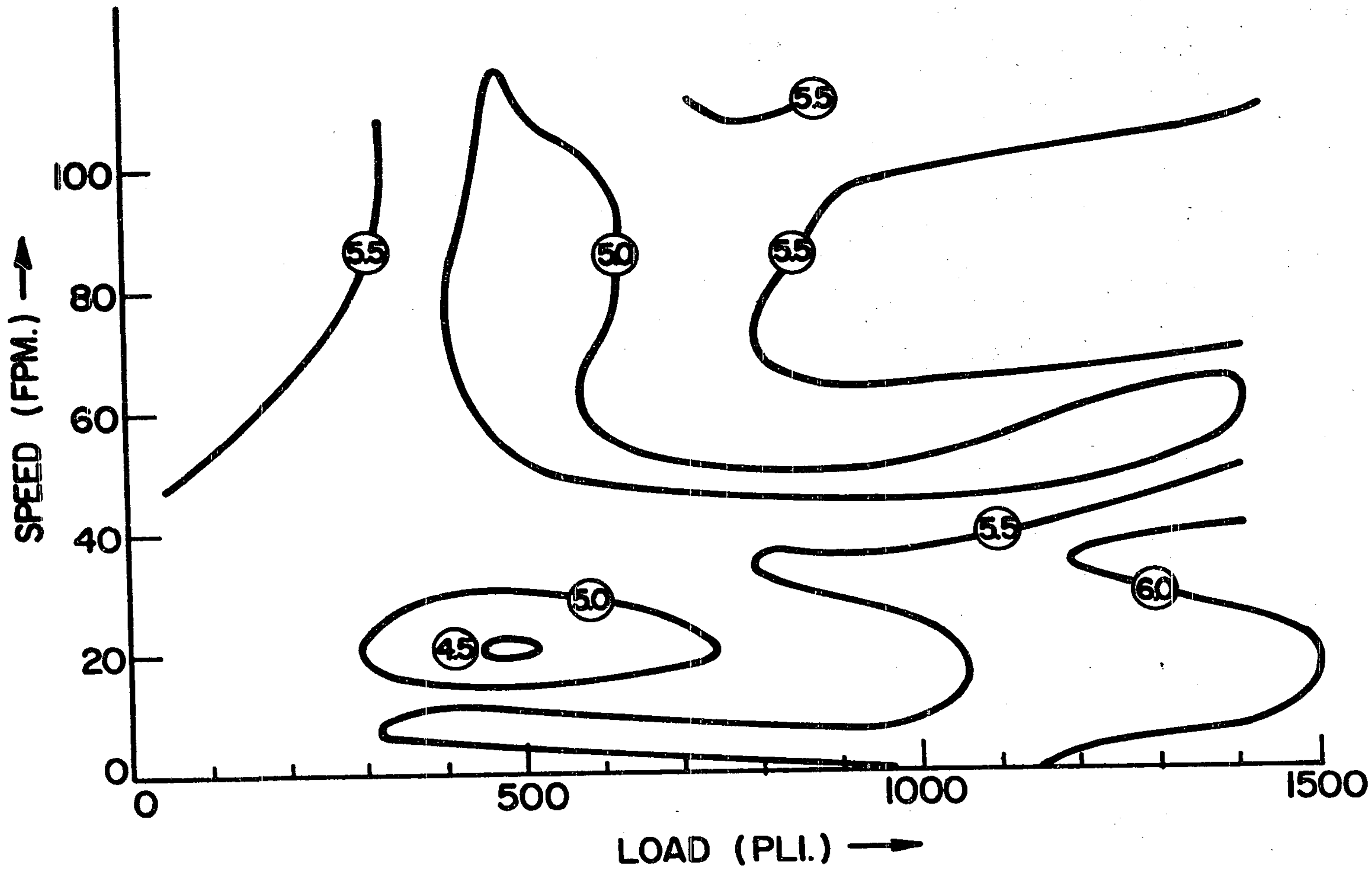

FIG. 61.

Roll A

$\mu = (\mu_{high}+\mu_{low})/2$ = Rolling Friction Coefficient x 10^3.

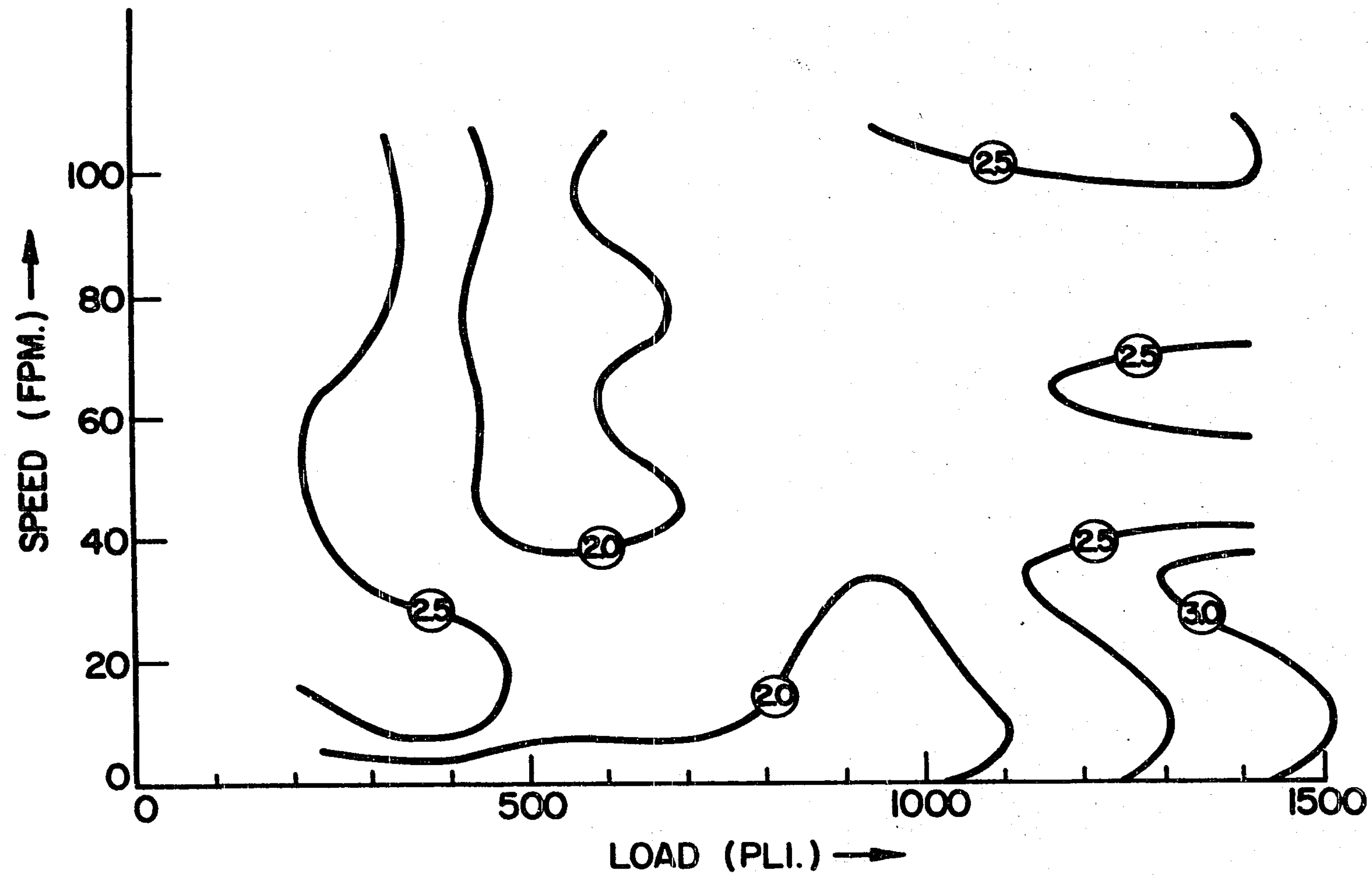

FIG. 62.

Roll B

$\mu = (\mu_{high} + \mu_{low})/2$ = Rolling Friction Coefficient x 10^3.

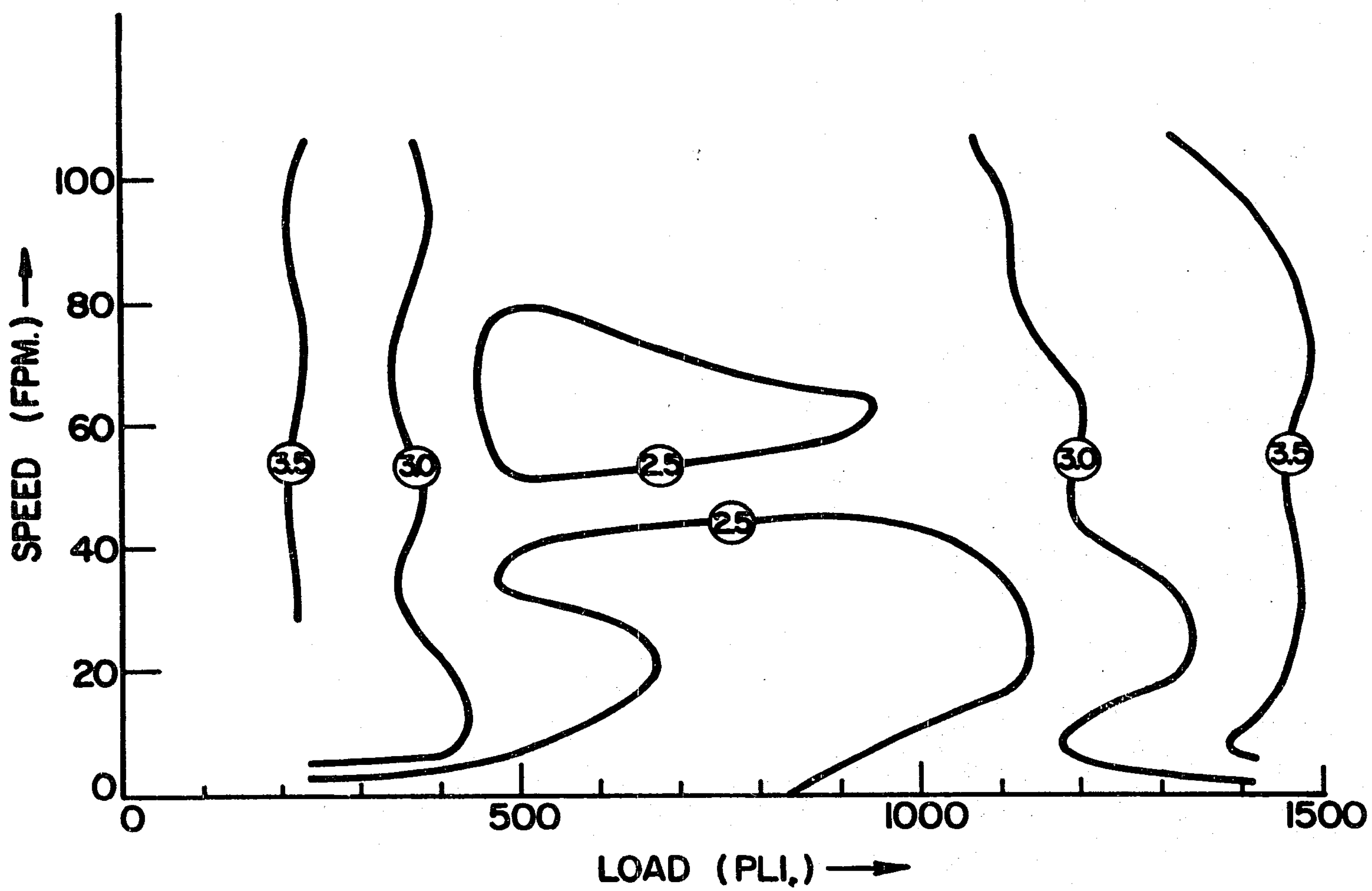

FIG. 63.

Roll C

$\mu = (\mu_{high}+\mu_{low})/2$ Rolling Friction Coefficient x 10^3.

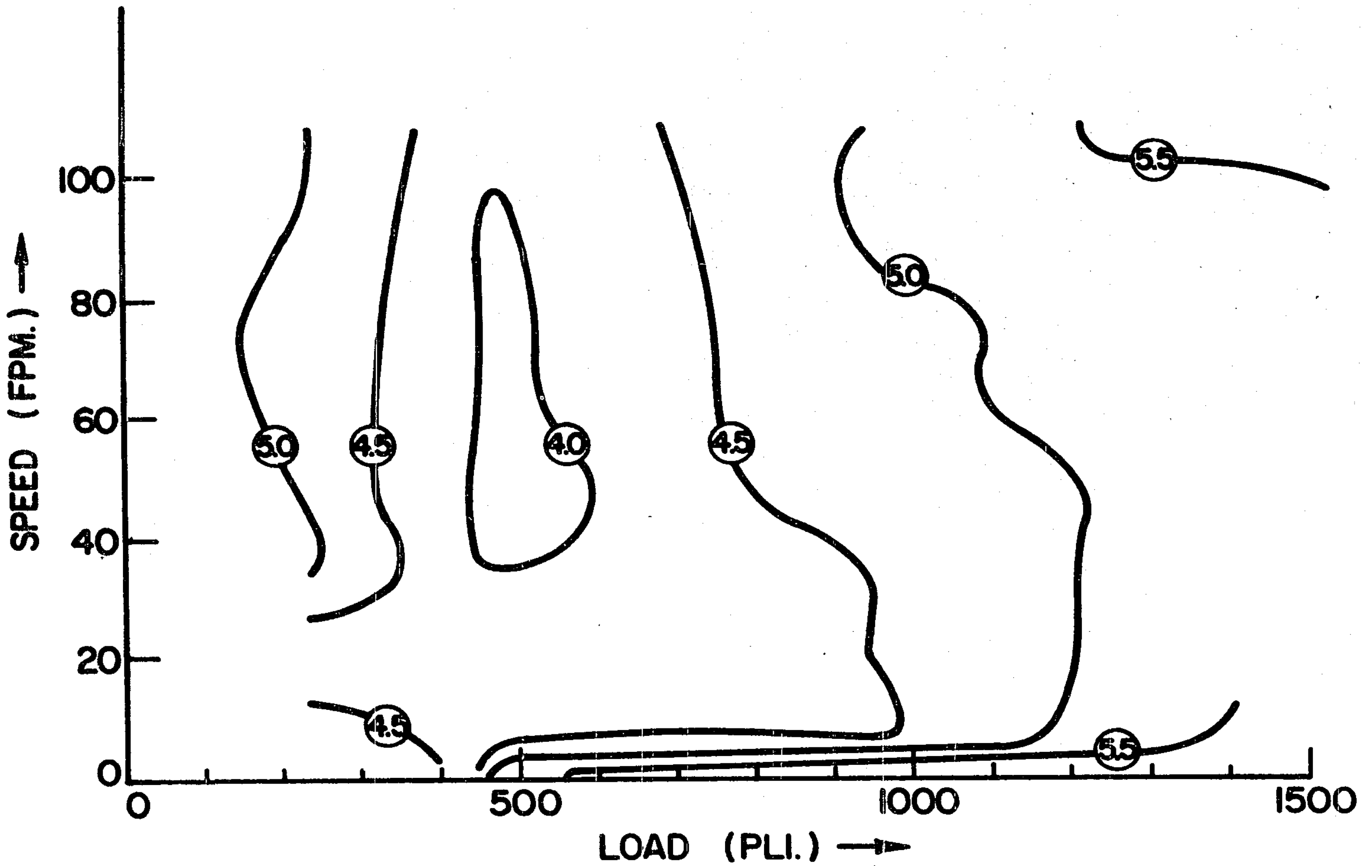

FIG. 64.

Roll D

$\mu = (\mu_{high}+\mu_{low})/2$ = Rolling Friction Coefficient x 10^3.

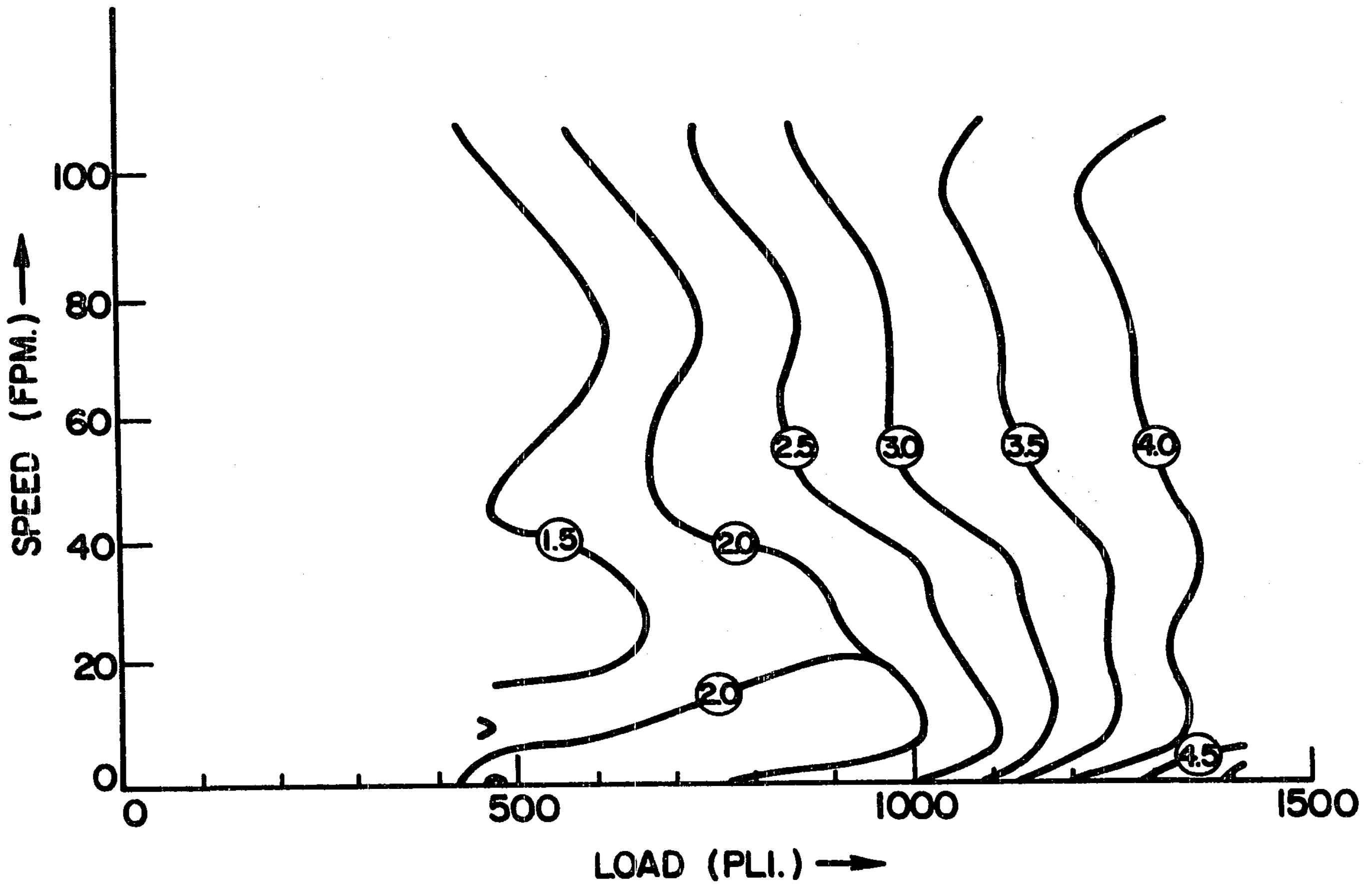

FIG. 65.

Roll E

$\mu = (\mu_{high} + \mu_{low})/2$ = Rolling Friction Coefficient x 10^3.

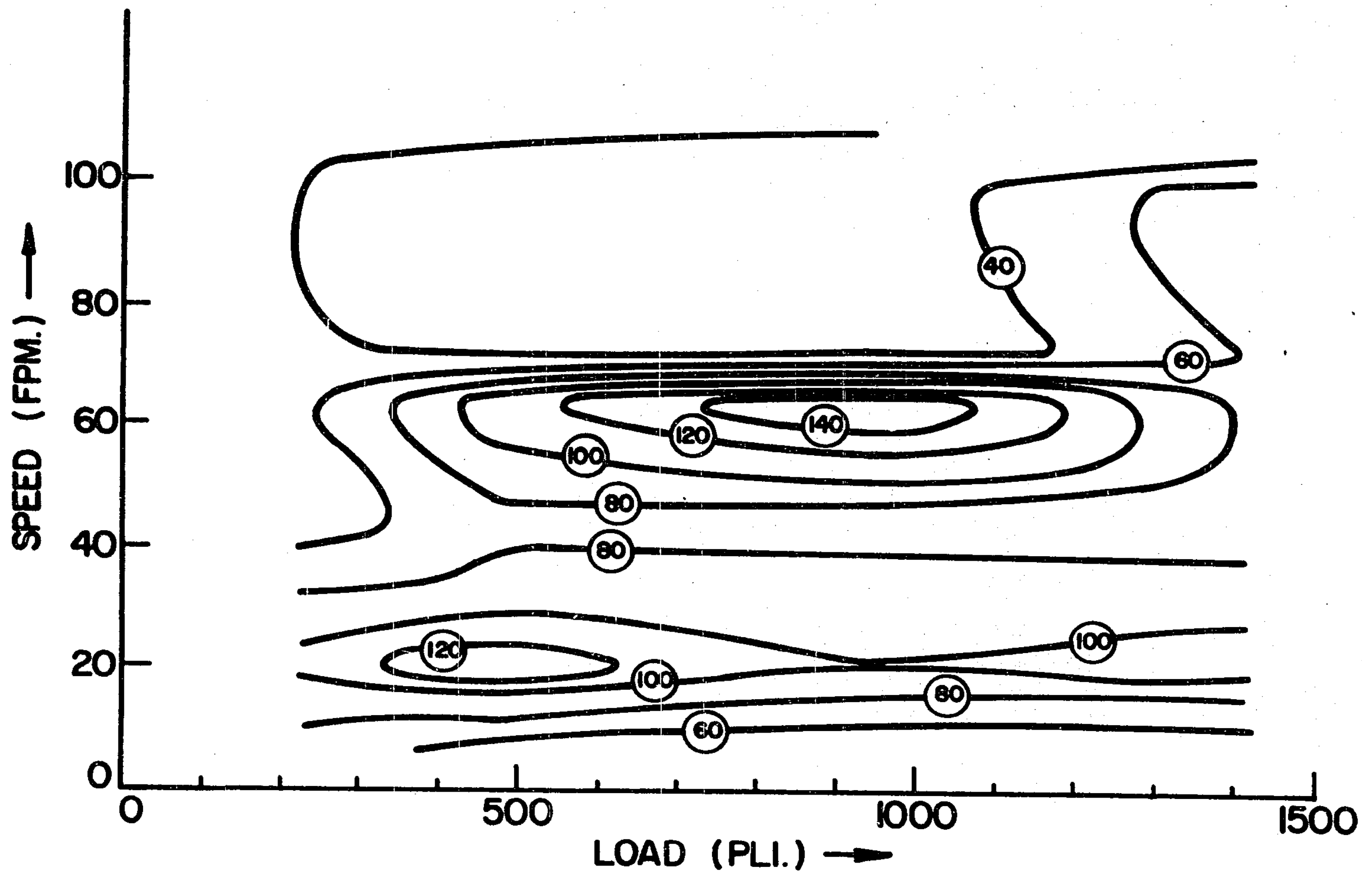

FIG. 66.

Roll A

$\frac{\Delta\mu}{\mu}$ = % Fluctuation in Rolling Friction Coefficient

$\Delta\mu = \mu_{high} - \mu_{low}$

$\mu = (\mu_{high} + \mu_{low})/2$

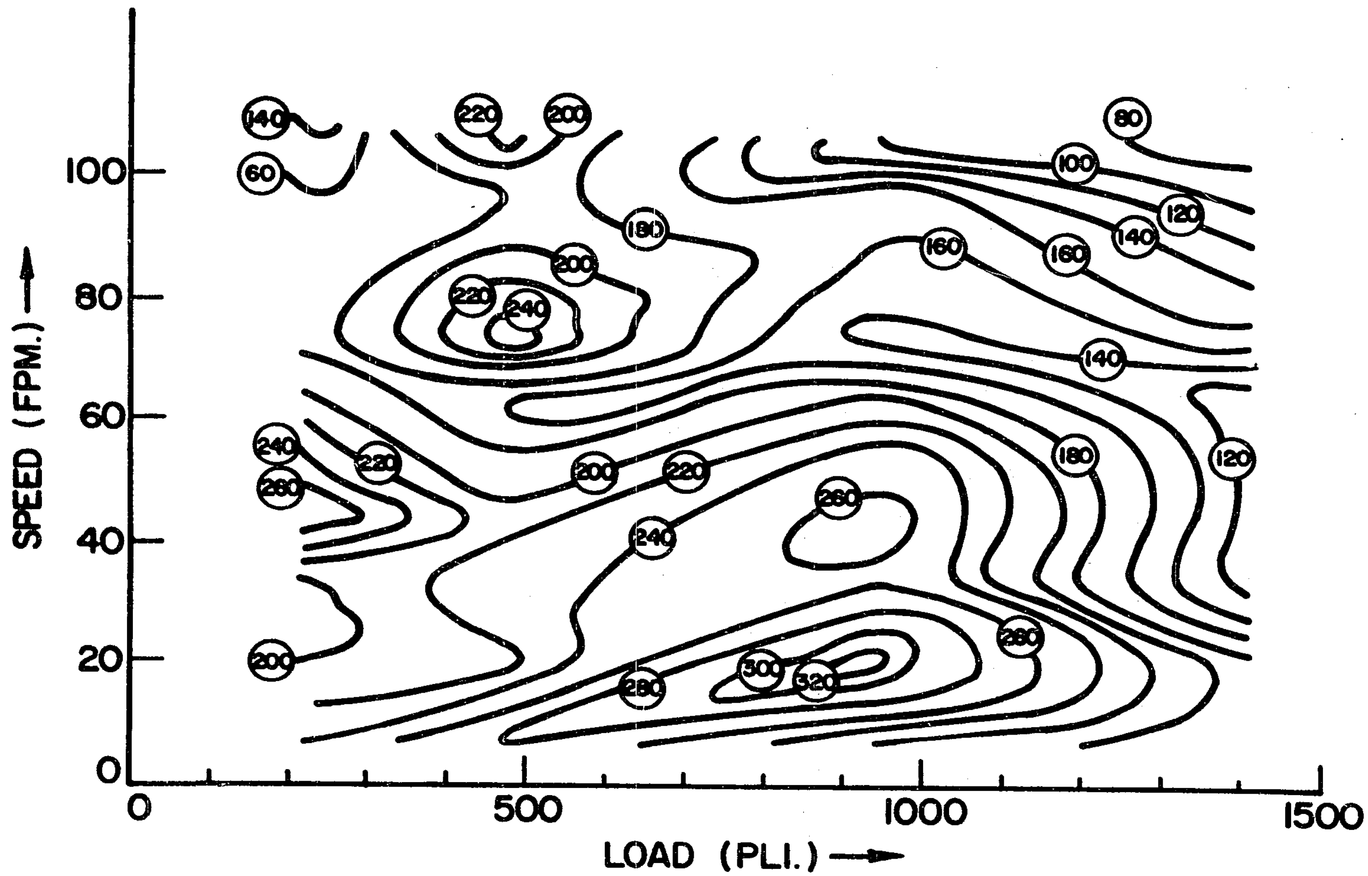

FIG. 67.

Roll B

$\frac{\Delta\mu}{\mu}$ = % Fluctuation in Rolling Friction Coefficient

$\Delta\mu = \mu_{high} - \mu_{low}$

$\mu = (\mu_{high} + \mu_{low})/2$

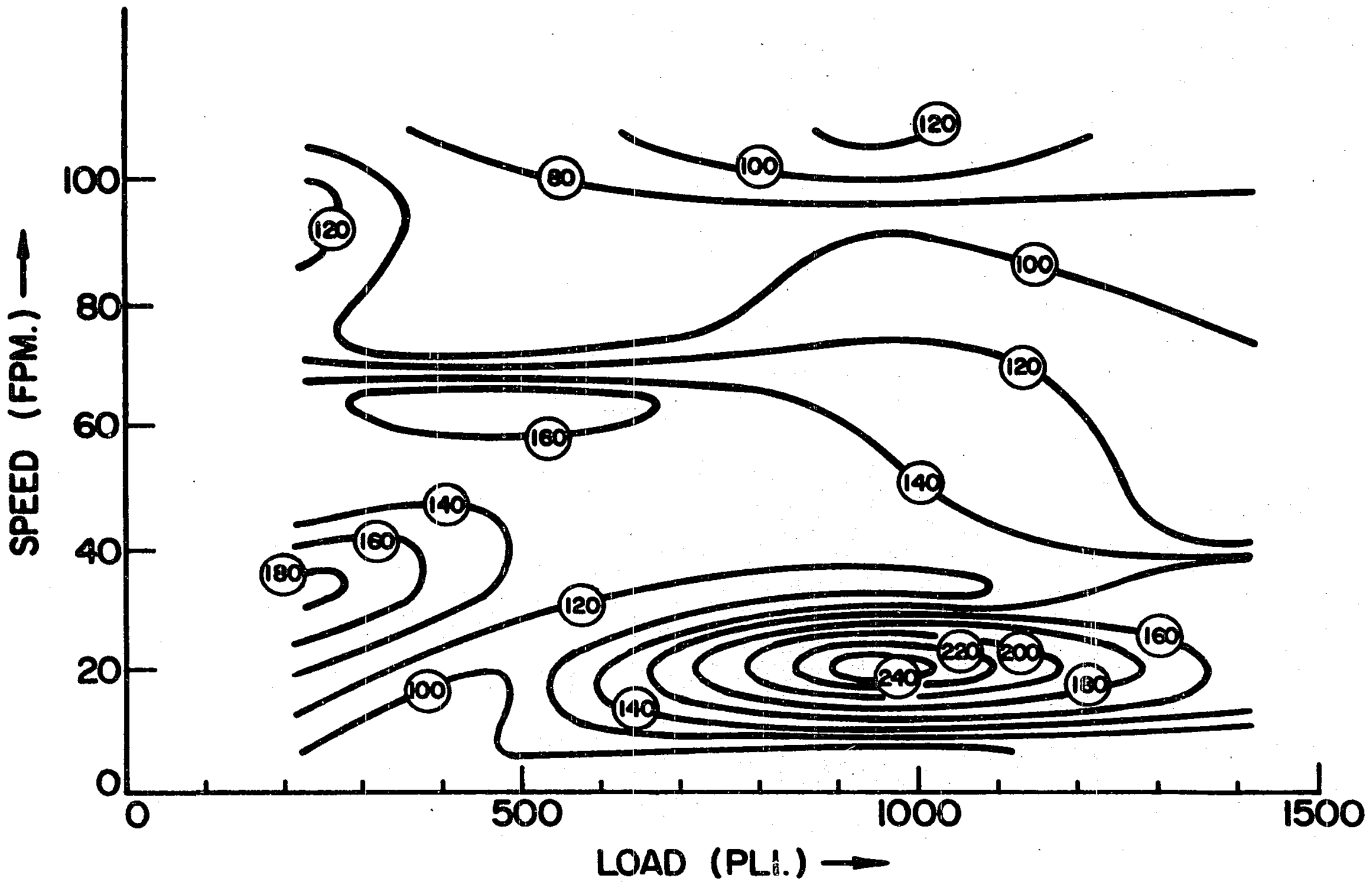

FIG. 68.

Roll C

$\frac{\Delta\mu}{\mu}$ = % Fluctuation in Rolling Friction Coefficient

$$\Delta\mu = \mu_{high} - \mu_{low}$$
$$\mu = (\mu_{high} + \mu_{low})/2$$

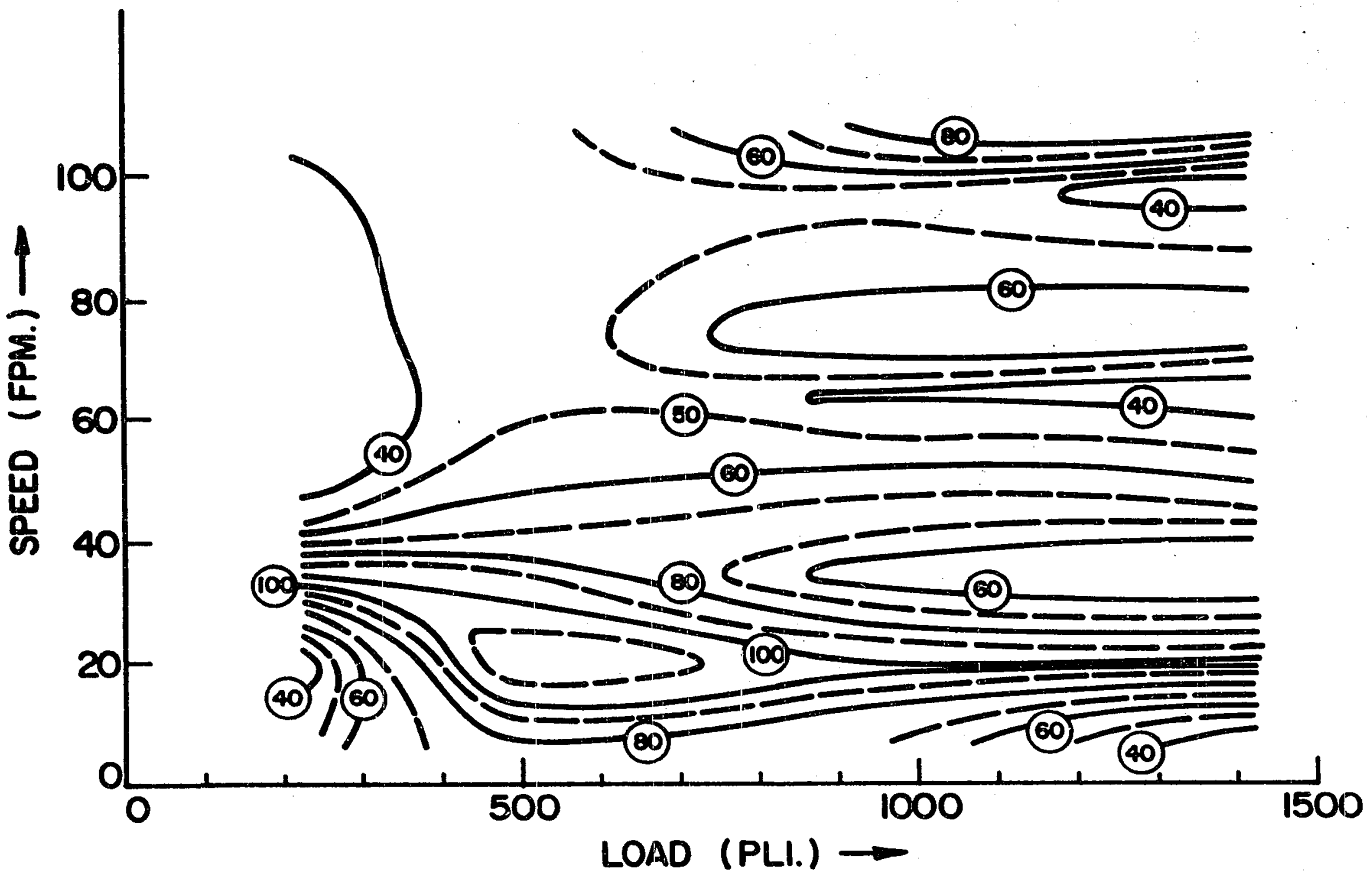

FIG. 69.

Roll D

$\frac{\Delta\mu}{\mu}$ = % Fluctuation in Rolling Friction Coefficient

$\Delta\mu = \mu_{high} - \mu_{low}$

$\mu = (\mu_{high} + \mu_{low})/2$

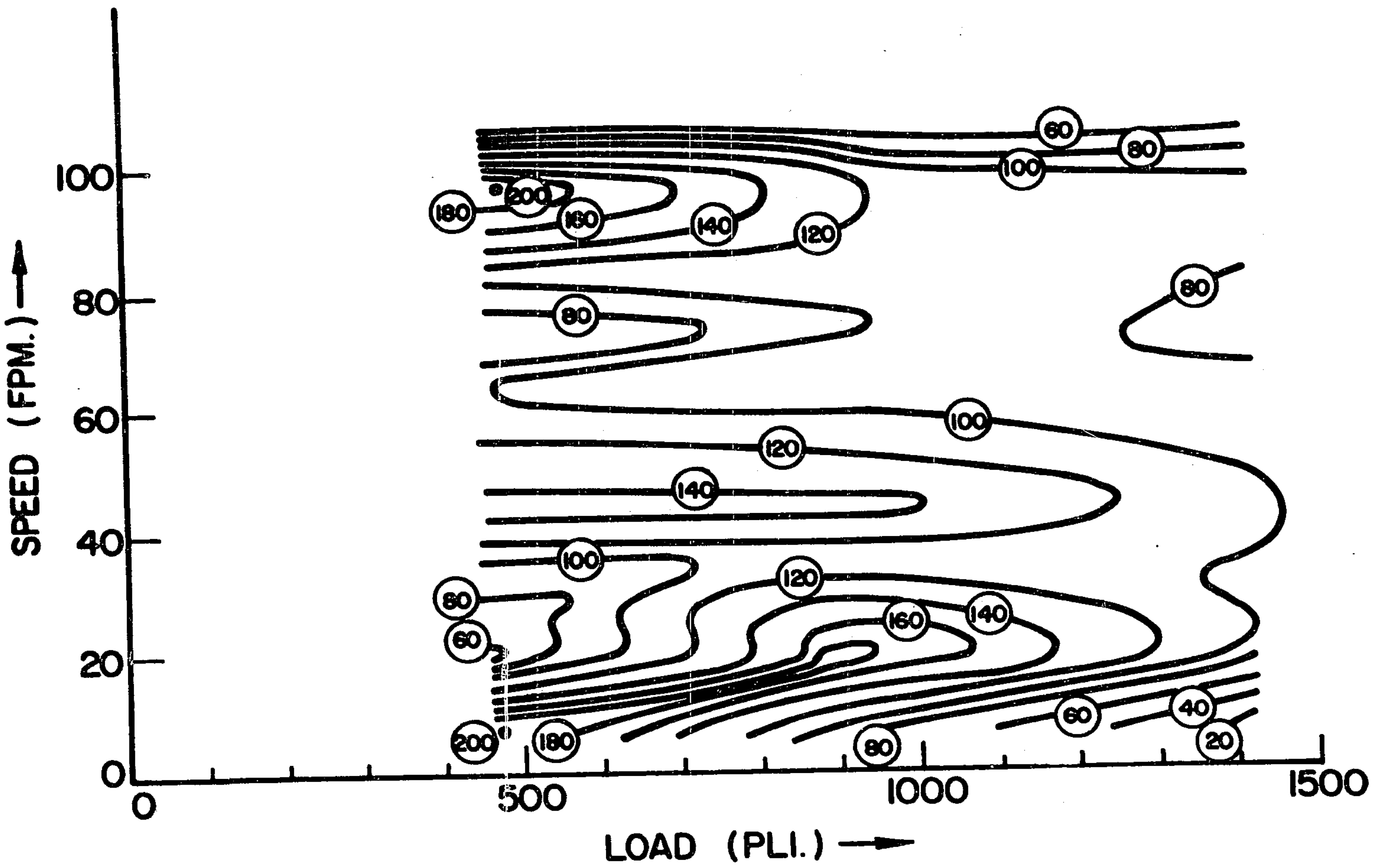

FIG. 70.

Roll E

$\frac{\Delta\mu}{\mu}$ = % Fluctuation in Rolling Friction Coefficient

$$\Delta\mu = \mu_{high} - \mu_{low}$$

$$\mu = (\mu_{high} + \mu_{low})/2$$

or driving traction to the filled roll. These conditions are indicated by a percent fluctuation in friction coefficient which is greater than 200%. This does not suggest that the rolling was self sustaining or produced net driving torque over an extended angle of rotation but that the filled rolls tended to revolve with jerky motion, sometimes springing forward. This behaviour was observed visually as well as reflected by the torque measurements. Surging motion, evident only during slow rolling, while the contacting rolls had negligible angular momentum was undoubtedly enhanced by the twisting of the long steel quill shaft. However, the natural oscillations of a flexible drive system in torsion are periodic. The fluctuations in torque shown in Fig. 60, reproducible with neither the period of rotation of the filled roll nor with a shorter period of oscillation, are not. This sort of irreproducibility suggests that, as well as the long-term effects detected in the experiments run at higher speed, short-term random deformations of the filled roll take place and that these show up as variations in the circumferential distribution of rolling friction coefficient.

As in the case of the high speed data shown in Fig. 59, correlation of the rolling friction coefficient with load and speed was attempted in the following manner. The values of average friction coefficient measured at every load for a specific speed were averaged over load and plotted against speed. Similarly these values measured at every speed for a specific load were averaged over speed and plotted against load. These averages over load and speed, plotted against speed (↓→) and load (←↓) respectively are shown in Fig. 71. For all five rolls there is little variation of average friction coefficient with speed. For three of the

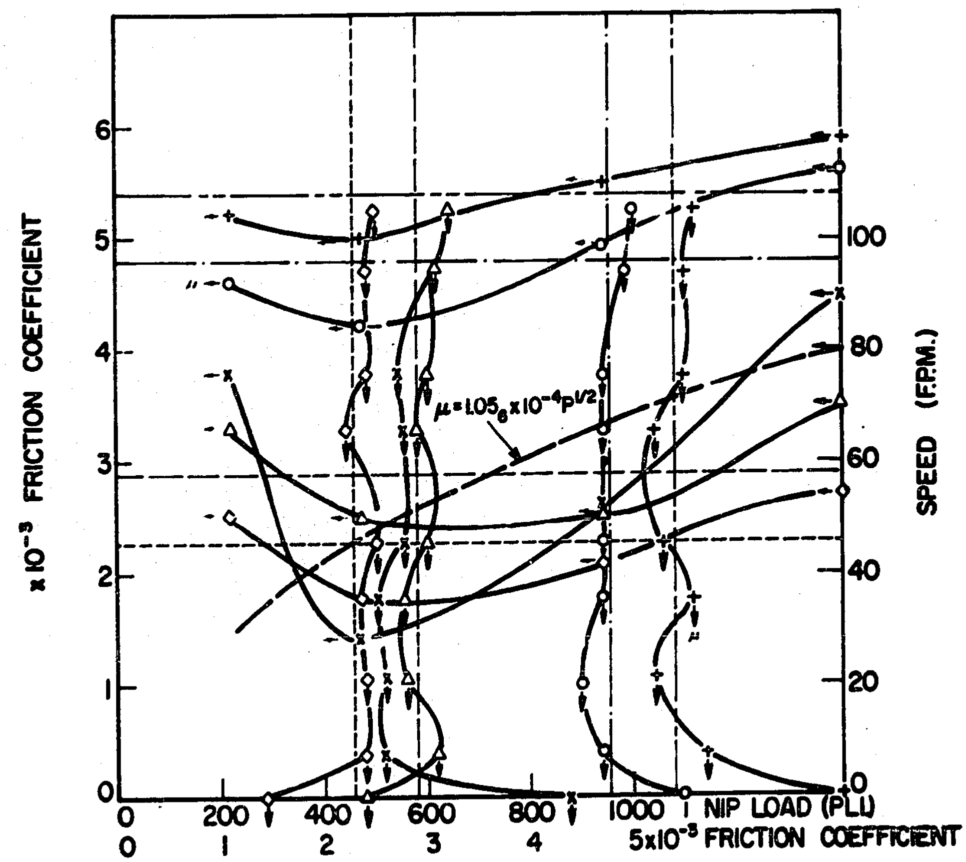

Overall averages

—— · ——	$\bar{\mu} = 4.8 \times 10^{-3}$	+	Roll A
————	$= 5.4 \times 10^{-3}$	◇	Roll B
— — — —	$= 2.9 \times 10^{-3}$	△	Roll C
- - - - - - -	$= 2.3 \times 10^{-3}$	○	Roll D
		X	Roll E

FIG. 71.

Average rolling friction coefficient for 5 rolls plotted against load and speed.

rolls the static friction coefficient, however, i.e. on impending motion, is seen to be higher than the reasonably constant average value at any finite speed. For rolls B and C the static coefficient appears to be lower. However, these measurements may have been unreliable as it may be recalled that these two rolls exhibited friction torque fluctuations of the greatest amplitude. The friction coefficients of all rolls increased with load above about 500 pli. and the relationship

$$\mu = 1.05_6 \times 10^{-4} \sqrt{P}$$

approximates the mean behaviour of the increasing portions of the curves for the five rolls tested. This relationship does not however predict the decrease in friction coefficient with load displayed by all rolls at loads less than 500 pli.

The following discussions of filled roll hardness, surface profile and deformation yield evidence which is compatible with irreproducible, random variations in friction torque described in the preceding pages and the irreproducible thermal behaviour reported in Part I.

Filled Roll Surface Hardness

Rho-meter hardness measurements were taken as shown in Figs.51-52, at 24 points on the surface of all five rolls. Measurements at each point were repeated 4-5 times and initial readings were always 2-3% lower than the subsequent readings because of local compaction of the roll surface under striker impact. By convention the latter, higher readings are taken as standard. It was found that the last three successive readings taken at a point did not differ by more than 1% of full scale. Pictorial diagrams, Figs. 72-74, are presented as a conceptual aid. These show the distribution over the roll surface of the hardness parameter, ρ, plotted vertically to scale on an oblique plane representing a geometric development of the surface which has been unwrapped circumferentially. The 24 hardness ordinates were joined by three circumferential and eight axial curves. These three pictorials show a variety of topographic features. However, hardness maps showing more quantitative detail were prepared for all five rolls by constructing, from measurements plotted on a rectangular grid, the contours of ρ shown in Figs. 75-77. The shorter dimension represents the width of a 7in. wide (5in. wide in the case of roll E) symmetrically located circumferential strip of the roll surface while the longer dimension represents the unwrapped circumference.

Roll D exhibits a hardness distribution shown in Figs. 73 and 75 which varies harmonically through two cycles in the circumferential direction and which decreases more or less linearly from one end of the roll to the other. Rolls A and E appear to have random circumferential variations but with a ridge of higher hardness at centre face. At a single plane (180°) in Fig. 72 an exception can be seen, here a central hardness depression exists. Roll C, Fig. 76, exhibits three central hardness peaks, $\rho = 66^{+}$, 66 and 65^{-}, of a slightly decreasing magnitude, top to bottom of the plot, followed by a rather severe central depression of $\rho = 60$. Fig. 77 shows roll B in three conditions of hardness distribution. This roll logged about one half of its total operation, which covered the period between the first and third hardness measurements in the period between the first and second hardness measurements. Note the progressive erosion of the hardness

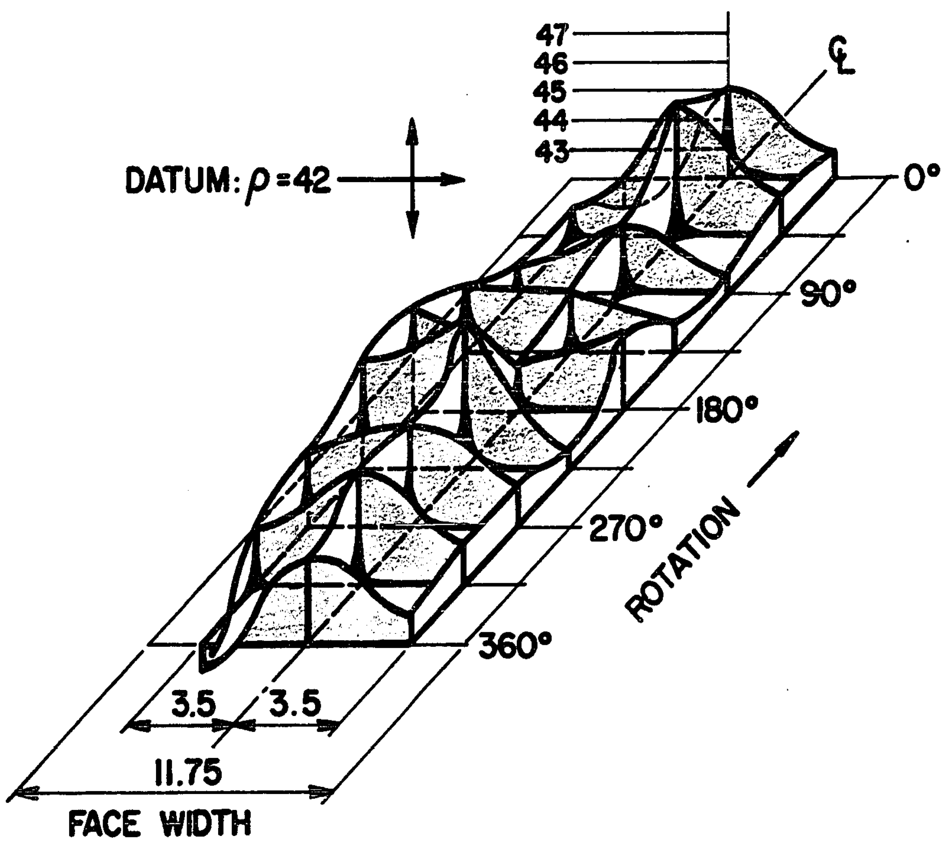

FIG. 72.

Typical Surface Hardness Profile of Roll A.

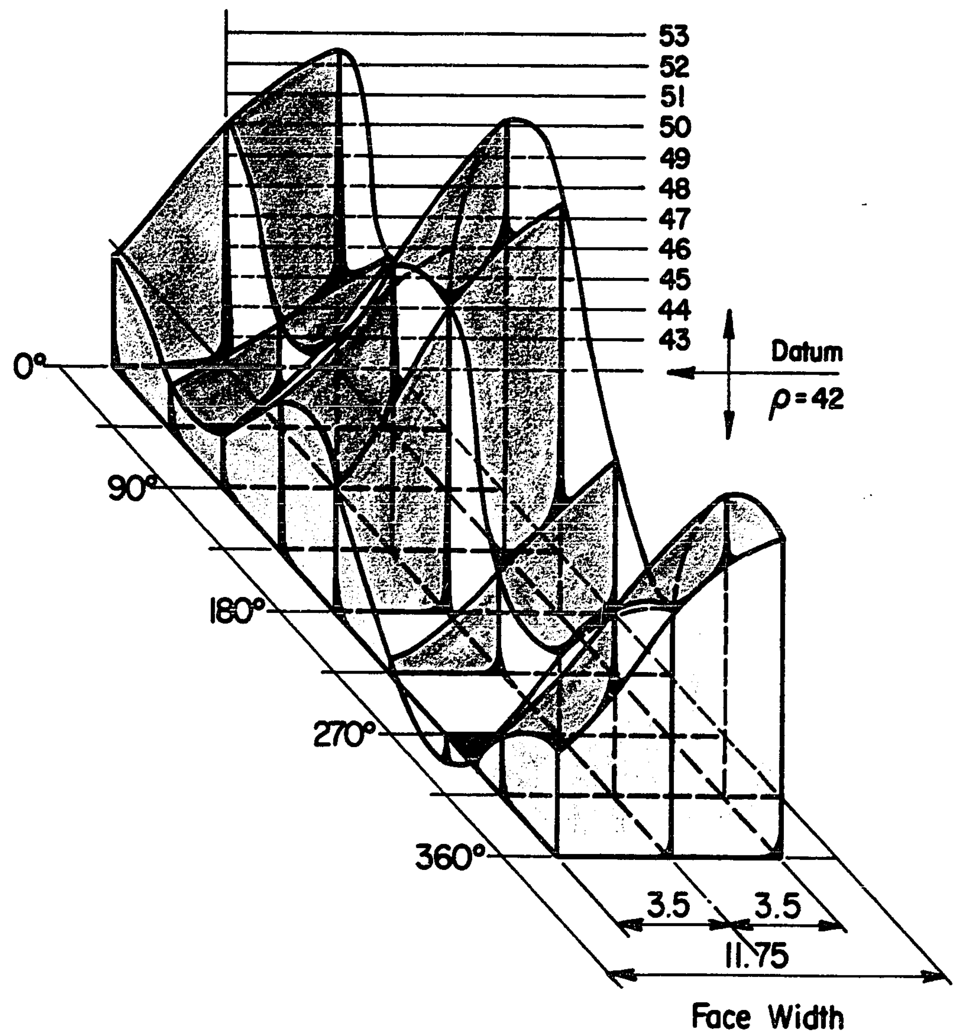

FIG. 73.

Typical Surface Hardness Profile of Roll D.

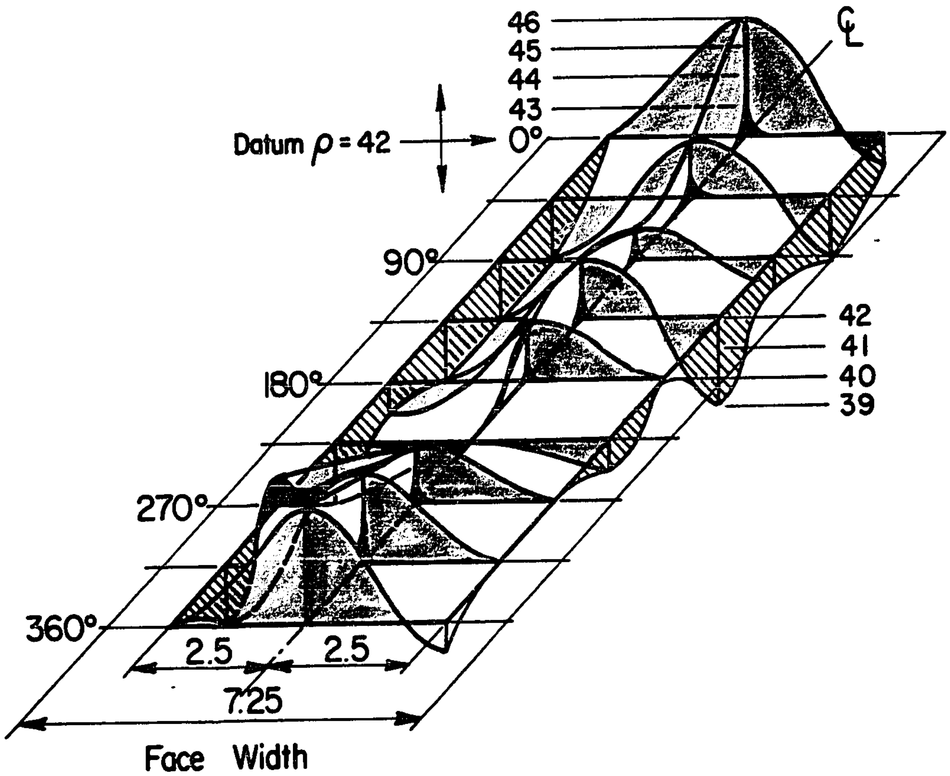

FIG. 74.

Typical Surface Hardness Profile of Roll E.

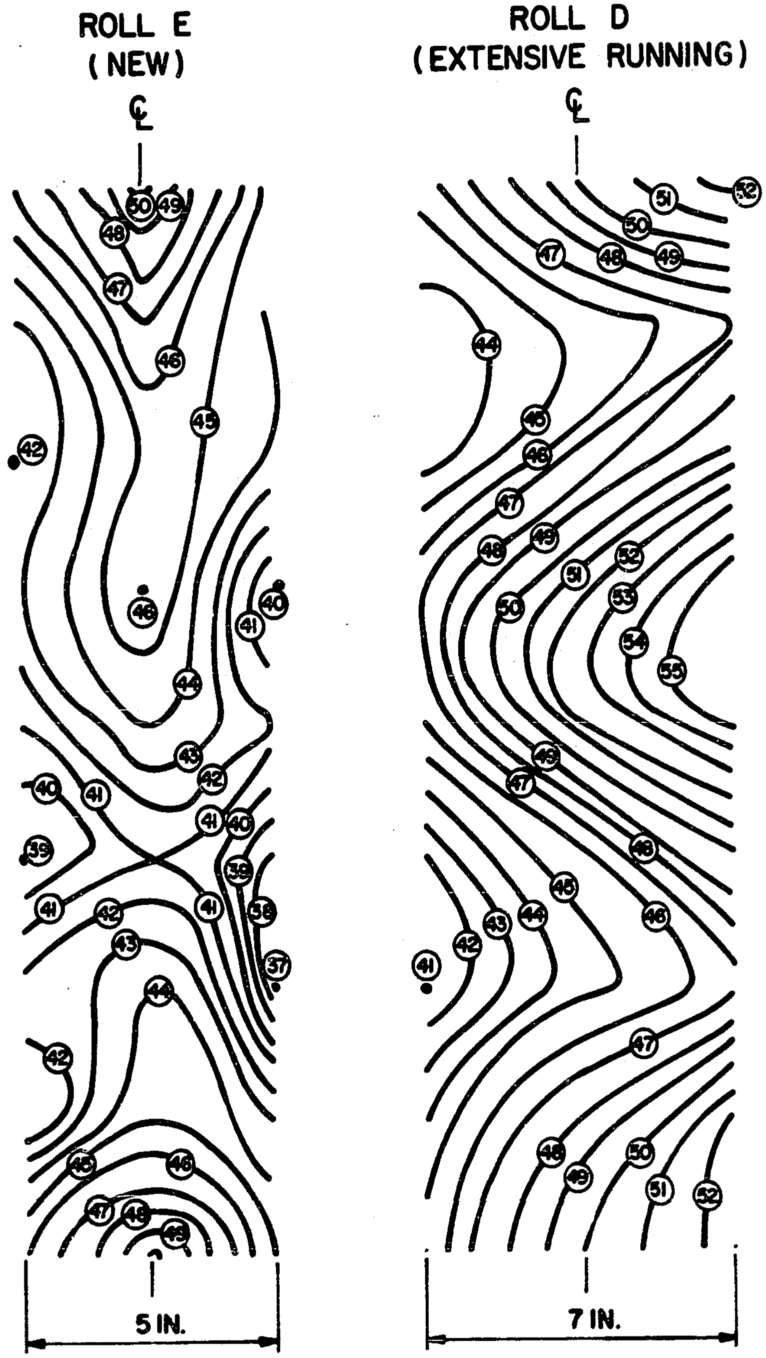

FIG. 75.

Hardness Contours of Rolls E and D.

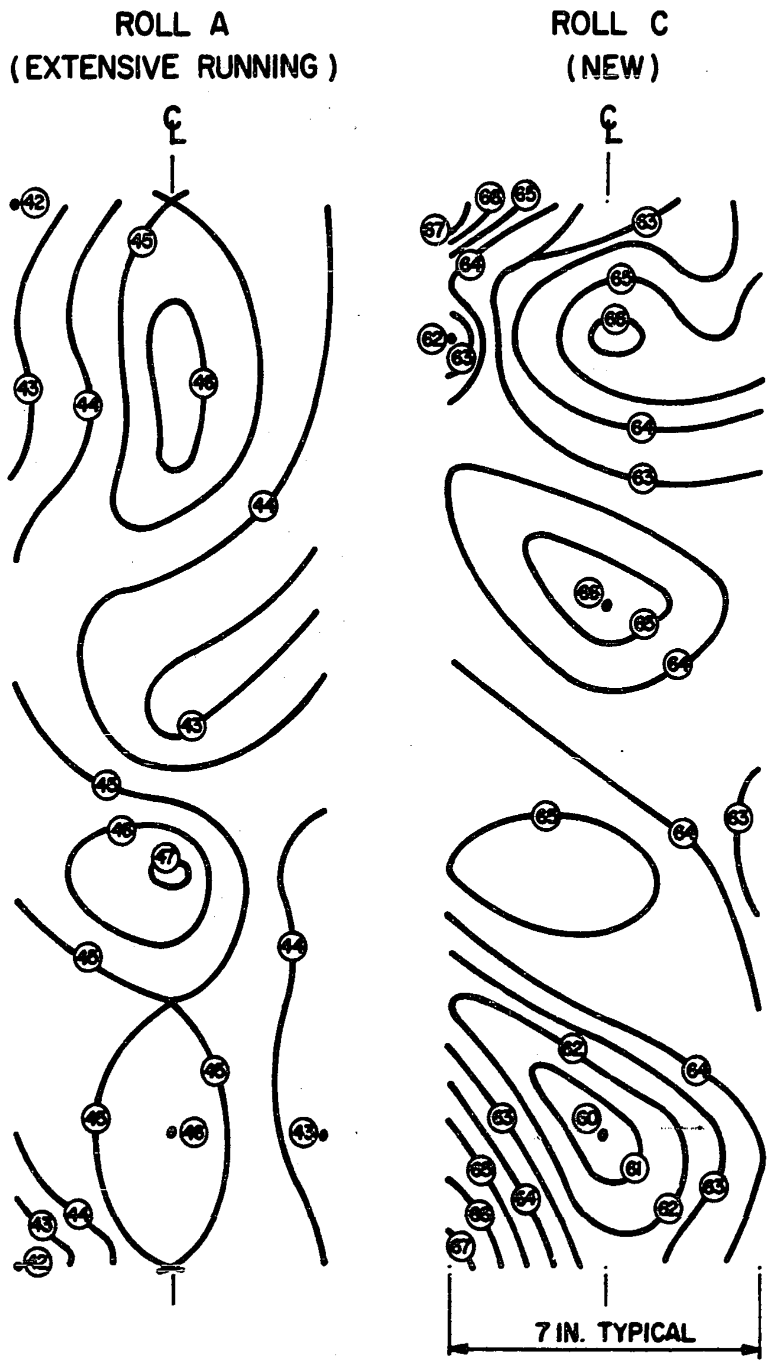

FIG. 76.

Hardness Contours of Rolls A and C.

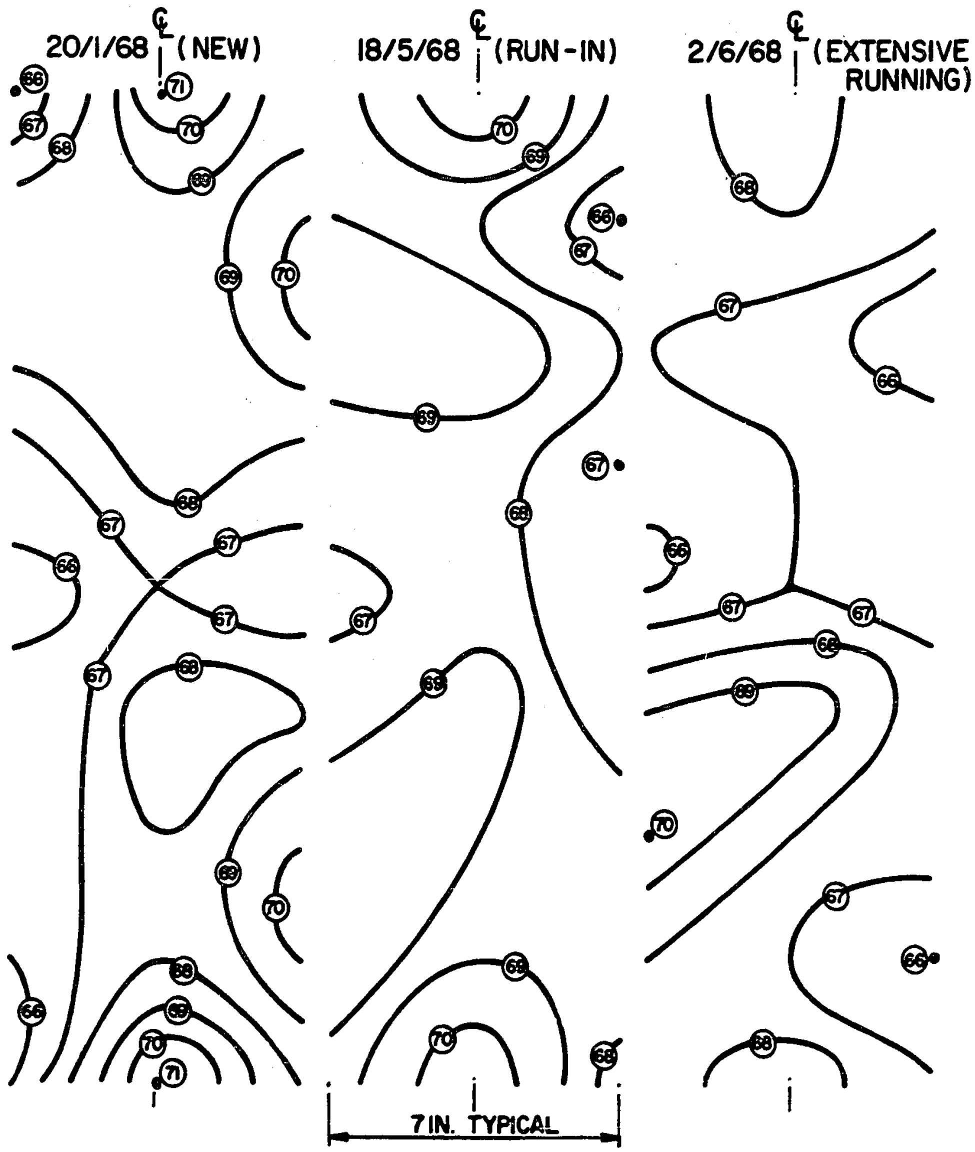

FIG. 77.

Hardness Contours of Roll B,
Successive Measurements.

peak on the line where the development of the cylindrical surface was parted, i.e. at the top and bottom of the contour plots showing Fig.77. Note also the less obvious but more significant changes which completely altered hardness profile as represented by both successive measurements.

It would appear that during its running-in period the surface of a filled roll undergoes complete transformation in hardness profile. There was no evidence that, in the case of rolls A and B, changes in surface hardness had ceased. On the other hand, there was evidence that the severe two wavelength circumferential hardness undulation in roll D had become a permanent feature. Whenever roll D was operated, the side on which the higher amplitude hardness irregularity was located caused the stack to bounce and the piston rod of the pneumatic cylinder to reciprocate twice per revolution of the roll with an amplitude of 1/16-1/8in. This behaviour was not caused by an oval cross-section as it might be assumed. On the contrary; roll D was more nearly circular and had a more uniformly coaxial cross-section than rolls B and C, which were not observed to bounce. It is possible that this undesirable oval hardness profile, like wash-board on a gravel road, is self-propagating and tends to become accentuated by continued operation and the forced oscillation of the loading system. In this regard it is not known to what extent filled roll imbalance affects supercalender performance and roll deterioration.

Except for roll D the plots of hardness profile, Figs. 72-77, give a picture of random hardness distribution which is subject to change during operation. This is entirely consistent with the friction torque fluctuations and general lack of reproducibility of friction measurements previously reported. If filled rolls undergo random deformation, as has been considered with progressively increasing conviction throughout this investigation, and if the fill material retains even a small fraction of its bulk compressibility displayed during the pressing phase of filled roll manufacture then fill density changes of the order of the hardness variations measured are highly probable. If variations in roll surface hardness are responsible for circumferential variations in rolling friction coefficient, then the average surface hardness of a filled roll should strongly influence its average rolling friction coefficient. Thus a significant correlation between the average coefficient and average hardness might be expected.

If mean friction coefficient for slow rolling is plotted against mean hardness, Fig. 78, four of the five experimental filled rolls show a fair negative linear correlation.

It may be noted that the four rolls which indicate this correlation between hardness and rolling friction coefficient all exhibit a difference between their maximum and minimum surface hardness which is between 8 and 11% of their mean hardness. The fifth roll, which does not conform, has a range of hardness which is about 30% of its mean. It is noted that the variations in hardness do not appear to have any significance as the roll which had 30% variation in hardness produced the least, not the most, variation in friction torque in circumferential direction and Fig. 60 does not exhibit any two cycle fluctuation in torque corresponding to the hardness distribution of roll A shown in Figs. 73 and 76.

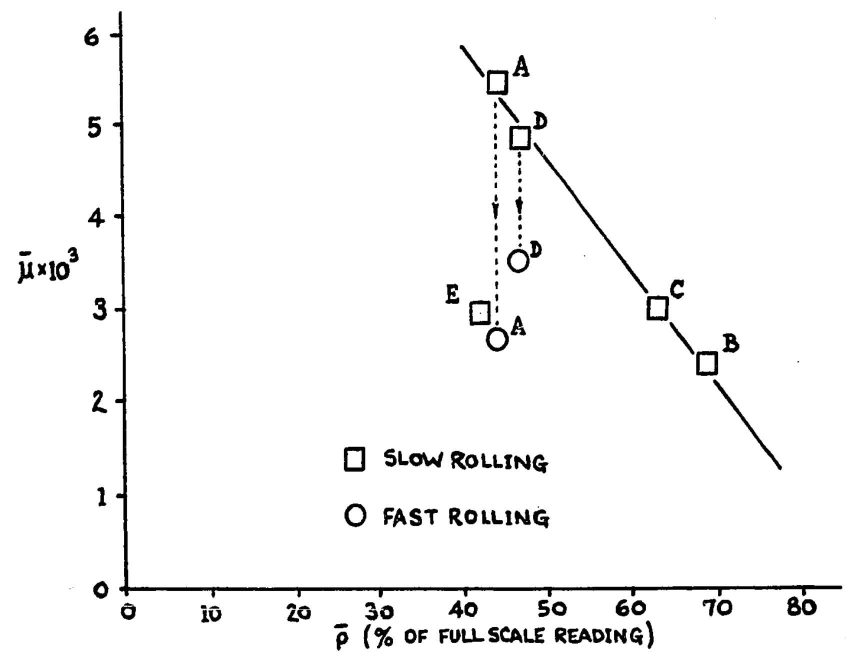

FIG. 78.

Average Friction Coefficient $\bar{\mu}$ versus average hardness, $\bar{\rho}$, for five filled rolls A, B, C, D and E.

Note the complete lack of correlation of the fast rolling average friction coefficients obtained from Fig. 59 for rolls A and D. Unless it is assumed that over 100 rpm. these two rolls undergo a marked increase in hardness, no consistent evidence of a correlation between hardness and friction has been revealed. No evidence of hardness increase with speed has been produced. In fact it has been reported (35) that areas on the surface of a filled roll which have become abnormally hot through operation exhibit correspondingly *low* "Rho" hardness.

Filled Roll Surface Profile Measurement

The pictorial developments of the cylindrical filled roll surfaces are described in Figs. 79-83. The irregular vertical planes represent the clearance gaps between a rigid flat plane and the roll surface at circumferential angular intervals of 45°. Although all rolls were originally turned to within 0.001in. of a true cylindrical surface, large irregularities in the axial direction have developed. In the case of the smoothest roll the radial differences are as much as 0.003in. In the case of the most irregular, radial differences up to 0.014in. can be seen. There appears to be no relation between hardness and surface irregularity. Evidence of this can be obtained by comparing Figs. 74 and 83. The surface irregularities in Fig. 82 in no way betray the two cycle circumferential hardness wave which is the most striking feature of the hardness profile represented by Fig. 74.

Without knowing the effect of axial macro-irregularities, as shown in Figs. 79-83, on cylindrical rolling friction it is not possible to suggest with confidence a roughness parameter which will produce a meaningful correlation with friction coefficient. The maximum difference, ΔR, in filled roll radius is, however, a measure of irregularity which can be easily determined. Correlation between this difference and the average slow rolling friction coefficient for all five rolls was therefore attempted by plotting $\bar{\mu}$ vs. ΔR as shown in Fig. 84. In the case of surface hardness, recall that three consecutive hardness maps of roll B shown in Fig. 77 indicated that there was little change in *average* hardness during normal operation. However, no data were obtained to show that the

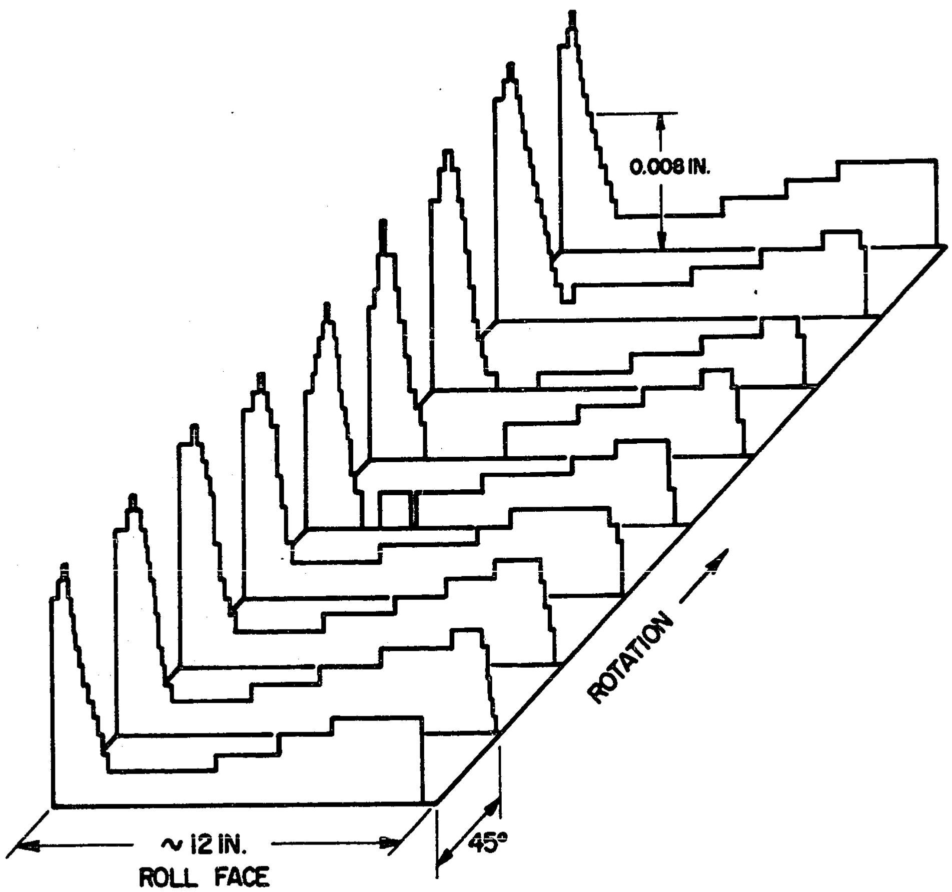

FIG. 79.

Surface Profile Roll A.

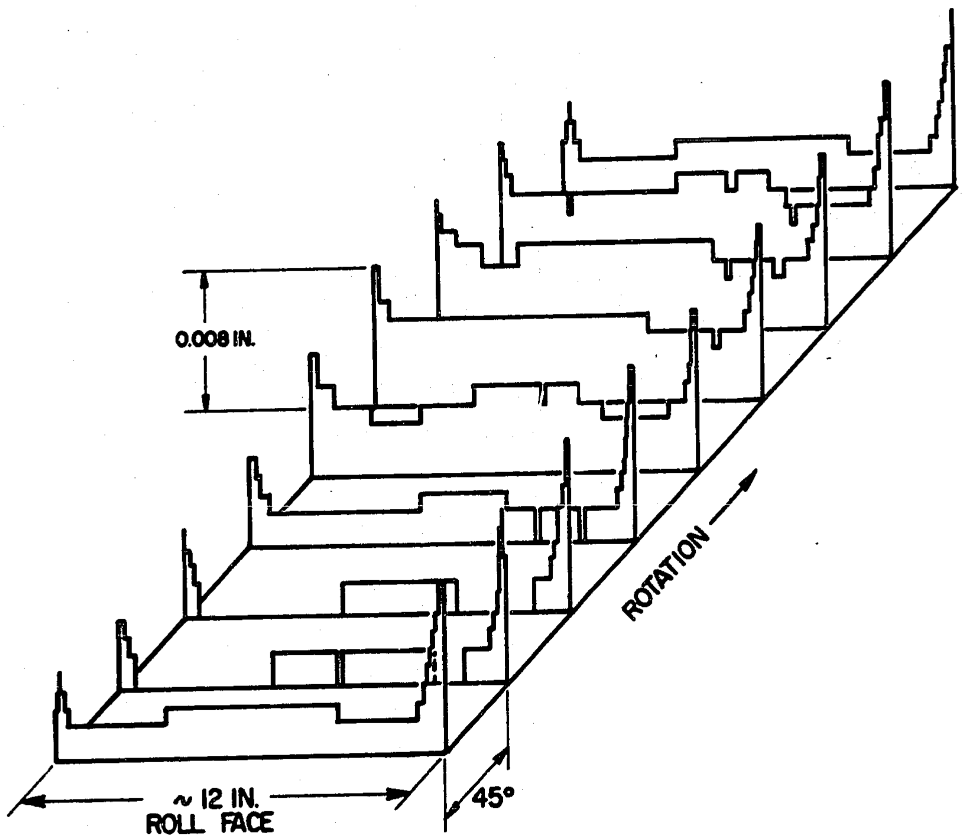

FIG. 80.

Surface Profile Roll B.

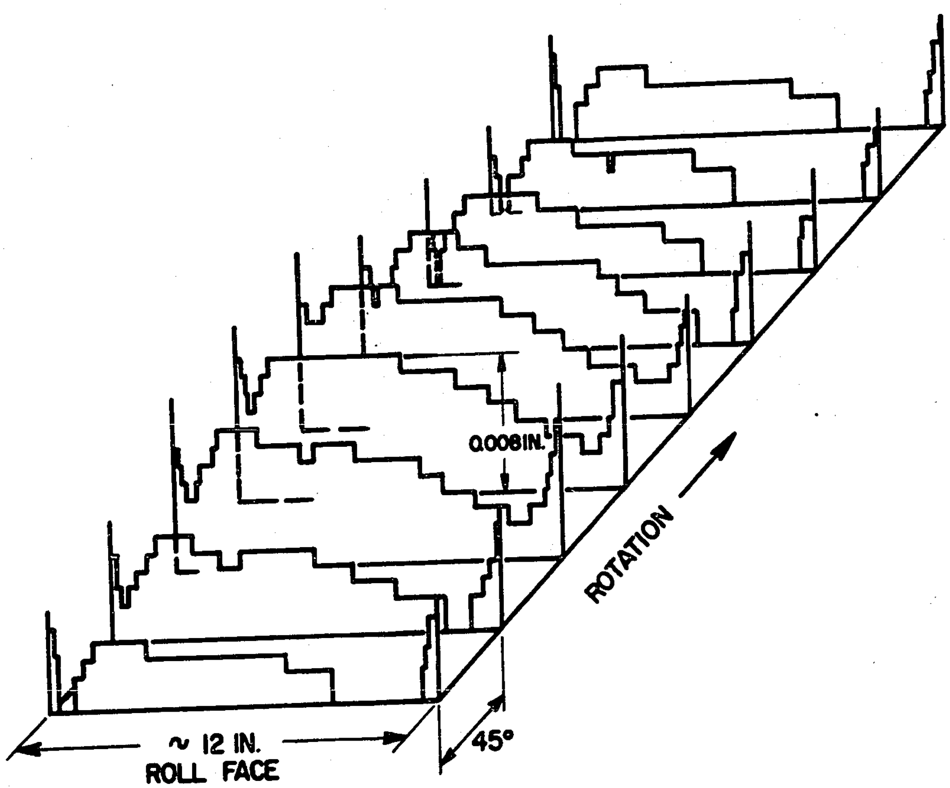

FIG. 81.

Surface Profile Roll C.

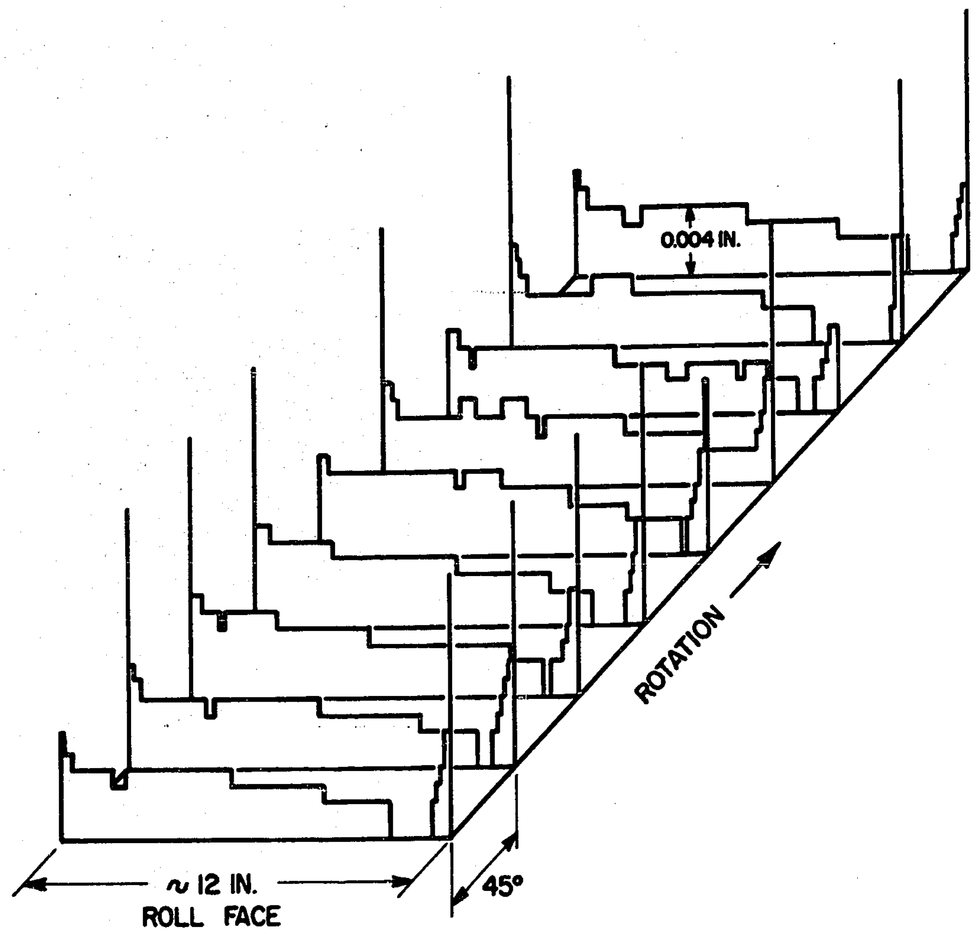

FIG. 82.

Surface Profile Roll D.

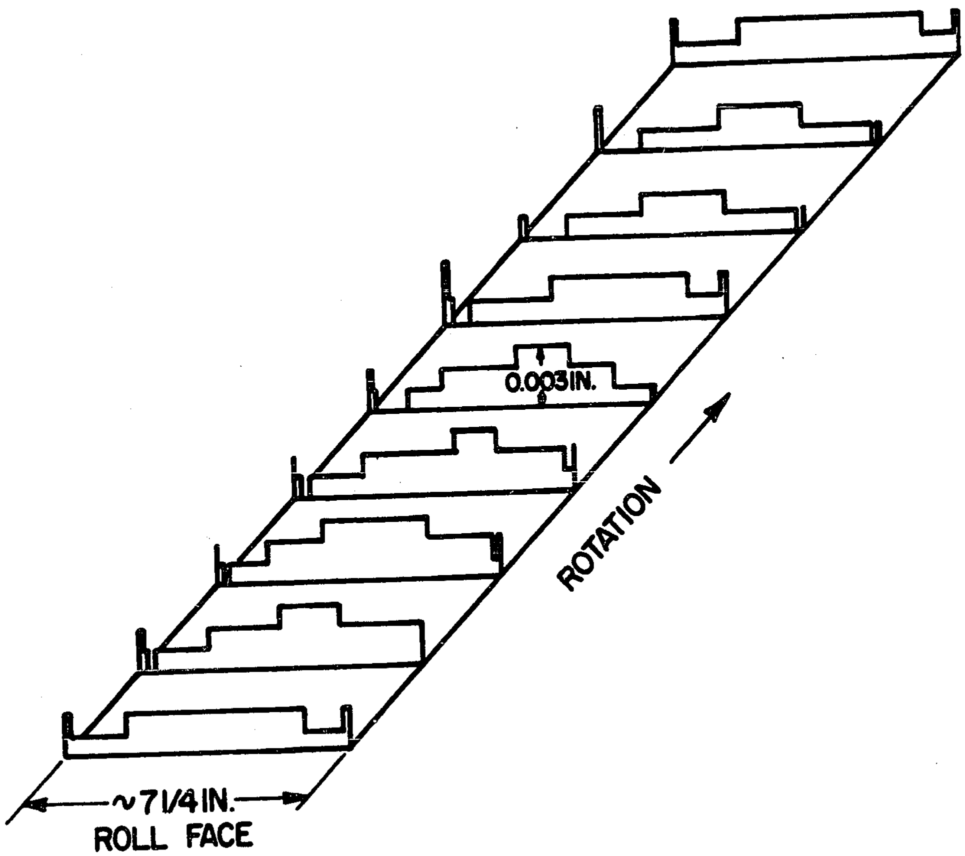

FIG. 83.

Surface Profile Roll E.

magnitude of maximum irregularity does not change with operation. On the other hand, although it is known that these irregular profiles did not exist initially, but somehow developed after the filled rolls were manufactured, there is no evidence that the large radial differences were stimulated by operation or that once such irregularities develop they are appreciably altered through further operation. It is therefore reasonable to expect a significant correlation between the average friction coefficient, $\bar{\mu}$, and the maximum radial difference, ΔR.

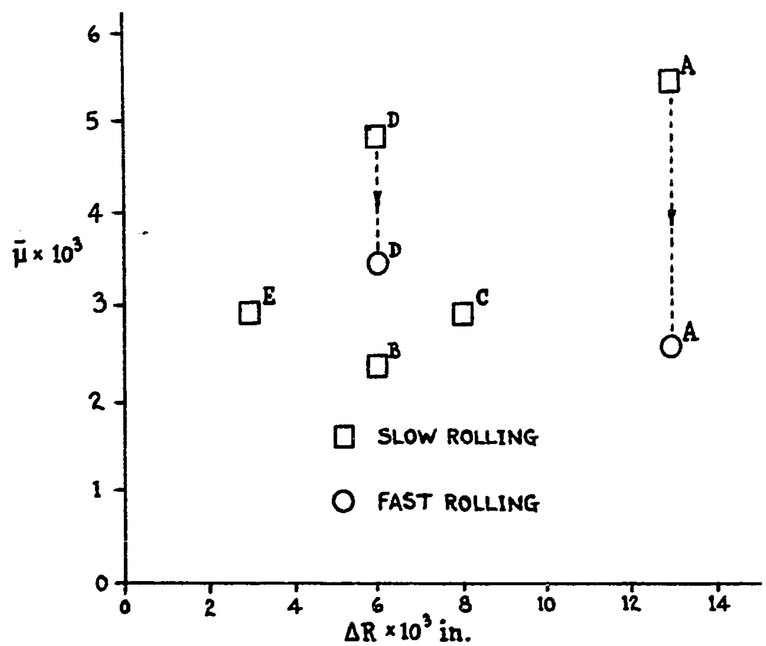

FIG. 84.

Average Friction Coefficient, $\bar{\mu}$, versus Maximum Difference in roll Radius, ΔR, for five filled rolls A, B, C, D and E.

The impossibility of a positive correlation between maximum difference in filled roll radius and average friction coefficient is emphasized by the inclusion of the two fast rolling coefficients. It is however, inconceivable that surface irregularities of the magnitude which were measured can fail to affect the rolling friction. Clearly the axial profile of the filled roll must influence the axial pressure distribution in the nip. Once again there is indirect evidence that a process of random deformation is involved and that mean parameters, or in this case maxima, have no immediately useful significance.

X-ray Measurement of Fill Deformation

X-radiograms of an axial view of the nip between 12in. diameter steel and filled rolls and containing the spherical metal tracers embedded in the filled roll were obtained on film mounted in a cassette attached to the filled roll as shown in Fig. 85. Static and low speed tests at 6.5 and 62 fpm. were conducted at loads of 0, 240, 470, 940 and 1400 pli. Load was progressively increased and decreased through all steps with the rolls stationary, then at the lower speed and finally at the higher speed. Out of the 46 radiograms which were taken of both patterns, about 30 were of satisfactory quality for tracer coordinate measurement. Data obtained from the tracer images were extracted and processed in the following manner.

1) All negatives of the tracer patterns were contact printed at two exposures producing a light and dark print of each pattern as shown in Fig. 86. This was done because the two tiers of sphere images closer to the filled roll surface are more clearly defined at the longer exposure which produces darker prints.

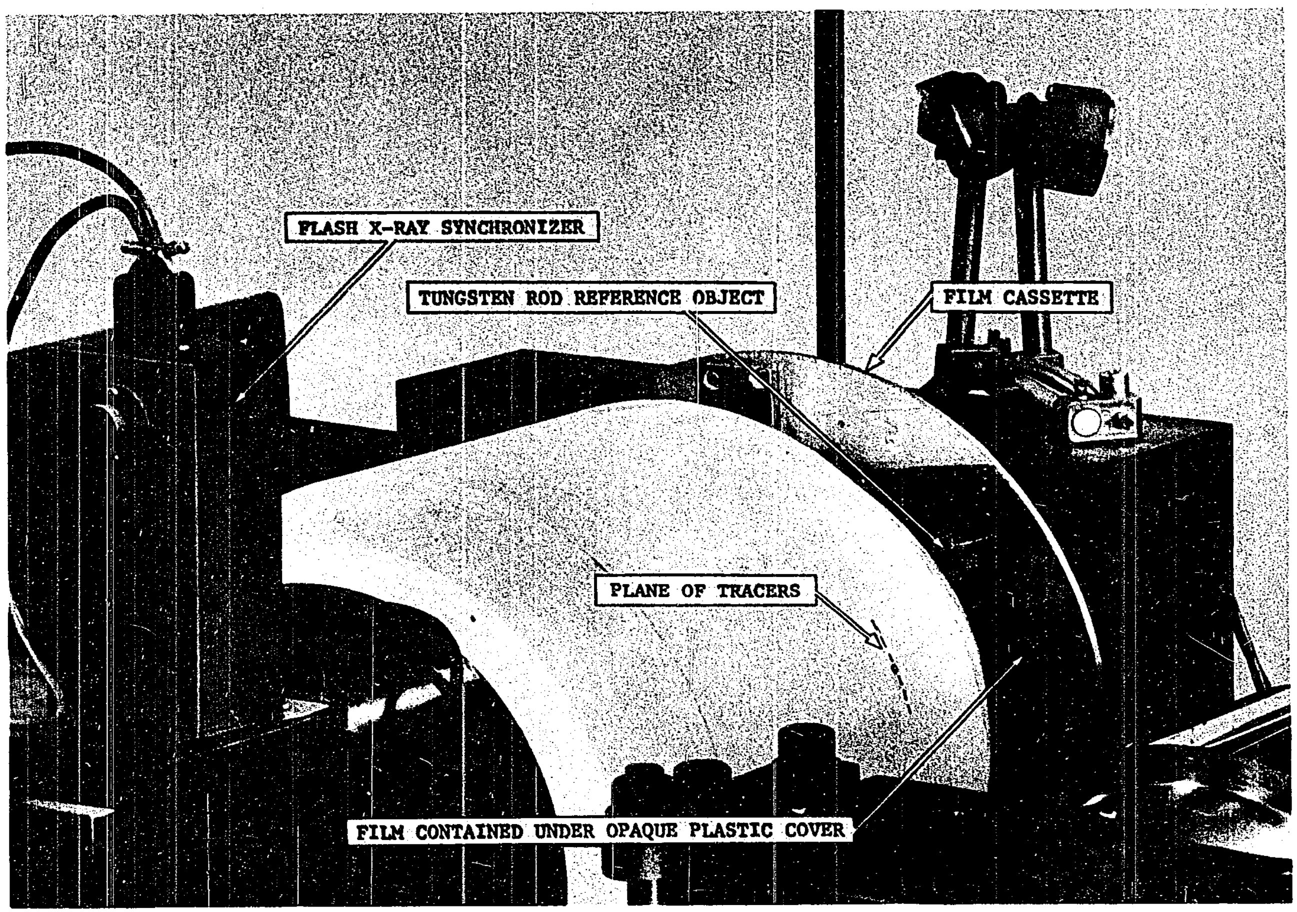

FIG. 85.

Roll E in Stack with Attached X-ray Film Cassette.

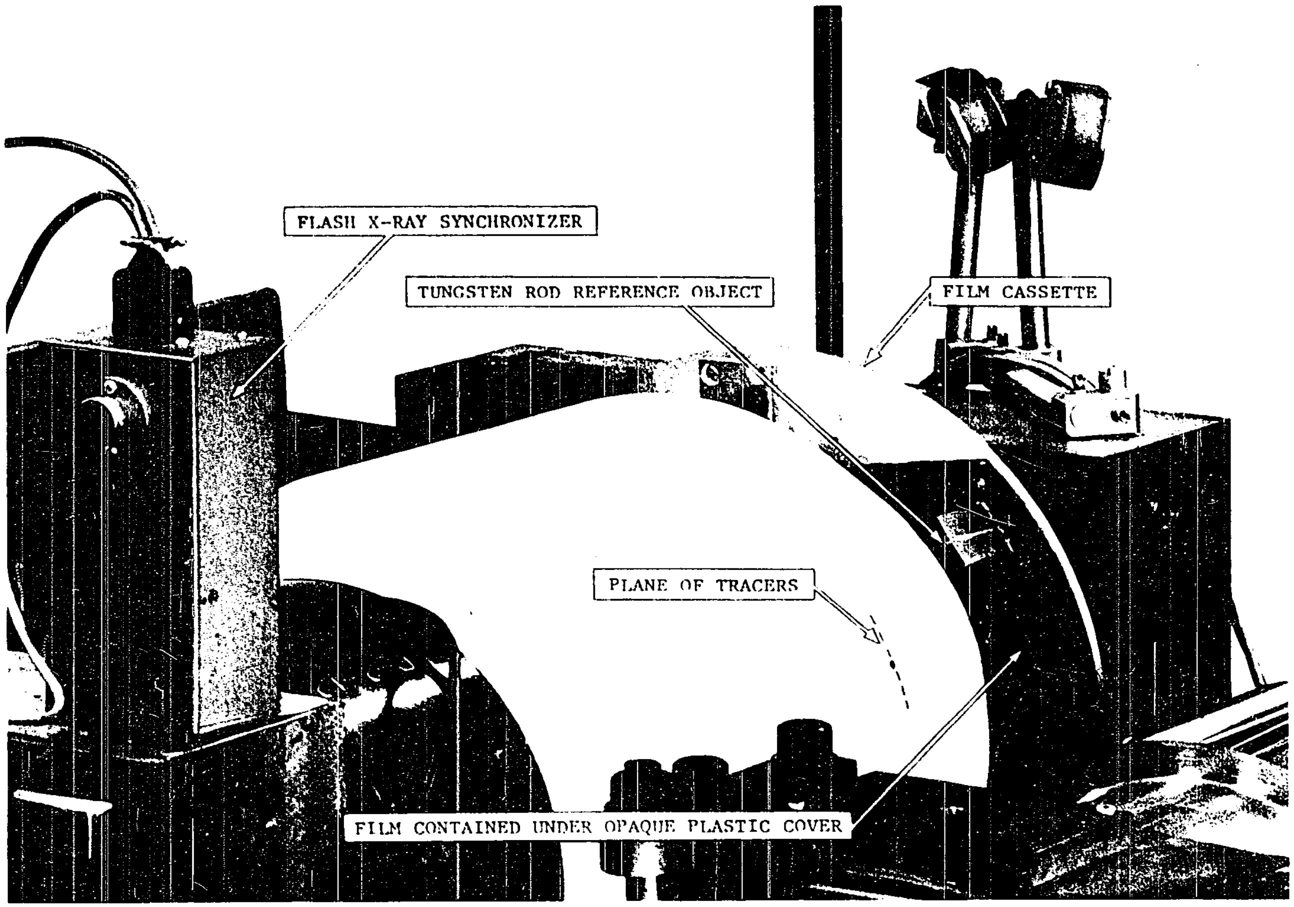

FIG. 85.

Roll E in Stack with Attached X-ray Film Cassette.

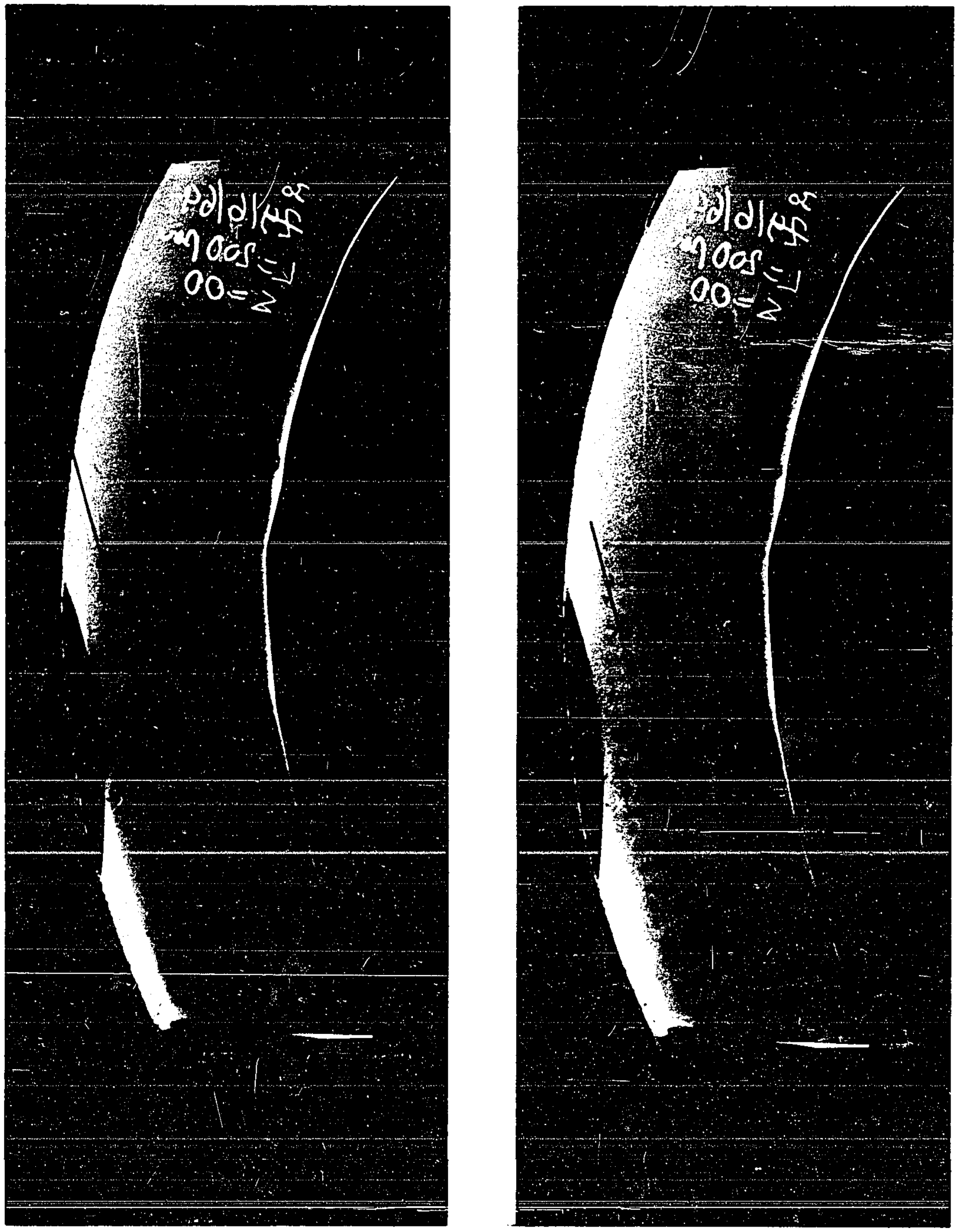

FIG. 86.

Contact Prints of a Transaxial View
of a Loaded Supercalender Nip.

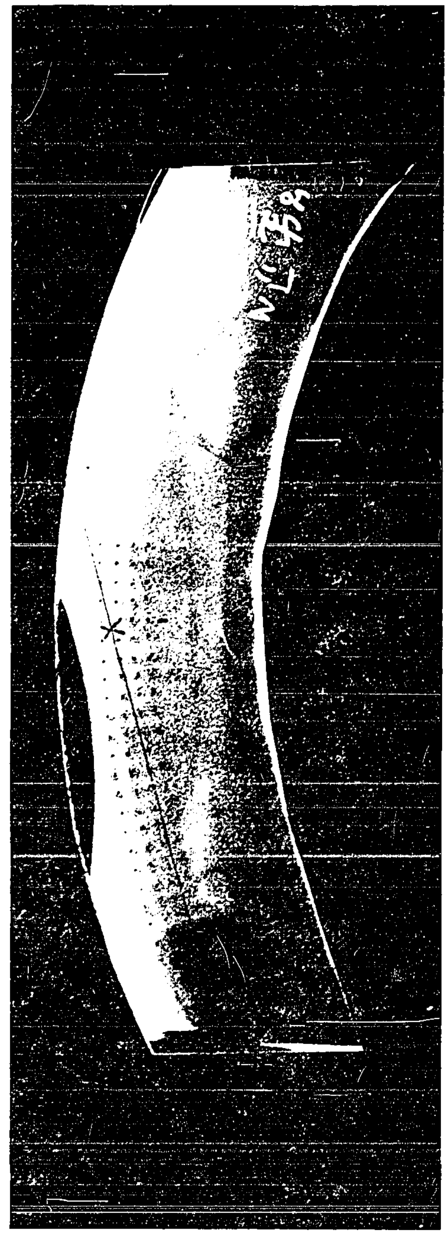

On the other hand images of the reference object and spheres at greater depth which were X-rayed through a greater thickness of intervening fill material are more clearly defined at the shorter exposure which produces the lighter prints. As can be seen on this pair of prints, of the 155 sphere, dense pattern, the centre of each sphere image was marked with an ink spot. Positions of sphere images in the four rows nearest the roll surface were measured. Images at the fifth level were in all cases not sufficiently well defined and those at even greater depth were not visible. The image of length D_4 of the reference object, a 1/16in. diameter by 1 1/2in. long tungsten rod used to correct the tracer image coordinates, is visible in Fig. 86, faintly, within the dark major sector which is the image of the plastic block containing the reference object as shown in Fig. 85. Also visible in Fig. 86 are a projection of a sector of the steel roll and a faint projection of the filled roll surface. It should be noted that these roll surface images do not show their true arc of contact because they do not represent the surfaces at a common transaxial plane. They are, as shown as A and B in Fig. 55, projections of those portions of the roll surfaces nearest the X-ray source. Because the cylindrical edge of the steel roll is nearer the source than is the bevelled edge of the filled roll, the steel surface obscures the true projection of the nip.

2) The location of the X-ray beam centre, i.e. the foot of the

perpendicular from the X-ray source to the film plane, was established separately for each radiogram, at a distance D_5, as shown in Fig. 87, along a line produced through the reference object shadow from its base. It may immediately be seen that

$$D_5 = D_1 D_4/D_3$$

This constructed line and the centre (X) are shown in the prints, Fig. 86.

3) The angular coordinate, measured from the line used to locate the beam centre of each sphere image centre, relative to the X-ray beam centre was measured to 0.2° using a draughting machine protractor. Relative to the same origin the radial coordinate of each image was measured to 0.005in. with micrometer dividers and a machinist's steel rule. Measurements were made on both prints of all negatives.

4) In order to correct for parallax, the position error, D_7 in Fig. 87, was subtracted from each radial measurements. It can be seen that

$$D_7 = D_2 D_6/D_1$$

5) If a coordinate measured on the two prints of the same negative did not agree within 0.01in. the offending image position was remarked and remeasured. If, after this procedure, the error was not resolved, that coordinate was represented by the mean coordinates of the two, three or four immediately adjacent

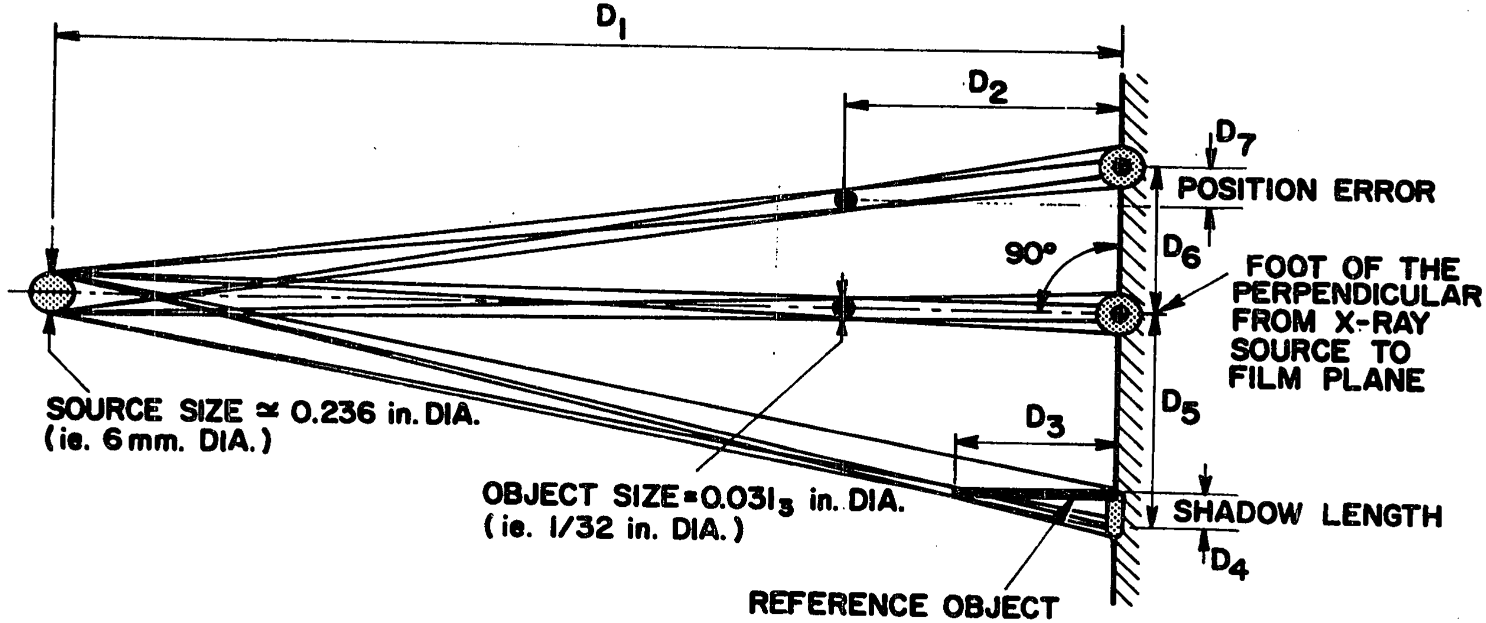

FIG. 87.

Tracer Image Parallax and Its Correction.

images. Measurements within the required tolerances were represented by the mean coordinates of the image on two prints of the same negative.

6) The coordinates of theoretically perfect polar grids, as described in Fig. 54, were taken as datum or a condition of zero deformation. The actual sphere patterns were located to within the limiting accuracy of the measuring technique, i.e. ± 0.005in. as described in 3). Polaroid X-ray prints of these patterns were taken before the card was placed in the filled roll during its manufacture. Measurements of sphere coordinates obtained from these prints fit the theoretical pattern to within 0.010in. as required in 5). However, in the absence of X-ray film negatives which would have permitted a two-print measurement it is felt that the perfect-pattern is the best available representation of the undeformed state of the roll. In this regard it should be noted that none of the X-ray negatives subsequently obtained at no-load could provide a satisfactory datum. The first was not taken until after roll E had undergone low speed rolling friction measurements and reveals, along with the others, that the roll sustained irrecoverable deformations which were different in all cases. It was felt that to adopt a number of so-called datum distributions would be confusing if not meaningless.

7) Cartesian components of circumferential and radial displacements were calculated by a least squares fit of the deformed patterns to the datum. Thus estimates of the minimum displacement at 92 points within the dense pattern and at 18 points within the T-shaped pattern were obtained for each radiogram. These are shown graphically, for both patterns at the highest load of 1400 pli. and at 0, 6.5 and 62 fpm., in Figs. 88-89. The datum tracer positions appear as (+) in the dotted fields while the measured tracer positions are marked (*). Line and character spacings represent 0.01in. and define a cartesian field about each datum position which is shown to scale; i.e. the radial and circumferential components of the displacement vector between any given tracer sphere and its datum are represented in 0.01in. increments where this increment is the distance between adjacent dots. Note that the datum tracer positions are not plotted to scale, the circular curvature of the tracer tiers is not shown and dimensional continuity is broken at the field boundaries (=). The relative position of adjacent spheres has been preserved, however, as well as the general shape of the two patterns. Thus by examining Figs. 88-89 one can obtain a qualitative impression of the exaggerated deformation field within the filled roll in the nip region.

8) For displacement fields obtained from all radiograms the numerical differences between displacements of adjacent

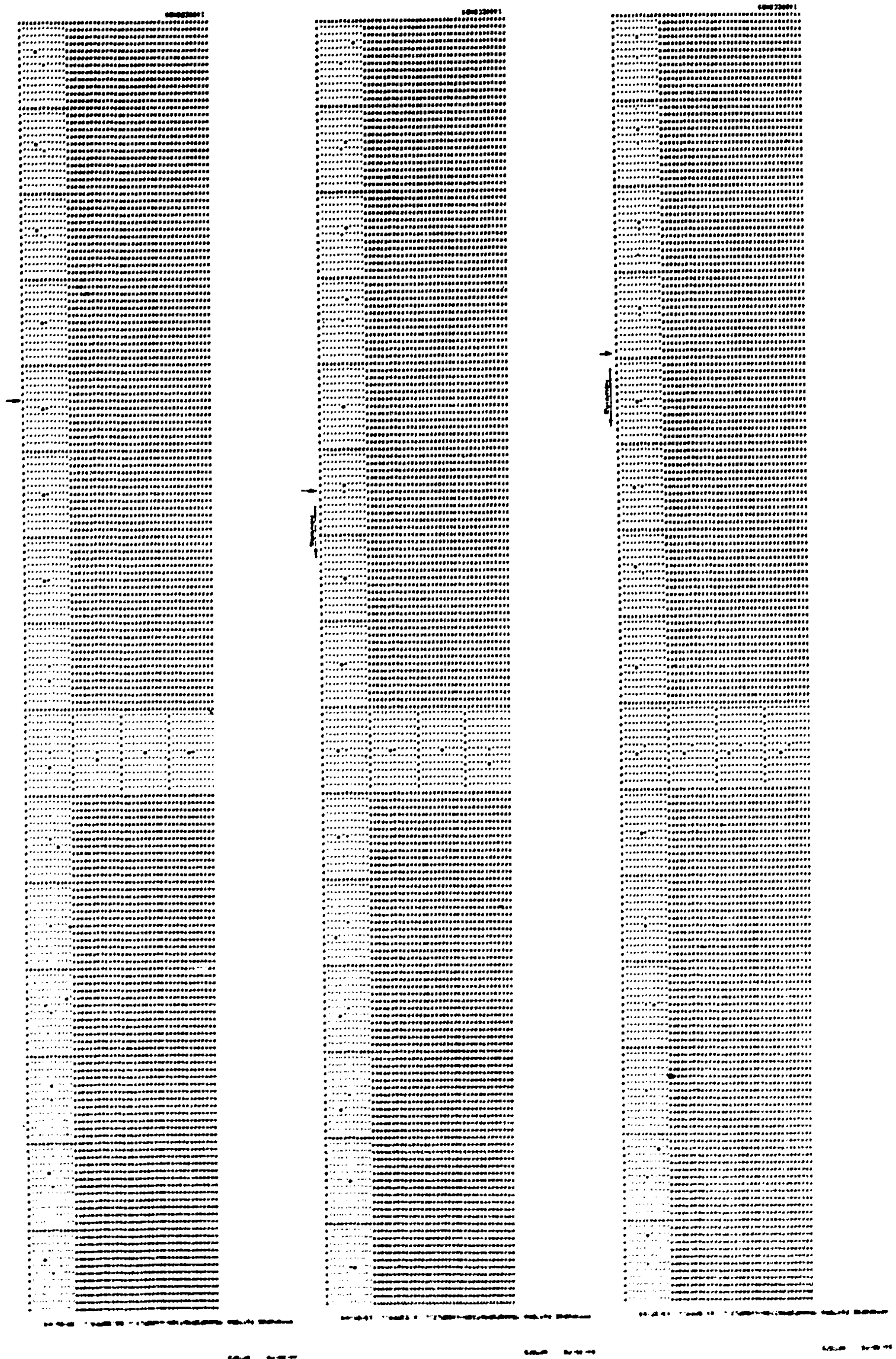

FIG. 88.
Tracer Displacements in Sparse Array.

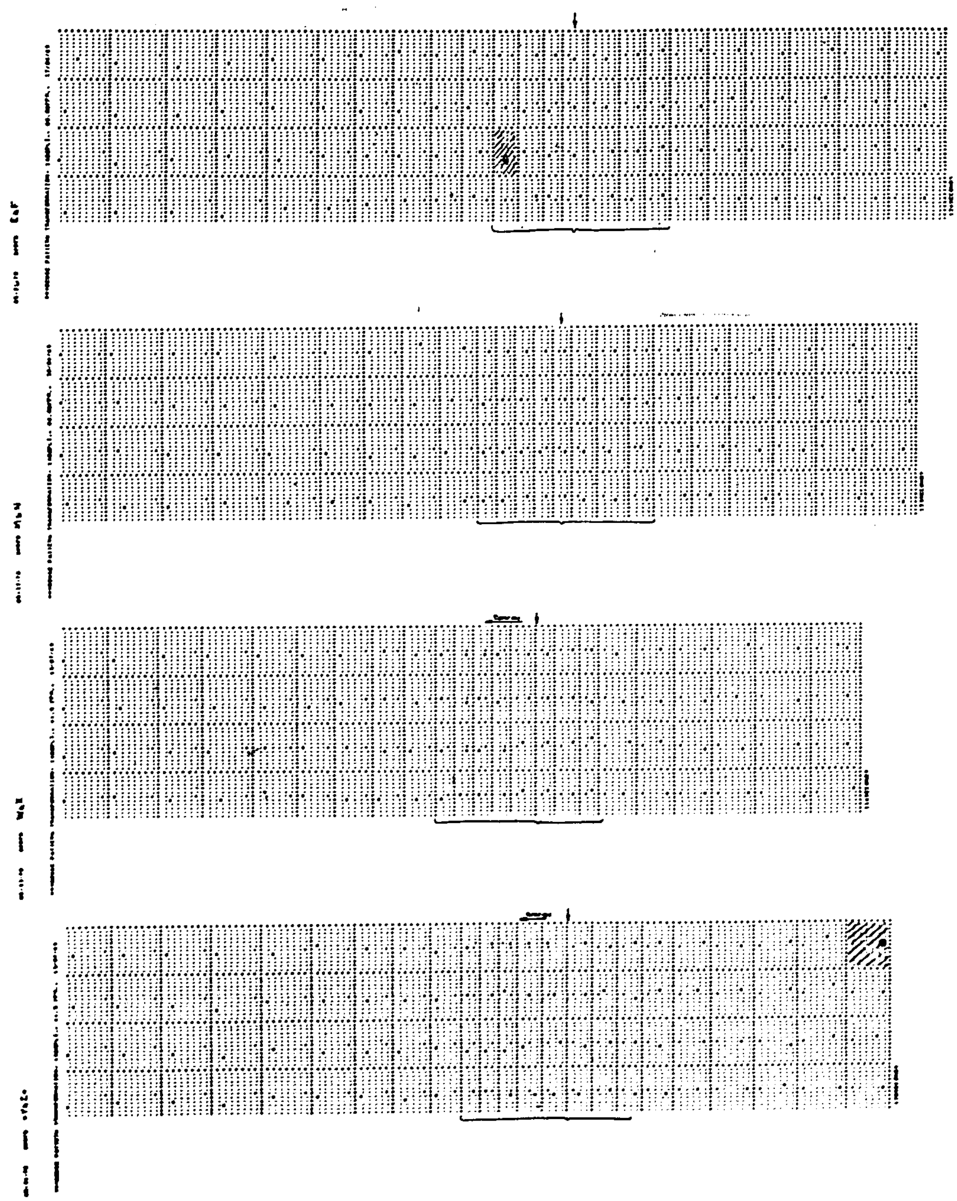

FIG. 89.

Tracer Displacements in Dense Array.

images from datum were calculated to give, as shown in Fig. 90:-

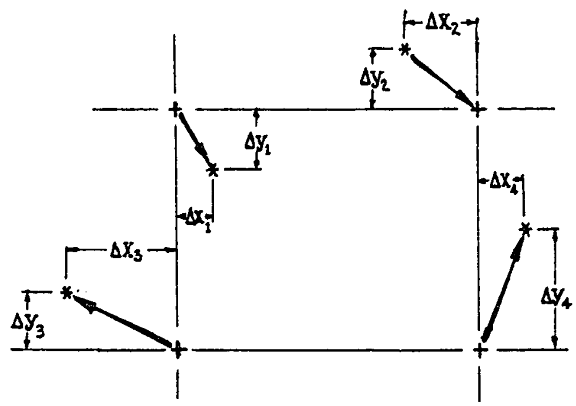

FIG. 90.

Relative position of four adjacent tracers, 1 , 2 , 3 , and 4 . Datum positions are shown (+), actual positions are shown (*) and the displacement vectors are shown (⟶). Circumferential and radial components of these vectors are dimensioned Δx_i and Δy_i respectively.

(a) Differences in circumferential displacement in the circumferential direction: e.g.

$DXX_{12} = \Delta x_2 - \Delta x_1$ and $DXX_{34} = \Delta x_4 - \Delta x_3$.

(b) Differences in circumferential displacement in the radial direction: e.g.

$DXY_{13} = \Delta x_1 - \Delta x_3$ and $DXY_{24} = \Delta x_2 - \Delta x_4$.

(c) Differences in radial displacement in the radial direction: e.g.

$DYY_{13} = \Delta y_1 - \Delta y_3$ and $DYY_{24} = \Delta y_2 - \Delta y_4$.

(d) Differences in radial displacement in the circumferential direction: e.g.

$DYX_{12} = \Delta y_2 - \Delta y_1$ and $DYX_{34} = \Delta y_4 - \Delta y_3$.

These differences are proportional to:-

(a) Finite, circumferential, direct strain,

(b) Finite, circumferential, shear strain,

(c) Finite, radial, direct strain,

(d) Finite, radial, shear strain.

The circumferential strains can be calculated by dividing the displacement differences by the chord length between adjacent spheres at datum. These lengths are 0.103, 0.101, 0.100 and 0.098in. respectively at the first four radii closest to the fill surface. The radial strains are obtained by dividing the relevant displacement differences by the radial increment between adjacent tiers of tracers, i.e. 0.094in.

Figs. 88-89 show the least squares fits of the measured tracer coordinates with respect to the datum pattern. The three diagrams of the T-shaped pattern and the four of the fan-shaped pattern were all obtained from radiograms taken at the maximum nip load of 1400 pli. There is no evidence of radial deformation under the nip, the centre of which is indicated by an arrow at the top edge of each diagram. These patterns of displacement are typical in that none, even those at no-load, show any close approximation to the datum and none, even these at maximum load, show appreciable concave bowing of material under the nip.

In Fig. 91 the displacement differences DXX and DYY are plotted at 1° circumferential increments for the first two tracer tiers and for the radial increments between the first and second and between the second and third tiers respectively. These two series of displacement difference at two depths beneath the fill surface are shown for a sequence of stationary loading in which the load, initially at 0 pli., was increased to 350 pli., then to 1400 pli. and finally decreased to 0 pli. again. It should be noted that the position of the nip is slightly different in the two loaded conditions of 350 and 1400 pli. In any given static test the required load was applied and released completely. When the film cassette was removed between X-ray shots the roll was rotated hard and repositioned in order to avoid permanent surface indentation.

Using the same data, Fig. 92 was constructed in a similar manner to Fig. 91. In Fig. 92, however, the difference between DXX and DYY at 0 and 350 pli., at 350 and 1400 pli. and at 1400 and 0 pli. are shown, representing the change in displacement difference as the filled roll was loaded, then unloaded while stationary.

It can be seen in Figs. 91-92 that the maximum direct strains and the maximum changes in direct strain in both the circumferential and radial directions are of the order of 10-15% and that strains and changes in strain are completely random. No appreciable compressive radial strain can be seen under the nip; neither between the tracer tiers at 3/32 and 3/16in. depth nor between those at 3/16 and 9/32in. Similarly, in Fig. 92, the changes in circumferential and radial displacement difference, i.e. DXX_t and DYY_t, reveal no sequence of deformative events during a loading-unloading sequence.

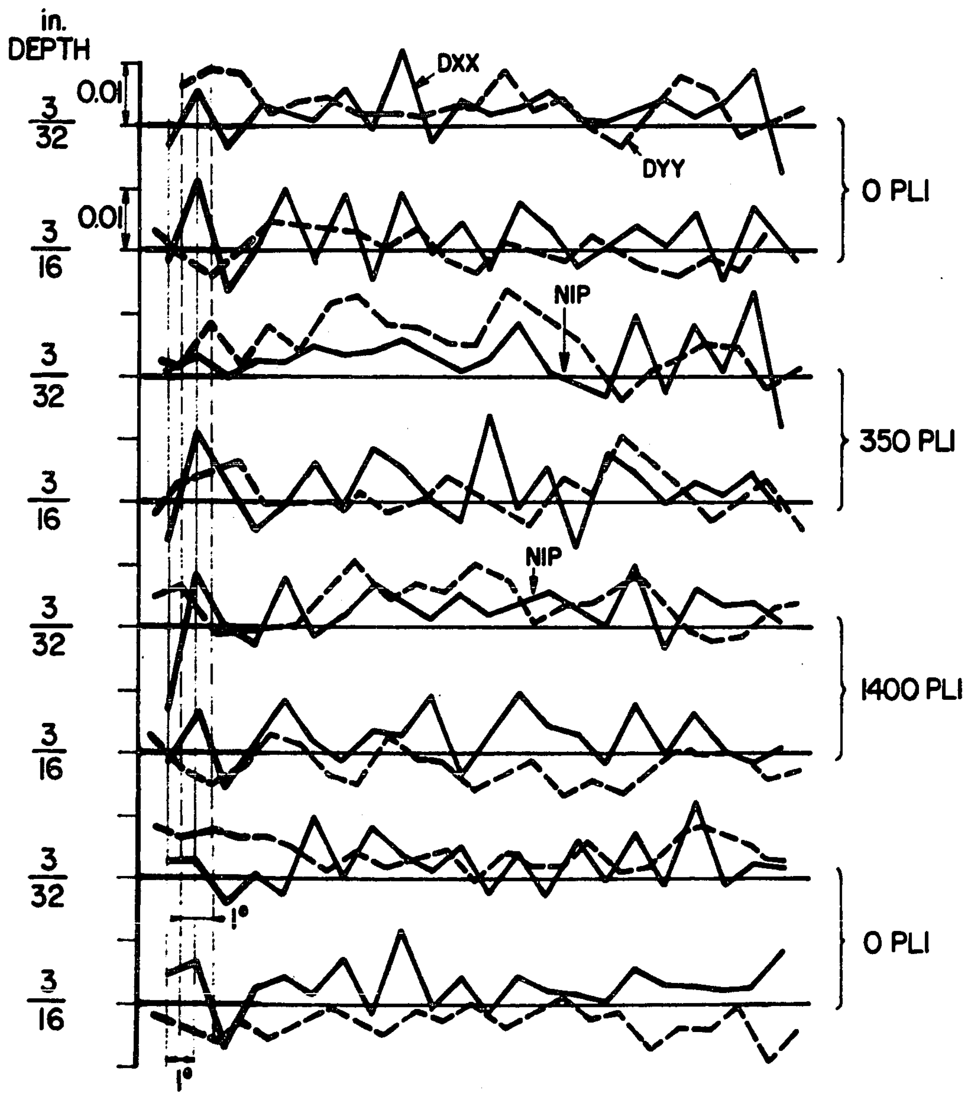

FIG. 91.

Direct circumferential (DXX) and radial (DYY) displacement differences in roll E while stationary.

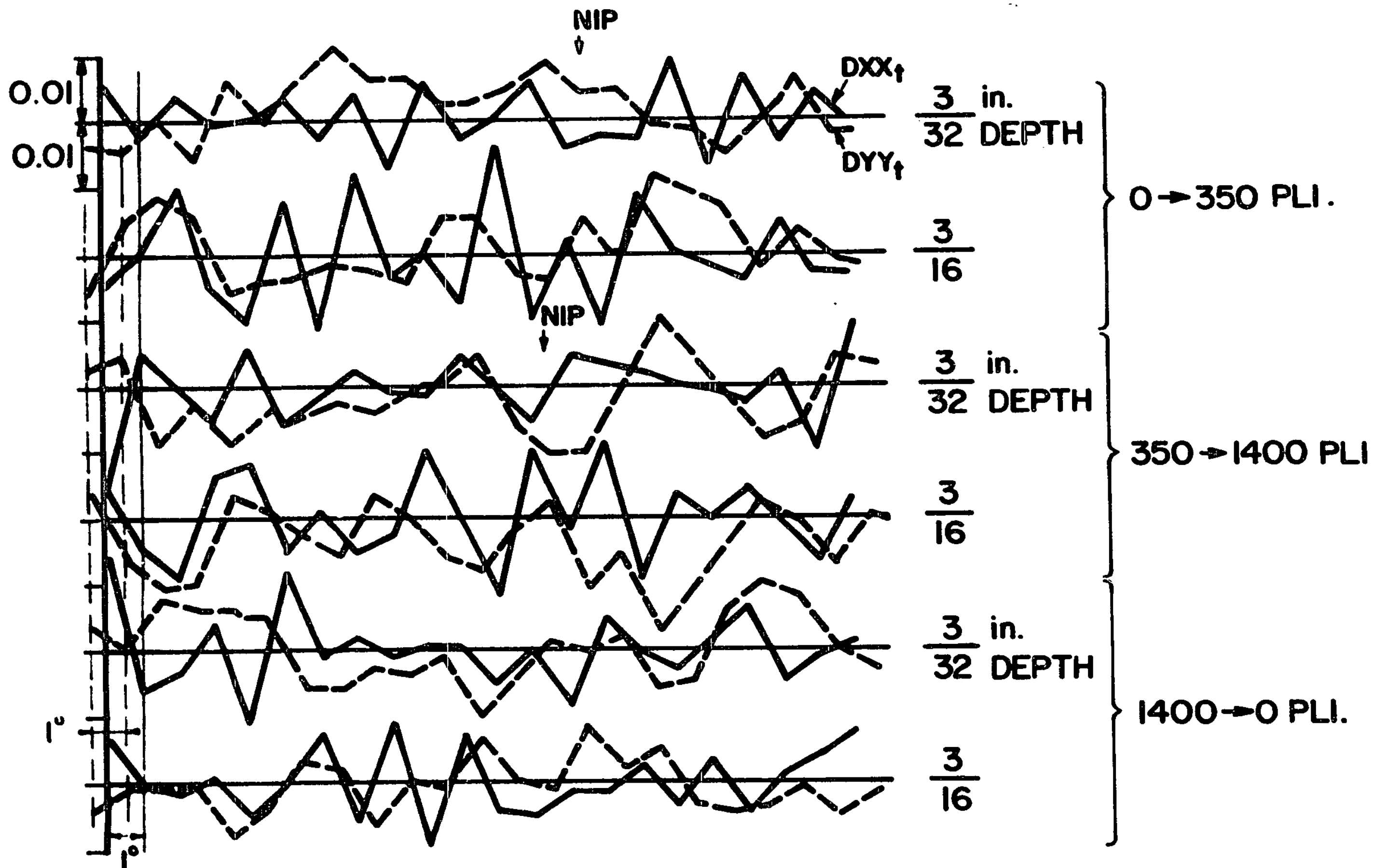

FIG. 92.

Changes in direct circumferential (DXX_t) and radial (DYY_t) displacement difference during a chronological sequence of static loading of roll E.

It would appear that subsurface stresses and strains locked into the roll by axial pressing during manufacture are triggered and redistributed by subsequent nip loading.

It has been pointed out that the load induced strains at all points throughout the fill appear to be entirely random. However, certain general observations concerning large scale non-random deformative behaviour with the fill can be made with regard to the least squares fits of tracer distributions shown in Figs. 88-89.

1) The images of the long circumferential row of tracers in the T-shaped pattern shown in Fig. 88 describe a one-cycle standing wave which suggest an undulatory deformation. These images, taken in sequence from left to right, are successive positions of clockwise rotation about their datum positions and execute a full revolution in the 14° circumferential span of the pattern. Although no radiograms of any single sphere were obtained at successive 1° intervals of roll rotation, every fit diagram, including those at lower load which were not shown, exhibits this undulation but with the attitude or phase angle of any given tracer appreciably different in each diagram, e.g. the tracer at extreme left in the 0 fpm. diagram and that at 6.5 fpm. is at 6 and 2 o'clock, respectively, to datum position. This supports the conclusion that the tracers rotate about their datum position and cause the layer of fill at 3/32in. beneath the roll surface to undulate with

a wave-like motion.

2) The T-shaped patterns show maximum radial displacement in regions remote from the nip. Circumferential displacements show a scattering of possible regions of circumferential stretching and contraction. There is therefore no evidence, in any of the T-shaped patterns, of traction induced strain.

3) The undulatory circulation of fill which was the predominant feature of the T-shaped patterns is not evident in the 4-tier 92 image patterns, i.e. the reduced versions of the fan-shaped array of 155 spheres, because of very small radial excursions at all angles. However, the greatest radial excursions, small as they are, occur far from nip centre and are maximum in the direction of rotation and tractive force exerted upon the filled roll. In the diagram for 0 fpm., i.e. a condition of no traction, these greater radial excursions do not exist.

4) Furthermore, in all 4-tier patterns the material seems to be in circumferential compression under the nip, an unexpected phenomenon since a radially compressed material with a finite and positive Poisson's ratio tends to expand in the circumferential direction.

5) There is a distinct indication that the region of greatest circumferential contraction is slightly downstream of the nip, i.e. in the direction of the transmitted tractive force. This indication is supported by the two diagrams at 0 fpm. In both

the contraction is reasonably symmetrical about the nip centre such as might be expected when there is no traction.

6) In the region of fill where the 4-tier pattern was located the nip kinematics due to deformation may be best described in terms of a combination of effects described by Figs. 3 and 5a-5d except that in the first instance the lateral extension caused by a direct compression under the nip and a positive Poisson's ratio there is an apparent circumferential contraction or negative Poisson's ratio. In the second instance the situation due to tractive strain is one of assymetric circumferential contraction rather than that of assymetric extension depicted in Fig. 5a-d. However, the strain gradient is in the same direction, i.e. circumferential strain increases or becomes more extensive in a direction opposite to tractive force on the surface of the deformable roll. At this position on the roll surface it would appear that the effects due to direct load and traction combine so as to produce a peripheral velocity of the filled roll external to the nip which is less than that of the steel roll. Note that this velocity difference was not measured. It is mentioned here as a concept to relate observed phenomena to the theoretical behaviours described in Figs. 3 and 5. As shown by deformations of the T-shaped pattern this nip condition does not apply to all points on the filled roll surface passing in contact with the steel roll.

CONCLUSIONS

Direct Conclusions

Certain conclusions proceed directly from results obtained in Part I and Part II of this work.

1) Heating of a filled roll which occurs during its operation originates in regions of the fill which are very close to the surface. It is reasonable simplification to assume that all heat is generated on the surface.

2) The effect of rotation of the filled roll, which causes a point on the surface to pass through the nip on successive revolutions, can be adequately simulated by a periodically recurring instantaneous plane heat source in a one-dimensional half-space continuum and the change of temperatures at various depths in the filled roll with time can be approximated by such a one-dimensional model.

3) Certain observations, notably variations in radial temperature distribution with time, and its variation in the axial and circumferential directions, indicate that the heat source is not uniform or constant but has a random distribution which varies with time.

4) Temperature fluctuations within the filled roll, although periodic with each successive revolution of the filled roll, do not conform to the sudden rise and exponential decay of temperature suggested by a one-dimensional instantaneous source continuum model.

5) The measurement of transient temperature within a filled roll is complicated by the possibility that a thermoelectric junction is affected by stress transients.

6) The one-dimensional continuum model with a high rate of surface cooling describes a radial temperature distribution which is compatible with the radial distribution of discolouration in a typical cross-section of a filled roll which has been charred.

7) Measurements of rolling friction of a supercalender nip, at typical and at very low speeds of operation, confirm the conclusion put forward by Malmstrom and Nash (16) that the energy dissipated in a supercalender nip is approximately proportional to $\sqrt{P^3}$, where P is nip load per unit axial length of contact between rolls.

8) Irreproducibility of rolling friction measurements at high speed and irreproducible fluctuations in rolling friction at low speed support the observations of non-uniform, randomly varying heat source distribution and suggest random deformations of the filled roll.

9) Hardness and profile measurements of the surface of five filled rolls reveal a highly irregular, random distribution of hardness and radial differences and there is indication that these surface features are altered by operation. This is further evidence that filled rolls undergo random deformations in the course of operation.

10) Conclusive evidence of random strain within a filled roll was obtained from X-rays of small metal objects embedded in a specific transaxial plane of a filled roll by measuring the displacements sustained by these objects as they passed under a loaded nip at various speeds.

11) The random nature of filled roll deformation was emphasized by the fact that rolling friction could not be related to speed or temperature nor to filled roll hardness or variations in surface profile. Deformations in the transaxial plane of a filled roll showed no systematic variation with load or speed.

12) Deformations within a transaxial plane of a filled roll indicated

    a) undulating displacements at some distance from the nip which were larger in the direction of applied tractive force,

    b) circumferential contraction under the nip as if the material had a Poisson's ratio < 0,

    c) circumferential contraction gradient in the direction of applied tractive force.

<u>Suggested Hypothetical Mechanism of Energy Dissipation</u>

Certain conclusions, based somewhat on indirect evidence and somewhat on conjecture, may be presented by way of the two following hypotheses. Although these cannot be put forth with the same certainty and authority as those preceding they are by far the most exciting. It is strongly held that they outline the path for further study of supercalendering mechanisms.

Consider that torsion is one way in which maximum strain energy, hence energy dissipation, may be produced at the surface of a cylindrical body. A dimensionally random collection of rigid circular elements in traction with a rigid cylinder and connected with slight eccentricity to torsionally flexible tubes or cylinders might conceivably be a valid mechanical approximation of a filled roll, with variations in surface hardness and radius, in rolling contact with a rigid steel roll. The fundamental or primitive element of such a collection might be represented by a pair of tractive circular discs of equal radius, one concentric with, the other slightly eccentric to connecting flexible cylindrical components. Suppose that the circular discs are in contact with a rigid cylinder and the axis of the coupled disc assembly is constrained to be at all times coplanar with the axis of the rigid cylinder. Such an element is shown in Fig. 93.

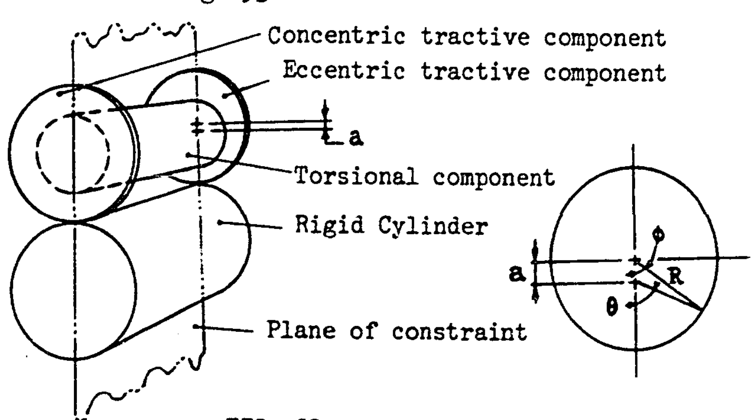

FIG. 93.

An Elementary Mechanism of Torsional Strain Energy Dissipation.

The radius of the discs is R and the eccentricity is a. It can be seen that elements will rotate, under the assumed constraint, against the rigid cylinder so that the angle of rotation of the concentric disc is ϕ and of the eccentric disc is θ. If an initial position with $\theta = \phi = 0°$ is assumed the angle of twist, $(\theta - \phi)$, in the torsionally flexible coupling is given in terms of its angle of rotation, ϕ, at the end of the concentric disc as

$$(\theta - \phi) = \left\{ \tan^{-1} \left(\frac{\sin \phi}{\cos \phi - (a/R)} \right) \right\} - \phi$$

For small eccentricity, a, this is very nearly a sinusoidal variation of $(\theta - \phi)$ with ϕ. Although this mechanism will produce a distribution of energy dissipation, hence heat source strength, which varies directly with radius and a maximum will occur at the surface it must be at first glance subject to some skepticism. This mechanism suggests a circumferentially uniform rate of dissipation. Recall that the one dimensional thermal model which successfully simulates the thermal behaviour of a filled roll was derived as an approximation of a rotating axial line source which, at any point in the fill, would in passing cause a steep increase in temperature followed by an exponential decay continuing until the next revolution when the process would be repeated. This source distribution is anything but circumferentially uniform. However, the instantaneous periodic plane source, which was chosen as a valid approximation because it was intuitively felt that thermal gradients in all but the radial direction could be ignored, does, inadvertantly, satisfy the conditions of periodicity and uniformity. It may thus be seen that the one dimensional model, used to simulate the heating up of a filled roll, approximates the heating due to torsional strain energy dissipation as well as it does the intuitively more plausible rotating axial line source. In addition, the continuous temperature signals measured with an oscilloscope during successive revolutions of the filled roll and shown in Figs. 36a-b and 37a are sinusoidal except for small negative perturbations. Thus the torsional hypothesis is supported by direct experimental evidence as well as indirectly by temperature, hardness and profile measurements and by the preceding theoretical argument.

Certain observations support the existence of another mechanism which would produce surface dissipation. The microscopic examination of a filled roll surface indicated that fill fibres, originally laid down in random transaxial directions, on the surface are pressed into a glossy mat with predominantly circumferential orientation as shown in Fig. 48. It may be considered that these fibres form a stiff surface layer or skin of somewhat higher density than and discontinuous with the underlying fill. It is suspected that such a skin, subject to axial line loading and supported on a softer substrate, would buckle into outwardly convex ridges parallel to and some distance from the nip line. In the absence of traction this wrinkling would be symmetrical about the nip but under the influence of a tractive force the wrinkles on the ingoing side of the nip would be attenuated under the influence of tension. On the downstream side of the nip the wrinkles would tend to be exaggerated by compression. A travelling wave would account for energy dissipation through the flexure of the skin. The phenomenon illustrated in Fig. 38a is consistent with the above hypothesis. There are two temperature peaks about 90° apart. If these are equidistant from the nip they lie 45° on either side, a plausible location for primary buckling in a tube loaded by an axial line force. The waveform shown in Fig. 38a is an observation obtained with a single thermocouple located at 3/32in. below the roll surface and is thus somewhat unique. However, it contains another piece of evidence which is consistent with skin buckling. The first peaks, i.e. those on the left, are somewhat lower than the second thus supporting the observation that dissipation on the upstream side of the nip would be attenuated by tractive tension while that on the outgoing side would be enhanced by tractive compression. Furthermore, evidence of deformations in the fill shown in Figs. 87-88 indicated that maximum deformation occurs some distance from the nip and on the outgoing side.

Claims of Original Contribution

1) A theoretical thermal model which takes into account rotation of the filled roll has been developed which adequately describes its heating behaviour.

2) Through the measurement of temperature, rolling friction, deformation and surface hardness and profile of filled rolls it has been conclusively demonstrated that the rolling behaviour of a supercalender nip involve strains within

the filled roll which are predominantly random and thus, over a finite time span and a finite number of experiments, largely irreproducible.

3) Certain techniques of high speed X-radiography were extended to study dynamic deformations in supercalender filled rolls.

4) Three hypothetical mechanisms have been put forth to account for rolling friction in random, inhomogeneous and discontinuous bodies such as a supercalender filled roll:

   a) irreversible compression or pumping of entrapped gas,

   b) axial torsion of fill due to random irregularities,

   c) instability under nip load of a dense skin.

Topics for Further Study

1) The application of a scanning thermographic instrument, e.g. "AGA - Thermovision" (36), to accurately map the development of surface temperature distribution as a filled roll.

2) The measurement of temperature and deformation, by techniques described herein, of a filled roll composed of a monolithic annulus of synthetic plastic to determine to what extent random and irreproducible behaviour is due to conventional fibrous fill materials and to the filled roll manufacturing process.

3) The investigation of stress produced effects in thermoelectric junctions.

4) The development of a reliable and accurate high speed measurement technique to study temperature transients in filled rolls and the short-term fluctuations in supercalendering function losses.

5) A dynamic measurement of filled roll surface profile to detect the existence of possible wrinkling of the filled roll surface produced by traction and nip loading, e.g. by using a proximity sensor such as described in (37).

6) The application of high speed ciné-photography to detect possible regions of torsional deformation of a filled roll surface produced by variations in roll radius.

7) Investigation, using Eldredge's apparatus (38), of rolling friction of a steel sphere pressed against samples of compressed fill material in order to determine local friction coefficient and the effect of temperature and humidity thereon.

8) Development of hydrostatic bearing dynamometers, for installation on each of the stack bearings, whose output signals could be electronically summed and subtracted from the signal of the drive torque measuring instrument. This difference would provide a direct measurement of the mechanical losses in the nip.

BIBLIOGRAPHY

1. Mardon, J., Delisle, J.C. and Monahan, R.E. "The Change in Paper Properties by Supercalendering", Norsk Skogindustri (Euceda/Study Group Konferanse, 1966), March 1965, pp. 112-118.

2. Anon. "Supercalender Operation: A Review of Problems and Solutions", Paper Trade J. 147, (49): 41-43 (1963).

3. Gavelin, G. "New Developments in Coating and Supercalendering in Sweden", Paper Trade J. 153, (31): 34-37 (1969).

4. Anon. "Calendering and Supercalendering" pub: Lockwood Trade J. Co. Inc., 1964.

5. Anon. "How the Supercalender Operates and What it Does", Paper Trade J. 147, (52): 29-34 (1963).

6. Schiller, F.E. "How to Operate a Supercalender Particularly on Coated Papers", Paper Trade J. 144, 28-33 (1960).

7. Schiller, F.E. "Supercalendering Coated Papers is One of the Important Finishing Operations", Paper Trade J. 144, 24-28 (1960).

8. Martinek, R.W. "Swimming Roll Applications for Calendering Fine Papers", Paper Industry, 46, (8): 740-741 (1964).

9. Cooper, E.W.G. "Calender Operation", Appita Proceedings, 1953 pp. 24-53.

10. Schoonkind, G.A. "Fundamentals of Calendering", The Paper Industry and Paper World, 28, (10): 1443-1446 (1947).

11. Schacht, W. and Kirchner, E. "Mechanism of the Supercalender", Wochenblatt fur Papierfabrikation, 42, (23): 2109-2112 (1911).

12. Mackin, G.E., Keller, E.L. and Baird, P.K. "Effect of Calendering Pressure on Sheet Properties", Paper Trade J. 113, (5): 53-61 (1941).

13. Van den Akker, J.A. "The Possible Role of Shear in Calendering", The Paper Industry and Paper World", 28, (1): 57-59 (1946).

14. Bridgeman, P.W. "Effects of High Shearing Stress Combined with High Hydrostatic Pressure", Phys. Review, 48, (10): 825-847 (1935).

15. Parish, G.J. "Apparent Slip Between Metal and Rubber-Covered Pressure Rollers", Brit. J. Appl. Phys. 9, 428-433 (1958).

16. Malmstrom, H.E. and Nash, J.P. "Elastic Theory of Nip Stress and Hysteresis Effect", Tappi, 37, (12): 654-661 (1954).

17. Larsson, K.O. and Gregersen, A. "Temperature Build-up in Filled Supercalender Rolls: Its Nature and Possible Elimination", Paper Trade J. 149, (33): 39-41 (1965).

18. Mack, H. and Schlegel, P. "Investigations of the Glazing Process in Supercalendering", Das Papier, 16, (7): 277-285 (1962).

19. Leporte, L.E. "Analysis of Interfacial Shear Strain in the Supercalender Nip", Tappi, 50, (7): 357-362 (1967).

20. Peel, J.D. and Hudson, F.L. "Application of Elasticity Theory to a Supercalender Nip", Paper Technology, 7, (5): 460-470 (T164-T174) (1966).

21. Pfeiffer, J.D. "The Finishing Action of a Supercalender Nip", (Preprint of a paper submitted at Tappi Fall Finishing Conference, October 1970).

22. Peel, J.D. (Private communication)

23. Hertz, H. "On the Contact of Elastic Solids", J. fur die reine und angewandte Mathematik, 92, 156-171 (1881).

24. Hertz, H. "On the Contact of Rigid Elastic Solids and on Hardness", Verhandlungen des Vereins zur Beforderung des Gewerbeffleisses, November, 1882.

25. Carter, F.W. "On the Action of Locomotive Driving Wheel", Proceedings of the Royal Society of London, Series A, 112, 151-157 (1926).

26. Poritsky, H. "Stresses and Deflections of Cylindrical Bodies in Contact with Application to Contact of Gears and of Locomotive Wheels" J. Appl. Mech. 17, 191-201 (1950).

27. Morland, L.W. "Rolling Contact Between Dissimilar Cylinders", J. Appl. Mech. 25, (4): 363-376 (1958).

28. Morland, L.W. "Exact Solution for Rolling Contact Between Viscoelastic Cylinders", Quart. J. Mech. & Appl. Math. 20, part 1, 73-106 (1967).

29. Harris, T.A. "Rolling Bearing Analysis, Chap. 14: Friction in Rolling Bearings", John Wiley & Sons 1966, pp. 421-451.

30. Palmgren, A. "Ball and Roller Bearing Engineering", SKF, 3rd Ed. 1959, pp. 34-41.

31. Carslaw, H.S. and Jaeger, J.C. "Conduction of Heat in Solids", Oxford University Press, 2nd Ed. 1960, pp. 358-359 and Appendix VI.

32. Eckert, E.R.C. and Drake, R.M. Jr., "Heat and Mass Transfer", McGraw Hill, 2nd Ed. 1959, p. 508

33. Ardonox Radiation Pyrometer, Instructions for Installation and Operation, Cal A 0302e, Siemens Measuring Instruments, Karlsruhe, Germany.

34. Beloit Rho-Meter Maintenance Manual RM-002-0 (1966), Beloit Eastern Corporation, Downington, Pa. 19335.

35. Kilmartin, J., Wheeler Roll Company, (Private communication).

36. Agronin, T., Appleton Machine Company, (Private Communication).

37. AGA Thermovision Models 661, 665 and 669 infrared cameras for live presentation of temperature distribution and development in fixed or moving objects, AGA Infrared Instruments Department, S-181 20 Lidingö, Sweden. (AGAtronics Ltd., 41 Horner Avenue, Unit 5, Toronto 18, Ont.)

38. Photonic Sensor Operating Instructions, Model KD-45, M.T.I., Latham, New York.

39. Eldredge, K.R. and Tabor, D. "The Mechanism of Rolling Friction: I. Plastic Range", Proceedings of the Royal Society, 1954, A 229, pp. 181-198.

40. Model DY-2010B Data Acquisition System Operating and Service Manual, 1-2, (June 1964), Hewlett-Packard Dymec Division, 395 Page Mill Road, Palo Alto, Calif., U.S.A.

41. GEPAC-4000 Process Fortran Language: PCP-122 (1969) General Electric Company, Process Computer Department, Phoenix, Ariz. U.S.A.

42. GEPAC-4000 Free Time System Manual: PCP-117.

43. GEPAC-4020 Programming Manual: GET-3471A.

44. Instruction Manual, Fexitron Flash X-ray System Model 730 Series, Field Emission Corporation, 611, 3rd Street, McMinnville, Ore., U.S.A.

45. Bentall, R.H. and Johnson, K.L. "Slip in the Rolling Contact of Two Dissimilar Elastic Rollers", International Journal of Mechanical Science, 9, 389-404 (1967).

46. Greenwood, J.A., Minshall, H. and Tabor, D. "Hysteresis Losses in Rolling and Sliding Friction", Proceedings of the Royal Society of London, Series A, 259, 480-507 (1961).

APPENDIX I

Data Logging and Signal Conditioning Instrumentation

Some tests in the supercalendering experimental program involved reading up to fortyeight separate measuring instruments for test durations of over six hours. At times, due to rapidly changing conditions, certain specific measurements had to be carried out as often as five times per second. Transducer outputs included analogue signals of D.C. voltage of various levels as well as signals of variable frequency. The voltage signals required full scale ranges of 0.010 v. to 10 v. Frequency signals were from 50 Hz. to 1200 Hz. At times it was desirable to resolve voltage changes of less than 0.5×10^{-6} v. and frequency changes of 1 Hz. Often it was necessary to determine to within 1 second the actual time at which all readings, in a sequence of hundreds of measurements, were made. Surrounding the tests with different types of special indicating and analogue recording instruments seemed to pose an impossibly tedious data gathering problem. Some readings would have to be hand logged, recording instrument outputs would have to be synchronized so that all readings could be identified as to the exact time when they were taken. All readings would have to be digitally transcribed on a common log sheet along with a running time scale so that data reduction calculations could be carried out. It would be impossible to record some rapidly varying readings at a sufficiently high sampling rate with conventional potentiometric instruments. Multichannel, high impedance oscillographic instruments, providing sufficient amplitude required for measurement accuracy, would produce considerable trace cross-over so as to pose further inconvenience in data reduction. A careful study of experimental requirements and available measuring equipment specifications resulted in the choice of a high speed integrated system with fifty analogue signal input channels and an analogue-to-digital converter with both digital and analogue recording capabilities.

This data logging system (40) is shown, with the various módular components identified, in Fig.94. A brief description of individual component functions and specifications will be presented.

The uppermost unit is the digital clock which accumulates time in hours, minutes and seconds in 24 hour cycles. Front panel display is provided by six "Nixie" digital display tubes. Time is also presented electrically as a six digit binary coded decimal signal for recording on punched paper tape via the tape punch coupler or directly on the digital recorder. A train of variable frequency pulses is generated for reading initiation, synchronization and control in real time. This control pulse frequency can be selected via five front panel push-buttons to provide pulses at 1 second, 10 second, 1 minute, 10 minute and 1 hour intervals. Time hold logic provides for a delay of up to 0.9998 seconds in time signal output so that the time record output will not interfere with the recording of measurement readings which may be in progress. This delay will not result in an internal time error; the clock will remain on time in spite of it. The basic clock intervals can be generated either by an external 100 kHz. crystal oscillator or by 60 Hz. line frequency and the clock will be, at all times, within 1 second of the time represented by the accumulated periods of oscillation. In case of power failure or setting error, the clock can be reset to the correct time of day by setting up the desired time on six thumb-wheel switches and depressing

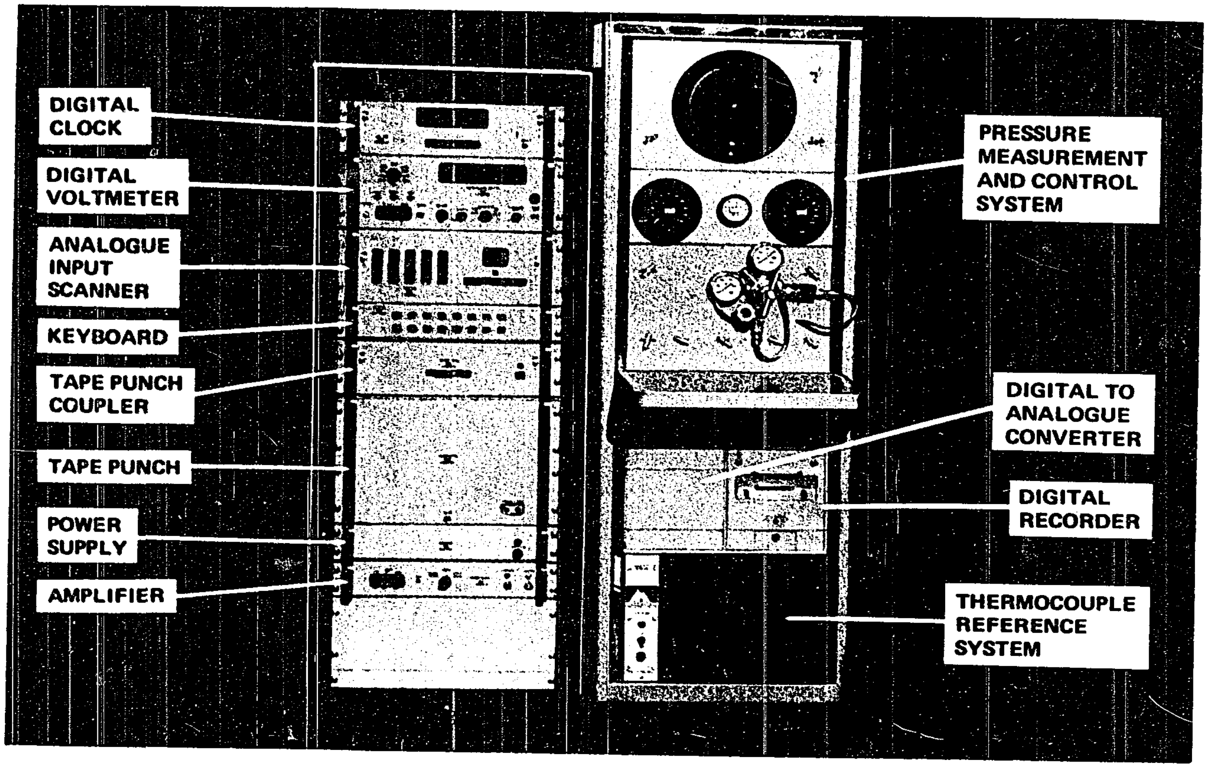

FIG. 94.

Data Logging and Signal Conditioning Instrumentation.

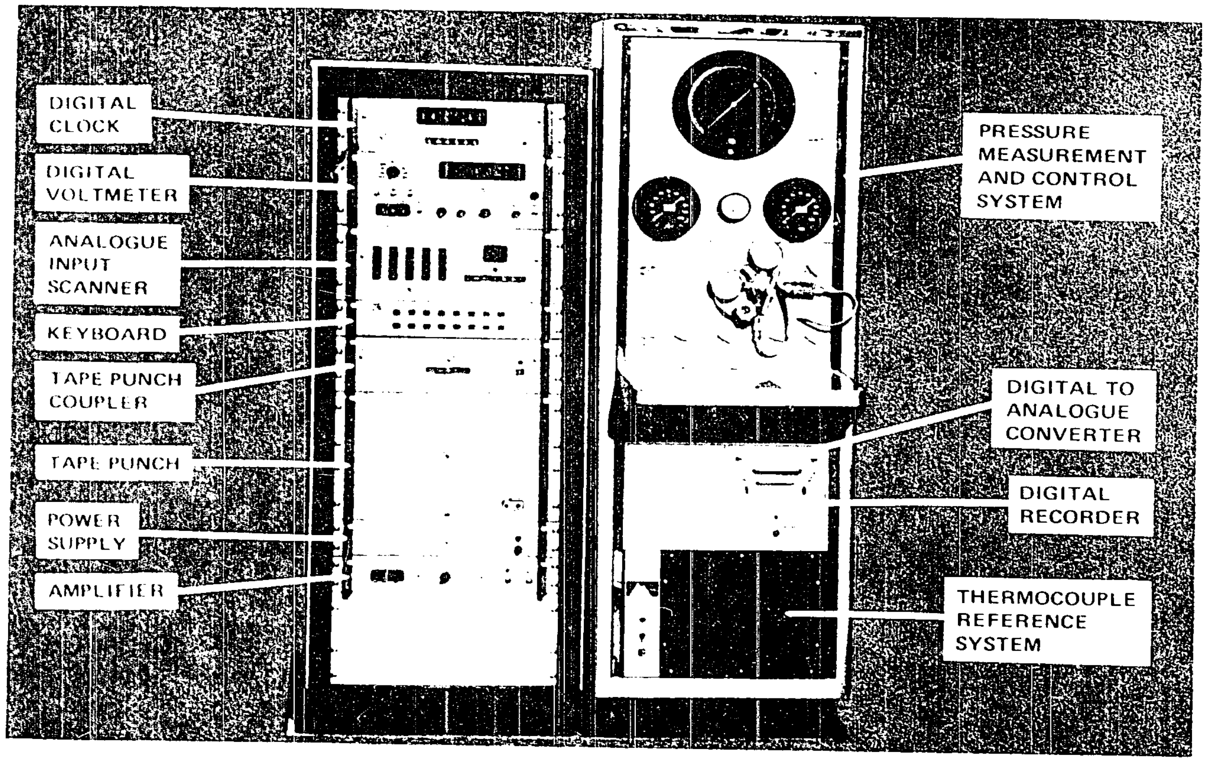

FIG. 94.

Data Logging and Signal Conditioning Instrumentation.

the time reset button when the actual time corresponds to the preset switch reading. Any time error due to power failure or clock malfunction is indicated by the illuminated time error pilot lamp. Time signals transmitted to either the paper tape punch or digital printer include an extra binary coded decimal digit "8" which is interpreted as the character "T" to identify a time entry on either paper tape or print out.

All measurements are made by a true integrating digital voltmeter which, through a precision attenuator, accepts full scale D.C. voltage signals of ± 1000 v., 100 v., 10 v., 1 v. and 0.1 v. Frequencies from 5 Hz to 300 kHz. can also be measured. The measurement is visible on a six digit "Nixie" tube front panel display which also indicates the location of the decimal point, sign (+ or -) and mode (voltage or frequency) of the reading. Voltage conversions are made by a stable, linear voltage-to-frequency converter. Frequency measurements bypass the V-F converter and are routed directly into the counter. To arrive at the digital value of a reading the frequency signal, either from the V-F converter or directly from a frequency producing transducer, is counted for one of three selectable sample periods (viz. 0.01, 0.1 or 1 sec.). The sample periods are provided by decade division of the output of a 100 kHz. reference oscillator. This oscillator also serves as the external clock frequency previously mentioned. The counter will either accumulate or decrement depending on the polarity of an input voltage signal. The frequency produced by the V-F converter is proportional to the instantaneous value of the input voltage which it represents. As the frequency has no polarity, the V-F converter also supplies the counter with a logic signal which identifies the instantaneous polarity of the incoming signal voltage causing the counter to either add or subtract the pulses according to signal polarity. A true algebraic average of the input voltage over the sample period is thus produced. Thus a signal which has passed through zero, once or many times, during the measurement sample period will result in a reading which is the modular difference, with correct sign appended, between the positive and negative portions of the voltage-time integral divided by the sample time period magnitude. The voltmeter is designed to minimize voltage measurement errors due to extraneous noise. With the guarded data amplifier and shielded and guarded analogue signal lines, changes in instrument readings as small as 0.5×10^{-6} v. can be reliably resolved. The digital voltmeter is overload protected so that even a 1000 v. signal applied to the lowest measuring range will cause no damage. On all measuring ranges except the highest, a 300% overranging capability is provided. This improves measurement accuracy. For example, a voltage of up to 3 v. can be measured on the 1 v. full scale range giving one more significant digit than would be available on the next, i.e. 10 v., range. The selection of mode (i.e. voltage or frequency), range (i.e. 1000 v. to 0.1 v. D.C.) and integration times (i.e. 0.01, 0.1 and 1 second) is externally programmable on all readings via simple contact closures.

The analogue scanner provides the means by which a sequence of readings can be carried out. With the addition of a slave scanner, which expands the number of instrument transducers which can be simultaneously connected to the system, up to 50 sequential readings can be made in a measurement cycle. This cycle may be initiated either by operator demand or by a control pulse from the digital clock. In this way logging can take place manually or at specific intervals over a long period of time, unattended. The depression of any of the self latching channel buttons on the scanner front panel will include in the scan cycle any channel corresponding to a depressed button. As the scan cycle proceeds, the number of the channel which is connected to the digital voltmeter at a given instant is displayed on the two digit "Nixie" tube window in the front panel of the master scanner module. A plugboard matrix in each scanner module permits the selection or programming of mode, range, integration period and settling time on each measurement channel addressed by that module. The provision of a settling time is a feature which is important when switching analogue signals. By this means a selectable delay of 30, 60, 120 or 910 msec. can be invoked, after a given transducer has been connected to the digital voltmeter via the input scanner, to allot time for the stabilization of switching transients which would incur measurement error if included in the time integral. With the incorporation of the settling time feature this interval must elapse before the counter in the digital voltmeter is activated and the actual measurement begins.

The keyboard permits manual entry of data on punched paper tape.

Data records on tape can thus be prefixed or suffixed by record identification and tape processing information. The 16 keys include the numerals 0 through 9, "space", "stop", "carriage return", +, - and "end of scan" characters.

The paper tape punch, punch coupler and power supply make up the high speed tape punch set which records data, digitally encoded by the digital voltmeter, in IBM 8-level 4-2*-2-1 code. Recording is carried out at a maximum rate of 110 characters per second. Each reading is punched out in an 11 character sequence (word or record). The reading is presented as a six digit normalized fraction preceded by a scale factor digit representing the negative power of 10 by which the fraction is to be multiplied to obtain the magnitude of the reading. The ninth character represents mode and/or polarity while the last two digits identify the channel on which the reading was made. Buttons on the punch coupler front panel select either the manual keyboard entry of data or the automatic recording of scanned data. This data may be either punched, printed or recorded in both ways.

The guarded data amplifier with selectable gains of +1 and +10 extends the measuring range of D.C. voltage down to ±10 mv. full scale with overranging capacity to ±30 mv. This amplifier has an input resistance of 10^{10} ohms hence low power signal sources, such as strain gauge bridges and thermocouples, can be measured. The amplifier and digital voltmeter combination will maintain a reading accuracy of ±0.002% of the full scale range. Via a front panel rotary selector switch the amplifier can be set unconditionally to +1 or +10 gain or bypassed. A fourth switch position places the selection of the previous three amplifier function alternatives under control of the analogue input scanners. Diode pins inserted into or removed from appropriate channel positions in the scanner programming plugboards (also used to select range, mode, integration and settling times as previously mentioned) will select, in turn, the required amplification mode for each channel scanned.

The digital printer records, on a paper strip, the readings as they occur in a measurement sequence. Each sequence is preceded by a print out of the time at which the sequence was initiated. Time is presented as a six digit sequence of hours (up to 24), minutes and seconds prefixed by an identification character "T". Voltage measurements are preceded by a two digit channel number and a polarity sign and superceded by a single digit which indicates the location of the decimal point. A frequency reading is similar to voltage except an identifying "F" precedes the 6 digit record which is a right justified integer count of the frequency magnitude in Hz. Built into the digital printer module is a digital to analogue converter. This can produce an analogue record or indication on either a potentiometric or galvanometric instrument. A particularly useful feature for trend monitoring is the ability to select for conversion and analogue output any sequence of three digits, from most to least significant. Thus seven analogue output ranges can be selected. A zero offset adjustment of size corresponding to the range selected is also available.

To conveniently accommodate up to 24 iron-constantan thermocouples a 0°C. thermoelectrically cooled ice bath reference system was also included in the measuring system. This piece of signal conditioning apparatus was required because it was often necessary, in the course of the filled roll temperature distribution tests, to measure a large number of such thermocouples over a long period of time with the apparatus running unattended. A Dewar flask reference ice bath would have been unreliable for this application. In certain cases, however, where it was necessary to log more than 24 thermocouples the reference system had to be supplemented with a Dewar flask ice bath.

APPENDIX II

Numerical Computations to Simulate Filled Roll Heating

The computer program presented herein computes the temperature v using the equation

$$v = S \sum_{n=o}^{N} \left\{ \left[\frac{1}{2\sqrt{\pi K(t-nT)}} \quad e^{-(x-x')^2/4K(t-nT)} \right] + e^{-(x+x')^2/4K(t-nT)} \right.$$

$$\left. - he^{K(t-nT)h^2+h(x+x')} \operatorname{erfc} \left\{ \left[\frac{x-x'}{2\sqrt{K(t-nT)}} + h\sqrt{K(t-nT)} \right] \right\} \right.$$

at 7 depths, x(i). The input variables are

Program Notation	Description	Units
RPM	Speed of filled roll	RPM
DEG	Angle past nip	Degrees
TMAX	Duration of simulated run	Min.
H	Same as h	In^{-1}
DIFF	Same as K	$In^2/min.$
MPY	MPY = 0 Do at fixed multiples of revolutions, NREV MPY ≠ 0 Do at product multiples of revolutions, NREV	-
NREV	Integer whereby the time for next "Measurement" is indexed.	-
X(I)	Same as x(i)	In.
SS	Same as S	$^\circ F.\ in^3/in^2$
XP	Same as x'	In.

The only precautionary decision taken within the program is the determination of erfc(x)

1. If $0 \leq x < 2.04$ erfc $(x) = 1 - \text{erf}(x)$ where

$$\text{erf}(x) = \frac{2}{\sqrt{\pi}} \sum_{n=o}^{\infty} \frac{(-1)^n x^{2n+1}}{(2n+1)n\ !}$$

and n is increased until the last term is 0 to within the numerical precision of the machine.

2. If $1 < x \leq 2.04$ erfc$(x) = 1 - \text{erf}(x)$ where erf(x) is computed by a table look up with linear interpolation subroutine: FERF (x)

3. If $2.04 < x \leq 13.3$ the algorithm

$$\text{erfc}(x) \simeq \frac{e^{-x^2}}{|x|}\left(0.56418951 + \frac{[-.28208106 - .96210474\ x^2 - .14431247\ x^4]}{4.9078886\ x^2 + 4.1920066\ x^4 + x^6}\right)$$

is used.

4. If $x > 13.3$ the first 4 terms of the series expansion

$$\frac{2}{\sqrt{\pi}} \int_x^{\infty} e^{-\xi^2}\, d\xi = \frac{e^{-x^2}}{\sqrt{\pi}}\left(\frac{1}{x} - \frac{1}{2x^3} + \frac{1x3}{2^2x^5} - \dots + (-1)^{n-1}\frac{1x3\cdots(2n-3)}{2^{n-1}x^{2n-1}}\right)$$

$$+ (-1)^n \frac{1x3\ \cdots(2n-1)}{2^n\sqrt{\pi}} \int_x^{\infty} \frac{e^{-\xi^2}\, d\xi}{\xi^{2n}}$$

is used.

The program source listing* is shown on the following pages along with a sample output.

---

*These programs are written in Process Fortran, a superset of Fortran-II(41,42).

The program is not included as an example of computational sophistication or efficiency but simply as reference material to be used or modified or ignored as the reader sees fit.

```
      DIMENSION X(7),TEMP(7),VCOMP(7)
      CALL FAC1
      READ10,RPM,DEG,TMAX,H,DIFF,MPY,NREV,(X(I),I=1,7),SS,XP
10    FORMAT(5(F10.0,/),I1,/,I6,/,7(F10.0,/),F10.0,/,F10.0)
      PRINT(1)20,RPM
20    FORMAT($SINGLE SOURCE SUPERCALENDER ROLL MODEL$,//,$SPEED = $,
     1F6.1,$ RPM.$)
      PRINT(1)30,DEG,H,XP,DIFF,SS
30    FORMAT($ANGLE OF ROTATION PAST NIP = $,F5.1,$ DEG.$,/,$FILM CO
     1EFFICIENT/THERMAL CONDUCTIVITY = $,F6.1,$ 1/IN.$,/,$DEPTH OF SO
     2URCE = $,F6.4,$ IN.$,/,$THERMAL DIFFUSIVITY = $,F6.4,$ SQ.IN./M
     3IN.$,/,$SOURCE STRENGTH = $,F7.3,$ DEG.F.*CU.IN.$,/)
      PRINT(1)40,(X(I),I=1,7)
40    FORMAT(7(F6.4,4H IN.),$ TIME(MIN.)$)
      PI=3.14159
      ANGLE=DEG/360.
      NTMAX=XFIXF(TMAX*RPM)
      DO 45 I=1,7
45    VCOMP(I)=0
      NT=1
      NSUM=1
50    NX=1
60    XC=X(NX)
      XPX=XC+XP
      XPX2=XPX*XPX
      XMX2=(XC-XP)**2
      VPREV=0
      DO 80 I=NSUM,NT
      T=((I-1)+ANGLE)/RPM
      DNEX=4.*DIFF*T
      RKT2=SQRTF(DNEX)
      HRKT=H*RKT2/2.
      FSTAR=1./(SQRTF(PI*DNEX))
      TERM1=FSTAR*((EXPF(-(XMX2/DNEX)))+(EXPF(-(XPX2/DNEX))))
      EFCAR=(XPX/RKT2)+HRKT
      IF(EFCAR-13.3)70,70,65
65    ERTRM=(1./EFCAR)-(.5/(EFCAR**3))+(.75/(EFCAR**5))-(1.875/(EFCA
     1R**7))
      CTERM=TERM1-((ERTRM*H*EXPF(-(XPX2/DNEX)))/(SQRTF(PI)))
      GO TO 75
70    HTRME=H*EXPF((((DNEX/4.)*H)+XPX)*H)
      IF(EFCAR-2.04)701,701,71
701   CONTINUE
      IF(EFCAR-1.)710,710,72
710   ERF=EFCAR
      NN=1
      NDN=1
720   N2=(2*NN)+1
      NDN=NDN*NN
      LDA NDN
```

```
      NEG
      STA NDN
      PERF=(EFCAR**N2)/(N2*NDN)
      ERF=ERF+PERF
      IF((.1E-7)-ABSF(PERF))730,730,740
730   NN=NN+1
      GO TO 720
740   EFC=1.-(ERF*2./(SQRTF(PI)))
      GO TO 750
71    Z=EFCAR*EFCAR
      ZS=Z*Z
      ZC=ZS*Z
      F=.56419-((.282081+(.96105*Z)+(.144312*ZS))/((4.90789*Z)+(4.19
     1201*ZS)+ZC))
      EFC=(EXPF(-Z))*F/EFCAR
750   CTERM=TERM1-(HTRME*EFC)
      GO TO 75
72    CTERM=TERM1-(HTRME*(1.-FERF(EFCAR)))
75    VPREV=CTERM+VPREV
80    CONTINUE
      VCOMP(NX)=VPREV+VCOMP(NX)
      TEMP(NX)=VCOMP(NX)*SS
      IF(NX-7)300,400,400
300   NX=NX+1
      GO TO 60
400   PRINT(1)500,(TEMP(I),I=1,7),T
500   FORMAT(7E10.3,E10.3)
      NSUM=NT+1
      IF(NT-NTMAX)600,900,900
600   IF(MPY)700,700,800
700   NT=NT+NREV
      GO TO 50
800   NT=NT*NREV
      GO TO 50
900   CALL CTS(1)
      CALL FAC2
      STOP
     END
```

09-29-70

SINGLE SOURCE SUPERCALENDER ROLL MODEL

SPEED = 100.0 RPM.
ANGLE OF ROTATION PAST NIP = 45.0 DEG.
FILM COEFFICIENT/THERMAL CONDUCTIVITY = 0.0 1/IN.
DEPTH OF SOURCE = 0.0000 IN.
THERMAL DIFFUSIVITY = 1.0000 SQ.IN./MIN.
SOURCE STRENGTH = 1.000 DEG.F.*CU.IN.

0.0001 IN.	0.0938 IN.	0.1875 IN.	0.3750 IN.	0.5000 IN.	0.7500 IN.	1.0000 IN.	TIME(MIN.
0.160E 02	0.275E 01	0.141E-01	0.000E 00	0.000E 00	0.000E 00	0.000E 00	0.125E-02
0.120E 03	0.104E 03	0.951E 02	0.796E 02	0.701E 02	0.536E 02	0.402E 02	0.100E 01
0.167E 03	0.151E 03	0.141E 03	0.125E 03	0.115E 03	0.959E 02	0.793E 02	0.200E 01
0.202E 03	0.187E 03	0.177E 03	0.160E 03	0.150E 03	0.130E 03	0.112E 03	0.300E 01
0.233E 03	0.217E 03	0.207E 03	0.190E 03	0.179E 03	0.159E 03	0.140E 03	0.400E 01
0.259E 03	0.243E 03	0.234E 03	0.217E 03	0.206E 03	0.184E 03	0.165E 03	0.500E 01
0.283E 03	0.267E 03	0.258E 03	0.241E 03	0.229E 03	0.208E 03	0.188E 03	0.600E 01
0.305E 03	0.289E 03	0.280E 03	0.263E 03	0.251E 03	0.230E 03	0.209E 03	0.700E 01

29/ 9/70 12- 4-17

80SECONDS

09-29-70

APPENDIX III

An Unsuccessful Attempt to Develop a Friction Model Based on Thermodynamically Irreversible Compression of Air Entrapped in the Fill Material.

A lumped ideal heat engine model to estimate rolling friction - is a detailed investigation justified ?

Consider a crude model based on the following assumptions:

1. There are inter- and intrafibral air spaces within the compressed fill of a supercalender roll. The air is initially at atmospheric temperature and pressure.
2. Compression of the material and accompanying air takes place under the leading half of the nip.
3. Recovery or decompression takes place under the trailing half of the nip.
4. The air is a perfect gas and compresses adiabatically.
5. Heat is transferred to the solid fill material from the air which is at minimum volume. This process can be approximated by a constant volume decompression.
6. The air returns to its original state via an isothermal expansion. The expansion proceeds more slowly than the compression and the solid material, although heated by the air, can be considered an infinite source/sink of heat. The change in temperature of the solid during a cycle (revolution) is negligible compared to the temperature changes experienced by the air.

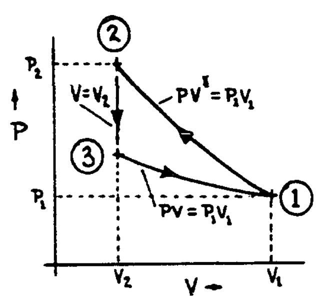

FIG. 95.

A cycle composed of reversible gas processes which combine to produce energy dissipation.

Let us calculate the coefficient of friction predicted by the cycle described if we assume a fill made up of 25% air by volume, initially at 1 atmosphere and 530°R., which is compressed to 300 atmospheres. Only the top 0.3in. thickness of fill is considered active.

Work done during adiabatic compression:

$$\int_{V_1}^{V_2} PdV = \frac{\hat{R}T_1}{\gamma-1}\left[1-\left(\frac{P_2}{P_1}\right)^{\frac{\gamma-1}{\gamma}}\right]$$

$\hat{R}$ = 53.3 ft.#/# °R

T_1= 530 °R

γ = 1.4

P_2/P_1= 300

$$= \frac{53.3\text{x}530}{0.4}\left[1 - 300^{\left(\frac{0.4}{1.4}\right)}\right]$$

$= -290000$ ft.#/# air

Work done during isothermal expansion:

$$\int_{V_2}^{V_1} PdV = \hat{R}T_1 \ \ln \frac{P_2}{P_1}$$

$= 53.3\text{x}530 \ \ln 300$

$= 160000$ ft.#/# air

Net work/revolution = $-$ 130000 ft. #/# air.

Mass of air/inch of nip width

$\frac{1}{4} \times \frac{0.3}{144} \times \pi \times .075 = 1.23 \times 10^{-4}$ #air/inch of nip width

Work done/revolution inch of nip width

$- 130000 \times 1.23\times10^{-4} = 16$ ft. #/rev.in.

This is a tractive force of $16/\pi$ on a 1ft. dia. roll which corresponds to a rolling friction coefficient of

.0025 at 2000 PLI.

or .005 at 1000 PLI.

Granted this calculation was not based on a pressure ratio calculated from a given nip load. However, the chosen values are of the correct order of magnitude. A more detailed investigation is most definitely justified.

Refining the model

The primitive model just described has two serious shortcomings.

1. No attempt was made to relate the air pressure to the compressive stress distribution in the fill material, which varies with fill pressure, roll geometry, nip load and depth beneath the surface.
2. There is no justification, other than convenience, for a gas cycle made up of three fundamental and reversible gas processes.

Let us refine the gas cycle by considering qualitative aspects of expected compression, decompression and heat transfer rates.

1. When the air begins compression it is at ambient temperature and heat transfer is negligible. At the end of the compression cycle it is hot and heat transfer to the solid material is more rapid compared to the rate of compression. Therefore let us assume that the compression characteristic has the slope of the adiabat through P_1, V_1 and the slope of either an isotherm or an isobar through P_2, V_2.
2. As expansion begins consider the return path on the PV plane to have

the vertical slope of a constant volume process at P_2, V_2, which increases continuously to the slope of the isotherm through P_1, V_1. Let us assume that these trajectories are simple analytic functions which can each be described by four respective constraints; two of coordinate and two of slope for each curve. Let us define these functions to be cubic polynomials, represented as either,

$$V = eP^3 + fP^2 + gP + h$$

$$\text{or} \quad P = EV^3 + FV^2 + GV + H$$

whichever is more convenient.

<u>The Expansion Process</u>

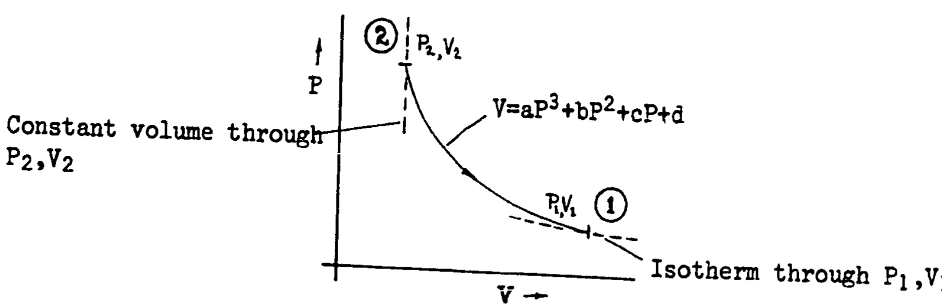

FIG. 96.
The Expansion Process.

Isotherm through P_1, V_1 : $PV = P_1V_1$

Inverse slope of this isotherm: $\frac{dV}{dP} = -\frac{P_1V_1}{P2}$

The four constraints on the polynomial:

at (1): $P = P_1$, $V = V_1$ and $\frac{dV}{dP} = -\frac{V_1}{P_1}$

at (2): $P = P_2$, $V = V_2$ and $\frac{dV}{dP} = 0$

$$a = -\left[\frac{(P_2-3P_1)V_1 + 2P_1V_2}{P_1(P_2-P_1)^3}\right]$$

$$b = \left(\frac{2P_2^2 - 4P_2P_1 - 4P_1^2}{P_1\,(P_2-P_1)^3}\right)V_1 + \left(\frac{3\,(P_2+P_1)}{(P_2-P_1)^3}\right)V_2$$

$$c = -\left(\frac{P_2^3+P_2^2P_1-8P_2P_1^2}{P_1(P_2-P_1)^3}\right)V_1 - \left(\frac{6P_2P_1}{(P_2-P_1)^3}\right)V_2$$

$$d = \left(\frac{2P_2^2(P_2-2P_1)}{(P_2-P_1)^3}\right)V_1 + \left(\frac{P_1^2(3P_2-P_1)}{(P_2-P_1)^3}\right)V_2$$

The work done by the decompression process is

$$\int_{V_2}^{V_1} PdV = -\left[\int_{V_2}^{P_1} VdP - (P_1-P_2)V_2\right] + P_1\quad(V_1-V_2)$$

where $$\int_{P_2}^{P_1} VdP = \int_{P_2}^{P_1} (aP^3+bP^2+cP+d)\,dP = \frac{a}{4}(P_1^4-P_2^4) + \frac{b}{3}(P_1^3-P_2^3) + \frac{c}{2}(P_1^2-P_2^2) + d\,(P_1-P_2)$$

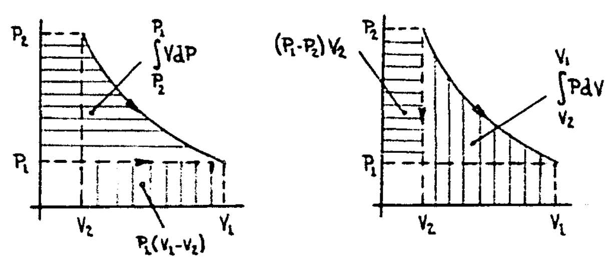

FIG. 97.

Work Done During Expansion Process.

Compression Processes

These may be represented by either of the following processes

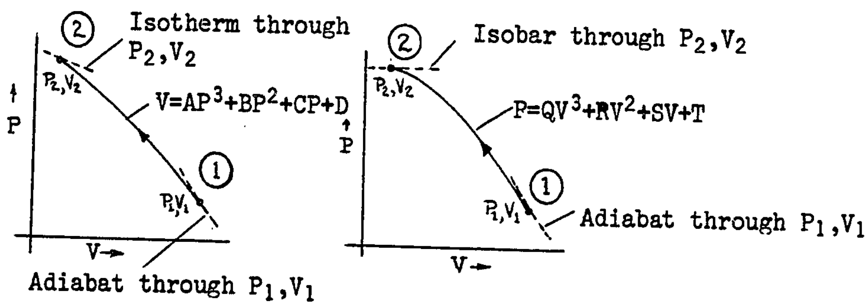

FIG. 98.

Compression Processes

For the left hand figure with a terminal isotherm:

Adiabat through P_1,V_1 : $PV^\gamma = P_1 V_1^\gamma$

Inverse of the slope of this adiabat: $$\frac{dV}{dP} = -\frac{P_1^{\frac{1}{\gamma}} V_1}{\gamma P^{\frac{\gamma+1}{\gamma}}}$$

The four constraints on the polynomial :

at (1) : $P = P_1$, $V = V_1$ and $\frac{dV}{dP} = -\frac{V_1}{\gamma P_1}$

at (2) : $P = P_2$, $V = V_2$ and $\frac{dV}{dP} = -\frac{V_2}{P_2}$ (similar to (1) on previous expansion cycle)

$$A = -\left[\left(\frac{P_2-(2\gamma+1)P_1}{\gamma P_1(P_2-P_1)^3}\right)V_1 + \left(\frac{3P_2-P_1}{P_2(P_2-P_1)^3}\right)V_2\right]$$

$$B = \left[\left(\frac{2P_2^2-(3\gamma+1)P_2P_1-(3\gamma+1)P_1^2}{\gamma P_1(P_2-P_1)^3}\right)V_1 + \left(\frac{4P_2^2+4P_2P_1-2P_1^2}{P_2(P_2-P_1)^3}\right)V_2\right]$$

$$C = -\left[\left(\frac{P_2^3 + P_2^2P_1 - 2(3\gamma+1)P_2P_1^2}{\gamma P_1(P_2-P_1)^3}\right)V_1 + \left(\frac{8P_2^2P_1 - P_2P_1^2 - P_1^3}{P_2(P_2-P_1)^3}\right)V_2\right]$$

$$D = \left[\left(\frac{(\gamma+1)P_2^3P_1 - (3\gamma+1)P_2^2P_1^2}{\gamma P_1(P_2-P_1)^3}\right)V_1 + \left(\frac{4P_2^2P_1^2-2P_2P_1^3}{P_2(P_2-P_1)^3}\right)V_2\right]$$

The work done during the compression process is

$$\int_{V_1}^{V_2} PdV = -\left[\int_{P_1}^{P_2} VdP - (P_2-P_1)V_2\right] + \left[P_1(V_2-V_1)\right]$$

where $$\int_{P_1}^{P_2} VdP = \int_{P_1}^{P_2} (AP^3+BP^2+CP+D)dP = \frac{A}{4}(P_2^4-P_1^4) + \frac{B}{3}(P_2^3-P_1^3) + \frac{C}{2}(P_2^2-P_1^2) + D(P_2-P_1)$$

The total work performed is the sum of the work performed during compression and decompression

$$= \left.\int_{V_2}^{V_1} PdV\right]_{\text{Decompression}} + \left.\int_{V_1}^{V_2} PdV\right]_{\text{Compression}} =$$

$$-\left\{\left.\int_{P_2}^{P_1} VdP\right]_{\text{Decompression}} + \left.\int_{P_1}^{P_2} VdP\right]_{\text{Compression}}\right\} = \left\{(P_2^4-P_1^4)\frac{(A-a)}{4} + (P_2^3-P_1^3)\frac{(B-b)}{3} + (P_2^2-P_1^2)\frac{(C-c)}{2} + (P_2-P_1)(D-d)\right\}$$

For the right hand figure terminating in an isobar:

Adiabat through P_1,V_1 : $PV^{\gamma} = P_1V_1^{\gamma}$

Slope of this adiabat : $\frac{dP}{dV} = -\gamma\left(\frac{P_1V_1^{\gamma}}{V^{\gamma+1}}\right)$

The four constraints on the polynomial :

at (1) : $V = V_1$, $P = P_1$ and $\frac{dP}{dV} = -\frac{\gamma P_1}{V_1}$

at (2) : $V = V_2$, $P = P_2$ and $\frac{dP}{dV} = 0$

$$Q = -\left[\left(\frac{\gamma V_2-(\gamma+2)V_1}{V_1(V_2-V_1)^3}\right)P_1 + \frac{2P_2}{(V_2-V_1)^3}\right]$$

$$R = \left[\left(\frac{2\gamma V_2^2 - (\gamma+3)V_2V_1 - (\gamma+3)V_1^2}{V_1(V_2-V_1)^3}\right)P_1 + \left(\frac{3(V_2+V_1)}{(V_2-V_1)^3}\right)P_2\right]$$

$$S = -\left[\left(\frac{\gamma V_2^3 + \gamma V_2^2V_1 - 2(\gamma+3)V_2V_1^2}{V_1(V_2-V_1)^3}\right)P_1 + \left(\frac{6V_2V_1}{V_2-V_1)^3}\right)P_2\right]$$

$$T = \left[\left(\frac{(\gamma+1)V_2^3V_1 - (\gamma+3)V_2^2V_1^2}{V_1(V_2-V_1)^3}\right)P_1 + \left(\frac{3V_2V_1^2 - V_1^3}{(V_2-V_1)^3}\right)P_2\right]$$

The work done by this compression process is

$$\int_{V_1}^{V_2} PdV = \frac{Q}{4}(V_2^4-V_1^4) + \frac{R}{3}(V_2^3-V_1^3) + \frac{S}{2}(V_2^2-V_1^2) + T(V_2-V_1)$$

If this form of the compression process is chosen the total work done is

$$-\left\{\frac{a}{4}\left(P_1{}^4-P_2{}^4\right)+\frac{b}{3}\left(P_1{}^3-P_2{}^3\right)+\frac{c}{2}\left(P_1{}^2-P_2{}^2\right)+d\left(P_1-P_2\right)-\left(P_1-P_2\right)V_2\right\}$$
$$+P_1\left(V_1-V_2\right)+\frac{Q}{4}\left(V_2{}^4-V_1{}^4\right)+\frac{R}{3}\left(V_2{}^3-V_2{}^3\right)+\frac{S}{2}\left(V_2{}^2-V_1{}^2\right)+T\left(V_2-V_1\right)$$

Thermal capacity of solid vs. air in fill material

When the heat engine model was developed it was assumed that a slow process would proceed isothermally because the heat capacity of the solid component of the fill is large compared to that of the air. Assuming a roll with a volumetric void fraction of 25% at atmospheric pressure and ambient temperature there is

$$\frac{\rho\ \text{cellulose}}{\rho\ \text{air}} \times \frac{V\ \text{cellulose}}{V\ \text{air}} = \frac{98}{0.075} \times \frac{3}{1} = 3920$$

times as much cellulose as air. The specific heats of cellulose and air both range between 0.2 and 0.3 Btu/lb. and can thus be considered equal. We can conclude that a quantity of heat which will raise the air temperature by almost 4000°F. is equivalent to only a 1°F. change in solid temperature. The isothermal expansion trajectory tangent is indeed valid.

The termination tangent to the compression process

Two possible slopes at the termination of the gas compression process were postulated. As the rate of compression decreases towards the end of the cycle it is strongly suspected that heat transfer to the solid fill will eventually equilibrate and then overbalance the temperature increasing tendency of gas compression. It is thus probable that the constant pressure, rather than isothermal tangent is appropriate. Furthermore, since we feel that the initial constant volume decompression is justified, there is less difference between the slopes of final compression and initial decompression. Therefore the isobaric tangent is more suitable from the point of view of smooth transition between compression and decompression. We expect this continuity intuitively and from experience with records of high speed cyclic gas processes (i.e. engine and compressor indicator diagrams).

Development of criteria by which the high pressure gas state may be determined.

Fill structure

1. Fill fibres are laid down in parallel planes. (i.e. they are all laid down horizontally).
2. The orientation of fibres is otherwise random.
3. The fill is pressed or compacted during manufacture in a direction perpendicular to the planes of orientation, and parallel to the axis of the roll.
4. The compressive effect of a nip is in a direction parallel to the planes of fill orientation, and perpendicular to the roll axis.
5. The reduction in fill volume accompanied by pressing occurs by the extrusion and compression of air. This reduction of void volume involves a decrease of dimension in the axial direction only. The compression of an accordian bellows is similar in that, here too, little change in cross sectional direction occurs.
6. It would seem that pressing results in little change in fill porosity in the axial direction. On the other hand resistance to flow in directions perpendicular to the roll axis is greatly increased as void

passages in all directions perpendicular to the roll axis undergo extensive reduction in cross sectional area. Note the reduction in area of the tunnel in the block at right angles to the direction of compression.

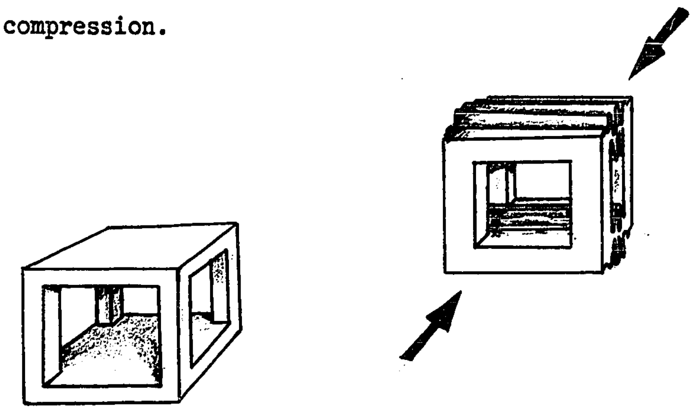

FIG. 99.
Decrease in Circumferential Porosity
Through Fill Compression.

7. The fill has tensile strength in directions parallel to the fibres. Only the axial pressure of the end plates upon the fill prevents delamination of the roll in the axial direction. The fill material cannot resist axial tension.

Let us see what sort of structure we have built from our assumptions.

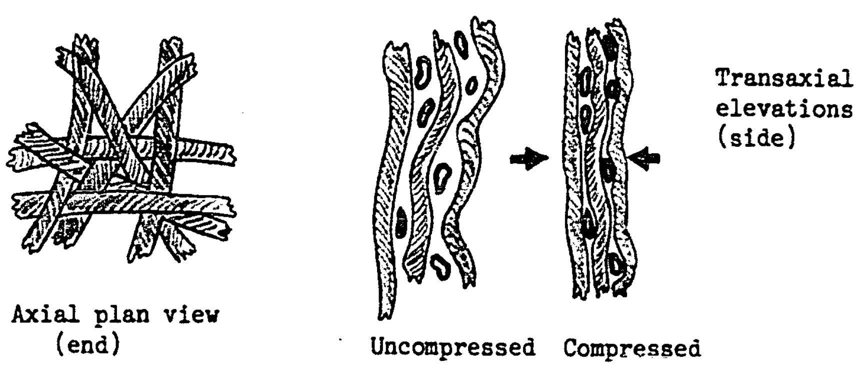

FIG. 100.
Axial Compression of Randomly Oriented
Fill Fibres in Transaxial Planes.

The void pockets which result from the preceding assumptions have continuity in only the axial direction. This could be represented by a series of slightly meandering long, thin, parallel tubes running in the axial direction; a fascia or bundle.

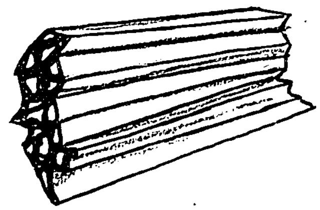

FIG. 101.
Fibre Compression Results in the
Formation of Tubular Fascia.

Let us be quite clear on the structure of these 'tubes'; they are not pipes. They are formed by pressing together many layers of 'chain-mail' made of very fine 'wire'. Only the fill pressure maintains the axial integrity of the tubes.

FIG. 102.
Possible Structure of Hypothetical Tubes.

Pressure is built up in these cavities as they sustain transverse loading under the rolling nip accompanied by further reduction in volume.

Relating pressure to stress within the solid

Fill material is by volume approximately 75% solid cellulose (occasionally some wool protein, glass or asbestos) and is by mass more than 99.9% solid. It is therefore assumed that gas pressure is a by-product of the compressive stress field within the essentially elastic solid surrounding the gas filled voids. Although the compression of gas filled cavities is in ways a complication, in another, most important way it provides a convenient simplification. It is assumed that a simple radial compressive stress field is set up by the nip contact and that the compressive stress is transmitted through the solid which is considered homogeneous for this purpose. What happens at the boundary between solid and void ? The fibre which forms the void wall is like a string or thread and can only sustain tension. The air filled cavity collapses until the hydrostatic pressure is in equilibrium with the compressive stress in the surrounding solid. A tension in the cavity walls in the appropriate regions maintains the hydrostatic stress.

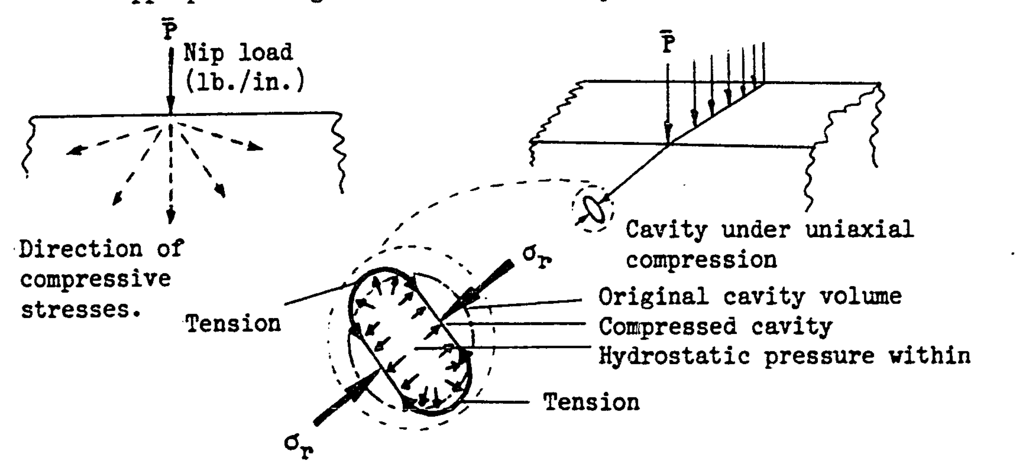

FIG. 103.

Deformation of Hypothetical Tubes Under Simple Radial Compression.

Consider that the tension is maintained at the ends of the cavity by a membrane-like boundary stress in the elastically stiff fibre. This results in negligible lateral expansion of the cell and does not appreciably alter the purely radial compressive stress field throughout the bulk of the solid. Except for regions very close to the roll surface we now have a simple but realistic estimate of the maximum air pressure, P_2, as a function of depth below the surface, r.

$$\sigma_r = - \frac{2\bar{P} \cos \theta}{\pi r}$$

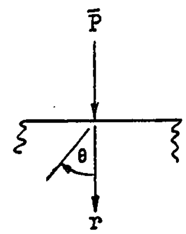

or along the vertical under P where $\theta = 0$

$$P_2 = \sigma_r \Big|_{\theta = 0} = \frac{-2\bar{P}}{\pi r}$$

The most serious objection to this pressure distribution is that the stress and pressure tend to ∞ near the surface. In order to resolve this problem consider the shape of the isobars generated by the assumed concentrated line force $\bar{P}$. These lines of constant pressure are a family of cylindrical surfaces contangential to the surface through the end view of the nip line.

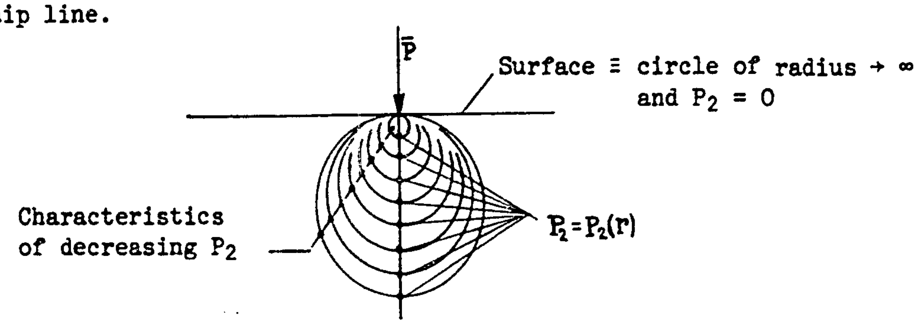

FIG. 104.
Isobars in Simple Radial Compression.

At some distance below the surface, along the vertical extension of the line of action of $\bar{P}$, $r = r_0$, $P_2 \geqq \sigma_{fill}$. The predicted pressure, P_2, is equal to or greater than the fill pressure, i.e. the tensile force in the roll shaft divided by the annular cross section area of fill material. As it has been postulated that the fill has no axial tensile strength the fill fibre will separate in this circular zone and somewhat beyond causing the air pressure to relax to σ_{fill}. Any air flow will proceed across the isobars, or in the direction of pressure gradient. This escape of gas will occur primarily in the region nearest the surface and possibly some will escape from the filled roll near the downstream side of the nip beyond where contact with the metal roll bars the surface. We will assume that air is not normally depleted in the surface region of the fill as it can be forced into the fill through compression on the ingoing side of the nip. This pumping of air will not be accounted for directly. The air within the fill is considered a closed system or one in mass equilibrium.

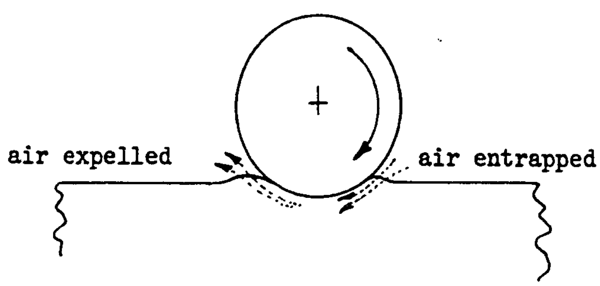

FIG. 105.
Possible Air Pumping Through a
Supercalender Nip.

This oversight will be compensated, at least in part, by a fictitious oscillatory flow proceeding alternately inward and outward in the fill along the vertical line under $\bar{P}$. It should be recalled at this point that the purpose of our argument is not to present a detailed analysis of how an element of air in the fill behaves as it travels under the nip along a trajectory parallel to the surface but merely to attempt to define a volume state, V_2, corresponding to the maximum pressure state, P_2, assumed to occur along the vertical line through $\bar{P}$.

This is basically a one dimensional analysis to present a plausible functional relationship between P_2,V_2 and the depth below the filled roll surface, r. The oscillatory vertical flow mentioned previously is merely an implication of the argument to define $V_2(r)$ which will be presented below; an implication of mass conservation.

<u>Relating compressed air volume to intrusion of the steel roll into the fill</u>.

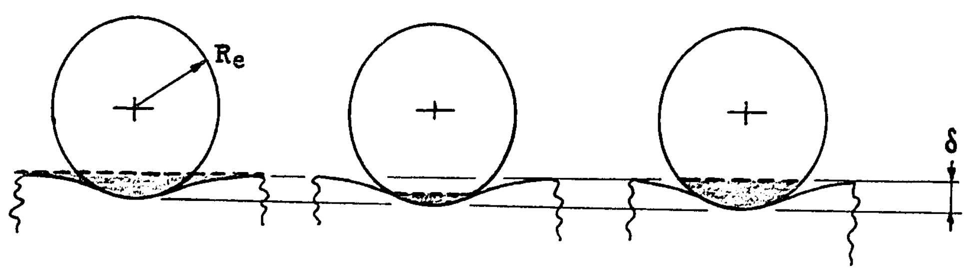

FIG. 106.
Estimated Volume of Air Expelled.

Consider a steel roll radius R_e which intrudes a distance δ into or causes a maximum deflection of δ in a half space of fill. The radius R_e can be reasonably approximated by adding the actual curvatures of the steel and filled roll, R_s and R_F respectively.

$$R_e = (R_s^{-1} + R_F^{-1})^{-1}$$

Let the total reduction in air volume within fill be defined arbitrarily as the volume of the cylinder segment defined by the chordal plane a distance δ into the steel roll, i.e. the diagram on the right. This choice is made as a realistic compromise between the two other obvious approximating attempts at left and centre, whose hatched sections would seem to define volumes too large and too small, respectively. In what reasonable manner may this total reduction in air volume be distributed as a function of r, the depth below the undeformed filled roll surface ?

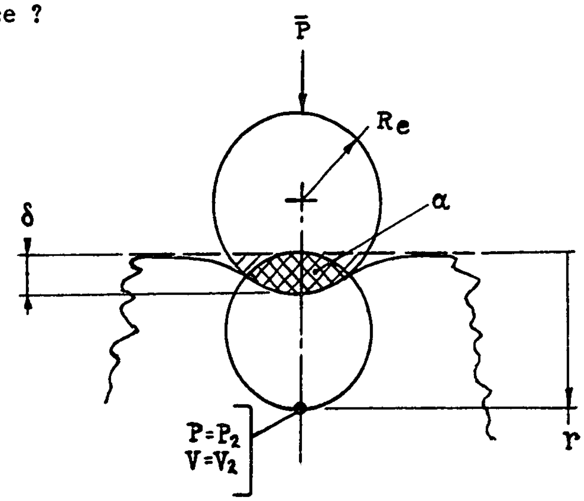

FIG. 107.
Overlap Between Intruding Cylinder
and a Typical Isobar.

Let it be argued that at any point a distance r beneath the nip at pressure P_2, the air volume has been reduced to V_2. V_2 will be defined as

$$V_2 = \frac{\left(\frac{\pi r^2}{4}\,\Omega - \alpha\right)}{(\pi r^2/4)\Omega} V_1$$

per unit length, where α can be determined from geometry as shown below, where Ω is the void fraction in the undisturbed fill, $\frac{V\ air}{V\ total}$ and α is the volume common to the effective steel roll of radius R_e and the cylindrical surface of the isobar through $P = P_2$, $V = V_2$ at depth r beneath the undisturbed filled roll surface. Displacement of air within and across the boundary of the isobar in some undefined manner is implied in order to satisfy continuity. At depths where $\alpha > \frac{\pi r^2 \Omega}{4}$, $V_2 = 0$, it is implied that along the vertical line under the nip, to a depth $r = 2\sqrt{\frac{\alpha}{\pi\Omega}}$, the air undergoes complete expulsion.

Determining the volume change, α, within an isobaric boundary of diameter r:

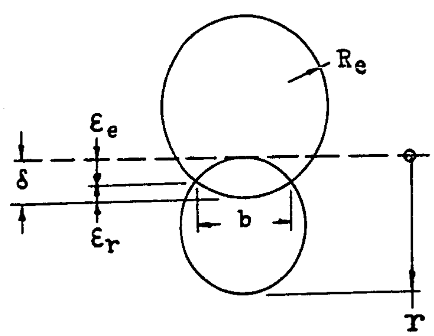

FIG. 108.
Dimensions of Overlap.

Note that the intersecting circles have a common chord b.

Maximum distance between chord and circumference ε
Chord length b

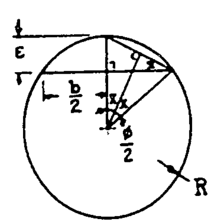

Circle radius R
Angle subtended by chord Q
Angles marked (x) are equal
Angles marked (∟) are 90°

FIG. 109.
Geometry of Overlap.

From the above figure it can be seen that

$$\varepsilon = \sin\frac{\phi}{4}\left[2R\sin\frac{\phi}{4}\right] = 2R\sin^2\frac{\phi}{4}$$

$$\sin\phi = 4\sqrt{f-5f^2+8f^3-4f^4}$$

where $$f = \frac{\varepsilon}{2R}$$

$$\phi = \tan^{-1}\frac{4\sqrt{f-5f^2+8f^3-4f^4}}{\sqrt{1-16(f-5f^2+8f^3-4f^4)}}$$

and area of the segment is

$$\alpha^* = \frac{1}{2}R^2\,(\phi - \sin\phi)$$

$$= \frac{1}{2}R^2\left(\frac{\phi^3}{3!} - \frac{\phi^5}{5!} + \frac{\phi^7}{7!} - \ldots\ldots\right)$$

Noting that $\frac{b}{2} = R_e \sin\frac{\phi_e}{2} = \frac{r}{2}\sin\frac{\phi_r}{2}$

where the subscripts e and r apply to the effective steel roll and the isobar, respectively, and that $\varepsilon_e + \varepsilon_r = \delta$

it can be seen that

$$\varepsilon_e = \frac{\delta\left(\frac{r}{2} - \frac{\delta}{2}\right)}{R_e + \frac{r}{2} - \delta}$$

and $$\varepsilon_r = \frac{\delta\left(R_e - \frac{\delta}{2}\right)}{R_e + \frac{r}{2} - \delta}$$

Finally the total volume reduction per unit length is

$$\alpha = \alpha_e^* + \alpha_r^*$$

$$= \frac{1}{2} R_e^2 \left(\frac{\phi_e^3}{3!} - \frac{\phi_e^5}{5!} + \frac{\phi_e^7}{7!} - \ldots \right) + \frac{1}{8} r^2 \left(\frac{\phi_r^3}{3!} - \frac{\phi_r^5}{5!} + \frac{\phi_r^7}{7!} - \ldots \right)$$

and the compressed volume is

$$V_2 = \left\{ \frac{\left(\frac{\pi r^2}{4} \Omega - \alpha \right)}{\frac{\pi r^2}{4} \Omega} \right\} V_1$$

as originally stated.

<u>Summing up the pressure-volume distribution under the nip and rolling friction</u>

We thus define three distinct regions of experience within the fill; or three layers at increasing depth. The first layer extends to a depth $r_o = \frac{2\bar{P}}{\pi \sigma_{fill}}$. From $r = o$ to $r = r_o$, $V_2 = o$ and $P_2 = \sigma_{fill}$. The next layer extends from $r = r_o$ to $r = 2\sqrt{\frac{\alpha}{\pi\Omega}} = r_1$. Within this layer the fill pressure has not been exceeded and $P_2 = \frac{2\bar{P}}{\pi r}$, i.e. the maximum pressure does not exceed σ_{fill} but transaxial diffusion still occurs in order to permit complete air expulsion : $V_2 = o$. In the final, deepest region below $r = r_1$ both P_2 and V_2 vary continuously with r, $P_2 = \frac{2\bar{P}}{\pi r}$ as in the second layer but V_2 is a function of δ, R_e and r. The rolling friction of the system can be calculated by integrating with respect to depth r the work done by the gas cycles described previously on an element of air mass flow.

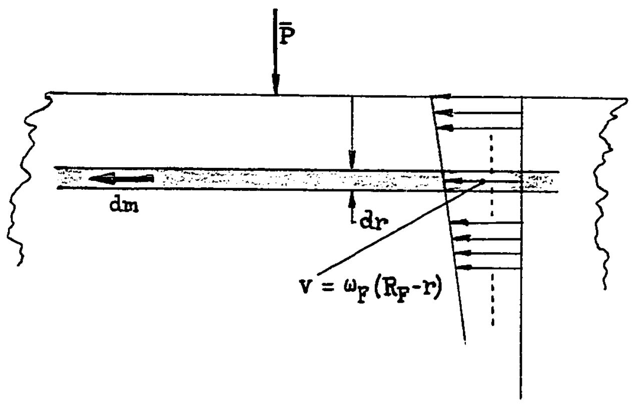

FIG. 110.

Air Mass Flow Carried by Rotating Fill.

The element of air mass flow, dm, through a strip of unit width and thickness dr can be expressed as

$$dm = \frac{P_1}{\hat{R}T_1}\left\{ vdr \right\} = \frac{P_1\omega_F(R_F - r)dr}{\hat{R}T_1}$$

then friction work done per unit time is

$$W_f = \int_{r=o}^{r=t} \left(\int PdV \right) \ dm \quad \text{ft.lb./min.}$$

and $\mu = \dfrac{W_f}{\bar{P}\omega_F R_F}$ is the rolling friction coefficient due to effects of irreversible gas processes.

APPENDIX IV

On the Determination of Friction in Rolling Element Bearings

Measurement of friction losses in rolling element bearings

Early in the test program which was conducted to measure the rolling friction of a supercalender nip it became evident that the friction torque contribution of the stack bearings was sizeable; usually over 20% of the gross drive torque requirement. This problem does not assume such magnitude in an industrial stack with 8 or 9 nips and rolls of up to 10 calibre lengths. Under these conditions only 4 or possibly only 2 of the 18 or 20 bearings are supporting the stack load and hence 2-5% of the drive torque is attributable to the bearings. In our case however the bearing torque had to be measured in order to determine the actual rolling friction of the nip.

When its necessity arose, this auxiliary experiment was regarded as a costly and inconvenient digression. Note the attempt to develop a direct reading bearing dynamometer as shown in Figs. 111-114. Because this dynamometer was not successful the stack bearings were calibrated by running them loaded as was shown in Fig. 8. The resulting load characteristics are shown in Figs. 115-116 for high and low speeds, respectively.

Aside from providing the required data for friction torque correction, the bearing calibration experiments provide incontestable evidence that the equipment and instruments were accurate and reliable throughout the test program, i.e. the high speed bearing data was obtained before nip friction tests were conducted while the low speed data was obtained after all tests on filled rolls were completed.

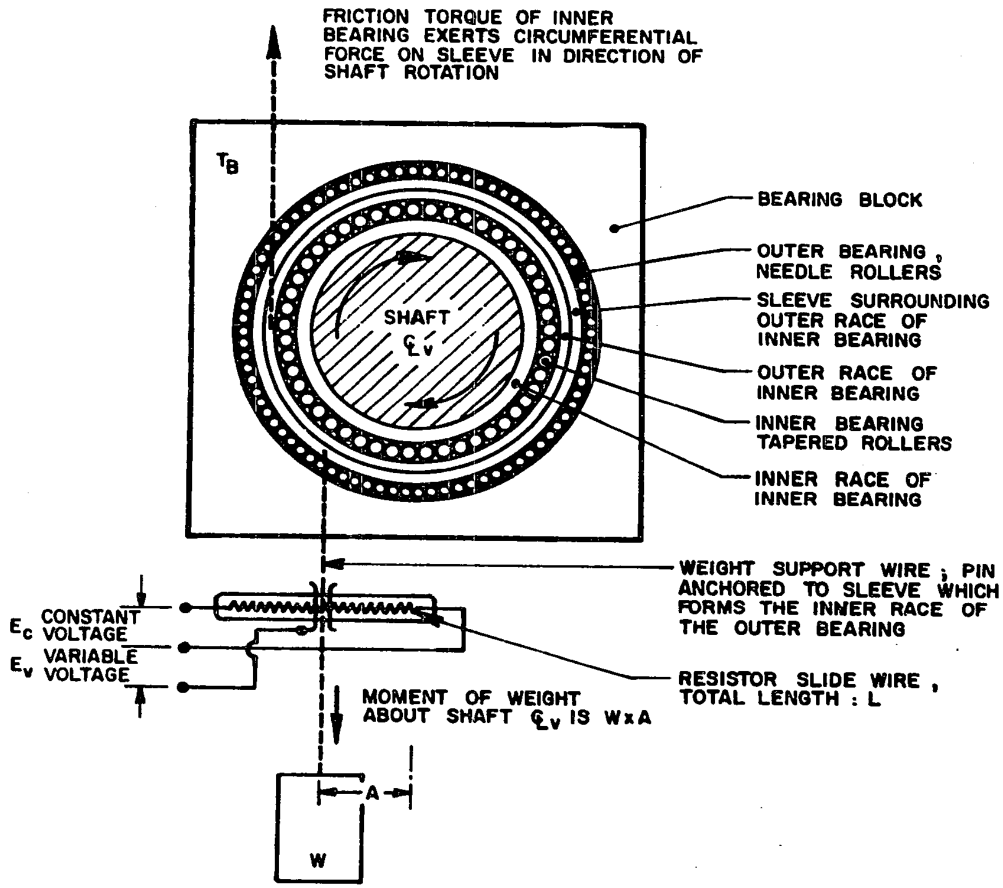

FIG. 111.

Schematic drawing of bearing dynamometer. Assuming that the static friction of the outer bearing is negligible (see text) W x A = T_b and Ev a T_b.

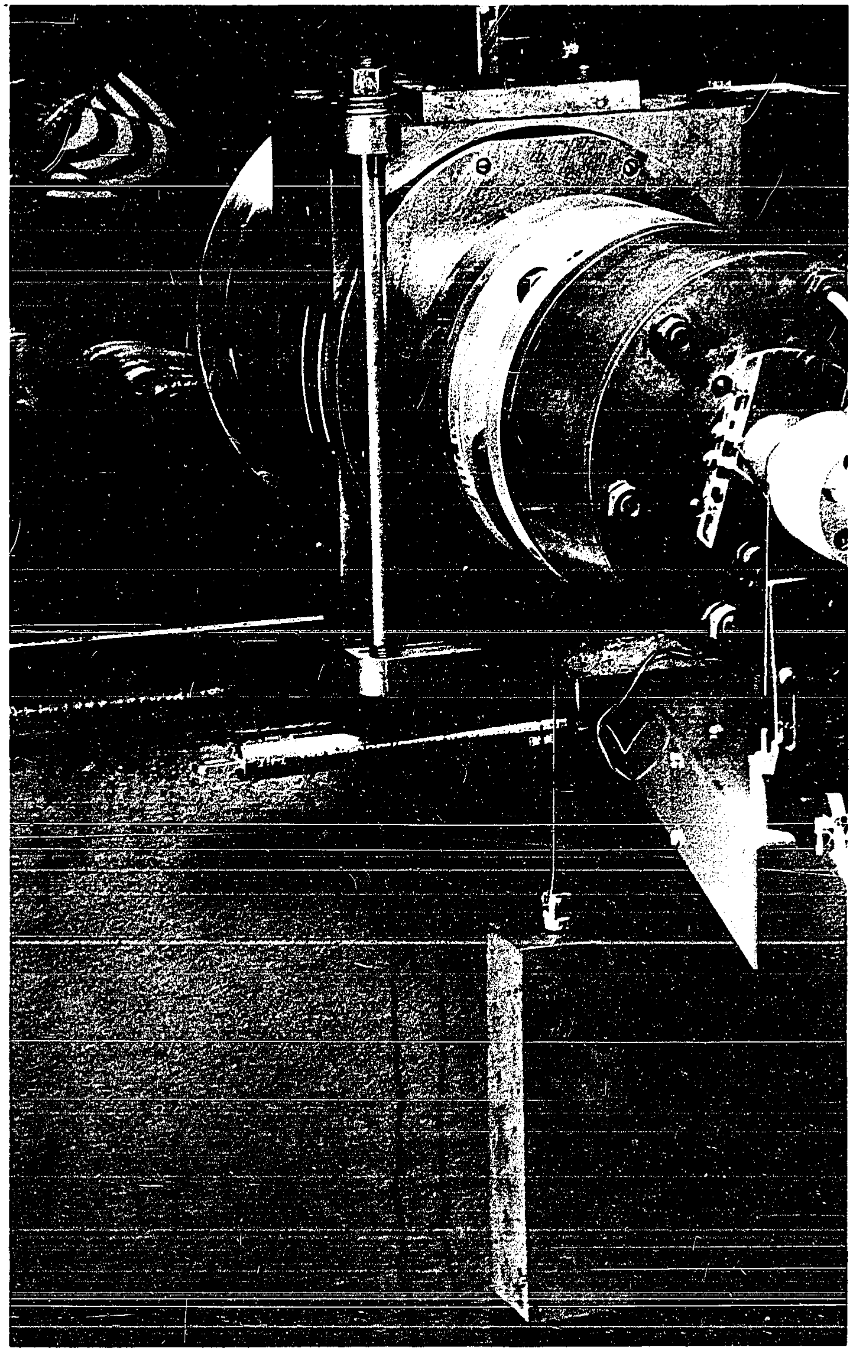

FIG. 112.

Bearing Dynamometer Installed in Stack.

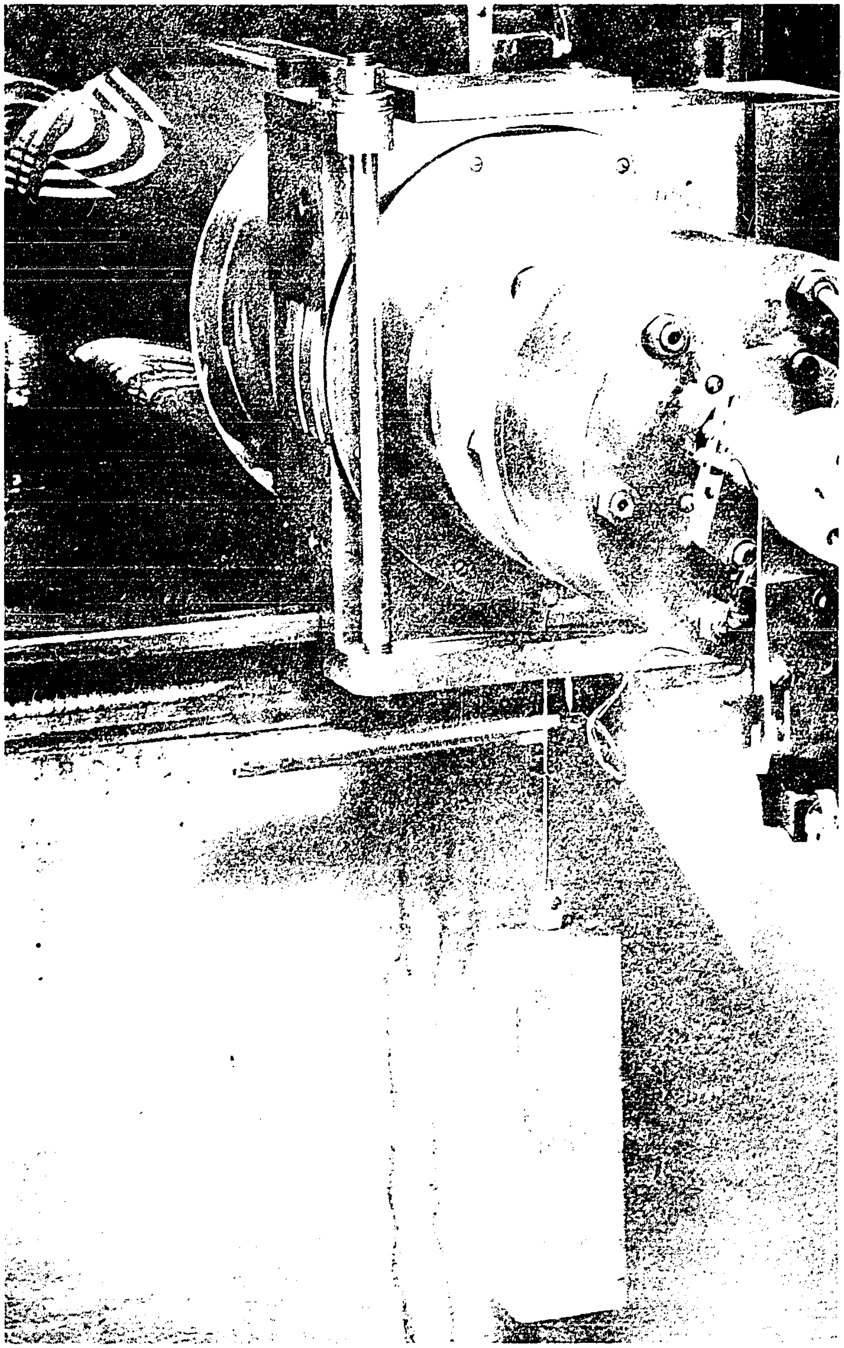

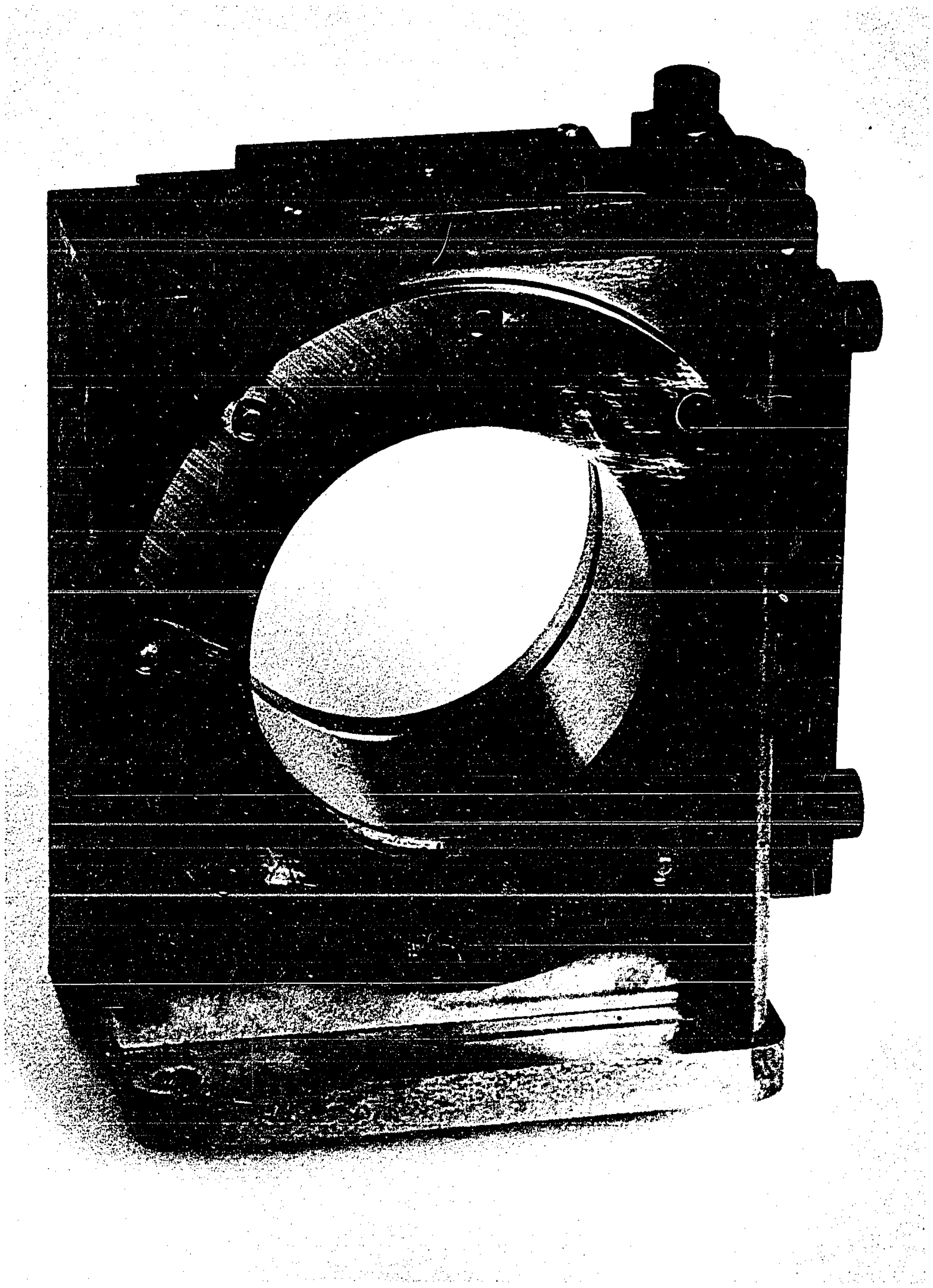

FIG. 113.

Bearing Dynamometer Assembly.

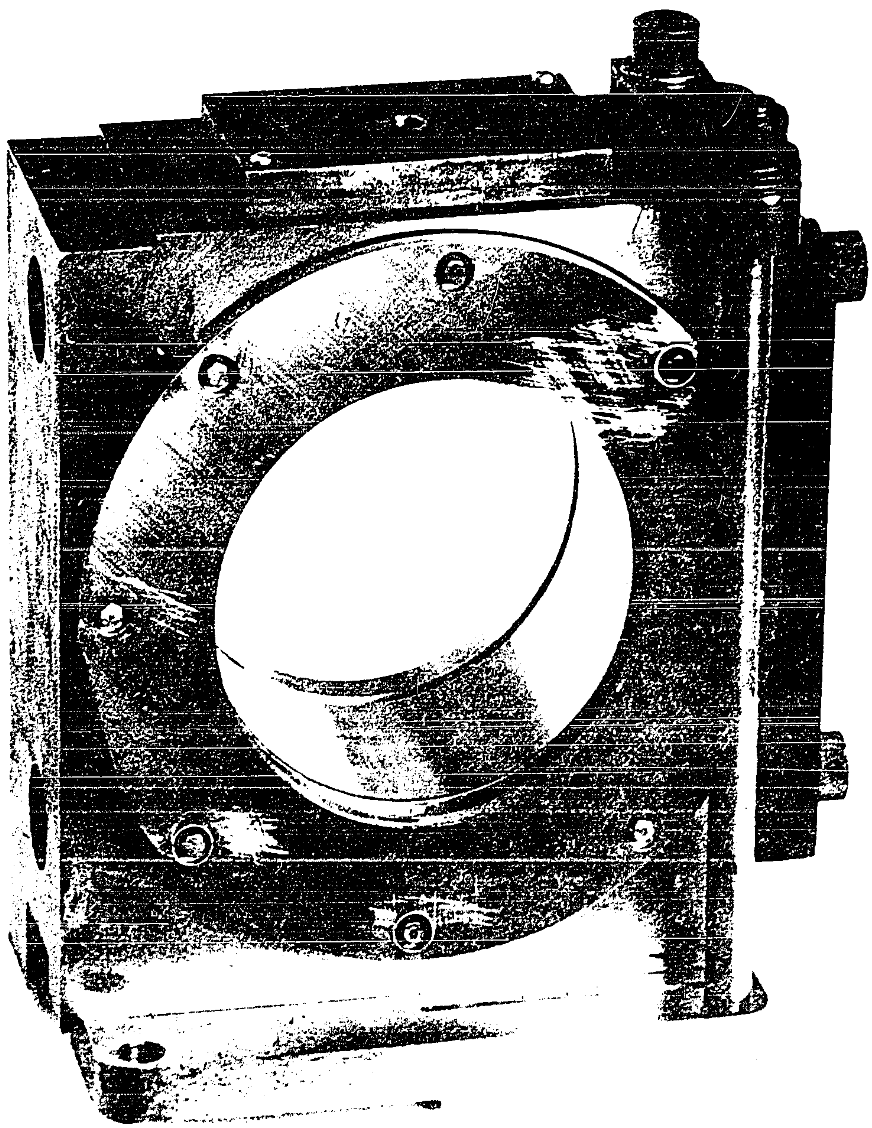

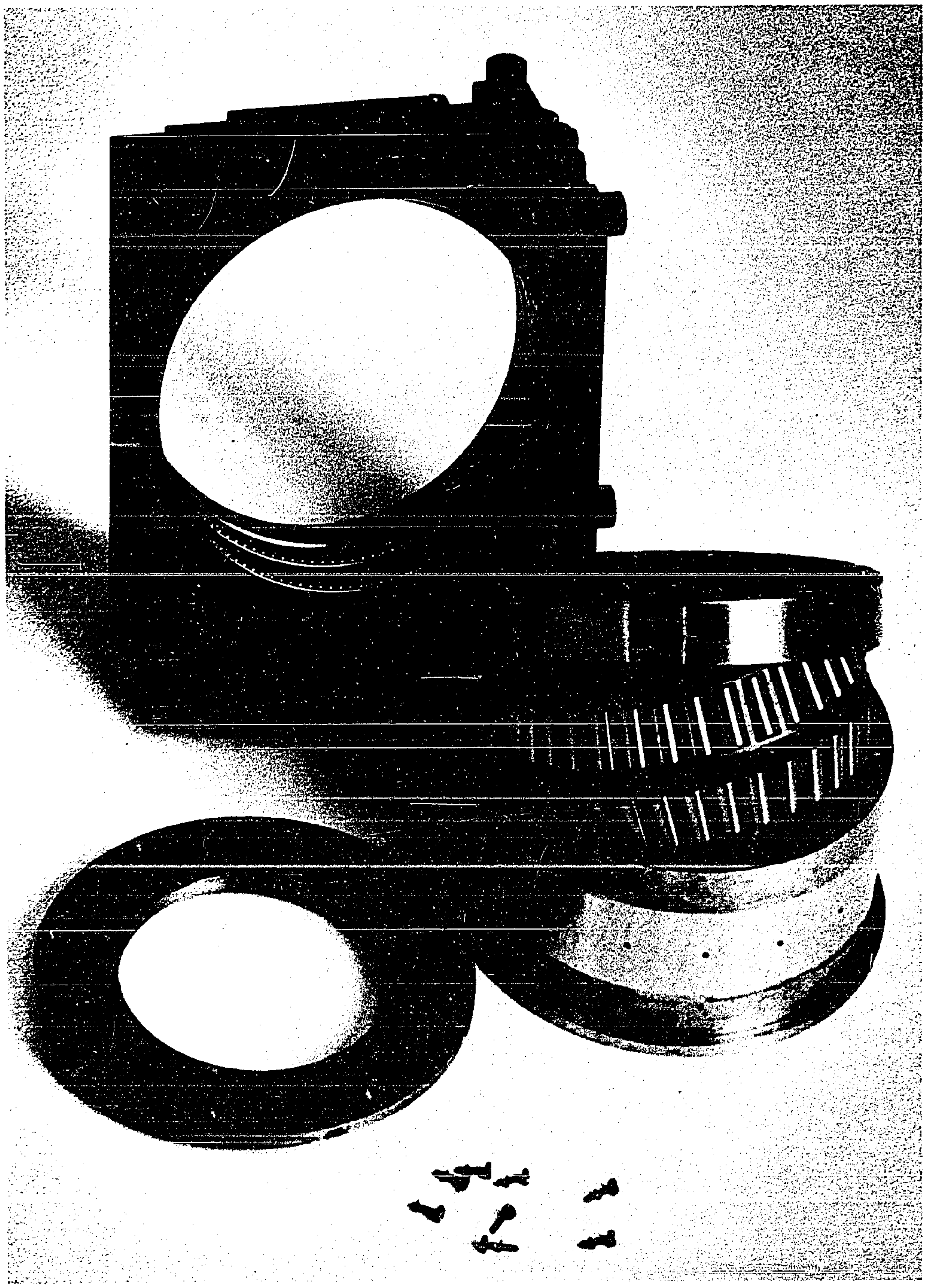

FIG. 114.

Bearing Dynamometer Components.

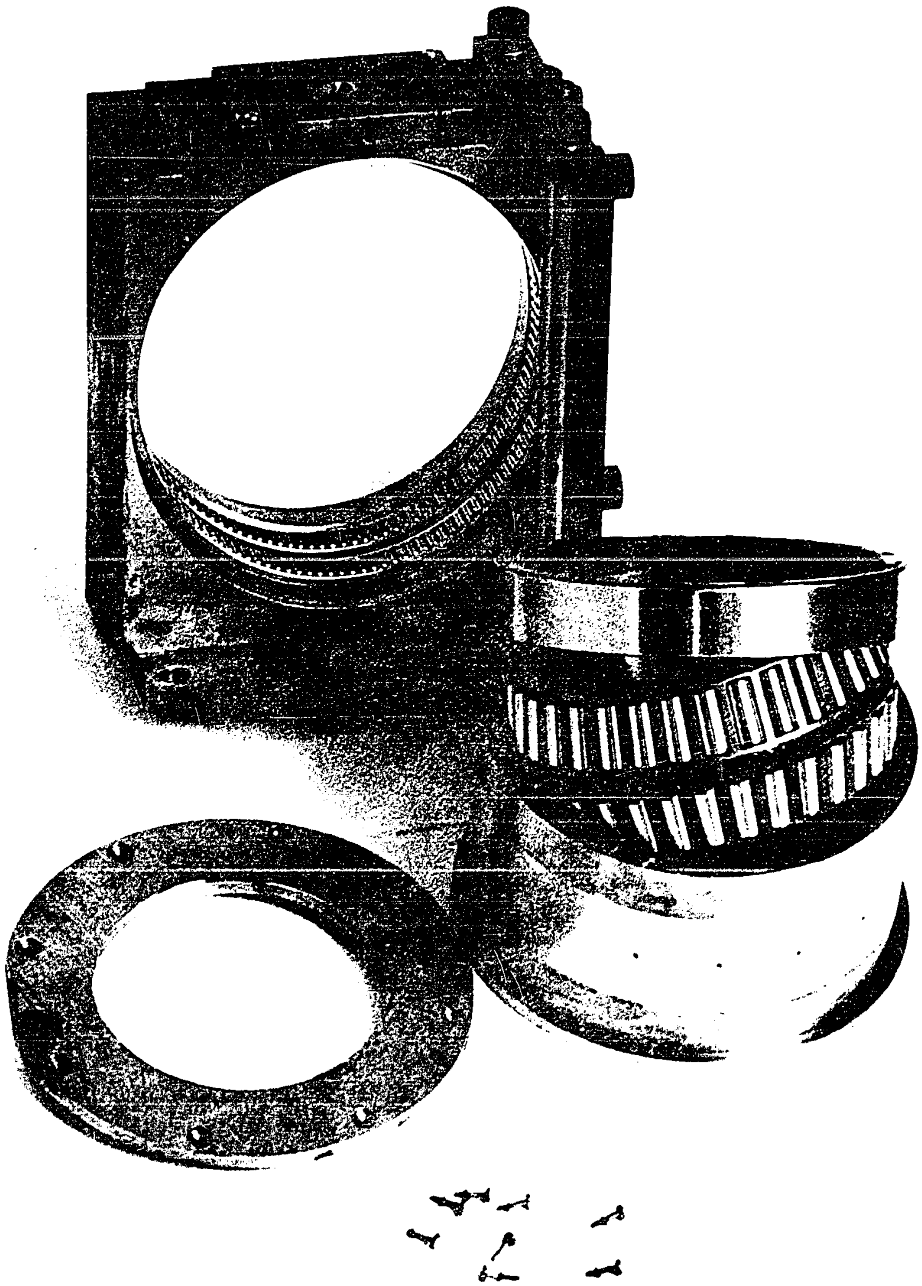

FIG. [illegible]

Bearing Dynamometer Components.

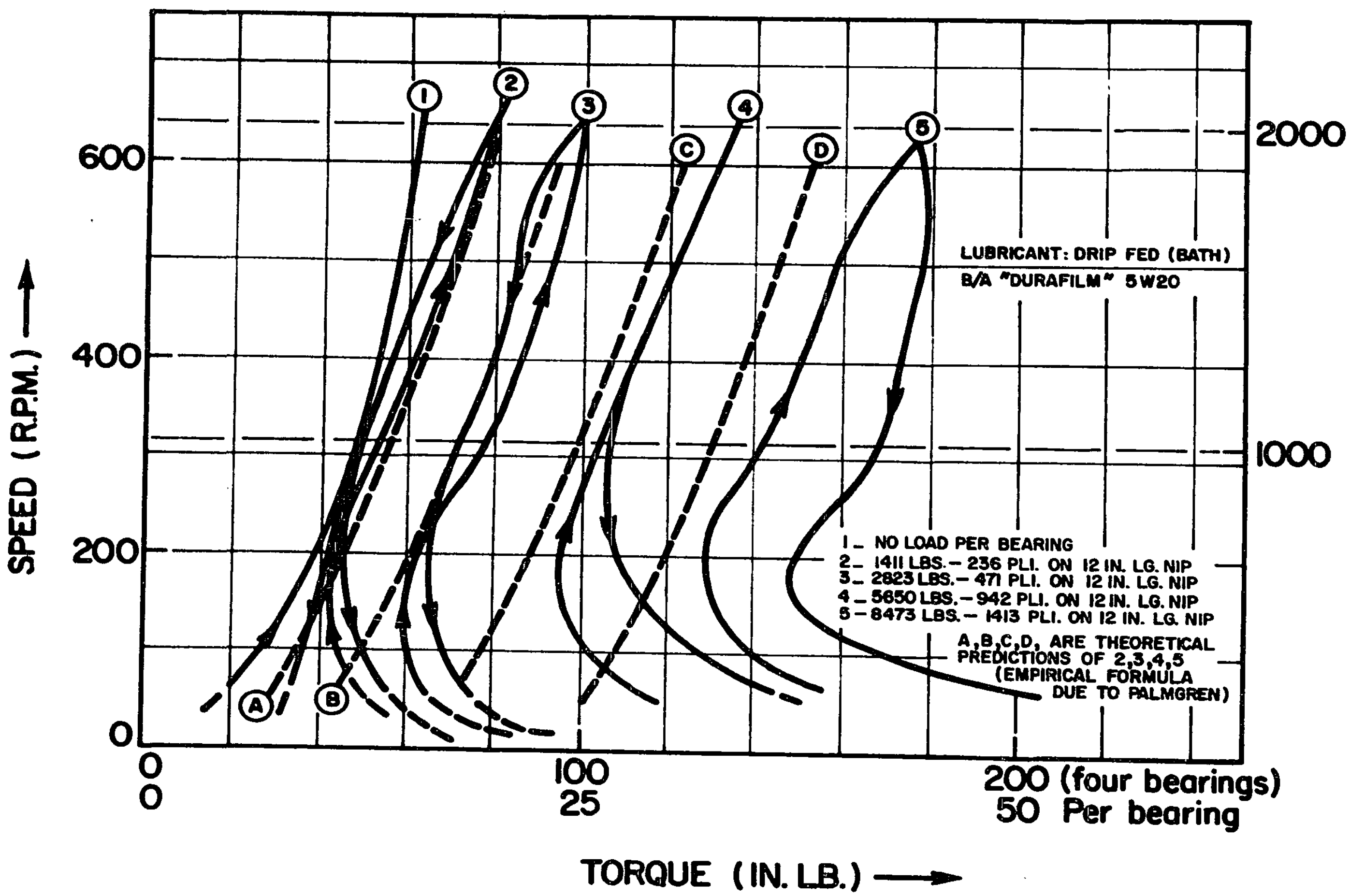

FIG. 115.

Friction Characteristics: Timken "TDI" (M224749D-M224710)

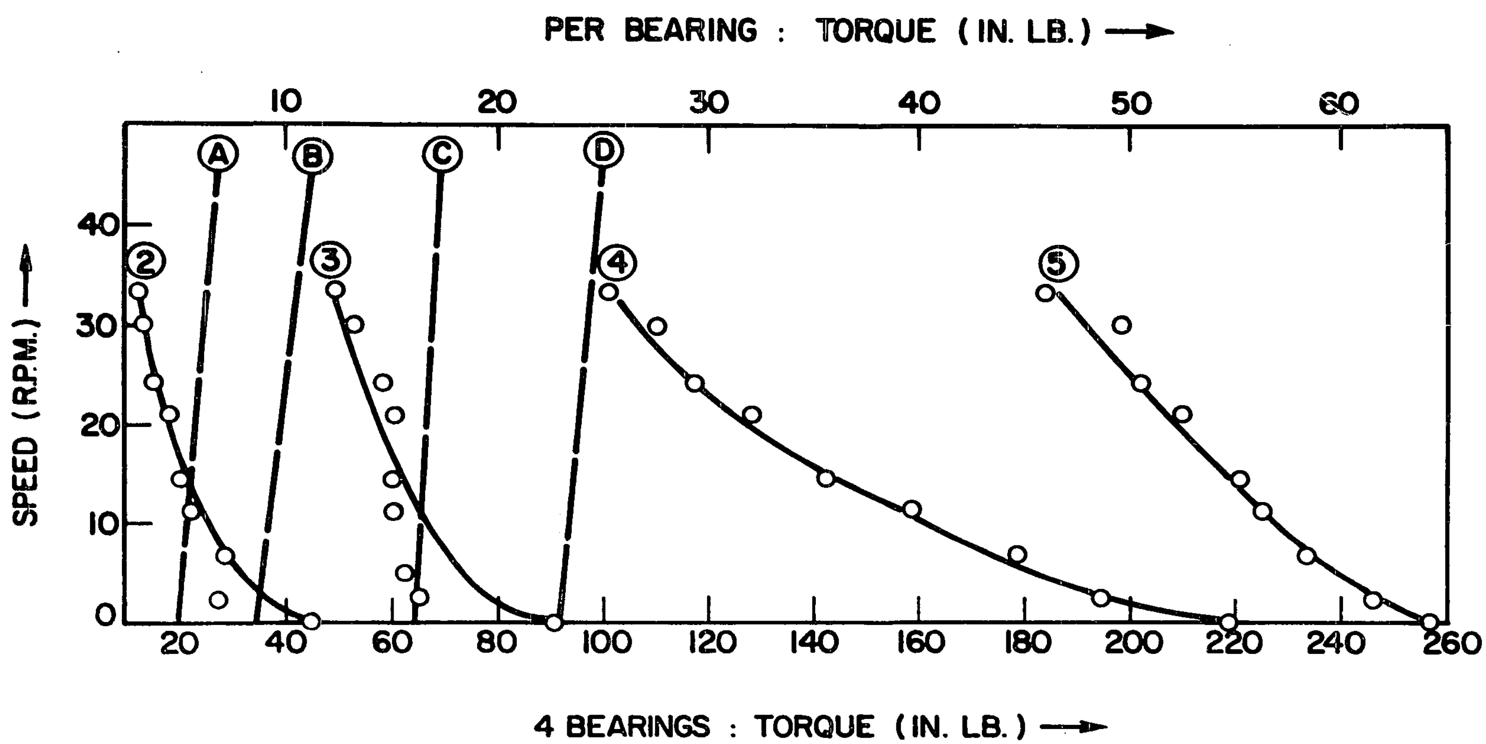

FIG. 116.

Friction Characteristics: Timken "TDI" (M224749D-M224710)

1) Data points shown in Figs. 115-116 are the averages of 2 to 5 tests in which there was considerable variation. Nevertheless, average values of bearing friction are seen to be continuous and reasonable functions of load and speed.
2) Fair agreement is noted, above 100 rpm., between friction torque predicted by an empirical formula developed by Palmgren (30) for rolling element bearings.
3) The opposing effects of lubricant viscosity decrease and bearing preload increase with operating temperature are indicated in load characteristics shown in Fig.115, i.e. the loops formed by connecting data points taken at a given load in a succession of steps of increasing, then decreasing speed.
4) The effect of hydrodynamic film lubrication, or more exactly, its absence, which was neglected in Palmgren's formula, is clearly shown by a decrease in friction torque with increasing speed up to about 200 rpm. This illustrates the initial importance of hydrodynamic film development with increasing speed. Once complete films have been established, the torque increases with increasing speed due to lubricant viscosity become evident.
5) The low speed torque measurements are a smooth continuation of the data taken much earlier at higher speed.

Although not directly relevant to supercalendering, these observations based on bearing friction measurements are presented to convince the reader that the random, unrepeatable data presented in this work are in fact a true reflection of supercalender nip behaviour and are not due to gross experimental incompetence and error.

The effect of bearing friction

It was soon discovered that a supercalender, started up quickly and run at constant speed and load exhibits a decreasing drive torque requirement of the approximate form

$$\Gamma = Ae^{-kt} - B$$

e.g. A = 220, B = 350 and k = 1/20 for Γ in lb.in. and t in min. for a two nip stack with 8in. diameter steel rolls and roll D running at about 500 pli. and 1000 ft./min. as shown in Fig. 117. Not shown on this plot are the ± 5% torque fluctuations which were recorded. This relationship cannot be used to determine supercalender torque vs. speed and load characteristics; most of the torque is due to bearing friction. By running a lightly loaded (about 345 pli. = 6560 lb. force/19in. long nip) steel-on-steel nip which can be assumed to be frictionless, it was found that most of this high starting torque can be eliminated by substituting drip-fed 5W20 motor oil for the original packed grease lubrication. For a specific load and speed (3280 lb./bearing at 480 rpm.) the initial bearing friction was decreased by over 60% as shown in Fig. 118. In spite of this improvement, bearing friction remained a large, if no longer predominant, part of drive torque. Strong dependence of bearing friction on load and speed remained, adding a false variable to the measurement of nip friction.

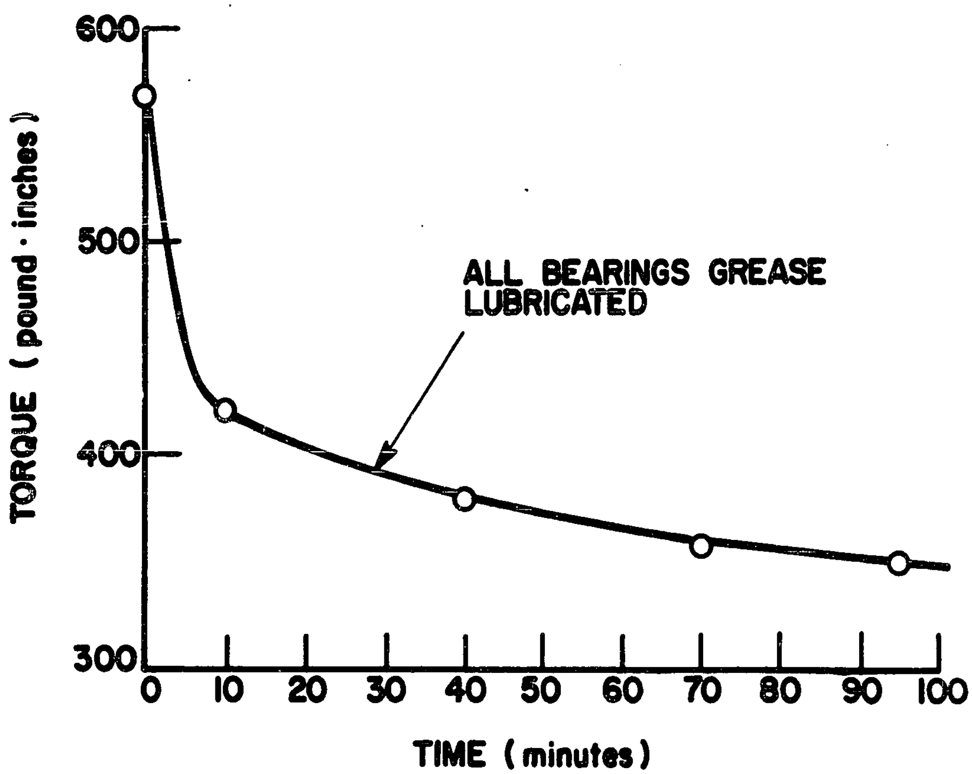

FIG. 117.

Total drive torque as a function of time for a three roll supercalender with a steel-cotton-steel roll configuration. Calender speed 965 f.p.m. Total nip force 550 lb.f. over a nip length of 12in.

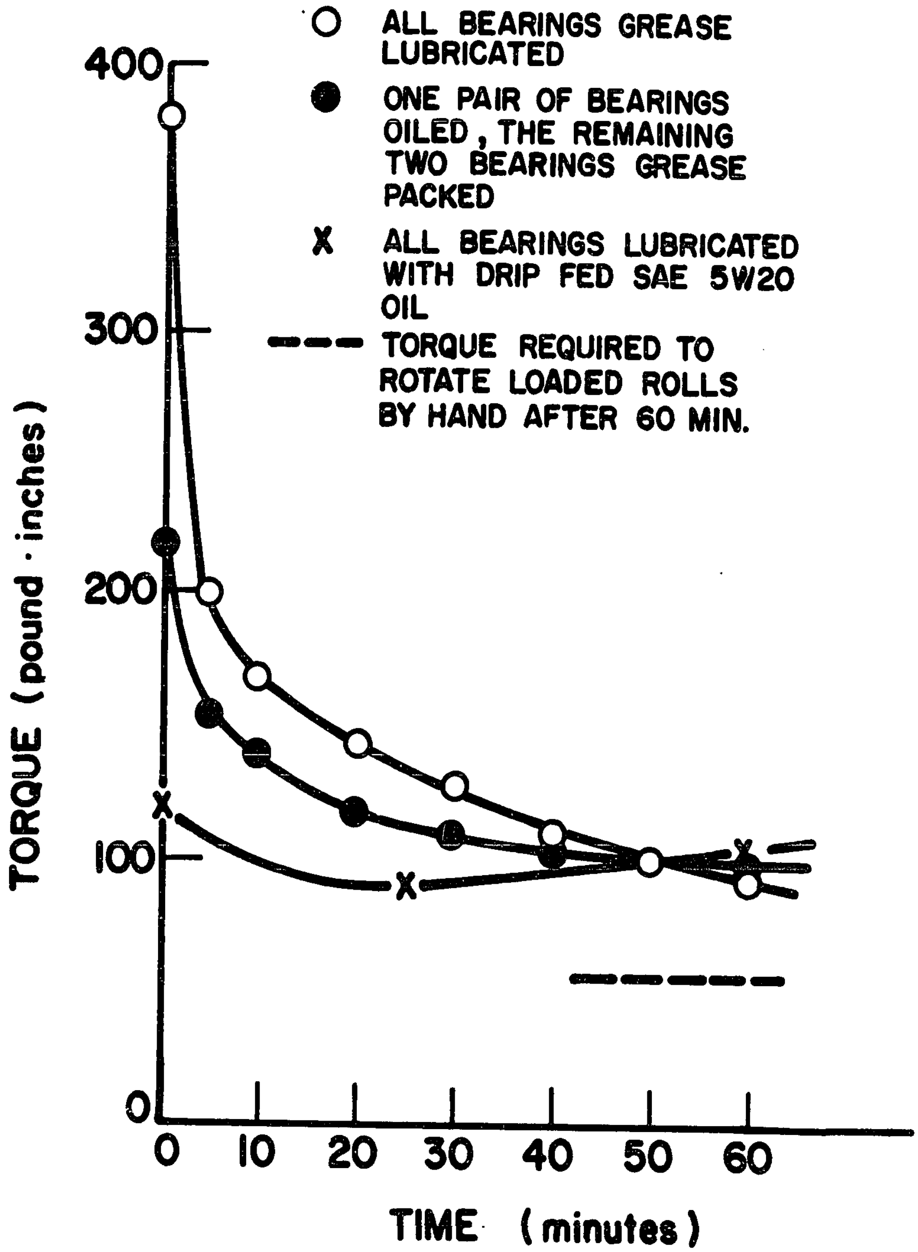

FIG. 118.

Total drive torque as a function of time for a two roll supercalender with a steel-steel roll configuration showing the effect of different types of bearing lubrication. Calender speed 1000 f.p.m. Total nip force 6560 lb.f. over a nip length of 12in.

Bearing calibration

In order to measure nip friction, bearing torque had to be measured somehow and subtracted from the gross torque input to the stack. As previously mentioned the direct measurement of bearing friction contribution proved impractical and a bearing calibration experiment was conducted. The apparatus for these tests is described in Fig. 8. Measurements of the torque necessary to drive four uniformly loaded bearings were made at speeds, varied in seven steps, from 75 rpm. to 750 rpm. Each test was performed at a preset oil feed rate of about 30 drops per minute per bearing. Speed was maintained at each step until approximate thermal equilibrium was reached, then the speed was increased to the next step. This procedure was reversed and torque measurements were made at steps of decreasing speed. Certain erratic behaviour was observed in that one or more bearing block temperatures would, during a test, differ considerably from the others, requiring adjustment of the lubricant feed rate. This behaviour persisted in spite of attempts to impose uniform thrust preloading on the bearings. Tests were carried out at 0, 1415, 2830, 5660 and 8480 lb./bearing. These loads were convenient as they represented pneumatic loading ram pressures of 0, 50, 100, 200 and 300 psi. respectively, and covered a specific nip load range of up to 1500 pli. for a 12in. long nip. Tests at each load were repeated, some as often as seven times. Later, when the stack drive had been modified for low speed operation, another series of bearing calibrations were performed. These tests were carried out at speeds between 2 and 40 rpm. which is equivalent to 10 to 125 fpm. with a 12in. diameter roll. Tests were conducted to determine the torque necessary to initiate rotation of statically loaded bearings, i.e. "breakaway" torque was measured at bearing loads of 0, 1415, 2830, 5660 and 8480 lb./bearing.

Bearing dynamometer

An instrument developed for use in the supercalender test series is the bearing block dynamometer. Although prototype instruments did not operate satisfactorily, a description of this device is relevant in that a similar dynamometer was developed and served as the principal instrument used to measure bearing friction torque in a project on hydrostatically augmented hydrodynamic journal bearings which was carried out using the supercalender test apparatus (C.R. Weldon, Department of Mechanical Engineering, McGill University: M.Eng. Thesis, 1971). Furthermore, further tests on the supercalender will incorporate dynamometers on the roll bearings as it has been demonstrated that this is the best way to account for bearing friction in any apparatus where drive torque absorbed by processes other than bearing friction must be measured.

The purpose of the bearing block dynamometer is to torsionally isolate roll shaft bearings so that friction in these bearings can be measured as the torque necessary to restrain the free sleeves which surround the bearings under test. Ideally the principle might be described as a frictionless bearing supporting a test bearing. This could be accomplished by supporting the roll bearings in hydrostatic bearings. Such a technique, although admittedly attractive, would have required a hydraulic supply and control system to feed pressurized lubricant to the hydrostatic bearings. Expense and an accompanying digression into hydrostatic bearing design rendered this solution impractical.

The prototype bearing dynamometers involved a relatively simple modification to the existing bearing blocks. These blocks, already pared to minimum size, were bored to accept a pair of 7 3/4in. outer diameter needle bearings. To form the inner race of these needle bearings, a sleeve, 7 1/4in. outer diameter, was provided. As the bearing surface, a circumferential belt of 0.025in. thick, hard chromium plating was applied to the outer surface of this sleeve and ground to size. The bore of this sleeve contains the double row tapered roller bearing which supports the roll shaft. Sixteen equidistant 1/8in. diameter radial holes drilled through the sleeve wall oil, supplied through the top of the bearing block to the bore containing the static needle bearings, to lubricate the roll bearing. The tapered roller bearing assembly is held in place within the sleeve by two flanged and stepped end caps attached to the sleeve by eight screws which fasten axially into the ends of the sleeve wall. The flanges of these end caps keep the needle bearing inner race/roller bearing assembly in place in the bearing block by constraining axial motion. The assembled bearing block is shown in Fig. 113 with the flange cap attachment screws clearly visible on the front face.

The bearing friction torque measurement principle is outlined in Fig. 111. Anchored to the free sleeve between the two concentric bearings is a wire which supports a lead weight. The shaft rotation, hence friction torque, is in the clockwise direction. Under the influence of any friction torque, the wire will tend to assume an equilibrium position to the left of bearing centre so that the restoring torque (W x A) counterbalances the friction torque. Restoring torque read-out is via a linear-variable slide-wire resistor across which is applied a constant voltage, E_c. The variable voltage signal, E_V, across the slider and one end of the resistor is proportional to the weight offset, A, and hence to the restoring torque (W x A). Although the needle supported interface cannot be considered frictionless as could be an externally pressurized hydrostatic interface, it is static therefore free from viscous friction effects which contribute to rolling element bearing losses. Furthermore, if the friction of the needle bearing is assumed to be identical, under conditions of impending rotation, in either direction, these conditions of limiting friction can be imposed on the dynamometer sleeve by an externally applied torque. The true friction torque of the roll bearing can be validly taken as the arithmetic mean of the two torques measured at conditions of impending rotation in opposite directions.

Operating problems arose at nip loads over 500 pli. The enlargement of the bearing block bores involved a partial breakout of the thin wall. The static needle bearings were thus unsupported over an arc of about 30°. This unfortunate feature is visible on the left side of the bearing block in Fig. 112. A stiffening rod was incorporated as an attempt to overcome load distortion effects. Sufficient deformation of the dynamometric bearing blocks occurred at loads over 500 pli. so as to introduce appreciable friction in the static needle bearings, thus obscuring the roll bearing friction even when the method of externally applied opposite torque was used to measure the range between the limits of static friction in either direction.

APPENDIX V

Description of Equipment, Test Apparatus and Instruments

This section is included in detail because a large portion of this project was comprised of equipment design and test instrumentation planning. It is considered, therefore to be a major engineering contribution to this thesis.

DESCRIPTION OF EQUIPMENT, INSTRUMENTS AND TEST APPARATUS

Unsuitability of conventional industrial and laboratory supercalenders for use in an experimental program

Any industrial supercalender is designed for a specific application. For example, a glassine stack with hard denim and chilled iron rolls designed to operate at 1000 ft./min. and 3000 pli. is not equipped to duplicate the conditions required to process gloss paper being run at 500 ft/min. and 500 pli. between chrome plated steel and soft natural cotton filled rolls. Conversely a gloss calender cannot operate as a glassine calender.

If an experimental study of supercalendering is undertaken it is necessary to approximate extreme as well as typical operating conditions. Furthermore it is desirable to run all tests on the same machine. In this way the effects of frame stiffness, motor characteristics and drive train behaviour will be uniform. (By "uniform" it is not implied that dynamics of the stack can be discounted as constant over all operating conditions in a given machine, but that variations will be continuous and sufficiently small so that significant effects on supercalendering action of roll material, speed and nip load can be at least qualitatively evaluated.) If tests were run on a number of different machines it would be impossible to determine what proportion of a measured difference in behaviour was due to stack differences. The purpose of this experimental study is to evaluate nip effects over a wide range of nip properties and operating parameters. To instrument a number of industrial supercalenders and schedule many hours of special test runs would be prohibitively expensive. To design, equip, instrument, build and man a small, flexible industrial sized stack would, as an initial step in this project, be unthinkable.

The only form of small scale commercial equipment available is the laboratory supercalender. Such units are normally of single nip and occasionally of two nip configuration. A single hydraulic pressure system loads both sides of the stack and the drive train is not suitable for dynamometry. High nip loads and more specifically accurate control of nip load are not available. A 10:1 speed range is maximum. The roll bearings have small inner diameter making it difficult to provide roll bores for instrument access. The bearing blocks are large, severely limiting the minimum roll diameter which can be installed. Axial view of the nip is obscured.

Probably the most serious deficiency of commercial lab stacks is the capped double frame. To change the test instrumented filled roll, which is at the bottom of the stack, it is necessary to first remove the frame caps, disconnect the drive train and lift out the top roll. To sum up, commercial supercalenders are unsuitable as test apparatus. They are intended to run paper in a mill or test hand sheets in a mill laboratory. They are not suitable for conducting experiments on supercalender nip mechanics. It was therefore decided to design and build a small, flexible and well instrumented supercalendering test apparatus.

The experimental laboratory supercalender

This lab supercalender was designed after a year of test, design, and operating experience on a small lab stack which was modified and instrumented for a series of tests on heated rolls. This test series was preliminary to the nip mechanics study which is the subject of this work. These preliminary experiments clearly showed the need for an experimental supercalender designed specifically for instrumentability and quick set up and roll change by one unskilled operator (the experimenter) with a minimum of handling equipment.

The bed of this new supercalender is made entirely of structural steel plate and rolled sections. A minimum amount of welding was required for reinforcement and gusseting. Bolts, with roll and taper dowel pins for accurate location, were used throughout in frame assembly. Although the frame weighs about two tons the heaviest component weighs less than the drive motor. The complete test apparatus including motor and instrument cabinetry can be manhandled and moved with a small hand truck and will pass through ordinary doorways. When assembled the apparatus and ancilliaries, weighing about eight tons, require 400 ft.^{2} of floor space.

The subframe (DWG.: SC-C-0001) consists of four 20in. I-sections. The two outer pieces (5) are four feet long and with the two 8ft. long centre pieces (1), which support the drive motor platform, form the base for the calender ways. The ways were formed by cutting away and machining a length of the centre portion of the upper flanges of the two 8ft. long 18in. ship channels (2) lying across the four I-beams. Rigidly separating the ways are two 3/8in. lightened plates (4) which span the gap between the two channels.

Two 6in. channels (6) lying parallel to the ways and across the protruding centre I-sections form the motor platform. By this arrangement the motor position can be conveniently adjusted to drive any roll in the stack.

A heavy gusset reinforced 8 x 8in. structural angle (8) is mounted across the 18in. channels at one end of the ways to support the roll stack. At the other end of each channel is a base plate (11) for each of two stack loading pneumatic cylinders. The position of the two cylinders with adjustable rod ends (1) and the stack end spacer blocks (3) (4) (5) (6) (7) and shims (8) are shown on DWG.: SC-C-0003.

Nip load instrumentation and control will be dealt with under the section on stack instruments. The nip loading mechanism is, however, stack hardware. Mounted on their previously mentioned base plates are two 6in. diameter by 4in. long stroke pneumatic cylinders which can provide a combined force of up to 12 tons. The choice of a pneumatic rather than hydraulic system was based on cost and convenience. The additional cost of larger cylinders was more than offset by the use of lighter, more flexible piping which was suitable for the maximum design pressure of 750 psi. Typical hydraulic systems operate between 2000 and 4000 psi. As no motors, pumps, compressors or filters are required in this system, their cost is avoided and their maintenance unnecessary.

Nip force is applied at the beginning of a test and released only upon its completion. The mass flow required in the system is very low. Low pressure test runs and ram retraction are served adequately by the building compressed air supply facilities. Pressures above 100 psi. are supplied from a manifold connected to five high pressure nitrogen cylinders (2500 psi.). The use of nitrogen permits the safe use of some hydraulic fluid in the cylinder voids on either side of the piston. "Stack bounce" which occurs occasionally as the result of elasticity in the loading system (in this case provided by "pneumatic springs") and irregularities in the filled roll surface, is thus controlled.

A standard roll shaft end has been adopted for all steel and filled rolls (DWG.: SC-B-0001). These shafts are disproportionally large in diameter to accommodate a 3in. diameter roll bore for signal leads from thermometric instrumentation mounted in the filled rolls and also to provide alignment clearance for the drive system. The roll bearings fit over the shaft ends with a cylindrical clearance rather than a more conventional tapered locking fit. Retaining rings spring loaded into grooves in the roll shaft which are on either side of one bearing prevent axial movement of the roll. The other bearing is axially unconstrained so as to permit thermal expansion without accompanying stress. Unfortunately, rotation of the shaft relative to the bearing bores can occur under conditions of high speed and light load in the presence of sufficient quantities of inviscid lubricant. This is not desirable as it results in erratic torque measurements at conditions between stable floating of the bearing inner race and synchronous rotation with the roll. Paradoxically however, the choice of cylindrical shafts over tapered shafts made possible, indirectly, the accurate measurement of nip friction.

The original steel rolls were 8in. in diameter with a 19in. long face. Later, to provide clearance for an X-ray film holder used in one of the test series, one roll was sleeved to 12in. diameter and 12in. face length. Although the stack was originally provided with two 8in. diameter steel rolls to operate with a 12in. diameter filled roll, the test program, which was geometrically constrained by the X-ray tests, was run completely in single nip configuration with 12in. by 12in. rolls throughout.

Although spherical self-aligning roller bearings would have been a better choice to facilitate the interchanging of test rolls and to ensure equalization of nip loading on either side of the stack, double row taper roller bearings were chosen. Again, the X-ray tests, which required an unobstructed axial view of the nip, were a critical influence. To meet this requirement small bearing blocks, hence small bearing outer diameters, are necessary. This coupled with the unusually large inner diameter of the roll shaft left little room and a bearing choice with no alternative (DWG.: SC-C-0002). (As relief, albeit temporary, from the boredom imposed upon him by his task, the reader is invited to make a more suitable choice of.....bearing, not task.) The bearing blocks are asymmetrical, one side is cut thin to further enhance the view of the nip, the other side is thicker to support the applied stack load. A machined groove in the bottom of each bearing block, perpendicular to the bore axis, aligns the stack on the ways.

The calender drive motor is controlled by a modified Ward/ Leonard system. This 30 hp. 230v. shunt-stabilized d.c. drive operates over a 40:1 range of speed regulation up to 1150 rpm. and can be switched to operate up to 2600 rpm. Motor overload protection is provided. Power is supplied by a d.c. generator with residual bucking field which permits the drive to operate down to 0 volts. The generator is driven by a 40 h.p. 550v. 3-phase motor with overload and low mains voltage protection. Drive motor speed is controlled by varying the generator excitation. A silicon controlled rectifier power supply varies the generator field so that linear acceleration and deceleration to the preset speed is obtained. There are emergency stop buttons at six locations to provide protection for the operator and equipment. Regenerative braking is provided. An auxilliary power supply maintains constant voltage for motor excitation and to the bucking field of the generator.

Unlike the roller chains, V-belts and pulleys, gears or shaft couplings commonly used in supercalender drive trains a unique drive configuration was designed. The following criteria had to be met:

1) In order to accurately measure nip rolling friction the dynamometer must be located so as to eliminate spurious friction contributions.

2) The dynamometer must be protected from shock loads such as may be introduced by backlash and sudden changes in speed and nip load.

3) In order to change rolls conveniently the drive must be easy to dismantle.

4) Large axial, lateral and angular misalignments must not interfere with smooth operation. These misalignments must be tolerated so that drive position can be conveniently moved to any roll in the stack.

The drive arrangement illustrated by DWG.: SC-C-002SA** and DWG.: SC-B-003SA meets these specifications. The main feature of this drive is a 32in. long 1in. diameter quill shaft which passes through the 3in. diameter axial bore of the driven roll. A sliding keyed fit in the quill end stubs provide over 1in. of unhampered axial movement. The lin. annular clearance between the roll bore and quill permits lateral offset up to lin. as well as angular misalignment of either the motor shaft or the roll axis and the quill up to 1 1/2° in all directions. The drive is therefore self-aligning in five degrees of freedom. (The sixth degree of freedom is rotation about the roll and motor axes which is, of course, unlimited.) A typical working twist of the quill is 17°. This twist can be tripled before the onset of torsional yielding. For good fatigue endurance the high strength steel shaft has been annealed and the surface shot-peined. Shaft articulation is provided at the motor and dynamometer ends by two sets of automotive type universal joints. A more radical design, with two homokinetic couplings which were sufficiently compact to permit their withdrawal, along with the quill shaft, through the roll bore, was prepared. This plan was rejected as the additional cost of manufacture was thought to be unjustified by the gain in experimental convenience. The advantage of a constant speed intermediate drive member, which is the usual reason for choosing a homokinetic rather than yoke and cross universal coupling, was in this case negligible considering the light quill, low speed of operation and small misalignment involved. It is interesting to note that the relatively small offset (at times 0°) between either the roll or motor shaft axis and the quill made necessary the modification of the automotive universal couplings. This was unforeseen and would have been unnecessary had the homokinetic coupling been adopted. A universal joint is commonly equipped with four needle roller bearings. If such a coupling is operated under load and exclusively at small offset angle, a premature failure will result. This occurs because the arcs of excursion, through which adjacent needle rollers oscillate, do not overlap and the bearing race is not uniformly cold worked, thus fatigue endurance is reduced. The modification of the drive couplings involved the replacement of the rolling bearing elements with conventional aluminum, grease lubricated sleeves.

The driven roll is connected to one of the universal joints through a blank cylindrical annulus (DWG.: SC-A-0004*) which is bolted to and concentric with the roll shaft end. The universal coupling is fastened on to the inside of the removable end plate (DWG.: SC-A-0005*) which forms the bottom of the blind sleeve mentioned above. The representation of the detail (DWG.: SC-A-0004*) is simplified on (DWG.: SC-C-002SA**). This is a subassembly (DWG.: SC-B-003SA) which contains the torque cell/dynamometer which is also annular in shape so that the drive quill and coupling can pass through it. Thus the only friction producing interfaces downstream of the dynamometer are the nips and stack bearings. This assembly will be further described in the subsection on stack instrumentation.

Stack modifications

In addition to the operating hardware described above, two major stack modifications were required during the course of the tests.

The first modification was to enable the calibration of the stack bearings (i.e. measure bearing friction over the full range of operating condition). This set up is shown in Fig. 8. A dummy roll or annular shaft was connected to the drive in the position of an ordinary roll. The shaft, unlike a conventional roll, carried all four bearings. A large WF beam section was laid, web horizontal, across the ways to fill the gap normally occupied by the filled roll. This permitted the measurement of friction torque of a system consisting solely of bearings, loaded and driven as they would be when operating conventionally. This set up illustrates the adaptability of the test apparatus. Note the manufacturing costs and difficulties that would be incurred by the bearing calibration test had tapered bore bearings been chosen. Hence the resolution of the apparent paradox mentioned above.

The second modification, to enable very low speed and "breakaway" (i.e. the limit of static rolling friction) tests to be conducted, was the installation of a 25:1 double gear reduction unit between the end of the motor shaft and the first universal joint in the drive train. Because the motor platform had been designed to accept various motor positions, this installation, shown in Fig. 7, was little less convenient than a normal roll and motor position change.

Stack control and instrumentation

In this section the nip load application and measuring system will be discussed along with instruments and operator controls used to regulate and measure drive torque and roll speed.

Nip load is applied to the stack by applying pressure to the rear ports of the pneumatic cylinders mentioned in the previous section. A good illustration showing the stack in two-nip configuration and the cylinders, five high pressure gas cylinders and the pressure control panel is Fig. 9. Five flexible 1/4in. diameter copper lines enter the control panel. Two supply loading pressure, independently, to the two cylinders, a third is shared by the cylinders and supplies air ahead of the pistons in order to retract them. The fourth line supplies high pressure nitrogen for loading pressures above 100 psi. while the fifth is a connection to the 100 psi. building compressed air service.

The layout of the loading pressure control panel, Fig. 10, is as follows. High pressure, above 100 psi., is supplied from the nitrogen cylinders (A) and enters the system via a pressure reducing and relief valve (B), provided with up and downstream pressure gauges, capable of supplying outlet pressure up to 750 psi. Below this reducing valve is a flow throttling needle valve (C) and a shut off cock (D). The high pressure supply branches (E) into the two separate legs which lead to the two pneumatic loading cylinders. Low pressure air at 100 psi. enters the panel through another line which first passes through an air filter (F). This line, equipped with a gauge (G) to monitor the low pressure supply, joins the high pressure line above the aforementioned branch (E). The low pressure inlet can also be isolated by a shut off cock (H). A check valve (I) prevents the escape of high pressure gas into the low pressure inlet. Either low or high pressure loading is supplied to either cylinder through separate check valves (J) and (K) and shut off cocks (L) and (M). The two sides of the stack can be loaded under equalized pressure by opening the shunt (N). The two loading pressure lines (O) and (P) can be monitored by separate gauges (Q) and (R). A third gauge (S) can be connected to either of both legs of the stack loading system through a confluent network containing the two shut off cocks (T) and (U). Isolation is provided by the three check valves (V), (W) and (X). (Y) is a safety valve which protects the low pressure side of the system from overload. All three gauges have individual vent valves (Z), (AA) and (AB). Low air pressure is also supplied to pressure reducing valve (AC) and gauge (AD). This valve is used to retract the loading pistons by applying low pressure air to the front ports of both cylinders through line (AE). Both pressure reducing valves (B) and (AC) provide relief (back flow venting) upon the reduction of loading pressure.

Originally it was intended to measure nip load by measuring force reactions at four corners of the stack. This was to be accomplished by attaching eight SR-4 wire strain gauges to the stack end spacer blocks (DWG.: SC-C-0003). The upper-most gauges are visible in Fig. 11. Each spacer block was equipped with two four-arm resistance strain gauge bridges with an adjustable trimming resistor. Load at each corner of the stack was to be measured as proportional to the cumulative out of balance voltage signal from the two resistance networks. A constant voltage of 10 v. was supplied to each bridge by a regulated d.c. power supply (±.02%). A complete nip load cell circuit is shown in Fig. 119. This load measuring system which was to give continuous nip force measurements at the four corners of the stack and to provide a compatible instrument signal for measurement by the automatic data logging system described in Appendix I, did not function satisfactorily. As the stack heated up under operation, thermal gradients were set up in material to which the strain gauges were attached. These effects were sufficient to overshadow the useful signal due to strain effects. This problem was not overcome in spite of attempts to control thermal effects by using "controlled melt" thermally compensated gauge elements, installing miniature gauges (1/4in. x 1/2in.) and trying various schemes to isolate or insulate the gauged areas. Fortunately a "cold stack" calibration was obtained (i.e. correlation between the measurements of the load cells, which had been calibrated in a hydraulic compression tester, and the precision test gauge in the pressure control rack Fig. 10) while the calender was not running. This gauge and the two side gauges were found to be satisfactory means of measuring the

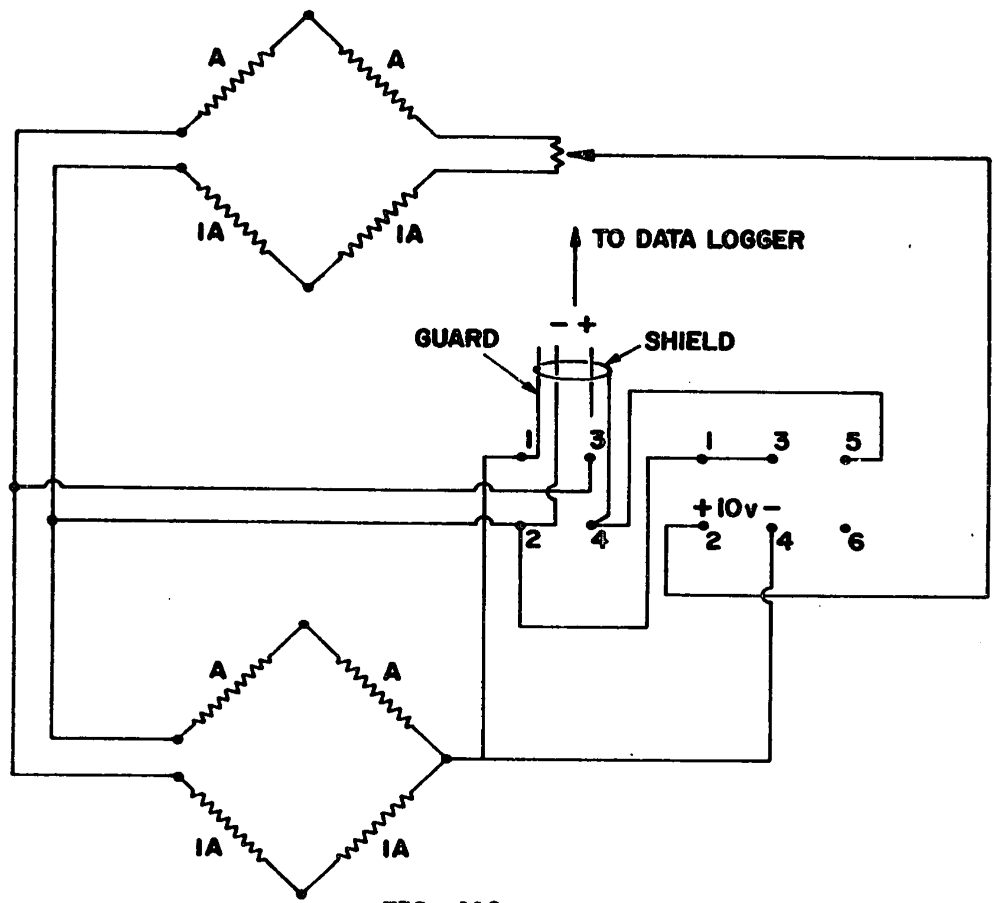

FIG. 119.

Nip Load Cell Circuit.

stack load on either side although not, as it was originally hoped, capable of making force measurements at all four corners. Using pressure gauge reading as an indication of nip load made it necessary to hand log this data rather than enabling the use of the more convenient multipoint data logger. However it was found easy to keep the nip load quite constant throughout a given test run, requiring little attention and few manual adjustments to the pressure control system.

Drive torque is measured by a reaction type bonded strain gauge torque cell shown in DWG.: SC-B-003SA. Fig. 9 shows the torque cell at left centre as a discontinuity in the cylindrical drive sleeve on the far end of the driven roll. This type of dynamometer is normally used in a application where a motor is supported by the torque cell with the power shaft protruding through the bore. Torque is measured as the torsional reaction of motor frame on the supporting member. In its application as a supercalender dynamometer this unit is an integral member of the drive train and rotates with the roll. No mount, requiring careful positioning, has to be provided as there are no bearings or slip rings as there would be if a conventional pedestal mounted shaft dynamometer were used. An additional advantage is thatthe dynamometer is designed to accept overhanging or shear loads. Power and signal leads rotate with the driven roll. A separate instrument slip ring assembly, supported by a bracket attached to the roll bearing block, forms the rotating-to-nonrotating interface in the instrument circuits. The stationary signal and power leads and the slip ring mount are clearly visible in the lower right foreground of Fig. 9. A flexible plastic tube is the coupling between the slip ring shaft and the sleeve containing the dynamometer. This tube accommodates any misalignment between the slip ring and driven roll axes.

The torque cell has the following specifications:

- Lebow Associates, Inc. Reaction Torque Cell #2406-101
- Output: linear to 40 mv. at 10,000 in.lb. torque
- Input: 20 v.
- Capacity: 10,000 in.lb. maximum with 50% overload provided
- Type: temperature compensated bonded wire strain gauge, single full bridge.

The instrument slip ring assembly has the following specifications:

- Northern Precision Laboratories #800050-1
- Number of conductors: 6 (4 used)
- Speed range: 0-3000 rpm.
- Ring material: coin silver
- Brush material: silver/graphite
- Maximum noise: no greater than 0.5 μv.

The torque cell was statically calibrated by applying dead weight loads to 1000 lb. in 25 lb. increments on a 10in. long arm of the calibrating yoke as shown in Fig. 12. Overhanging load and hysteresis (up-down) corrections were found to be negligible (about 1 lb.in.). The overhanging load test was performed by hanging 25 lb. weight increments on both calibrating arms of the yoke, up to 500 lb.

Each roll in the stack was equipped with a tachometric pulse generator. The angular velocity of each roll can thus be measured. The primary sensors proved to be inexpensive as well as effective. Each tachometer consists of a 72 tooth, 6in. diameter cast iron gear as shown in Fig. 11. The sensing heads are attached to the bearing blocks on adjustable supports so that each sensor can be brought tangentially to its gear and adjusted to the required clearance of 0.015 to 0.025in. The sensors are ordinary telephone receiver cartridges from which the ferrous diaphragms have been removed. The active element of the instrument is a small, permanent U-magnet around whose elbow is wound a coil. As gear teeth pass beneath the pole pieces of the magnet while the roll is rotating, a voltage is induced across the terminals of the coil. Thus the frequency of voltage fluctuation measured across the coil terminals is 72 times the speed of the roll in revolutions per second. This frequency signal was found to be suitable, without amplification or conditioning, for direct measurement by the data logging system. As the resolution of the frequency measuring function of the data logging equipment was ± 1 pulse count down to a lower limit of 20 Hz., roll speed could be determined to ± 5% at the lowest direct drive speeds. Measurement accuracy at a typical high operating speed was about ± 0.2%. For operation at very low speeds via the 25:1 gear reducer only a single tachometer unit was used. This instrument was mounted on the motor shaft which turns at 25.81 times the speed of the driven roll (i.e. the actual drive speed reduction ratio). Typical precision of speed measurements made in this operating configuration was ± 0.5%.

X-RAY INSTRUMENTATION FOR FILLED ROLL DEFORMATION MEASUREMENT

The subsurface deformation of a supercalender filled roll in the nip region in a specific transaxial plane was measured using a high speed X-ray apparatus. Radiograms taken while the supercalender was operating were used to map the disposition of an array of small dense metal spheres embedded within the filled roll. In this section the X-ray unit and accessories will be described. The X-ray test apparatus can, for convenience, be subdivided into four component groups. The major group is the X-ray unit itself consisting of the high voltage power supply, delay trigger amplifier, pulser, tube and tube head and the nitrogen and Freon high voltage insulation systems. The second subsystem consists of the film holder or cassette and a special fixture for film preparation. The third group to be described is the calender mounted firing circuit and interlock. Fourth is the radiation monitoring equipment which ensures safe and reliable operation of the X-ray unit. The X-ray unit is a 300 kv. cold cathode flash X-ray system. In a conventional X-ray system, radiation is produced by a low current, high voltage electron beam bombarding a metal annode. These electrons are the result of thermionic emission from a heated cathode. The beam is accelerated and collimated by electromagnetic and electrostatic fields. Typical metallographic units produce high radiation doses and require extensive shielding. Many seconds of irradiation are often necessary with this type of apparatus to penetrate even a few inches of metal and to obtain an acceptable radiogram. Such a device is clearly not suitable for operation in an open laboratory environment without radiation shielding, nor can it be used to record objects moving at up to 30 ft/sec. which must be located to within a few thousanths of an inch. The field emission flash X-ray (44) used in this work operates with a maximum cathode current of 1.4 kiloampères. The electron beam is, in this case, produced by the discharge of 15 high voltage capacitors connected in series across the gap in the flash tube. A mean X-ray output voltage of between 150 to 300 kilovolts can be obtained by varying the initial charge voltage applied to the capacitor bank. X-rays are produced for a time interval of only 10^{-8} seconds. Peak radiation is 10^8 Röengtens/sec. at the tube face. These characteristics make this unit suitable for recording high speed events. Sufficient radiation is produced to penetrate 10 inches of filled roll material and resolve a 1/32in. diameter metal sphere on film some 25 inches from the tube face.

To produce X-rays of 300 kv. average voltage the peak voltage across the capacitor bank or pulser must be about 450 kv. The pulser consists of 15 individual capacitor modules which are charged in parallel to 30 kv. The 5 milliamp (maximum) 30 kv. (variable) capacitor charging power supply can be seen at the top of the instrument rack in Fig. 13. In order to get the necessary high voltage for X-ray emission, the capacitors which are charged in parallel must be discharged in series. This is accomplished by the delayed trigger amplifier, the second module in the rack mentioned above, which provides, via a step-up pulse transformer, a triggering spark. An ionized region is created at a gap which now becomes the series connection between the first pair of capacitor modules. Thus begins a cascade of dielectric breakdown at successive interconnecting gaps to complete the series connection of capacitor modules. The gap between the cathode and annode in the X-ray flash tube is the last to break down; a brief but intense current flows from the capacitors across the flash tube. The delayed trigger amplifier unit not only amplifies the triggering signal to initiate the X-ray firing discharge, but permits a variable time delay between the instant when the triggering signal is received and the time when the high voltage trigger output pulse is delivered to the capacitor bank. This delay can be adjusted to about 0.2 μsec. over a range from 0 to 1000 μsec. Hence a sensitive adjustment, to synchronize the X-ray flash with the event to be recorded, is possible.

The X-ray tube can be mounted either directly in the pulser enclosure to minimize transmission losses or remotely within a tube head connected to the pulser via a 25 foot long twin lead cable. The arrangement with the tube within the pulser is inconvenient as the pulser is 9 inches in diameter and over 3 feet long, weighing close to 100 pounds. The pulser can be seen in Fig. 13. It cannot be brought into the position required to irradiate the supercalender nip. This requires the X-ray tube to be brought as close to the bearing blocks as possible with the axis of the tube parallel and coplanar with the roll axes and as close to colinear with the line of contact between the adjacent rolls as possible. The alternate arrangement with the tube in the insulating tube head and with 25 feet of cable incurred a 50% reduction in radiation output. A suitable compromise was achieved by mounting the tube head close coupled coaxially in front of the pulser with 3 feet of interconnecting cable.

To provide insulation at points, such as component interconnections, which cannot be encapsulated in plastic the tube cavities in both the pulser and the tube head are filled with "Freon-12" at 0.7 psig. To ensure that the unit can be operated over a range of output voltage from 150 to 300 kv. the capacitor modules are surrounded by pressurized dry nitrogen. By adjusting the nitrogen pressure the dielectric strength of capacitor spark gaps can be varied so that the output from the delayed trigger amplifier will fire the X-ray. If the pressure is too high, misfire will result due to the inability of the triggering spark to initiate a dielectric breakdown. Low nitrogen pressure causes spontaneous prefiring before the desired charging voltage is built up, as the voltage between individual capacitor terminals becomes sufficiently high to arc over the spark gaps.

Preliminary tests showed that although the tube head can be positioned between the roll shafts and close to the bearing blocks it is impossible to mount a conventional X-ray cassette so as to obtain a radiogram of the tracer spheres within the filled roll when the roll is installed in the stack. Furthermore as the tracers are in a transaxial plane 4 inches from the closer roll nut it is not possible to place a film pack close to these objects. To reconstruct an actual tracer pattern from a film image it is necessary to know the direction from which each sphere shadow was cast. These two difficulties were resolved by constructing a special X-ray film holder or cassette. This cassette is mounted concentric with the filled roll and is clamped to the nut nearest the tracer pattern. The frame of the cassette is a 1/4in. thick aluminum plate of annular form, 9 inches inside diameter to fit over the roll nut and 12 3/4in. outside diameter to overlap a 3/8in. deep sector of the steel roll. This plate is split diametrally and is held together with two dowel pinned double lap joints. Hence the cassette can be taken apart for installation on and removal from the test roll. Two film holders are attached to the symmetrical halves so that the assembly is balanced as it rotates with the filled roll on which it is mounted. Each holder consists of an arc shaped base, two intensifying screens and a cap or cover plate with four hold down screws which make a light-tight sandwich of base, film, intensifying screens and cap. The straight edges of the holder are along parallel chords, equidistant from the arc centres and 6 1/2in. apart. A standard 6 1/2 x 8in. sheet film yields three full width pieces which have only to be cut along concentric arcs to form the two curved edges to make the film compatible with the cassette. The bases are 1/4in. thick plates, arc shaped and with a 1/8in. deep step along the inner and outer curved edges to accept the circumferential lips of the cover plates. These lips prevent light from entering the cassette from the radial directions. A thickness of black felt, slightly thicker than the combined thickness of two intensifying screens and the film, is glued to either end of the bases to prevent circumferential light leakage.

Near the counterclockwise edge (viewed from the X-ray source) of each cover plate is a tapered, bevel-cut plastic block which contains a 1/16in. diameter by 1 1/2in. long tungsten rod which is perpendicular to the plane of the film. This rod acts as an X-ray "sun-dial" which casts a shadow on the film when it is exposed. The direction of the shadow from tip to base points towards the location of the ray which fell perpendicular to the film. The length of the shadow is proportional to the distance from the tip of the shadow to the point of impingement on the film of the perpendicular ray from the X-ray source. If the distance from the X-ray source and the tracer object plane to the film plane is measured the "sun-dial's" shadow on each radiogram permits a simple trigonometric correction to be applied to the apparent position of each tracer image on the film. Thus the actual disposition of the tracer pattern in the filled roll can be deduced.

As was mentioned before, the film shape was chosen to conform to the shape of the circular cassette and to make efficient use of a standard size of sheet film. Although it is not fraught with scientific interest, a simple jig to cut the required arc shaped film from 6 1/2in. width sheet is illustrated in Fig. 15. This film cutter made possible the convenient preparation of film. Frustrations caused by finger-printed, scissor-hacked film were thus alleviated. It is felt that anyone with limited dark-room experience who has faced anything other than the simplest of film cutting tasks will consider this appliance worthy of mention.

In order to obtain an X-ray picture of the deformation field within the filled roll in the region of the nip (i.e. while one of the two tracer patterns, embedded in the fill material of the test roll, is directly beneath the area of contact between the steel and filled roll) the X-ray unit must be synchronized so as to fire when an array of spheres is in position directly under the nip. The firing circuit is shown in Fig. 120.

The external trigger signal for the X-ray is provided by a rapidly decaying (+)30v. pulse from a 0.01 μf. capacitor discharging through a 10 kΩ resistor. Provision has to be made, however, for this event to occur on operator demand and within a specific arc of about 3° while the roll is turning at up to 1000 rpm. Thus the operator's push-button is merely an arming switch (PB) with a relay and microswitch interlock to prevent misfire or prefire. The operation of the firing circuit can best be described by following the sequence of events initiated by pressing the push-button. The push-button switch is used to energize the charging relay coil (RC). This, however, is enabled only when the roll has just passed its firing attitude, represented by the step in the triggering cam. The relay coil circuit is thus completed, in this limited arc of less than 90°, by the "normally closed" contacts of the microswitch (MS2). The push-button must be held down, and after (MS2) opens, the relay energizing circuit will remain complete through a pair of the relay contacts (R2) which are in parallel with (MS2). Therefore while the

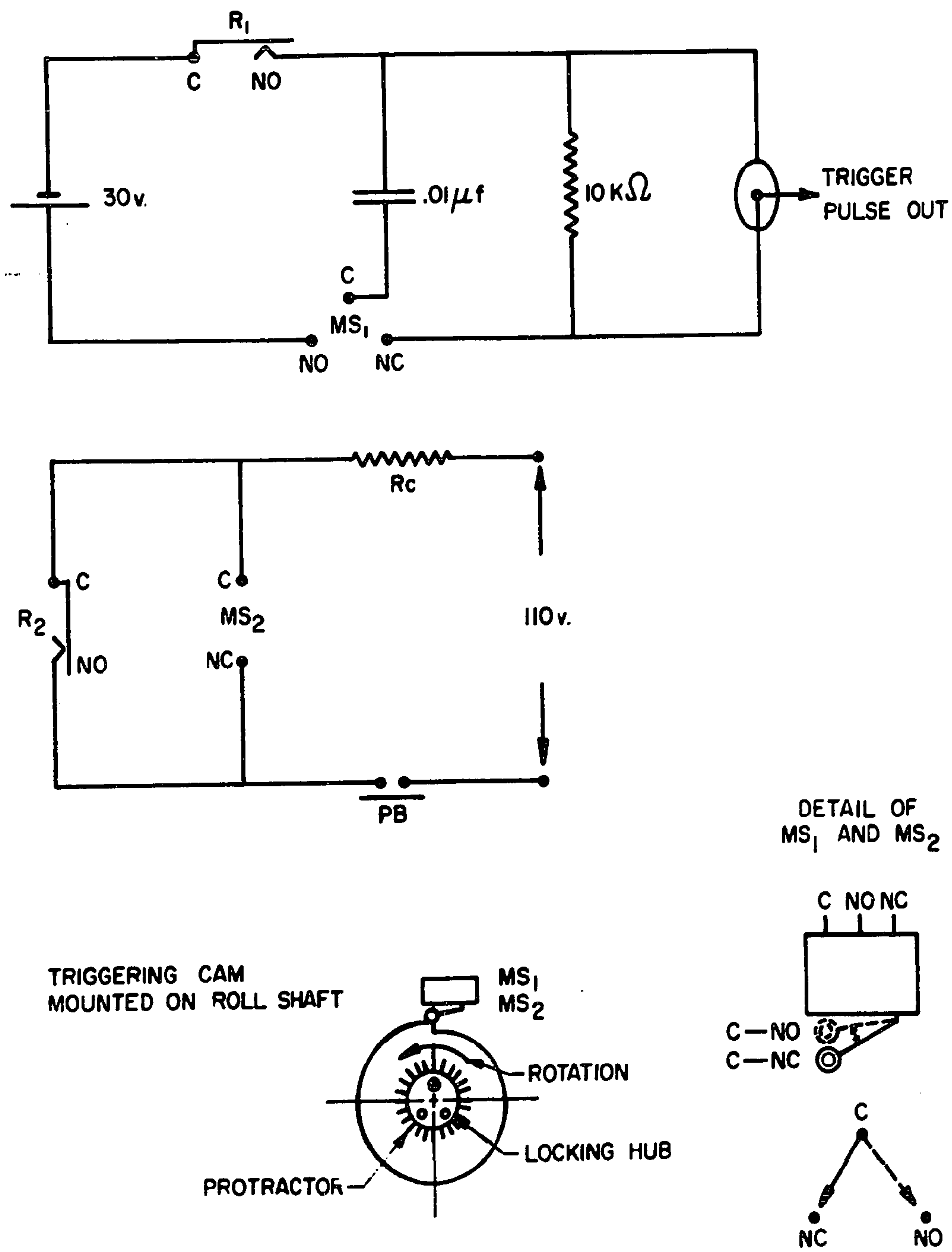

FIG. 120.

X-ray Firing Circuit.

relay is energized the capacitor charging circuit will be completed through another pair of the relay contacts (R1) which connect the (-) side of the battery to one of the capacitor terminals. Furthermore the (+) battery terminal is connected to the capacitor through the "normally open" contacts of the firing microswitch (MS1) which remain closed for about 270° of roll rotation (see triggering cam) prior to the firing step. As the microswitch actuating followers drop off this step, the "common" terminal of microswitch (MS1) is switched from the "normally open" to the "normally closed position, disconnecting the battery and connecting the capacitor, now charged, to the trigger output across the 10 kΩ ballast resistor.

In order to provide angular adjustment the triggering cam is friction locked to the supporting hub mounted on the filled roll shaft end. By loosening three screws, the cam can be hand rotated to place the triggering step in the required position. A protractor on the cam permits location to about ± 1° of cam angle. Part of the X-ray trigger synchronizer can be seen in Fig. 85. The trigger circuits are in the small chassis at left foreground. The two leads are connected to the microswitches (MS1 and MS2) whose support bracket is partially visible in the lower left corner near the roll shaft end. The receptacle in the chassis box is for the operator's push-button.

The two lowermost instrument modules in the rack shown in Fig. 13 contain radiation monitoring equipment which is connected to the scintillation probe, the cylindrical object on the stool. This equipment measures background radiation and gives a qualitative indication when the X-ray unit is fired. This indication is visible as a brief deflection of a galvanometer indicating ionization current from the probe. An audiable indication of the brief increase in radiation level is also given. Although this instrumentation does not measure accumulated radiation dosage, any significant deviation from normal operation can be noticed by the operator. For example, a prematurely deteriorated X-ray tube will, when fired, result in an abnormally low indication by this instrument. This reduces the risk of spoiled tests caused by an expired X-ray tube. Small electroscopic pocket dosimeters are used for monitoring accumulated dosage incurred by persons operating the X-ray equipment. The unit has been proved to be quite safe. Operators have received no more than 1 to 2 milliröengtens, (mR), of radiation during a day of operation involving between 10 and 20 firings. A safe monthly dose is up to 200 mR. while a medical chest X-ray might involve a dose of 30 to 60 mR.

APPENDIX VI

X-ray Deformation Data Reduction Programs*

*As per (41-43)

Sparse Pattern Datum Generation

```
* * * * * * * * * * * * * * *
            *
            *
            *
```

generate the polar coordinates of an arc shaped array of 15 points at radius = (6 - 3/32)in. and at 1° intervals; 0° at 7th point (clockwise)

generate the polar coordinates of 3 points under 7th point at 0° each radius successively 3/32in. less than previous

generate cartesian coordinates of all 18 points; origin 7th point; x-axis tangent at origin to arc radius (6 - 3/32)in.

print x and y coordinates in a T-array for reference purposes:

```
     x.xx                     0.00
.... y.yy .... .... .... .... 0.00 .... .... .... .... .... .... .... ....
                              ....
                              ....

                              ....
                              ....

                              ....
                              ....
```

```
      CALL FAC1
      DIMENSION SA(18),SR(18),SX(18),SY(18)
      DO 10 I=1,15
      SA(I)=(I-7.)*3.14159/180.
10    SR(I)=5.90625
      DO 20 I=16,18
      SA(I)=0.
20    SR(I)=SR(I-1)-0.09375
      DO 30 I=1,18
      SX(I)=SR(I)*(SINF(SA(I)))
30    SY(I)=SR(I)*(COSF(SA(I)))
      SX7=SX(7)
      SY7=SY(7)
      DO 40 I=1,18
      SX(I)=SX(I)-SX7
40    SY(I)=SY(I)-SY7
      PRINT(1) 50
      PRINT(1)60,(SX(I),I=1,15)
      PRINT(1)60,(SY(I),I=1,15)
      PRINT(1)70,(SX(I),SY(I),I=16,18)
      CALL FAC2
      STOP
50    FORMAT(///,$  ***SPARSE PATTERN TRANSFORMATION-DATUM$)
60    FORMAT(2X,5F5.2,5F5.2,5F5.2)
70    FORMAT(/,20X,12X,F5.2,/,20X,12X,F5.2)
     END

*PROGRAM END.    0 FORTRAN ERRORS
        END

170422 FIN
```

Fit-Sparse Pattern X-ray

```
* * * * * * * * * * * * * * *
            *
            *
            *
```

read identification record

is it valid ?   NO → STOP
YES
↓
print identification record

read length of "sundial" shadow (B1)

read 18 polar coordinates of tracers, origin; foot of perpendicular from x-ray source to film plane: (SR(I), SA(I)), 0° parallel to shadow

compute radial correction factor
(B1MB2 = (-5xB1)/17)

calculate corrected radial coordinates and transform from polar to cartesian, same origin abscissa along 0°

to approximate datum configuration choose new origin at 7th tracer, i.e. at crossing of T, new abscissa arbitrarily parallel to line through 1st and 13th tracers

print x and y coordinates as for sparse pattern datum generation so as to compare data accuracy by comparison of data from prints at 2 exposures (See Fig. 88)

repeat sequence; next data set

```
      CALL FAC1
      DIMENSION SR(18),SA(18),SX(18),SY(18),TAG(27)
1     READ 2,(TAG(I),I=1,27)
      CONTINUE
      LDA TAG
      SUB TAGTST
      TZE
      BTR $999
      PRINT(1)4,(TAG(I),I=1,27)
      READ 9,B1
      READ 10,(SR(I),I=1,18)
      READ 20,(SA(I),I=1,18)
      B1MB2=(-5.)*(B1/17.)
      DO 30 I=1,18
      SA(I)=SA(I)*3.14159/180.
      B=B1MB2/SR(I)
      SPMT=SINF(3.14159-SA(I))
      SA(I)=ATANF(SINF(SA(I))/(B+COSF(SA(I))))
      SR(I)=SPMT*SR(I)/SA(I)
      SA(I)=3.14159-SA(I)
      SR(I)=SR(I)-(SR(I)*5./22.)
      SX(I)=SR(I)*(COSF(SA(I)))
      SY(I)=SR(I)*(SINF(SA(I)))
30    CONTINUE
      SX7=SX(7)
      SY7=SY(7)
      DO 40 I=1,18
      SX(I)=SX(I)-SX7
      SY(I)=SY(I)-SY7
40    CONTINUE
      TNT=(SY(13)-SY(1))/(SX(13)-SX(1))
      CST=COSF(ATANF(TNT))
      SNT=TNT*CST
      DO 50 I=1,18
      SX(I)=(SY(I)*SNT)+(SX(I)*CST)
      SY(I)=(SY(I)*CST)-(SX(I)*SNT)
50    CONTINUE
      PRINT(1)60,(SX(I),I=1,15)
      PRINT(1)60,(SY(I),I=1,15)
      PRINT(1)70,(SX(I),SY(I),I=16,18)
      GO TO 1
999   CALL FAC2
      STOP
2     FORMAT(7A3,7A3,7A3,5A3,A2)
4     FORMAT(///,2X,7A3,7A3,7A3,5A3,A2,/)
9     FORMAT(F4.2)
10    FORMAT(7F6.3,6F6.3,2X,/,5F6.3)
20    FORMAT(7F6.1,6F6.1,2X,/,5F6.1)
60    FORMAT(2X,5F5.2,5F5.2,5F5.2)
70    FORMAT(/,20X,12X,F5.2,/,20X,12X,F5.2)
TAGTST CON A,3,***
      END
```

Sparse Pattern Deviation From Datum

* * * * * * * * * * * * * * *
*
*
*

read and validate data as per fit-sparse pattern x-ray for both prints; stop if data finished

calculate datum pattern as per sparse pattern deviation from datum; calculate final cartesian coordinates as per fit-sparse pattern x-ray and combine for mean

calculate difference between mean coordinates and datum; determine range of x and y deviation from datum; subtract x-range from x-coordinates, y-range from y-coordinates

calculate square of all deviations; sum and save

increment x and y deviations by 0.005in. and re-calculate squares and sum

is new squares sum > previous ? YES → print previous square sum as per fit-sparse pattern x-ray and repeat sequence: new data

NO

↓

replace previous squares sum with new squares sum and go back 2 steps

```
      CALL FAC1
      DIMENSION SASD(18),SRSD(18),SXSD(18),SYSD(18),SAS1(18),SRS1(1
     1),SXS1(18),SYS1(18),SAS2(18),SRS2(18),SXS2(18),SYS2(18),TAG(27
     2,SXS3(18),SYS3(18)
      DO 10 I=1,15
      SASD(I)=(I-7.)*3.14159/180.
10    SRSD(I)=5.90625
      DO 20 I=16,18
      SASD(I)=0
20    SRSD(I)=SRSD(I-1)-0.09375
      DO 30 I=1,18
      SXSD(I)=SRSD(I)*(SINF(SASD(I)))
30    SYSD(I)=SRSD(I)*(COSF(SASD(I)))
      SXSD7=SXSD(7)
      SYSD7=SYSD(7)
      DO 40 I=1,18
      SXSD(I)=SXSD(I)-SXSD7
40    SYSD(I)=SYSD(I)-SYSD7
1     READ 2,(TAG(I),I=1,27)
      CONTINUE
      LDA TAG
      SUB TAGTST
      TZE
      BTR $999
      READ 9,B1
      READ 100,(SRS1(I),I=1,18)
      READ 200,(SAS1(I),I=1,18)
      READ 2,(TAG(I),I=1,27)
      CONTINUE
      LDA TAG
      SUB TAGTST
      TZE
      BTR $999
      PRINT(1)4,(TAG(I),I=1,18),TAG(23),TAG(24),TAG(25)
      READ 9,C1
      READ 100,(SRS2(I),I=1,18)
      READ 200,(SAS2(I),I=1,18)
      B1MB2=(-5.)*(B1/17.)
      C1MC2=(-5.)*(C1/17.)
      DO 50 I=1,18
      SAS1(I)=SAS1(I)*3.14159/180.
      SAS2(I)=SAS2(I)*3.14159/180.
      B=B1MB2/SRS1(I)
      C=C1MC2/SRS2(I)
      SFMTB=SINF(3.14159-SAS1(I))
      SFMTC=SINF(3.14159-SAS2(I))
      SAS1(I)=ATANF(SINF(SAS1(I))/(B+COSF(SAS1(I))))
      SAS2(I)=ATANF(SINF(SAS2(I))/(C+COSF(SAS2(I))))
      SRS1(I)=SFMTB*SRS1(I)/SAS1(I)
```

```
      SRS2(I)=SPMTC*SRS2(I)/SAS2(I)
      SAS1(I)=3.14159-SAS1(I)
      SAS2(I)=3.14159-SAS2(I)
      SRS1(I)=SRS1(I)-(SRS1(I)*5./22.)
      SRS2(I)=SRS2(I)-(SRS2(I)*5./22.)
      SXS1(I)=SRS1(I)*(COSF(SAS1(I)))
      SXS2(I)=SRS2(I)*(COSF(SAS2(I)))
      SYS1(I)=SRS1(I)*(SINF(SAS1(I)))
50    SYS2(I)=SRS2(I)*(SINF(SAS2(I)))
      SXS17=SXS1(7)
      SXS27=SXS2(7)
      SYS17=SYS1(7)
      SYS27=SYS2(7)
      DO 60 I=1,18
      SXS1(I)=SXS1(I)-SXS17
      SXS2(I)=SXS2(I)-SXS27
      SYS1(I)=SYS1(I)-SYS17
60    SYS2(I)=SYS2(I)-SYS27
      TNT1=(SYS1(13)-SYS1(1))/(SXS1(13)-SXS1(1))
      TNT2=(SYS2(13)-SYS2(1))/(SXS2(13)-SXS2(1))
      CST1=COSF(ATANF(TNT1))
      CST2=COSF(ATANF(TNT2))
      SNT1=TNT1*CST1
      SNT2=TNT2*CST2
      DO 70 I=1,18
      SXS3(I)=(((SYS1(I)*SNT1)+(SXS1(I)*CST1)+(SYS2(I)*SNT2)+(SXS2(I
     1)*CST2))/2.)-SXSD(I)
70    SYS3(I)=(((SYS1(I)*CST1)-(SXS1(I)*SNT1)+(SYS2(I)*CST2)-(SXS2(I
     1)*SNT2))/2.)-SYSD(I)
      XMIN=MIN1F(SXS3(1),SXS3(2),SXS3(3),SXS3(4),SXS3(5),SXS3(6),SXS
     13(7),SXS3(8),SXS3(9),SXS3(10),SXS3(11),SXS3(12),SXS3(13),SXS3(1
     24),SXS3(15),SXS3(16),SXS3(17),SXS3(18))
      YMAX=MAX1F(SXS3(1),SXS3(2),SXS3(3),SXS3(4),SXS3(5),SXS3(6),SXS
     13(7),SXS3(8),SXS3(9),SXS3(10),SXS3(11),SXS3(12),SXS3(13),SXS3(1
     24),SXS3(15),SXS3(16),SXS3(17),SXS3(18))
      YMIN=MIN1F(SYS3(1),SYS3(2),SYS3(3),SYS3(4),SYS3(5),SYS3(6),SYS
     13(7),SYS3(8),SYS3(9),SYS3(10),SYS3(11),SYS3(12),SYS3(13),SYS3(1
     24),SYS3(15),SYS3(16),SYS3(17),SYS3(18))
      YMAX=MAX1F(SYS3(1),SYS3(2),SYS3(3),SYS3(4),SYS3(5),SYS3(6),SYS
     13(7),SYS3(8),SYS3(9),SYS3(10),SYS3(11),SYS3(12),SYS3(13),SYS3(1
     24),SYS3(15),SYS3(16),SYS3(17),SYS3(18))
      DLTX=XMAX-XMIN
      DLTY=YMAX-YMIN
      DO 71 I=1,18
      SXS3(I)=SXS3(I)-DLTX
71    SYS3(I)=SYS3(I)-DLTY
      SSQX=0
      J=0
710   SMSQX=0
```

```
          DO 72 I=1,18
 72       SMSQX=SMSQX+(SXS3(I)*SXS3(I))
          IF(J)73,73,74
 73       J=J+1
          GO TO 76
 74       IF(SMSQX-SSQX)76,76,700
 76       SSQX=SMSQX
          DO 75 I=1,18
 75       SXS3(I)=SXS3(I)+0.005
          GO TO 710
 700      SSQY=0
          J=0
 810      SMSQY=0
          DO 82 I=1,18
 82       SMSQY=SMSQY+(SYS3(I)*SYS3(I))
          IF(J)83,83,84
 83       J=J+1
          GO TO 86
 84       IF(SMSQY-SSQY)86,86,800
 86       SSQY=SMSQY
          DO 85 I=1,18
 85       SYS3(I)=SYS3(I)+0.005
          GO TO 810
 800      CONTINUE
          PRINT(1)80,(SXS3(I),I=1,15)
          PRINT(1)80,(SYS3(I),I=1,15)
          PRINT(1)90,(SXS3(I),SYS3(I),I=16,18)
          GO TO 1
 999      CALL FAC2
          STOP
 2        FORMAT(7A3,7A3,7A3,5A3,A2)
 4        FORMAT(///,2X,7A3,7A3,7A3,/)
 9        FORMAT(F4.2)
 80       FORMAT(2X,5F5.2,5F5.2,5F5.2)
 90       FORMAT(/,20X,12X,F5.2,/,20X,12X,F5.2)
 100      FORMAT(7F6.3,6F6.3,2X,/,5F6.3)
 200      FORMAT(7F6.1,6F6.1,2X,/,5F6.1)
TAGTST CON A,3,***
        END

*

*PROGRAM END.    0 FORTRAN ERRORS
        END
```

Sparse Pattern Least Squares Deviation From Datum Plot

```
====================================...........=
====================================...........=
====================================..*........=
====================================...........=
====================================...........=
====================================.....+.....= 6th coordinate
====================================...........=
====================================...........=
====================================...........=
====================================...........=
====================================...........=
================================================
...........=...........=...........=...........=
...........=...........=...........=...........=
...........=...........=...........=...........=
...........=...........=...........=.....*.....=
...........=...........=.....*.....=...........=
.....+*....=.....*.....=.....+.....=.....+.....= 7th coordinate
...........=...........=...........=...........=
...........=...........=...........=...........=
...........=...........=...........=...........=
...........=...........=...........=...........=
...........=...........=...........=...........=
================================================
====================================...........=
====================================...........=
====================================...........=
====================================...........=
====================================...........=
====================================.....+.....= 8th coordinate
====================================...........=
====================================...........=
====================================...........=
====================================...........=
====================================...........=
================================================
```

18th coordinate

This program combines the features of the 3 previous programs and, using a 48 x 12 character buffer, assembles a finite increment, 0.100in. field image of the tracer deviations from datum, i.e. deformations. The T-shaped pattern of the tracer distribution is represented. Provision is incorporated to assemble the 7th, 16th, 17th and 18th coordinates into the buffer together and then to revert to the blank field (=) and single coordinate pattern. The tracer datum position is represented by (+), the actual tracer position by (*). The 0.010in. grid is represented by (.). Actual tracer position supercedes datum (17th coordinate). Out of range deformation causes actual tracer position to be ignored (8th coordinate).

```
      CALL FAC1
      DIMENSION ISX(18),ISY(18),OUTBF(192)
      DIMENSION SASD(18),SRSD(18),SXSD(18),SYSD(18),SAS1(18),SRS1(18
     1),SXS1(18),SYS1(18),SAS2(18),SRS2(18),SXS2(18),SYS2(18),TAG(27)
     2,SXS3(18),SYS3(18)
      DO 10 I=1,15
      SASD(I)=(I-7.)*3.14159/180.
10    SRSD(I)=5.90627
      DO 20 I=16,18
      SASD(I)=0
20    SRSD(I)=SRSD(I-1)-0.09375
      DO 30 I=1,18
      SXSD(I)=SRSD(I)*(SINF(SASD(I)))
30    SYSD(I)=SRSD(I)*(COSF(SASD(I)))
      SXSD7=SXSD(7)
      SYSD7=SYSD(7)
      DO 40 I=1,18
      SXSD(I)=SXSD(I)-SXSD7
40    SYSD(I)=SYSD(I)-SYSD7
1     READ 2,(TAG(I),I=1,27)
      CONTINUE
      LDA TAG
      SUB TAGTST
      TZE
      BTR $999
      READ 9,B1
      READ 100,(SRS1(I),I=1,18)
      READ 200,(SAS1(I),I=1,18)
      READ 2,(TAG(I),I=1,27)
      CONTINUE
      LDA TAG
      SUB TAGTST
      TZE
      BTR $999
      PRINT(1)4,(TAG(I),I=1,18),TAG(23),TAG(24),TAG(25)
      READ 9,C1
      READ 100,(SRS2(I),I=1,18)
      READ 200,(SAS2(I),I=1,18)
      B1MB2=(-5.)*(B1/17.)
      C1MC2=(-5.)*(C1/17.)
      DO 50 I=1,18
      SAS1(I)=SAS1(I)*3.14159/180.
      SAS2(I)=SAS2(I)*3.14159/180.
      B=B1MB2/SRS1(I)
      C=C1MC2/SRS2(I)
      SPMTB=SINF(3.14159-SAS1(I))
      SPMTC=SINF(3.14159-SAS2(I))
      SAS1(I)=ATANF(SINF(SAS1(I))/(B+COSF(SAS1(I))))
      SAS2(I)=ATANF(SINF(SAS2(I))/(C+COSF(SAS2(I)))),
```

```
      SRS1(I)=SPMTB*SRS1(I)/SAS1(I)
      SRS2(I)=SPMTC*SRS2(I)/SAS2(I)
      SAS1(I)=3.14159-SAS1(I)
      SAS2(I)=3.14159-SAS2(I)
      SRS1(I)=SRS1(I)-(SRS1(I)*5./22.)
      SRS2(I)=SRS2(I)-(SRS2(I)*5./22.)
      SXS1(I)=SRS1(I)*(COSF(SAS1(I)))
      SXS2(I)=SRS2(I)*(COSF(SAS2(I)))
      SYS1(I)=SRS1(I)*(SINF(SAS1(I)))
50    SYS2(I)=SRS2(I)*(SINF(SAS2(I)))
      SXS17=SXS1(7)
      SXS27=SXS2(7)
      SYS17=SYS1(7)
      SYS27=SYS2(7)
      DO 60 I=1,18
      SXS1(I)=SXS1(I)-SXS17
      SXS2(I)=SXS2(I)-SXS27
      SYS1(I)=SYS1(I)-SYS17
60    SYS2(I)=SYS2(I)-SYS27
      TNT1=(SYS1(13)-SYS1(1))/(SXS1(13)-SXS1(1))
      TNT2=(SYS2(13)-SYS2(1))/(SXS2(13)-SXS2(1))
      CST1=COSF(ATANF(TNT1))
      CST2=COSF(ATANF(TNT2))
      SNT1=TNT1*CST1
      SNT2=TNT2*CST2
      DO 70 I=1,18
      SXS3(I)=(((SYS1(I)*SNT1)+(SXS1(I)*CST1)+(SYS2(I)*SNT2)+(SXS2(I
     1)*CST2))/2.)-SXSD(I)
70    SYS3(I)=(((SYS1(I)*CST1)-(SXS1(I)*SNT1)+(SYS2(I)*CST2)-(SXS2(I
     1)*SNT2))/2.)-SYSD(I)
      XMIN=MIN1F(SXS3(1),SXS3(2),SXS3(3),SXS3(4),SXS3(5),SXS3(6),SXS
     13(7),SXS3(8),SXS3(9),SXS3(10),SXS3(11),SXS3(12),SXS3(13),SXS3(1
     24),SXS3(15),SXS3(16),SXS3(17),SXS3(18))
      XMAX=MAX1F(SXS3(1),SXS3(2),SXS3(3),SXS3(4),SXS3(5),SYS3(6),SXS
     13(7),SXS3(8),SXS3(9),SXS3(10),SXS3(11),SYS3(12),SXS3(13),SXS3(1
     24),SYS3(15),SXS3(16),SXS3(17),SXS3(18))
      YMIN=MIN1F(SYS3(1),SYS3(2),SYS3(3),SYS3(4),SYS3(5),SYS3(6),SYS
     13(7),SYS3(8),SYS3(9),SYS3(10),SYS3(11),SYS3(12),SYS3(13),SYS3(1
     24),SYS3(15),SYS3(16),SYS3(17),SYS3(18))
      YMAX=MAX1F(SYS3(1),SYS3(2),SYS3(3),SYS3(4),SYS3(5),SYS3(6),SYS
     13(7),SYS3(8),SYS3(9),SYS3(10),SYS3(11),SYS3(12),SYS3(13),SYS3(1
     24),SYS3(15),SYS3(16),SYS3(17),SYS3(18))
      DLTX=XMAX-XMIN
      DLTY=YMAX-YMIN
      DO 71 I=1,18
      SXS3(I)=SXS3(I)-DLTX
71    SYS3(I)=SYS3(I)-DLTY
      SSQY=0
      J=0
```

```
710     SMSQX=0
        DO 72 I=1,18
72      SMSQX=SMSQX+(SXS3(I)*SXS3(I))
        IF(J)73,73,74
73      J=J+1
        GO TO 76
74      IF(SMSQX-SSQX)76,76,700
76      SSQX=SMSQX
        DO 75 I=1,18
75      SXS3(I)=SXS3(I)+0.005
        GO TO 710
700     SSQY=0
        J=0
810     SMSQY=0
        DO 82 I=1,18
82      SMSQY=SMSQY+(SYS3(I)*SYS3(I))
        IF(J)83,83,84
83      J=J+1
        GO TO 86
84      IF(SMSQY-SSQY)86,86,800
86      SSQY=SMSQY
        DO 85 I=1,18
85      SYS3(I)=SYS3(I)+0.005
        GO TO 810
800     CONTINUE
        DO 1000 I=1,18
        SXS3(I)=SXS3(I)*100.
        SYS3(I)=SYS3(I)*100.
        ISX(I)=XFIXF(SXS3(I))+5
1000    ISY(I)=XFIXF(SYS3(I))+5
        CONTINUE
        LXK 0,3
OK      LXK 0,7                   INITIALIZE OUTPUT BUFFER
        LDA BLANK1
        STA OUTPAT,7
        INX 1,7
        TXH 44,7
        BTR *-3
        LXK 0,7
        LDA BLANK2
        STA OUTBF,7
        INX 1,7
        TXH 192,7
        BTR *-3                   BUFFERS CLEAR
        LDA ORIGIN
        STA OUTBF+93
        STA OUTPAT+21
        LXK 0,7
        LDA END
```

```
STA OUTPAT+3,7
INX 4,7
TXH 44,7
BTR *-3
LDA ISX,3
TOD 23
BTS TOOBIG
SUB ELEVEN
TOD 23              IF X-DEVIATIONS ARE LARGER
BTR TOOBIG          THAN +-5 PRINT A BARE PATTERN
LDA ISX,3
MAQ
MPY FOUR            GENERATE ROW NUMBER
LDA Q
RBK 23
STA ROW
LDA ISY,3
TOD 23
BTS TOOBIG          BARE PATTERN IF Y TOO BIG
SUB ELEVEN
TOD 23
BTR TOOBIG
LDA ISX,3
SUB FIVE
TZE                 IS ROW ON X=0
LDA ISY,3
BTR *+2
ADD ELEVEN          IF IT IS, USE ORIGIN TABLE
STA 5               STORE ORG. TBL. ADDRESS IN X5
LDA ISY,3
LXK 0,4
SUB THREE
TOD 23
BTS *+3
INX 1,4             GENERATE COLUMN NUMBER
BRU *-4
LDA ROW
ADD 4
STA 4
LDA STRSTN,5        PICK UP PATTERNED BRICK
STA OUTPAT,4        AND PUT IT IN PLACE
LXK 12,7
LXK 0,6
LXK 0,5
LDA OUTPAT,6        PLACE OUTPUT PATTERN, RIGHT JUSTIFIED.
STA OUTBF,7
INX 1,5
INX 1,6
INX 1,7
```

```
        TXH 4,5
        BTR *-6
        INX 12,7
        TXH 188,7           IS BUFFER FINISHED
        BTR *-10
$2000   STX XREG3,3
        STX XREG4,4
        STX XREG5,5
        STX XREG6,6
        STX XREG7,7
        PRINT(1)3000 ,(OUTBF(I),I=1,192)
        CONTINUE
        LDX XREG3,3
        LDX XREG4,4
        LDX XREG5,5
        LDX XREG6,6
        LDX XREG7,7
        INX 1,3
        TXH 6,3             ARE WE AT CRITICAL 7TH ROW
        BTS *+2             NO
        BRU OK
        TXH 7,3             NOW
        BTR FTR             YES
        TXH 15,3            ARE WE FINISHED
        BTR OK              NO
        GO TO 1
999     CALL FAC2
        STOP
TOOBIG  LDA ORIGIN
        STA OUTPAT+21
        BRU $2000-13
FTR     LXK 0,7
BCKHER  INX 1,7
        LXK 0,6
        LDA BLANK1
        STA OUTPAT,6
        INX 1,6
        TXH 44,6
        BTR *-3
        LDA ORIGIN
        STA OUTPAT+21
        LXK 0,6
        LDA ENDL
        STA OUTPAT+3,6
        INX 4,6
        TXH 44,6
        BTR *-3
        XEC TIPTBL,7
        TOD 23
        BTS BIGTOO,7
```

```
SUB ELEVEN
TOD 23
BTR BIGTOO,7
XEC TIRTBL,7
MAQ
MPY FOUR
LDA Q
RBK 23
STA ROW
INX 1,7
XEC TIRTBL,7
TOD 23
BTS BIGTOO-1,7
SUB ELEVEN
TOD 23
BTR BIGTOO-1,7
XEC TIRTBL-1,7
SUB FIVE
TZE
XEC TIRTBL,7
BTR *+2
ADD ELEVEN
STA 5
XEC TIRTBL,7
LXK 0,4
SUB THREE
TOD 23
BTS *+3
INX 1,4
BRU *-4
LDA ROW
ADD 4
STA 4
LDA STRSTN,5
STA OUTPAT,4
INX 1,7
XEC TIRTBL,7
LXK 0,6
LXK 0,4
LDA OUTPAT,6
STA OUTBF,5
INX 1,6
INX 1,4
INX 1,5
TXH 4,4
BTR *-6
INX 12,5
TXH 176,5
BTR *-10
```

```
       TXH 11,7
       BTR BCKHER
       LXK 6,3
       BRU $2000
BIGTOO NOP
       LXK 12,5
       BRU BCKHER
       NOP
       LXK 8,5
       BRU BCKHER
       NOP
       LXK 4,5
       BRU BCKHER
       NOP
       LXK 0,5
       LXK 6,3
       BRU $2000
TIRTBL NOP
       LDA ISX+6
       LDA ISY+6
       LXK 12,5
       LDA ISX+15
       LDA ISY+15
       LXK 8,5
       LDA ISX+16
       LDA ISY+16
       LXK 4,5
       LDA ISX+17
       LDA ISY+17
       LXK 0,5
       STOP
2      FORMAT(7A3,7A3,7A3,5A3,A2)
4      FORMAT(///,2X,7A3,7A3,7A3,/)
9      FORMAT(F4.2)
100    FORMAT(7F6.3,6F6.3,2X,/,5F6.3)
200    FORMAT(7F6.1,6F6.1,2X,/,5F6.1)
3000   FORMAT(21X,7A3,7A3,2A3)
STRSTN CON A,3,*..
       CON A,3,.*.
       CON A,3,..*
       CON A,3,*..
       CON A,3,.*.
       CON A,3,..*
       CON A,3,*..
       CON A,3,.*.
       CON A,3,..*
       CON A,3,*.=
       CON A,3,.*=
       CON A,3,*..
```

```
        CON A,3,.*.
        CON A,3,..*
        CON A,3,*.+
        CON A,3,.*+
        CON A,3,..*
        CON A,3,*..
        CON A,3,.*.
        CON A,3,..*
        CON A,3,*.=
        CON A,3,.*=
ORIGIN  CON A,3,..+
ENDL    CON A,3,..=
BLANK1  CON A,3,...
BLANK2  CON A,3,===
ELEVEN  CON D,11
TAGTST  CON A,3,***
OPTMP   BSS 2
XREG3   BSS 1
XREG4   BSS 1
XREG5   BSS 1
XREG6   BSS 1
XREG7   BSS 1
ROW     BSS 1
OUTPAT  BSS 44
       END

*

*PROGRAM END.    0 FORTRAN ERRORS
        END

181715 FIN
```

Dense Pattern Datum Generation

```
* * * * * * * * * * * * * * * * * * * * * * *
* * * * * * * * * * * * * * * * * * * * * * *
* * * * * * * * * * * * * * * * * * * * * * *
* * * * * * * * * * * * * * * * * * * * * * *
```

generate the polar coordinates of an arc shaped array of 23 points at radius = (6 - 3/32)in. and at 1° intervals; 0° at 12th point clockwise, origin at arc centre

generate the polar coordinates of 3 additional, similar tiers of 23 points at decreasing radial intervals of 3/32in.

convert to cartesian coordinates; origin 12th coordinate, top tier; abscissa parallel to arc tangent through this coordinate

```
x.xx x.xx x.xx x.xx
y.yy y.yy y.yy y.yy

x.xx x.xx x.xx x.xx
y.yy y.yy y.yy y.yy

.... .... .... ....
.... .... .... ....

                  .
                  .

.
.

.... .... .... ....
.... .... .... ....

x.xx x.xx x.xx x.xx
y.yy y.yy y.yy y.yy
```

```
      CALL FAC1
      DIMENSION SAD(23,4),SRD(23,4),SXD(23,4),SYD(23,4)
      DO 10 J=1,4
      DO 10 I=1,23
      SAD(I,J)=(I-12)*3.14159/180.
      SRD(I,J)=6.-(0.09375*J)
      SXD(I,J)=SRD(I,J)*(SINF(SAD(I,J)))
10    SYD(I,J)=SRD(I,J)*(COSF(SAD(I,J)))
      SXD121=SXD(12,1)
      SYD121=SYD(12,1)
      DO 20 J=1,4
      DO 20 I=1,23
      SXD(I,J)=SXD(I,J)-SXD121
20    SYD(I,J)=SYD(I,J)-SYD121
      PRINT(1)40
      DO 30 I=1,23
      PRINT(1)50,SXD(I,4),SXD(I,3),SXD(I,2),SXD(I,1)
30    PRINT(1)60,SYD(I,4),SYD(I,3),SYD(I,2),SYD(I,1)
      CALL FAC2
      STOP
40    FORMAT(///,$  *** DENSE PATTERN TRANSFORMATION-DATUM$,//)
50    FORMAT(23X,F5.2,2X,F5.2,2X,F5.2,2X,F5.2)
60    FORMAT(23X,F5.2,2X,F5.2,2X,F5.2,2X,F5.2,/)
     END

*

*PROGRAM END.    0 FORTRAN ERRORS
      END

131101 FIN
```

Fit-Dense Pattern X-ray

* *
* *
* *
* *

read identification record

is it valid ? NO → STOP
YES
↓

print identification record

read 23 x 4 array of polar coordinates of tracers, origin foot of perpendicular from x-ray source to film plane: (SR(I,J), SA(I,J)), 0° parallel to shadow of "sundial"

calculate corrected radial coordinates and transform to cartesian, same origin, abscissa along 0°

to approximate datum configuration choose new origin at 12th tracer, top tier, new abscissa chosen arbitrarily parallel to line through 1st and 23rd tracers, top tier

print x and y coordinates as for sparse pattern datum generation so as to compare data from prints at 2 exposures (see Fig. 89)

repeat sequence; next data set

```
        CALL FAC1
        DIMENSION SR(23,4),SA(23,4),SX(23,4),SY(23,4),TAG(27)
1       READ 2,(TAG(I),I=1,27)
        CONTINUE
        LDA TAG
        SUB TAGTST
        TZE
        BTR $999
        PRINT(1)4,(TAG(I),I=1,27)
        READ 10,((SR(I,J),I=1,23),J=1,4)
        READ 20,((SA(I,J),I=1,23),J=1,4)
        DO 30 J=1,4
        DO 30 I=1,23
        SA(I,J)=(180.-SA(I,J))*3.14159/180.
        SR(I,J)=SR(I,J)-(SR(I,J)*5./22.)
        SX(I,J)=SR(I,J)*(COSF(SA(I,J)))
30      SY(I,J)=SR(I,J)*(SINF(SA(I,J)))
        SX121=SX(12,1)
        SY121=SY(12,1)
        DO 40 J=1,4
        DO 40 I=1,23
        SX(I,J)=SX(I,J)-SX121
40      SY(I,J)=SY(I,J)-SY121
        TNT=(SY(23,1)-SY(1,1))/(SX(23,1)-SX(1,1))
        CST=COSF(ATANF(TNT))
        SNT=TNT*CST
        DO 50 J=1,4
        DO 50 I=1,23
        SX(I,J)=(SY(I,J)*SNT)+(SX(I,J)*CST)
50      SY(I,J)=(SY(I,J)*CST)-(SX(I,J)*SNT)
        DO 55 I=1,23
        PRINT(1)60,SX(I,4),SX(I,3),SX(I,2),SX(I,1)
55      PRINT(1)70,SY(I,4),SY(I,3),SY(I,2),SY(I,1)
        GO TO 1
999     CALL FAC2
        STOP
2       FORMAT(7A3,7A3,7A3,5A3,A2)
4       FORMAT(///,2X,7A3,7A3,7A3,5A3,A2,/)
10      FORMAT(8F6.3,5F6.3,/,5F6.3,5F6.3)
20      FORMAT(8F6.1,5F6.1,/,5F6.1,5F6.1)
60      FORMAT(23X,F5.2,2X,F5.2,2X,F5.2,2X,F5.2)
70      FORMAT(23X,F5.2,2X,F5.2,2X,F5.2,2X,F5.2,/)
TAGTST  CON A,3,***
       END

*

*PROGRAM END.    0 FORTRAN ERRORS
        END
```

Dense Pattern Deviation From Datum

```
* * * * * * * * * * * * * * * * * * * * * * *
* * * * * * * * * * * * * * * * * * * * * * *
* * * * * * * * * * * * * * * * * * * * * * *
* * * * * * * * * * * * * * * * * * * * * * *
```

See "Sparse Pattern Deviation from Datum" Program Description Procedure for calculation is identical.

```
          CALL FAC1
          DIMENSION SAD(23,4),SRD(23,4),SXD(23,4),SYD(23,4),SR(23,4),SA(
         123,4),SX(23,4),SY(23,4),SXT(23,4),SYT(23,4),TAG(27)
          DO 10 J=1,4
          DO 10 I=1,23
          SAD(I,J)=(I-12)*3.14159/180.
          SRD(I,J)=6.-(0.09375*J)
          SXD(I,J)=SRD(I,J)*(SINF(SAD(I,J)))
10        SYD(I,J)=SRD(I,J)*(COSF(SAD(I,J)))
          SXD121=SXD(12,1)
          SYD121=SYD(12,1)
          DO 20 J=1,4
          DO 20 I=1,23
          SXD(I,J)=SXD(I,J)-SXD121
          SYD(I,J)=SYD(I,J)-SYD121
          SXT(I,J)=0
20        SYT(I,J)=0
1         DO 60 K=1,2
          READ 2,(TAG(I),I=1,27)
          CONTINUE
          LDA TAG
          SUB TAGTST
          TZE
          BTR $999
          READ 100,((SR(I,J),I=1,23),J=1,4)
          READ 200,((SA(I,J),I=1,23),J=1,4)
          DO 30 J=1,4
          DO 30 I=1,23
          SA(I,J)=(180.-SA(I,J))*3.14159/180.
          SR(I,J)=SR(I,J)-(SR(I,J)*5./22.)
          SX(I,J)=SR(I,J)*(COSF(SA(I,J)))
30        SY(I,J)=SR(I,J)*(SINF(SA(I,J)))
          SX121=SX(12,1)
          SY121=SY(12,1)
          DO 40 J=1,4
          DO 40 I=1,23
          SX(I,J)=SX(I,J)-SX121
40        SY(I,J)=SY(I,J)-SY121
          TNT=(SY(23,1)-SY(1,1))/(SX(23,1)-SX(1,1))
          CST=COSF(ATANF(TNT))
          SNT=TNT*CST
          DO 50 J=1,4
          DO 50 I=1,23
          SX(I,J)=(SY(I,J)*SNT)+(SX(I,J)*CST)
50        SY(I,J)=(SY(I,J)*CST)-(SX(I,J)*SNT)
          DO 60 J=1,4
          DO 60 I=1,23
          SXT(I,J)=SXT(I,J)+SX(I,J)
60        SYT(I,J)=SYT(I,J)+SY(I,J)
```

```
      DO 70 J=1,4
      DO 70 I=1,23
      SXT(I,J)=(SXT(I,J)/2.)-SXD(I,J)
70    SYT(I,J)=(SYT(I,J)/2.)-SYD(I,J)
      CONTINUE
      XYINC=0.005
      SSQX=0
      L=0
      K=0
710   SMSQX=0
      DO 72 J=1,4
      DO 72 I=1,23
72    SMSQX=SMSQX+(SXT(I,J)*SXT(I,J))
      IF(K)73,73,74
73    K=1
      GO TO 76
74    IF(SMSQX-SSQX)76,76,7000
76    SSQX=SMSQX
      DO 75 J=1,4
      DO 75 I=1,23
75    SXT(I,J)=SXT(I,J)+XYINC
      GO TO 710
7000  SSQX=SMSQX
      IF(L)7001,7001,7002
7001  L=1
      XYINC=-XYINC
      GO TO 710
7002  DO 7003 J=1,4
      DO 7003 I=1,23
7003  SXT(I,J)=SXT(I,J)-XYINC
      SSQY=0
      L=0
      K=0
7100  SMSQY=0
      DO 720 J=1,4
      DO 720 I=1,23
720   SMSQY=SMSQY+(SYT(I,J)*SYT(I,J))
      IF(K)730,730,740
730   K=1
      GO TO 760
740   IF(SMSQY-SSQY)760,760,8000
760   SSQY=SMSQY
      DO 750 J=1,4
      DO 750 I=1,23
750   SYT(I,J)=SYT(I,J)+XYINC
      GO TO 7100
8000  SSQY=SMSQY
      IF(L)8001,8001,8002
8001  L=1
```

```
          XYINC=-XYINC
          GO TO 7100
8002      DO 8003 J=1,4
          DO 8003 I=1,23
8003      SYT(I,J)=SYT(I,J)-XYINC
          PRINT(1)4,(TAG(I),I=1,18),TAG(23),TAG(24),TAG(25)
          DO 55 I=1,23
          PRINT(1)600, SXT(I,4),SXT(I,3),SXT(I,2),SXT(I,1)
55        PRINT(1)700,SYT(I,4),SYT(I,3),SYT(I,2),SYT(I,1)
          CONTINUE
          LXK 0,7                INITIALLIZE COUNTER TO REZERO RUNNING SUM
          LDZ                    PREPARE ZERO IN ACCUMULATOR
          STA SXT,7              STORE ZERO IN SXT(I,J) VECTOR
          STA SYT,7              STORE ZERO IN SXT(I,J) VECTOR
          INX 1,7                INDEX VECTOR SUBSCRIPT COUNTER
          TXH 92,7               HAVE SXT(23,4) AND SYT(4,23) BEEN DONE
          BTR *-4                IF NOT GO BACK 4 INSTRUCTIONS
          GO TO 1
999       CALL FAC2
          STOP
2         FORMAT(7A3,7A3,7A3,5A3,A2)
4         FORMAT(///,2X,7A3,7A3,7A3,/)
100       FORMAT(8F6.3,5F6.3,/,5F6.3,5F6.3)
200       FORMAT(8F6.1,5F6.1,/,5F6.1,5F6.1)
600       FORMAT(23X,F5.2,2X,F5.2,2X,F5.2,2X,F5.2)
700       FORMAT(23X,F5.2,2X,F5.2,2X,F5.2,2X,F5.2,/)
TAGTST CON A,3,***
        END

*

*PROGRAM END.    0 FORTRAN ERRORS
         END


144407 FIN
```

Dense Pattern Least Squares Deviation From Datum Plot

```
...........=...*.......=...........=...........=
..*........=...........=...*.......=...........= typical 1st
...........=...........=...........=...........= row coordinates
...........=...........=...........=....*......=
...........=...........=...........=...........=
...........=...........=...........=...........=
...........=...........=...........=...........=
.....+.....=.....+.....=.....+.....=.....+.....=
================================================
......*....=....*......=...*.......=...........= typical 12th
.....+.....=.....+.....=.....+.....=.....*.....= row coordinates
================================================
.....+.....=.....+.....=.....+.....=.....+.....=
...........=...........=...........=...........=
...........=...........=...........=...........= typical 23rd
...........=...........=...........=...........= row coordinates
...........=.....*.....=...........=...........=
.....*.....=...........=....*......=...........=
...........=...........=...........=...........=
...........=...........=...........=........*..=
================================================
```

This program combines the features of the 3 previous programs and is similar to "Sparse Pattern Least Squares Deviation from Datum Plot". Because of large circumferential displacements the x-coordinate was increased to accommodate ± 0.070in. while the y-range remains ± 0.050in. (i.e. 0.100in.). In order to reduce the circumferential length of the plot, only the circumferential range between the outermost actual tracer positions as well as the datum position is printed. Hence the fields containing the smallest x-deformations are the narrowest. Buffering and character manipulation is described in detail in the comments to the right of the assembler language listing among the Fortran.

```
      CALL FAC1
      DIMENSION SAD(23,4),SRD(23,4),SXD(23,4),SYD(23,4),SR(23,4),SA(
     123,4),SX(23,4),SY(23,4),SXT(23,4),SYT(23,4),TAG(27)
      DIMENSION IX(92),IY(92),OUTBF(512)
      DO 10 J=1,4
      DO 10 I=1,23
      SAD(I,J)=(I-12)*3.14159/180.
      SRD(I,J)=6.-(0.09375*J)
      SXD(I,J)=SRD(I,J)*(SINF(SAD(I,J)))
10    SYD(I,J)=SRD(I,J)*(COSF(SAD(I,J)))
      SXD121=SXD(12,1)
      SYD121=SYD(12,1)
      DO 20 J=1,4
      DO 20 I=1,23
      SXD(I,J)=SXD(I,J)-SXD121
      SYD(I,J)=SYD(I,J)-SYD121
      SXT(I,J)=0
20    SYT(I,J)=0
1     DO 60 K=1,2
      READ 2,(TAG(I),I=1,27)
      CONTINUE
      LDA TAG
      SUB TAGTST
      TZE
      BTR $999
      READ 100,((SR(I,J),I=1,23),J=1,4)
      READ 200,((SA(I,J),I=1,23),J=1,4)
      DO 30 J=1,4
      DO 30 I=1,23
      SA(I,J)=(180.-SA(I,J))*3.14159/180.
      SR(I,J)=SR(I,J)-(SR(I,J)*5./22.)
      SX(I,J)=SR(I,J)*(COSF(SA(I,J)))
30    SY(I,J)=SR(I,J)*(SINF(SA(I,J)))
      SX121=SX(12,1)
      SY121=SY(12,1)
      DO 40 J=1,4
      DO 40 I=1,23
      SX(I,J)=SX(I,J)-SX121
40    SY(I,J)=SY(I,J)-SY121
      TNT=(SY(23,1)-SY(1,1))/(SX(23,1)-SX(1,1))
      CST=COSF(ATANF(TNT))
      SNT=TNT*CST
      DO 50 J=1,4
      DO 50 I=1,23
      SX(I,J)=(SY(I,J)*SNT)+(SX(I,J)*CST)
50    SY(I,J)=(SY(I,J)*CST)-(SX(I,J)*SNT)
      DO 60 J=1,4
      DO 60 I=1,23
      SXT(I,J)=SXT(I,J)+SX(I,J)
```

```
60      SYT(I,J)=SYT(I,J)+SY(I,J)
        DO 70 J=1,4
        DO 70 I=1,23
        SXT(I,J)=(SXT(I,J)/2.)-SXD(I,J)
70      SYT(I,J)=(SYT(I,J)/2.)-SYD(I,J)
        CONTINUE
        XYINC=0.005
        SSQX=0
        L=0
        K=0
710     SMSQX=0
        DO 72 J=1,4
        DO 72 I=1,23
72      SMSQX=SMSQX+(SXT(I,J)*SXT(I,J))
        IF(K)73,73,74
73      K=1
        GO TO 76
74      IF(SMSQX-SSQX)76,76,7000
76      SSQX=SMSQX
        DO 75 J=1,4
        DO 75 I=1,23
75      SXT(I,J)=SXT(I,J)+XYINC
        GO TO 710
7000    SSQX=SMSQX
        IF(L)7001,7001,7002
7001    L=1
        XYINC=-XYINC
        GO TO 710
7002    DO 7003 J=1,4
        DO 7003 I=1,23
7003    SXT(I,J)=SXT(I,J)-XYINC
        SSQY=0
        L=0
        K=0
7100    SMSQY=0
        DO 720 J=1,4
        DO 720 I=1,23
720     SMSQY=SMSQY+(SYT(I,J)*SYT(I,J))
        IF(K)730,730,740
730     K=1
        GO TO 760
740     IF(SMSQY-SSQY)760,760,8000
760     SSQY=SMSQY
        DO 750 J=1,4
        DO 750 I=1,23
750     SYT(I,J)=SYT(I,J)+XYINC
        GO TO 7100
8000    SSQY=SMSQY
        IF(L)8001,8001,8002
8001    L=1
```

```
       XYINC=-XYINC
       GO TO 7100
8002   DO 8003 J=1,4
       DO 8003 I=1,23
8003   SYT(I,J)=SYT(I,J)-XYINC
       PRINT(1)4,(TAG(I),I=1,18),TAG(23),TAG(24),TAG(25)
       CONTINUE
       LXK 0,7              INITIALLIZE INTEGER ARRAY COUNTER
LOOP   LDA SXT,7            LOAD X-COORDINATE VALUE
       FMP F100             CHANGE SCALE BY 100
       FIX 23               CREATE INTEGER
       ADD FFTEEN           ADD FIFTEEN TO ENSURE NONNEGATIVE X-COORD.
       STA IX,7             STORE INTEGER X-COORDINATE
       LDA SYT,7            DO PREVIOUS
       FMP F100             FIVE STEPS
       FIX 23               TO PREPARE
       ADD FIVE             Y-COORDINATE AS
       STA IY,7             NONNEGATIVE INTEGER
       INX 1,7              INCREMENT COORDINATE COUNTER
       TXH 92,7             HAVE 92 POINTS IN ARRAY BEEN DONE
       BTR LOOP             IF NOT, DO NEXT COORDINATE
       LXK 0,7              ACTIVE AREA COUNTER
       LDA BLANK1           ... THREE PERIODS
       STA OUTPAT,7         INITIALLIZE PRELIM. BUFFER
       INX 1,7              NEXT WORD
       TXH 124,7            IS ACTIVE AREA FINISHED
       BTR *-3              ACTIVE AREA IS FINISHED
       LXK 3,7              VERTICAL BORDER COUNTER
       LDA ENDLIN           ..= TWO PERIODS AND AN EQUAL SIGN
       STA OUTPAT,7         PREPARE VERTICAL BORDER
       INX 4,7              NEXT LINE DOWN
       TXH 124,7            IS VERTICAL BORDER FINISHED
       BTR *-3              IF NOT, GO BACK THREE INSTRUCTIONS
       LXK 0,7              LOWER HORIZONTAL BORDER COUNTER
       LDA BOTLIN           === THREE EQUAL SIGNS
       STA OUTPAT+124,7     PREPARE HORIZONTAL BORDER
       INX 1,7              NEXT THREE ACROSS
       TXH 4,7              IS HORIZONTAL BORDER FINISHED
       BTR *-3              IF IT IS, KEEP ON
       LDA ORIGIN           ..+ TWO PERIODS AND A PLUS SIGN
       STA OUTPAT+61        PLACE ORIGIN IN ARRAY
       LXK 0,3              INITIALLIZE COORDINATE COUNTER
       LXK 0,6              BIG BUFFER COUNTER
NXTCRD LDA IX,3             PICK UP AN X-COORDINATE
       TOD 23               IS IT NEGATIVE
       BTS TOOBIG           IF IT IS, IT IS OUT OF RANGE
       SUB THRTY1           SUBTRACT 31
       TOD 23               IS IT LARGER THAN 31
```

```
        BTR TOOBIG      IF IT IS, IT IS OUT OF RANGE
        LDA IX,3        RELOAD COORDINATE RUINED BY SUBTRACTION
        MAQ             PREPARE FOR MULTIPLICATION
        MPY FOUR        MULTIPLY COORDINATE BY 4
        LDA Q           MOVE PRODUCT FOR STORAGE
        RBK 23          DESTROY SPURIOUS BIT
        STA ROW         STORE MANUFACTURED ROW NUMBER
        LDA IY,3        PICK UP A Y-COORDINATE
        TOD 23          IS IT NEGATIVE
        BTS TOOBIG      IF IT IS, IT IS OUT OF RANGE
        SUB ELEVEN      SUBTRACT 11
        TOD 23          IS IT LARGER THAN 11
        BTR TOOBIG      IF IT IS, IT IS OUT OF RANGE
        LDA IX,3        LOAD ROW NUMBER
        SUB FFTEEN      SUBTRACT 15
        TZE             IS IT ON LINE, X = 0
        LDA IY,3        LOAD COLUMN NUMBER
        BTR *+2         IF X = 0, SKIP NEXT INSTRUCTION
        ADD ELEVEN      IF X = 0, USE ORIGIN TABLE
        STA 5           STORE COLUMN NUMBER FOR INDEXING
        LDA IY,3        LOAD COLUMN COORDINATE
        LXK 0,4         INITIALLIZE PATTERN WORD COUNTER
        SUB THREE       SUBTRACT 3
        TOD 23          TEST IF RESULT NEGATIVE
        BTS *+3         IF NEGATIVE, SKIP 2 INSTRUCTIONS
        INX 1,4         IF NOT, INDEX WORD COUNTER
        BRU *-4         AND GO BACK 4 INSTRUCTIONS
        LDA ROW         RETRIEVE ROW NUMBER BUILT PREVIOUSLY
        ADD 4           ADD ROW WORD COUNT
        STA 4           STORE MODIFIED WORD COUNT BACK IN XCELL7
        LDA OUTPAT,4    GET WORD TO BE RELACED
        STA TEMPAT      AND SAVE IT
        LDA STRSTN,5    PICK UP PATTERNED WORD FROM TABLE
        STA OUTPAT,4    AND PLACE IT IN PRELIMINARY BUFFER
BIGBUG  LXK 0,7         INITIALLIZE COUNTER TO EMPTY OUTPAT
        LDA OUTPAT,7    LOAD WORD FROM OUTPAT
        STA OUTBF,6     INTO OUTPUT BUFFER
        INX 1,7         INDEX PRELIMINARY BUFFER
        INX 1,6         INDEX OUTPUT BUFFER
        TXH 128,7       IS PRELIMINARY BUFFER TRANSFER FINISHED
        BTR *-5         IF NOT GO BACK 5 INSTRUCTIONS
        INX 23,3        INDEX COORDINATE SUBSCRIPT
        LDA TEMPAT      RETRIEVE AND REPLACE
        STA OUTPAT,4    OVERWRITTEN WORD IN PRELIMINARY BUFFER
        TXH 512,6       IS OUTPUT BUFFER FULL
        BTR NXTCRD      IF NOT DO NEXT COORDINATE POINT
        STX I,3         PUT COORDINATE INDEX IN I
        LDA MNTXTW      DECREASE COORDINATE COUNTER IN ORDER
        ADD 3           TO GET BACK TO A TOP ROW COUNT
```

```
        STA XREG3              STORE X-CELLS, INCLUDING MODIFIED NO. 3,
        STX XREG4,4            NUMBER 3 THROUGH 7
        STX XREG5,5            PRIOR TO A PRINT
        STX XREG6,6
        STX XREG7,7
        LEAST=(XMINOF(IORGN,IX(I-91),IX(I-68),IX(I-45),IX(I-22)))*4
        MOST=(XMAXOFF(IORGN,IX(I-91),IX(I-68),IX(I-45),IX(I-22)))*4
        DO 777 I=LEAST,MOST,4
777     PRINT(1)3000,OUTBF(385+I),OUTBF(386+I),OUTBF(387+I),OUTBF(388+
      1I),OUTBF(257+I),OUTBF(258+I),OUTBF(259+I),OUTBF(260+I),OUTBF(12
      29+I),OUTBF(130+I),OUTBF(131+I),OUTBF(132+I),OUTBF(1+I),OUTBF(2+
      3I),OUTBF(3+I),OUTBF(4+I)
        PRINT(1)3333
        CONTINUE
        LDX XREG3,3            RESTORE INDEXING REGISTERS
        LDX XREG4,4            NUMBER 3 THROUGH 7
        LDX XREG5,5            AFTER  FORTRAN PRINT
        LDX XREG6,6            WHICH USUALLY BUGGERS
        LDX XREG7,7            LOCATIONS 6 AND 7 AT LEAST
        TXH 22,3               TEST IF ALL 23 COLUMNS IN ARRAY ARE DONE
        BTS *+3                IF DONE, PREPARE VARIABLES SXT, SYT
        INX 1,3                IF NOT, INCREMENT COORDINATE COUNTER
        BRU NXTCRD-1           GO BACK TO PATTERN FORMING ROUTINE
        LXK 0,7                INITIALLIZE COUNTER TO REZERO RUNNING SUM
        LDZ                    PREPARE ZERO IN ACCUMULATOR
        STA SXT,7              STORE ZERO IN SXT(I,J) VECTOR
        STA SYT,7              STORE ZERO IN SXT(I,J) VECTOR
        INX 1,7                INDEX VECTOR SUBSCRIPT COUNTER
        TXH 92,7               HAVE SXT(23,4) AND SYT(4,23) BEEN DONE
        BTR *-4                IF NOT GO BACK 4 INSTRUCTIONS
        BRU $1                 IF THEY HAVE GO TO 1
999     CALL FAC2
        STOP
TOOBIG  LDA BLANK1             LOAD A SAFE PATTERN INTO TEMPORAY
        STA TEMPAT             STORAGE SO THAT PATTERN REPLACING ROUTINE
        LXK 1,4                WILL HAVE SOMETHING HARMLESS TO DO.
        BRU BIGBUG             AFTER LOADING SAFE  X4, GO TO OUTPUT
2       FORMAT(7A3,7A3,7A3,5A3,A2)
4       FORMAT(///,2X,7A3,7A3,7A3,/)
100     FORMAT(8F6.3,5F6.3,/,5F6.3,5F6.3)
200     FORMAT(8F6.1,5F6.1,/,5F6.1,5F6.1)
3000    FORMAT(21X,7A3,7A3,2A3)
3333    FORMAT(21X,$=============================================$)
TAGTST  CON A,3,***
STPSTN  CON A,3,*..
        CON A,3,.*.
        CON A,3,..*
        CON A,3,*..
        CON A,3,.*.
```

```
          CON  A,3,..*
          CON  A,3,*..
          CON  A,3,.*.
          CON  A,3,..*
          CON  A,3,*.=
          CON  A,3,.*=
          CON  A,3,*..
          CON  A,3,.*.
          CON  A,3,..*
          CON  A,3,*.+
          CON  A,3,.*+
          CON  A,3,..*
          CON  A,3,*..
          CON  A,3,.*.
          CON  A,3,..*
          CON  A,3,*.=
          CON  A,3,.*=
ORIGIN    CON  A,3,..+
BLANK1    CON  A,3,...
ENDLIN    CON  A,3,..=
BOTLIN    CON  A,3,===
THRTY1    CON  D,31
ELEVEN    CON  D,11
          DEFINE IORGN(*)
FFTEEN    CON  D,15
F100      CON  F,100.
MNTYTW    CON  D,-92
ROW       BSS  1
TEMPAT    BSS  1
XREG3     BSS  1
XREG4     BSS  1
XREG5     BSS  1
XREG6     BSS  1
XREG7     BSS  1
OUTPAT    BSS  128
        END

*

*PROGRAM END.    0 FORTRAN ERRORS
         END


140331 FIN
```

Numerical Deformation Difference

This program combines the features of the first three dense pattern programs.

in addition, the direct and orthogonal (shear) differences between deformations shown by circumferentially adjacent tracer positions are computed; i.e. DXX(I,J) and DYX(I,J)

the direct and orthogonal (shear) differences between deformations shown by radially adjacent tracer positions are computed; i.e. DYY(I,J) and DXY(I,J)

these deformation differences (numerical strains) are printed in an array between representations of the adjacent tracer positions

DXX = TANGENTIAL DEFORMATION GRADIENT IN TANGENTIAL DIRECTION
DXY = TANGENTIAL DEFORMATION GRADIENT IN RADIAL DIRECTION
DYY = RADIAL DEFORMATION GRADIENT IN RADIAL DIRECTION
DYX = RADIAL DEFORMATION GRADIENT IN TANGENTIAL DIRECTION

```
         DXY          DXY          DXY
         DYY          DYY          DYY
   DXX          DXX          DXX          DXX
   DYX          DYX          DYX          DYX

       -0.003       -0.008        0.012
    *   0.001    *   0.007    *   0.014    *

 -0.000       -0.007       -0.004       -0.007
  0.014        0.004       -0.005       -0.006

       -0.010       -0.004        0.009
    *  -0.009    *  -0.002    *   0.013    *

  0.012        0.016        0.023        0.011
 -0.002        0.003       -0.001        0.003

    *            *            *            *
```

....etc.

```
      CALL FAC1
      DIMENSION SAD(23,4),SRD(23,4),SXD(23,4),SYD(23,4),SR(23,4),SA(
     123,4),SX(23,4),SY(23,4),SXT(23,4),SYT(23,4),TAG(27)
      DIMENSION DXX(22,4),DYX(22,4),DYY(23,3),DXY(23,3)
      DO 10 J=1,4                 5-6
      DO 10 I=1,23
      SAD(I,J)=(I-12)*3.14159/180.
      SRD(I,J)=6.-(0.09375*J)
      SXD(I,J)=SRD(I,J)*(SINF(SAD(I,J)))
10    SYD(I,J)=SRD(I,J)*(COSF(SAD(I,J)))
      SXD121=SXD(12,1)
      SYD121=SYD(12,1)
      DO 20 J=1,4
      DO 20 I=1,23
      SXD(I,J)=SXD(I,J)-SXD121
      SYD(I,J)=SYD(I,J)-SYD121
      SXT(I,J)=0
20    SYT(I,J)=0
1     DO 60 K=1,2
      READ 2,(TAG(I),I=1,27)
      CONTINUE
      LDA TAG
      SUB TAGTST
      TZE
      BTR $999
      READ 100,((SR(I,J),I=1,23),J=1,4)
      READ 200,((SA(I,J),I=1,23),J=1,4)
      DO 30 J=1,4
      DO 30 I=1,23
      SA(I,J)=(180.-SA(I,J))*3.14159/180.
      SR(I,J)=SR(I,J)-(SR(I,J)*5./22.)
      SX(I,J)=SR(I,J)*(COSF(SA(I,J)))
30    SY(I,J)=SR(I,J)*(SINF(SA(I,J)))
      SX121=SX(12,1)
      SY121=SY(12,1)
      DO 40 J=1,4
      DO 40 I=1,23
      SX(I,J)=SX(I,J)-SX121
40    SY(I,J)=SY(I,J)-SY121
      TNT=(SY(23,1)-SY(1,1))/(SX(23,1)-SX(1,1))
      CST=COSF(ATANF(TNT))
      SNT=TNT*CST
      DO 50 J=1,4
      DO 50 I=1,23
      SX(I,J)=(SY(I,J)*SNT)+(SX(I,J)*CST)
50    SY(I,J)=(SY(I,J)*CST)-(SX(I,J)*SNT)
      DO 60 J=1,4
      DO 60 I=1,23
      SXT(I,J)=SXT(I,J)+SX(I,J)
```

```
60      SYT(I,J)=SYT(I,J)+SY(I,J)
        DO 70 J=1,4
        DO 70 I=1,23
        SXT(I,J)=(SXT(I,J)/2.)-SXD(I,J)
70      SYT(I,J)=(SYT(I,J)/2.)-SYD(I,J)
        CONTINUE
        XYINC=0.005
        SSQX=0
        L=0
        K=0
710     SMSQX=0
        DO 72 J=1,4
        DO 72 I=1,23
72      SMSQX=SMSQX+(SXT(I,J)*SXT(I,J))
        IF(K)73,73,74
73      K=1
        GO TO 76
74      IF(SMSQX-SSQX)76,76,7000
76      SSQX=SMSQX
        DO 75 J=1,4
        DO 75 I=1,23
75      SXT(I,J)=SXT(I,J)+XYINC
        GO TO 710
7000    SSQX=SMSQX
        IF(L)7001,7001,7002
7001    L=1
        XYINC=-XYINC
        GO TO 710
7002    DO 7003 J=1,4
        DO 7003 I=1,23
7003    SXT(I,J)=SXT(I,J)-XYINC
        SSQY=0
        L=0
        K=0
7100    SMSQY=0
        DO 720 J=1,4
        DO 720 I=1,23
720     SMSQY=SMSQY+(SYT(I,J)*SYT(I,J))
        IF(K)730,730,740
730     K=1
        GO TO 760
740     IF(SMSQY-SSQY)760,760,8000
760     SSQY=SMSQY
        DO 750 J=1,4
        DO 750 I=1,23
750     SYT(I,J)=SYT(I,J)+XYINC
        GO TO 7100
8000    SSQY=SMSQY
        IF(L)8001,8001,8002
8001    L=1
```

```
      XYINC=-XYINC
      GO TO 7100
8002  DO 8003 J=1,4
      DO 8003 I=1,23
8003  SYT(I,J)=SYT(I,J)-XYINC
      PRINT(1)4,(TAG(I),I=1,18),TAG(23),TAG(24),TAG(25)
      PRINT(1)5                106-107
      PRINT(1)6
      PRINT(1)7
      PRINT(1)8
      PRINT(1)9
      DO 9000 J=1,4
      DO 9000 I=1,22
      DXX(I,J)=SXT(I+1,J)-SXT(I,J)
9000  DYX(I,J)=SYT(I+1,J)-SYT(I,J)
      DO 9001 J=1,3
      DO 9001 I=1,23
      DYY(I,J)=SYT(I,J)-SYT(I,J+1)
9001  DXY(I,J)=SXT(I,J)-SXT(I,J+1)
      I=1                 119-120
9006  PRINT(1)9002,DXY(I,3),DXY(I,2),DXY(I,1)
      PRINT(1)9003,DYY(I,3),DYY(I,2),DYY(I,1)
      IF(I-22)9007,9007,9008
9007  PRINT(1)9004,DXX(I,4),DXX(I,3),DXX(I,2),DXX(I,1)
      PRINT(1)9004,DYX(I,4),DYX(I,3),DYX(I,2),DYX(I,1)
      I=I+1
      IF(I-23)9006,9006,9008
9008  CONTINUE
      LXK 0,7             INITIALLIZE COUNTER TO REZERO RUNNING SUM
      LDZ                 PREPARE ZERO IN ACCUMULATOR
      STA SXT,7           STORE ZERO IN SXT(I,J) VECTOR
      STA SYT,7           STORE ZERO IN SXT(I,J) VECTOR
      INX 1,7             INDEX VECTOR SUBSCRIPT COUNTER
      TXH 92,7            HAVE SXT(23,4) AND SYT(4,23) BEEN DONE
      BTR *-4             IF NOT GO BACK 4 INSTRUCTIONS
      BRU $1              IF THEY HAVE GO TO 1
999   CALL FAC2
      STOP
2     FORMAT(7A3,7A3,7A3,5A3,A2)
4     FORMAT(///,2X,7A3,7A3,7A3,/)       140-141
5     FORMAT($ DXX = TANGENTIAL DEFORMATION GRADIENT IN TANGENTIAL D
     1IRECTION$)
6     FORMAT($ DXY = TANGENTIAL DEFORMATION GRADIENT IN RADIAL DIREC
     1TION$)
7     FORMAT($ DYY = RADIAL DEFORMATION GRADIENT IN RADIAL DIRECTION
     1$)
8     FORMAT($ DYX = RADIAL DEFORMATION GRADIENT IN TANGENTIAL DIREC
     1TION$,/)
```

```
9        FORMAT(19X,8X,$DXY$,9X,$DXY$,9X,$DXY$,/,19X,8X,$DYY$,9X,$DYY$
        19X,$DYY$,/21X,$DXX$,9X,$DXX$,9X,$DXX$,9X,$DXX$,/,21X,$DYX$,9X,
        2DYX$,9X,$DYX$,9X,$DYX$,/)
100      FORMAT(8F6.3,5F6.3,/,5F6.3,5F6.3)
200      FORMAT(8F6.1,5F6.1,/,5F6.1,5F6.1)
9002     FORMAT(/,25X,F6.3,6X,F6.3,6X,F6.3)
9003     FORMAT(22X,$*  $,F6.3,$   *  $,F6.3,$   *  $,F6.3,$   *$,/)
9004     FORMAT(19X,F6.3,6X,F6.3,6X,F6.3,6X,F6.3)
TAGTST CON A,3,***
       END

*

*PROGRAM END.    0 FORTRAN ERRORS
         END

141643 FIN
```

Chronological Strain Difference

This program is identical to the previous one except for the additional statements shown on the next page.

the difference between chronologically successive data as before [i.e. $DXX(I,J) = DXX(I,J)_i - DXX(I,J)_{i-1}$, $DYX(I,J) = DYX(I,J)_i - DYX(I,J)_{i-1}$, $DYY(I,J) = DYY(I,J)_i - DYY(I,J)_{i-1}$ and $DXY(I,J) = DXY(I,J)_i - DXY(I,J)_{i-1}$] are computed and printed out in identical format as shown in the preceding program.

Additional Statements to Convert Numerical Strain (Deformation Differences) to Chronological Strain Differences - Insert as Shown

```
          DIMENSIØN DPXX(22,4),DPYX(22,4),DPYY(23,3),DPXY(23,3)
                                                  (between 5 and 6)

          PRINT(1)44
                                                  (between 106 and 107)

          DØ 9010 J=1,4
          DØ 9010 I=1,22
          TEMP=DXX(I,J)
          DXX(I,J)=DXX(I,J)-DPXX(I,J)
          DPXX(I,J)=TEMP
          TEMP=DYX(I,J)
          DYX(I,J)=DYX(I,J)-DPYX(I,J)
9010      DPYX(I,J)=TEMP
          DØ 9020 J=1,3
          DØ 9020 I=1,23
          TEMP=DYY(I,J)
          DYY(I,J)=DYY(I,J)-DPYY(I,J)
          DPYY(I,J)=TEMP
          TEMP=DXY(I,J)
          DXY(I,J)=DXY(I,J)-DPXY(I,J)
9020      DPYX(I,J)=TEMP
                                                  (between 119 and 120)

44        FØRMAT($ CHRØNØLØGICAL RUNNING STRAIN DIFFERENCES $)
                                                  (between 140 and 141)
```

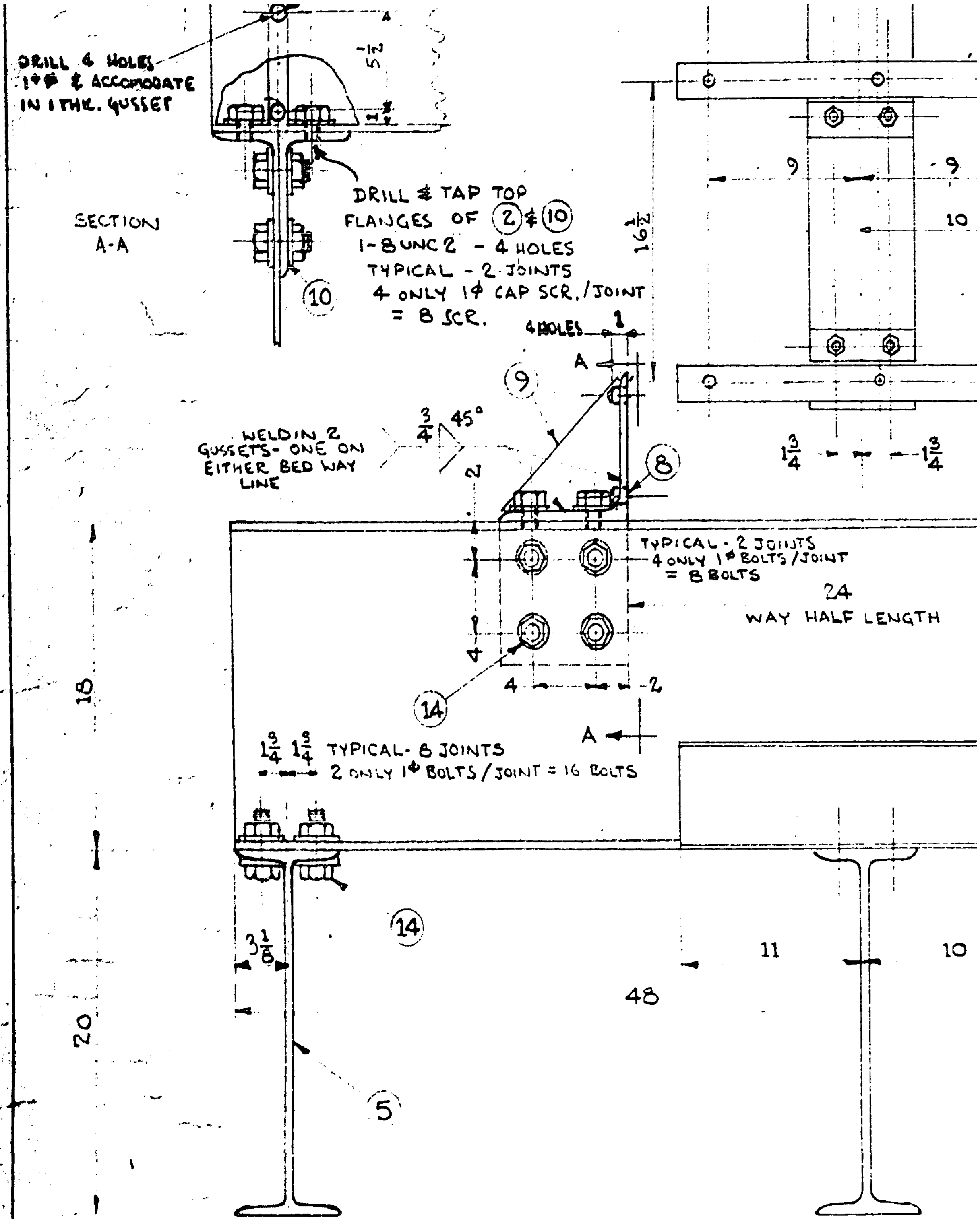

PLANE OR MILL FLAT (125√) STRUCTURAL STEEL SURFACES FOR ALL JOINTS

BED CHANNEL
ORIGINAL TOP FL

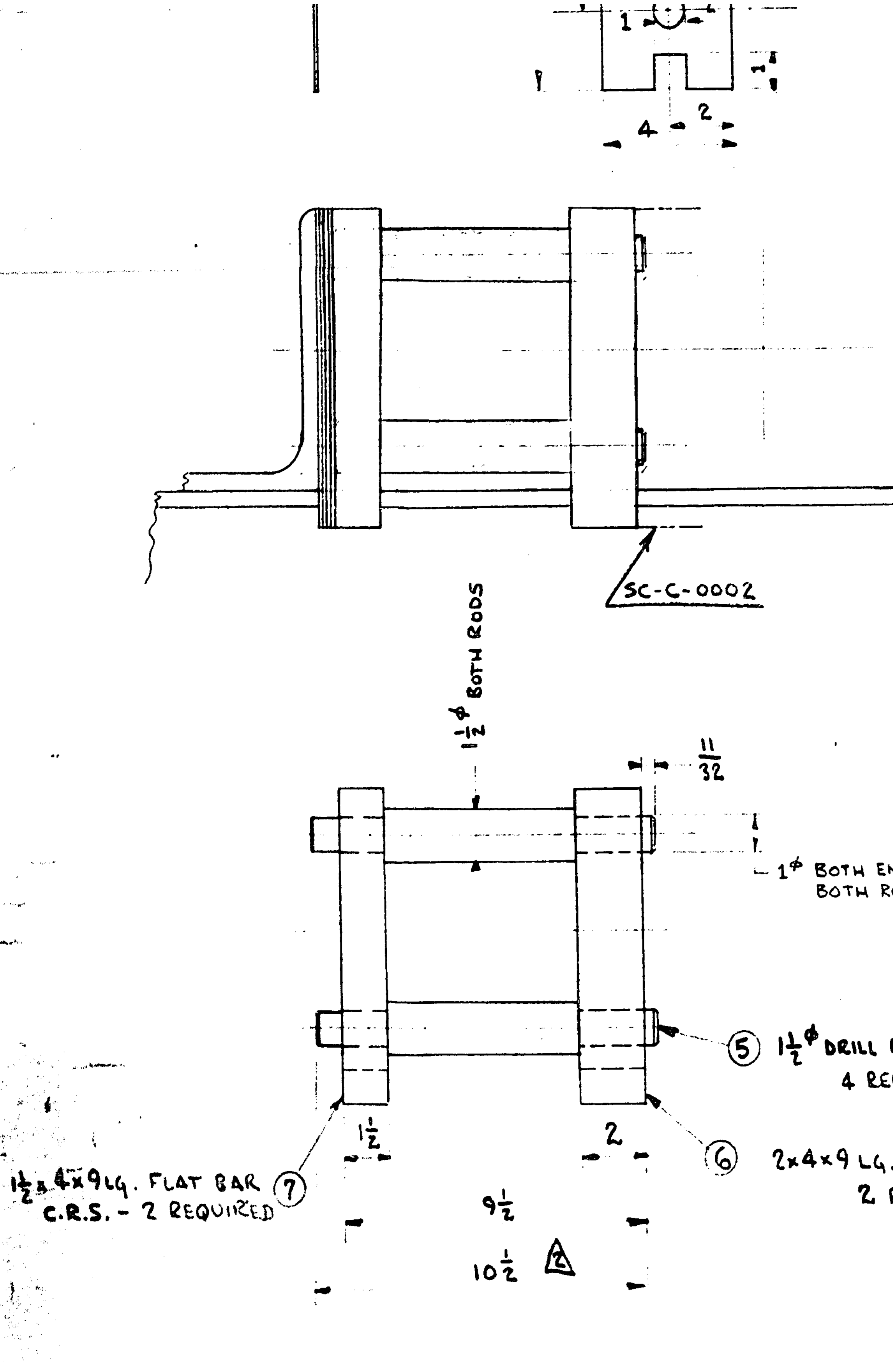

FINISH ALL DETAILS
ALL OVER

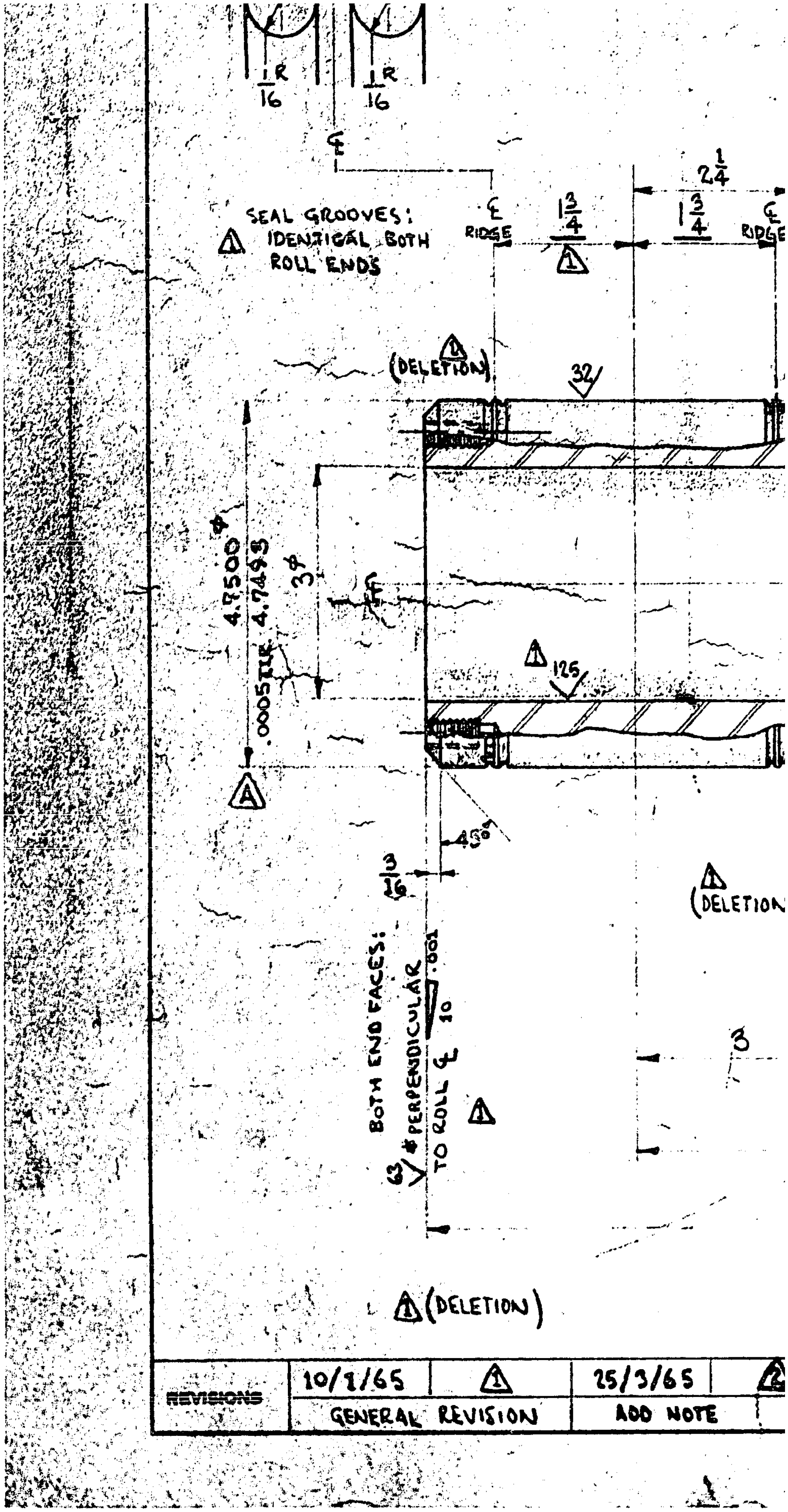
1/16 R
1/16 R
SEAL GROOVES: IDENTICAL BOTH ROLL ENDS
RIDGE
1 3/4
2 1/4
1 3/4
RIDGE
(DELETION)
32
4.7500 4.7493
.0005 TIR
3 1/8
125
A
45°
3/16
(DELETION
BOTH END FACES:
63 PERPENDICULAR TO ROLL ℄ .001 10
3
(DELETION)
REVISIONS
10/1/65
GENERAL REVISION
25/3/65
ADD NOTE

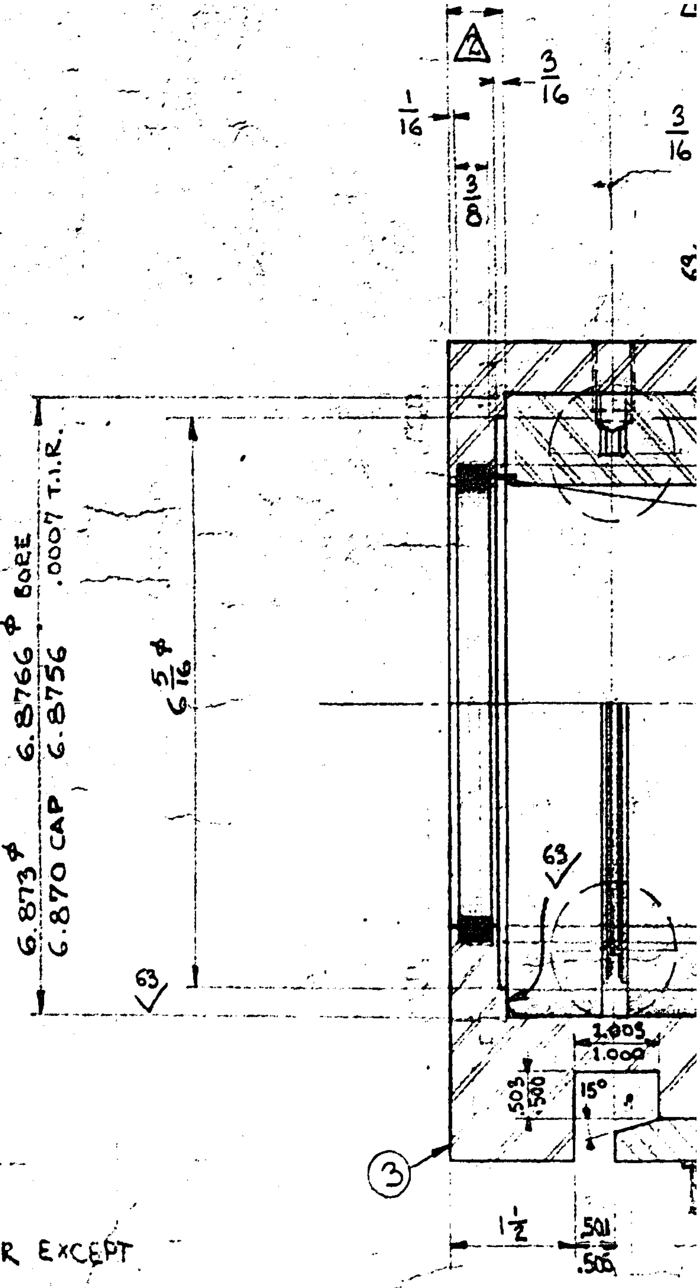

FINISH 125 ALL OVER EXCEPT AS NOTED

3 DELETION

FINIS
SURF
MILL
AT E
2 ALL
PERP
SPEC

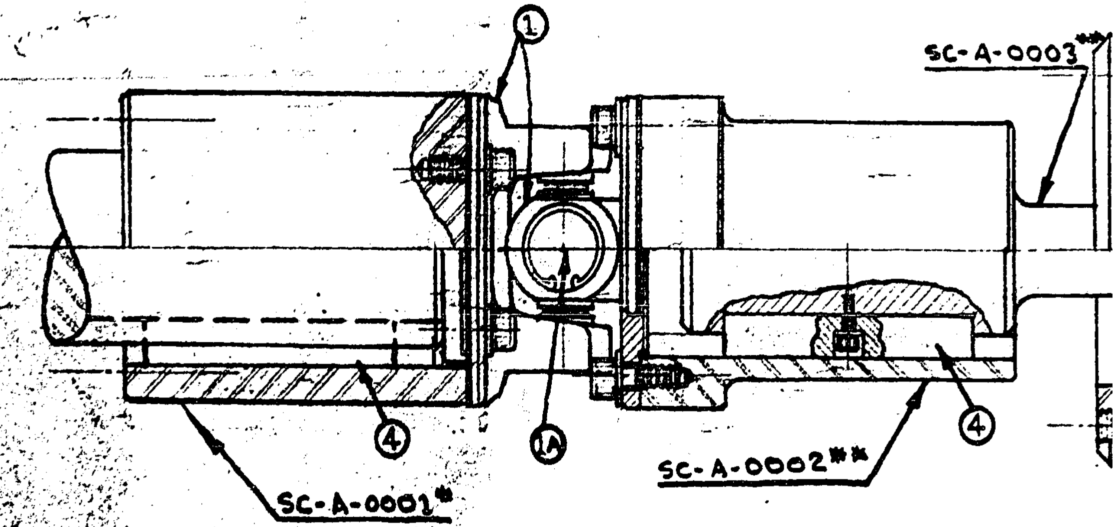

- DISASSEMBLE 1A
- REMOVE NEEDLE ELEMENTS
- REPLACE WITH SNUG FITTING, HIGH LOAD BRONZE SLEEVES (8 SLEEVES 4 PER CROSS)
- GREASE WITH MOLYBDENUM-DISULFIDE GREASE ON REASSEMBLY

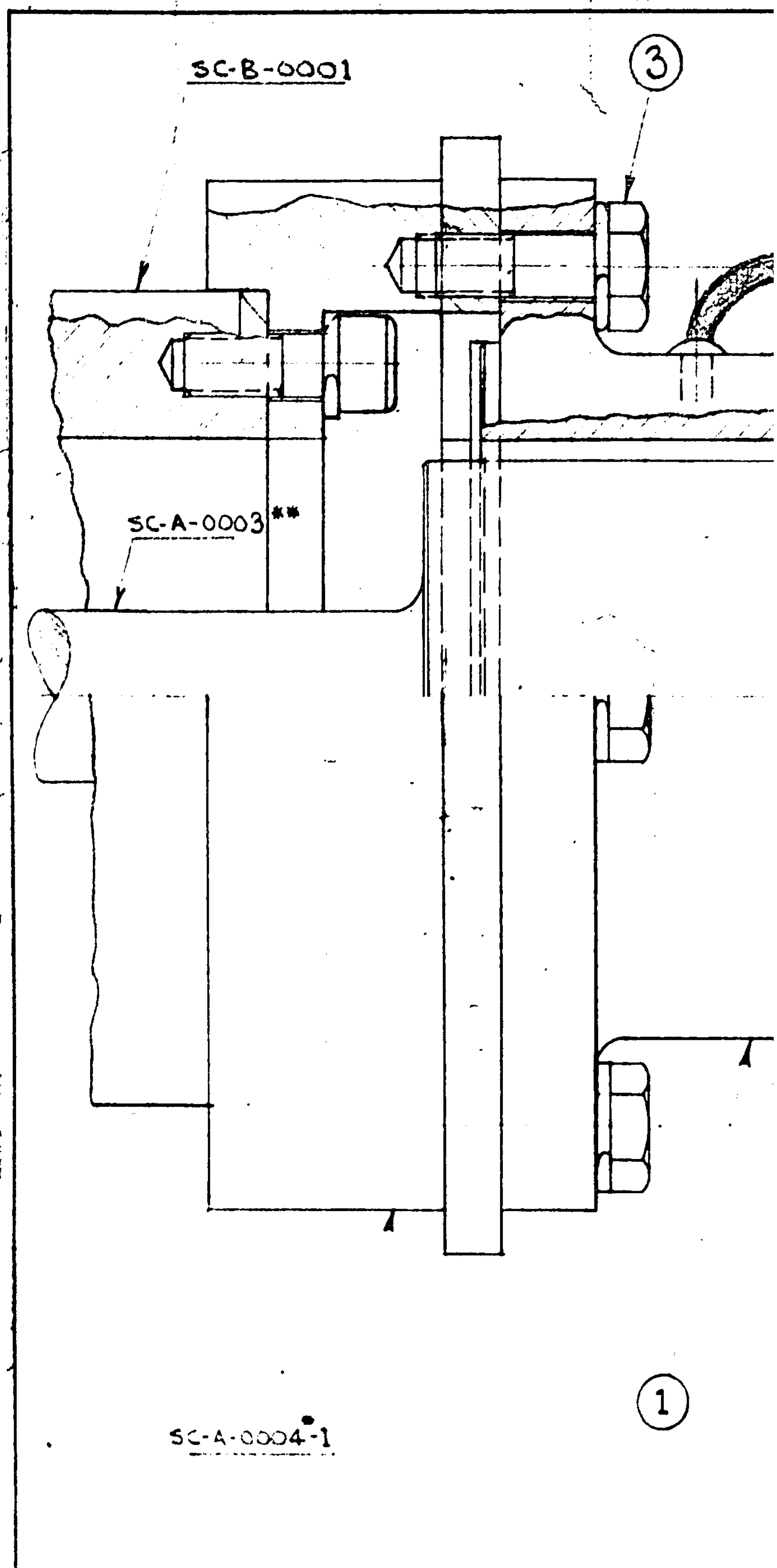

REVISIONS

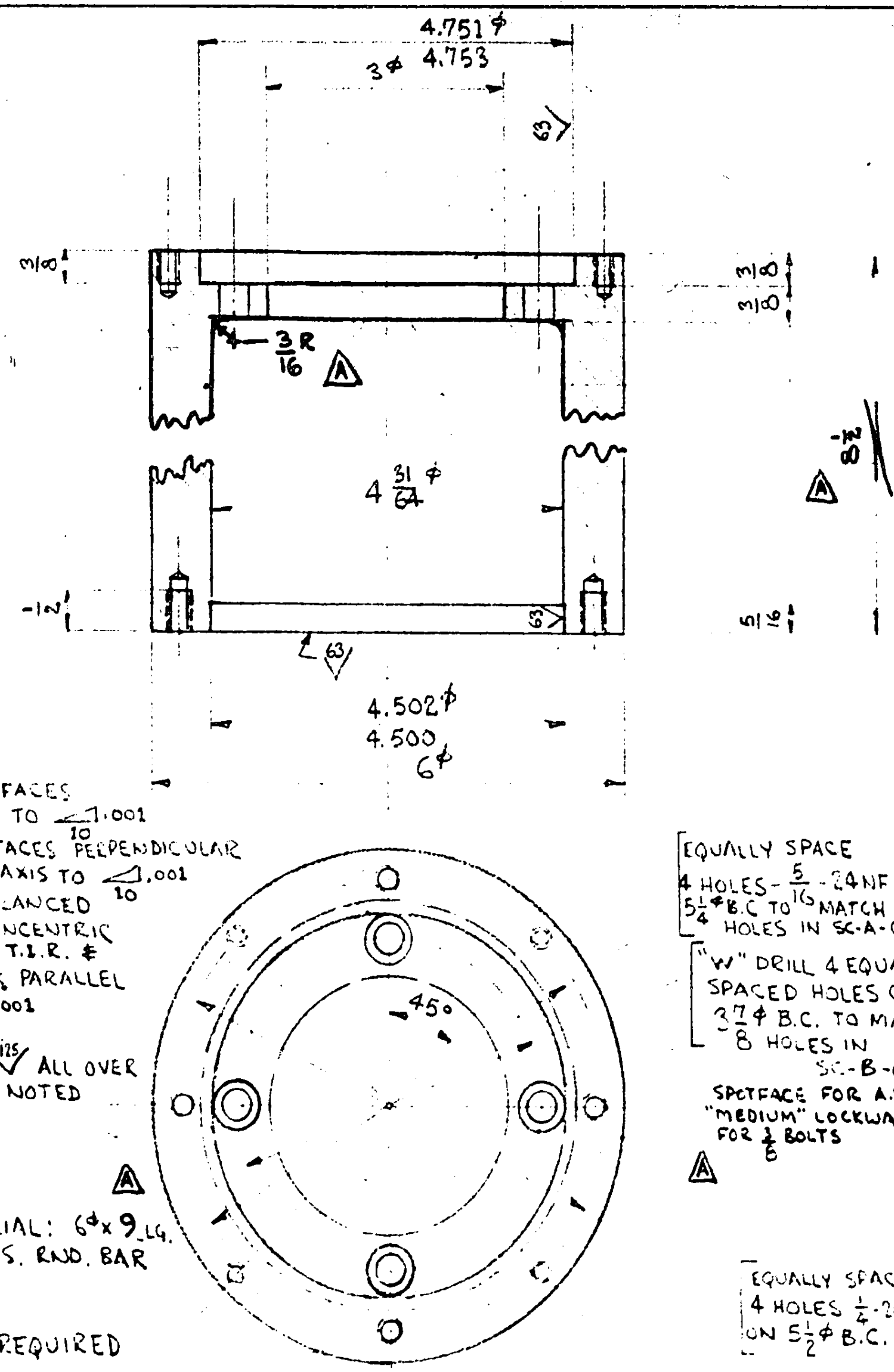

ALL FLAT FACES PARALLEL TO 1/10 .001
ALL FLAT FACES PERPENDICULAR TO BORE AXIS TO 1/10 .001
ALL TOLERANCED BORES CONCENTRIC TO .001 T.I.R. & SURFACES PARALLEL TO 1/10 .001

FINISH 125 ALL OVER EXCEPT AS NOTED

A

MATERIAL: 6ϕ x 9 LG. C.R.S. RND. BAR

1 REQUIRED

EQUALLY SPACE 4 HOLES - 5/16 - 24NF ON 5 1/4 ϕ B.C. TO MATCH HOLES IN SC-A-0005

"W" DRILL 4 EQUALLY SPACED HOLES ON 3 7/8 ϕ B.C. TO MATCH HOLES IN SC-B-0001

SPOTFACE FOR A.S. "MEDIUM" LOCKWASHER FOR 3/8 BOLTS

A

EQUALLY SPACE 4 HOLES 1/4 - 20NC ON 5 1/2 ϕ B.C.

REVISIONS: 23/3/65 A GENERAL REVISION		SCALE: HALF SIZE
DRAWN: P.J. Zsombor - Murray	McGILL UNIVERSITY — MONTREAL	DATE: 8 JANUARY, 1965
CHECKED	EXPERIMENTAL LABORATORY SUPERCALENDER COUPLING BELL HOUSING	DRAWING NO: SC-A-0004 *

ALL FINISHED FLAT SURFACES PARALLEL TO $\frac{\triangleleft}{10}$.001 & PERPENDICULAR TO BORE AXIS $\frac{\triangleleft}{10}$.001

ALL TOLERANCED BORES CONCENTRIC TO .001 T.I.R. & CYL. SURFACES PARALLEL TO $\frac{\triangleleft}{10}$.001

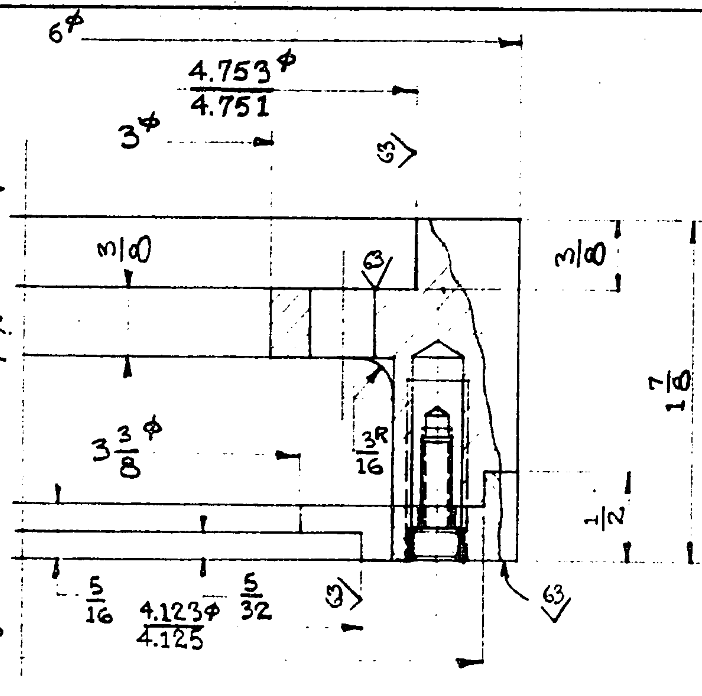

"W" DRILL 4 EQUALLY SPACED HOLES ON $3\frac{7}{8}$⌀ B.C. TO MATCH HOLES IN SC-B-0001
- SPOTFACE FOR A.S. "MEDIUM" LOCKWASHER

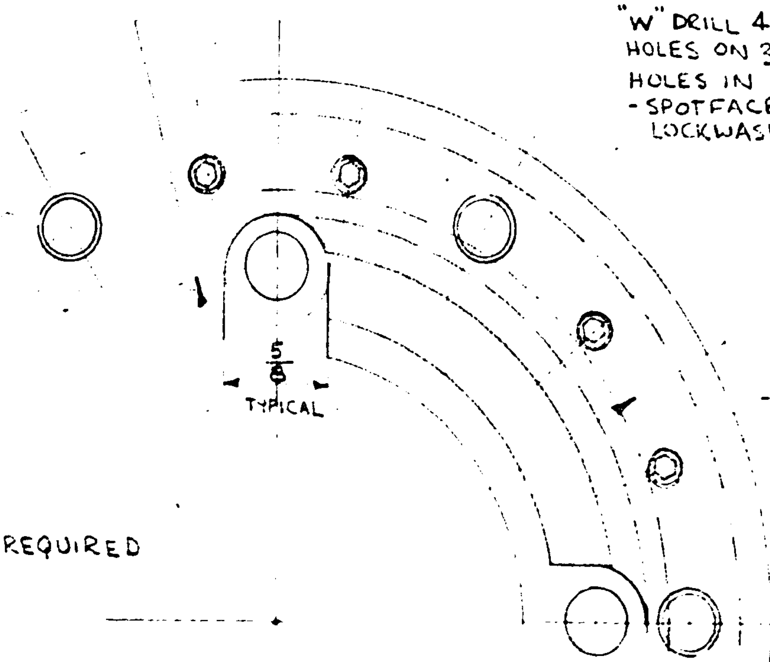

TAP 6 HOLES 1 DEEP $\frac{3}{8}$-24-NF EQUALLY SPACED ON 5⌀ B.C.

- PLACE 12 SKT. HD. CAP SCR. @ 20° ON EITHER SIDE OF TAPPED HOLES: #10-32NF × $\frac{1}{2}$ LG. TO SECURE FLANGE RING: C'BORE SCR. HDS. FLUSH

1 REQUIRED

MATERIAL: SC-A-0004* AND {12 ONLY #10-32NF × $\frac{1}{2}$ LG. SCKT. HD. CAP SCR. / 6⌀ × 1 LG. CRS. RND. BAR

REVISIONS						SCALE: FULL SIZE

DRAWN	McGILL UNIVERSITY — MONTREAL	DATE
P.J. ZSOMBOR-MURRAY		15 JULY 1965
CHECKED	EXPERIMENTAL LABORATORY SUPERCALENDER COUPLING BELL HOUSING - ROLL END DYNAMOMETER ADAPTER	DRAWING NO: SC-A-0004*-1

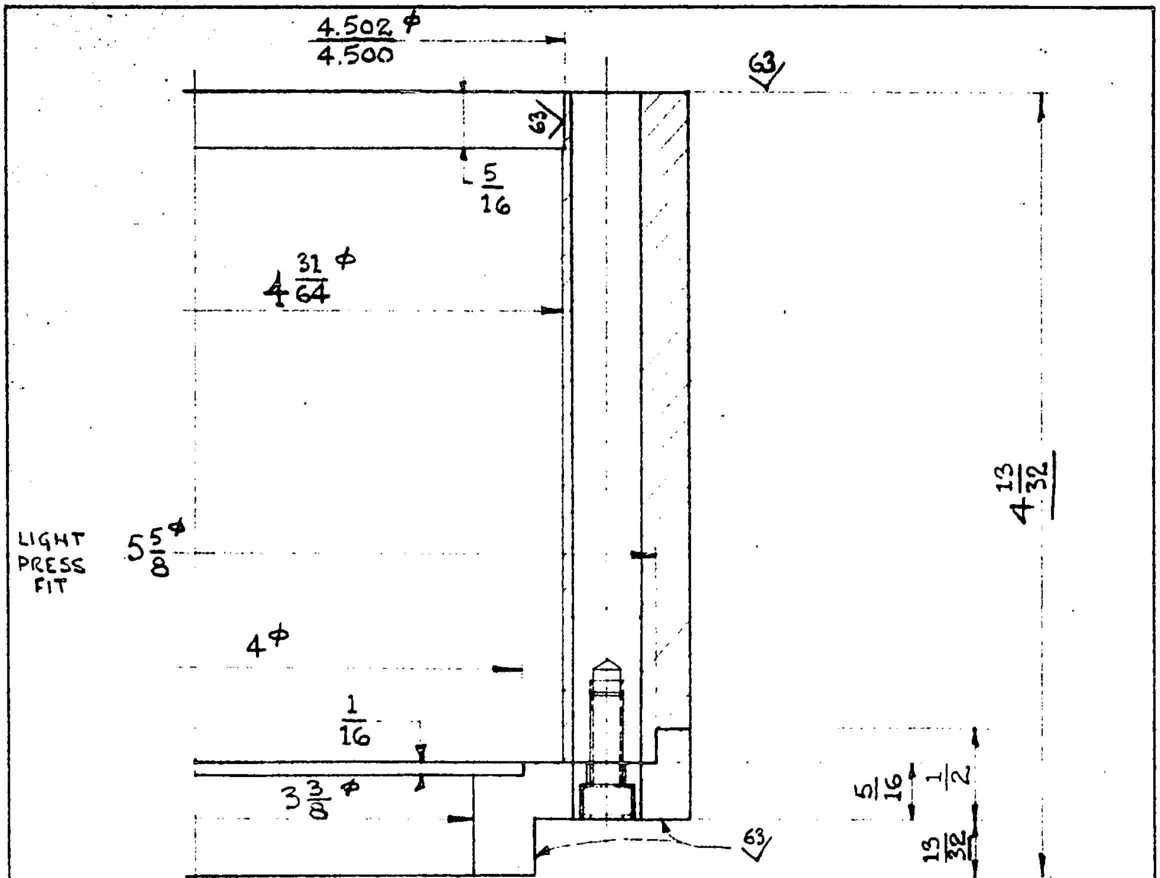

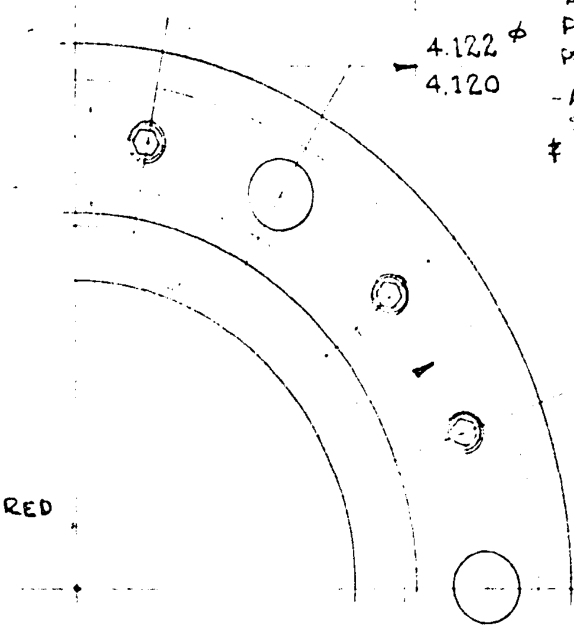

ALL FINISHED FLAT SURFACES PARALLEL TO ◁ .001/10 & PERPENDICULAR TO BORE AXIS ◁ .001/10
- ALL TOLERANCED CYLINDRICAL SURFACES CONCENTRIC TO .001 T.I.R. & SURFACES PARALLEL TO ◁ .001/10

"Y" DRILL THROUGH 6 EQUALLY SPACED HOLES ON 5ϕ B.C.
- PLACE 12 SCKT. HD. CAP SCRS. @ 20° ON EITHER SIDE OF DRILLED HOLES : #10-32NF × 1/2 LG. TO SECURE FLANGE RING : C'BORE SCR. HDS. FLUSH

MATERIAL: SC-A-0004*
AND { 6ϕ × 1 1/2 LG. CRS RND BAR
12 ONLY #10-32NF × 1/2 LG. SCT. HD. CAP SCRS.

1 REQUIRED

REVISIONS		SCALE: FULL SIZE
DRAWN: P.J. ZSOMBOR-MURRAY	McGILL UNIVERSITY — MONTREAL	DATE: 15 JULY 1965
CHECKED	EXPERIMENTAL LABORATORY SUPERCALENDER COUPLING BELL HOUSING - DRIVE END DYNAMOMETER ADAPTER	DRAWING NO: SC-0004*-2

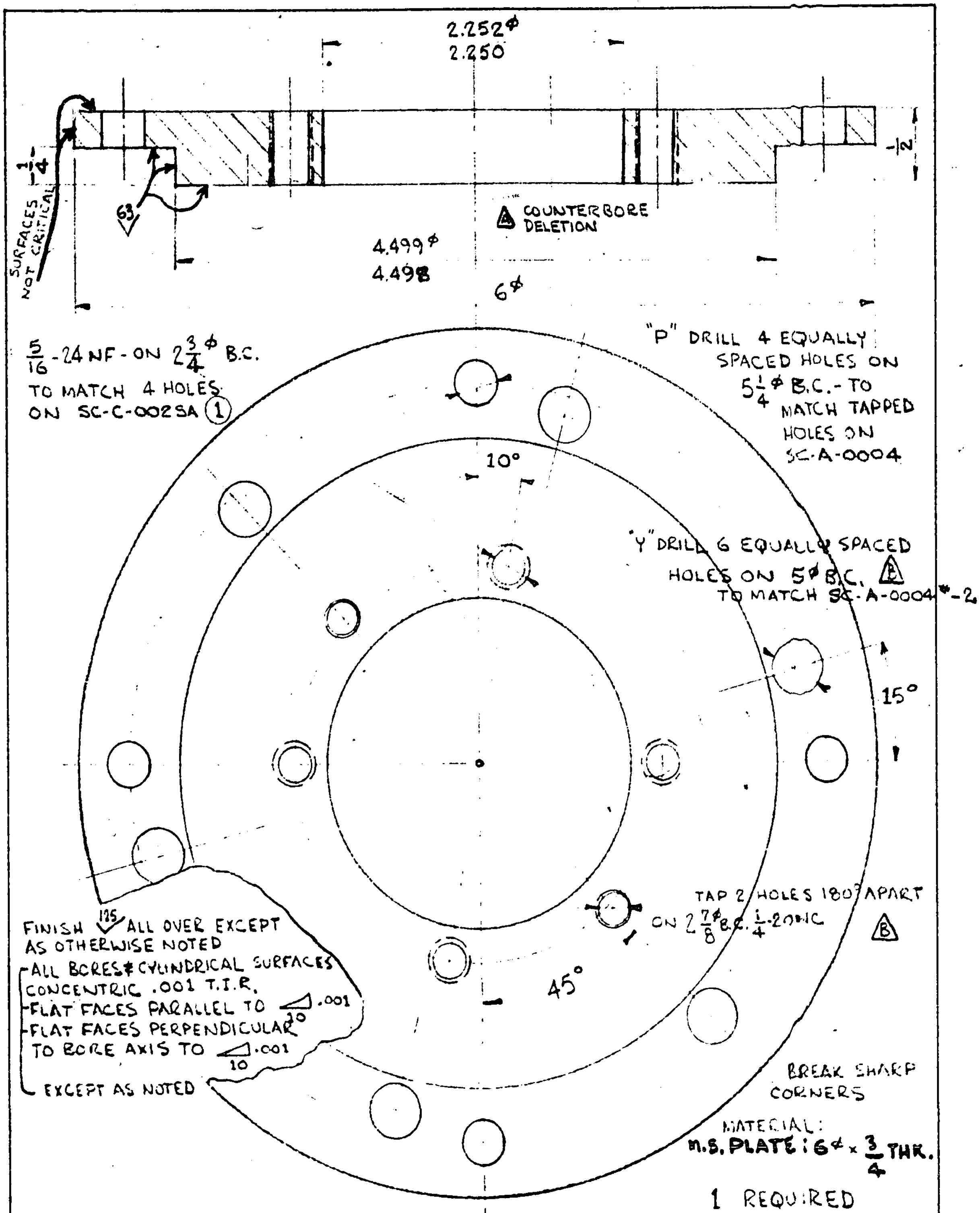

REVISIONS	23/3/65 (A)	15/7/65 (B)	SCALE: FULL SIZE
	GENERAL REVISION	ADD "Y" & 1/4-20NC HOLES	

DRAWN: P.J. ZSOMBOR-MURRAY	McGILL UNIVERSITY — MONTREAL	DATE: 7 JANUARY, 1965
CHECKED:	EXPERIMENTAL LABORATORY SUPERCALENDER ROLL END COUPLING ADAPTER	DRAWING NO: * SC-A-0005